

ISSN 1880-8468

Technical Report of  
International Development Engineering  
国際開発工学報告

TRIDE-2006-01

February 20, 2006

Abstracts of Master Theses

Presented in February 2006

Department of International Development Engineering,  
Graduate School of Science and Engineering,  
Tokyo Institute of Technology  
<http://www.ide.titech.ac.jp/TR>

# Technical Report of International Development Engineering

## TRIDE-2006-01

### Table of Contents

卷頭言 Preface (in Japanese)	太田秀樹 Hideki OHTA	1
A Study on the Decomposition of Nitrous Oxide over Titania Supported Metal Catalysts	Kiyoto YANAGIDA	3
Investigation of Natural Zeolite-based Catalyst Activity toward Soot Oxidation	Winarto KURNIAWAN	7
A Study on the Selective Catalytic Reduction of NO by Metal Oxides Supported on Titania	Cunfu TANG	11
A Study on New Approach to Prepare CoMo / Al <sub>2</sub> O <sub>3</sub> Catalyst for Deep Hydrodesulphurization	Haibo ZHANG	15
Improvement of Rubberwood Process Using the Thermally Treated Products from Wood Residue	Shunsuke KONISHI	19
Enzymatic Treatment of Phenol Waste Water with Thermo-Responsive Chitosan	Shuichi KAWATOKO	23
Extraction of Coal Tar Absorption Oil by a Continuous Counter Current Spray Column	Jun SAITO	27
Preparation and Structure Control of Plasma Polymerized Films by Utilizing Afterglow Region in Atmospheric Non-thermal Plasma	Takuo MIURA	31
Numerical Analysis for Solidification of Melt Plastic with a Spectral Finite Difference Scheme	Aya FUJITA	35
The Effect of Probe Shape and Wettability for Expanding Applicability of Micromanipulation Using Capillary Force	Kenichi J. OBATA	39
A Manipulation Method of a Dielectric Micro-Particle by Electrostatic Force	Min HAN	43
Beneficial 2-Way International Cooperation between Japan and Developing Countries in Asia: Technology Transfer of Welding Technology Case Study	Bruno Martins BRAGA	47
A Study on Plastic Deformation Mechanism without Dislocations in Metals by Transmission Electron Microscopy	Hidetoshi FUJII	51
Study of Mahalanobis Metric	Naoya INOUE	55
Study of Improvement of Kernel Sample Space Method	Chenghan PIAO	59

<b>Support Vector Machine with Asymmetric Kernels</b> .....	Shen LIU	63
<b>Moving Picture Coding with Pixel Motion Compensation Prediction</b> .....	Takayuki SHINOZAKI	67
<b>Propagation Paths Measurement System for Electronic Toll Collection Systems (ETC)</b> .....	Yumihiko ANNAKA	71
<b>Analysis of Radio Wave Propagation in Highway Electronic Toll Collection Gate</b> .....	Junsheng LU	75
<b>Location Estimation for Wild Animals</b> .....	Jun-ichi ABE	79
<b>Investigation of the Wave Scattering Characteristics by Using Physical Optics Approximation</b> .....	Navarat LERTSIRISOPON	83
<b>Sorption and Flushing Characteristic of Heavy Metal Ion Response to Sand</b> .....	Masatoshi AOKI	87
<b>Possible Mechanism of Hydraulic Fracturing Initiation</b> .....	Emiko TAKAHASHI	91
<b>Proposed Design Method of Cathodic Protection for Reinforced Concrete Member under Chloride Attack</b> .....	Keiyu KAWAAI	95
<b>Influence of Chloride Ion And ITZ around Horizontal Steel Bars on the Corrosion of Steel Bars in Concrete</b> .....	Yang SONG	99
<b>Seasonal and Diurnal Fluxes of Momentum, Energy, Water Vapor and CO<sub>2</sub> over Tokyo Bay</b> .....	Ryoko ODA	103
<b>Turbulent Flow Similarity in Open Air Scaled Models for Urban Micro Meteorology</b> .....	Masahiko KANEGA	107
<b>Observation Study on Water and Heat Transfer Processes in Urban Sewage System</b> .....	Yu NAKAYAMA	111
<b>Airport Capacity Analysis Considering Terminal Air Traffic Flow Control and Airlines' Aircraft Sizing Behavior</b> .....	Naoki YAMADA	115

## 巻頭言 Preface

国際開発工学専攻長 太田秀樹

Hideki OHTA, Head, Department of International Development Engineering

東京工業大学の工学部に、開発システム工学科が発足して10年たった。大学院には国際開発工学専攻が設置されて、学部から大学院までの一貫した体制がつくられ、特定の既存分野に偏ることなく、工学分野を広くカバーするため、いろいろな専門性をもった教員が集められた。学生も、日本人学生と外国人学生が半分ずつという構成である。「(1) アジア向け工学技術者の養成・(2) アジア人と日本人の混在教育・(3) 基幹4科目の専門教育とその連携・(4) 文化・歴史・ディベートなどの相互文化理解」という理念をかかげて、それを追求する体制である。

野心的な試みであったが、着実に教育・研究上の成果をあげてきた。教員ならびに学生が大変な努力をして、教育・研究上のあたらしい試みを実施し、実績を積み上げてきたのが国際開発工学専攻である。こういった10年間の蓄積をふまえて、新たな機運が教員のあいだで盛り上がってきた。10年の節目を契機に、「国際開発工学」という学問分野そのものを創りあげよう、というわけである。学問上の新たな目標として、「国際開発工学」とは何であるかを追求したい。具体的な研究成果を公表することで、「国際開発工学」のあるべき実体をしめす努力をしようという機運が熟した。

ひとくちに「国際開発工学」といっても、その実体はあいまいである。取り扱う内容が多岐にわたるうえ、既存の工学分野との協働が不可欠であるから、試行錯誤の連続から出発することになるであろう。そういった努力を公表する場として、ここに「国際開発工学報告 Technical Report of International Development Engineering (TRIDE)」を創刊する。

「国際開発工学」創出の学問的努力のなかから、従来 of 既存分野にはなかった全く新しい概念がつつぎと誕生することを期待したい。



# A study on the decomposition of nitrous oxide over titania supported metal catalysts

Student Number : 04M18185 Name : Kiyoto YANAGIDA Supervisor : Hirofumi HINODE

## チタニア担持金属触媒による N<sub>2</sub>O 分解

柳田 希与人

本研究では、チタニア担持金属触媒（銅、鉄、マンガン、ニオブ）の N<sub>2</sub>O 分解活性について検討した。チタニア担持銅触媒とチタニア担持鉄触媒は、反応温度 650 °C において N<sub>2</sub>O をほぼ完全に分解した。また、チタニア担持銅触媒の N<sub>2</sub>O 分解における担体チタニアの影響について検討したところ、最適銅担持量はチタニアの比表面積に比例し、ルチル構造を有するチタニアが有効であることがわかった。

### 1. Introduction

Nitrous oxide (N<sub>2</sub>O) is one of the powerful greenhouse gases with a global warming potential per molecule of about 300 times that of carbon dioxide (CO<sub>2</sub>). N<sub>2</sub>O is also identified as a contributor to the destruction of ozone layer in the stratosphere. Therefore, it is important to study decomposition of N<sub>2</sub>O from the environmental point of view. Recently, a considerable number of studies have been conducted on the catalytic decomposition and the selective catalytic reduction of N<sub>2</sub>O [1-8].

In our laboratory, selective catalytic reduction of NO to N<sub>2</sub> over TiO<sub>2</sub> supported metal catalysts in the presence of hydrocarbon had been studied, and TiO<sub>2</sub> supported metal catalysts had shown a good activity [9]. In the reaction of NO to N<sub>2</sub>, N<sub>2</sub>O is produced only at low temperature region and not at high temperature region. From this result, it can be interpreted that N<sub>2</sub>O produced from NO reduction is completely decomposed at high temperature region. It was assumed that TiO<sub>2</sub> supported metal catalysts will also show a good activity for N<sub>2</sub>O decomposition. And another advantage for using TiO<sub>2</sub> as a support is the high tolerance to water vapor, which is an important characteristic for N<sub>2</sub>O decomposition catalyst.

In this research, the decomposition of N<sub>2</sub>O over TiO<sub>2</sub> supported various metal catalysts was investigated.

### 2. Experimental

#### 2.1 Catalyst preparation

M/TiO<sub>2</sub> (M=Cu, Fe, Mn, Nb) catalysts were prepared by impregnation method. TiO<sub>2</sub> (JRC-TIO-1, 2, 4, 5 and 6; reference catalyst, Catalysis Society of Japan) were used as supports.

In the case of preparation of Cu/TiO<sub>2</sub>, TiO<sub>2</sub> was impregnated in an aqueous solution of Cu(NO<sub>3</sub>)<sub>2</sub>·3H<sub>2</sub>O (99.9%, Wako Co.). Each of the solutions was stirred at room

temperature for one day followed by 24 hours drying up at 60 °C. Then the catalysts were calcined at 600 °C for 5 hours under air flow. In order to reduce pressure drop, the catalysts were pelletized, crushed and sieved to between 0.71mm to 1.00mm. The following nomenclatures for the catalyst samples are used: Cu(xwt%)/TiO<sub>2</sub> y where x means Cu loading levels, and y represent reference support number (e.g. Cu(1wt%)/TiO<sub>2</sub> means JRC-TIO-1 with Cu loading of 1wt%).

The sources of Fe, Mn and Nb were Fe(NO<sub>3</sub>)<sub>3</sub>·9H<sub>2</sub>O (99.9%, Wako Co.), MnCO<sub>3</sub>·nH<sub>2</sub>O (99.9%, Wako Co.) and NH<sub>4</sub>[NbO(C<sub>2</sub>O<sub>4</sub>)<sub>2</sub>(H<sub>2</sub>O)<sub>2</sub>]·nH<sub>2</sub>O (CBMM), respectively.

#### 2.2 Catalytic activity experiment

The catalytic reaction was carried out in a fixed-bed flow reactor under atmospheric pressure, and the reactant gas was prepared by mixing N<sub>2</sub>O, O<sub>2</sub> and He as a balance gas. Then the mixed gas of 1000ppm N<sub>2</sub>O, 10% O<sub>2</sub> and He was fed to the catalyst at flow rate of 5.0-6.0ml/s, which correspond to 16000h<sup>-1</sup> of space velocity. Water vapor was introduced by using the bubbling system, and the concentration of water vapor was approximately 5vol%.

Gas chromatography (GC323w; GL Science Co., with Porapak N, Porapak Q and Molecular Sieve 13X column) was used to analyze N<sub>2</sub>O, N<sub>2</sub> and O<sub>2</sub>.

#### 2.3 Catalyst characterization

Characterization of catalyst was performed by XRD (MultiFlex; Rigaku) and BET (SA3100; COULTER).

### 3. Result and discussion

#### 3.1 The activity for the decomposition of N<sub>2</sub>O over M/TiO<sub>2</sub> (M = Cu, Fe, Mn, Nb)

Figure 1 shows the catalytic activity of M/TiO<sub>2</sub> (M=Cu, Fe, Mn, Nb) catalysts for

N<sub>2</sub>O decomposition. The loading level for each sample here was selected from the loading level of the sample with the best performance result.

The product of NO and NO<sub>2</sub> were not detected in all condition.

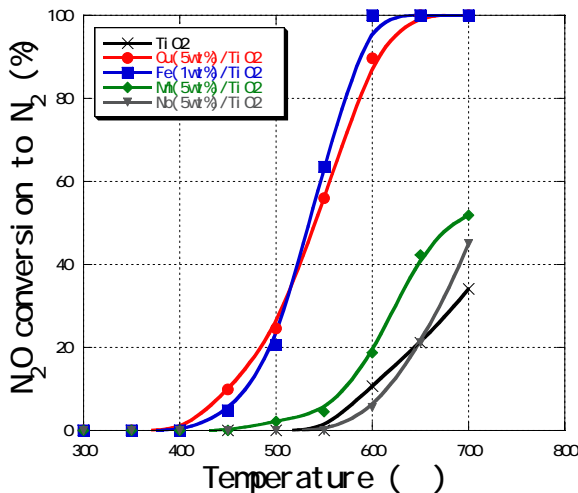


Fig.1 Comparison of the catalytic activity for the decomposition of N<sub>2</sub>O over each catalyst

Parent JRC-TIO-4 calcined at 600 decomposed only 34% of N<sub>2</sub>O to N<sub>2</sub> even at 700 °C, however when the copper was supported on TiO<sub>2</sub>, the catalytic activity was promoted. When Cu loading level was 5wt%, the highest catalytic activity for the decomposition of N<sub>2</sub>O was achieved. Decomposition of N<sub>2</sub>O to N<sub>2</sub> over Cu(5wt%)/TiO<sub>2</sub> catalysts began at 400 °C, and the conversion of N<sub>2</sub>O to N<sub>2</sub> reached 100% at 650 °C. Fe(1wt%)/TiO<sub>2</sub> completely decomposed N<sub>2</sub>O at 650 °C.

Mn(5wt%)/TiO<sub>2</sub> and Nb(5wt%)/TiO<sub>2</sub> decomposed only approximately 50% of N<sub>2</sub>O even at 700 °C.

Copper showed better activity for N<sub>2</sub>O decomposition than the other active metals, Fe, Mn and Nb. Therefore, Cu/TiO<sub>2</sub> was used for the next investigations.

### 3.2 The effect of TiO<sub>2</sub> as support

In order to study the effect of TiO<sub>2</sub> as support on the catalytic activity of Cu/TiO<sub>2</sub> for N<sub>2</sub>O decomposition, Cu/TiO<sub>2</sub> catalysts were prepared from JRC-TIO-1, 2, 4, 5 and 6. The relationship between the optimum Cu loading level of Cu/TiO<sub>2</sub> and the specific surface area of TiO<sub>2</sub> support and also between the catalytic activity and the crystal structure of TiO<sub>2</sub> were evaluated.

Figures 2 to 5 show the catalytic activity of Cu/TiO<sub>2</sub> for N<sub>2</sub>O decomposition prepared from JRC-TIO-1, 2, 4 and 6, respectively.

From the results of Figures 2 to 5, the

optimum Cu loading levels of Cu/TiO<sub>2</sub> prepared from JRC-TIO-1, 2, 4 and 6 were 10wt%, 1wt%, 5wt% and 5wt%, respectively. The difference of the optimum Cu loading level was considered to be related with the difference of the specific surface area of each TiO<sub>2</sub>.

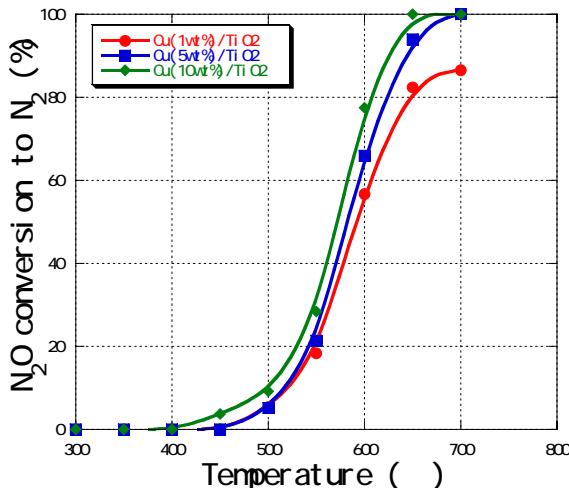


Fig.2 The catalytic activity for the decomposition of N<sub>2</sub>O over Cu/TiO<sub>2</sub>

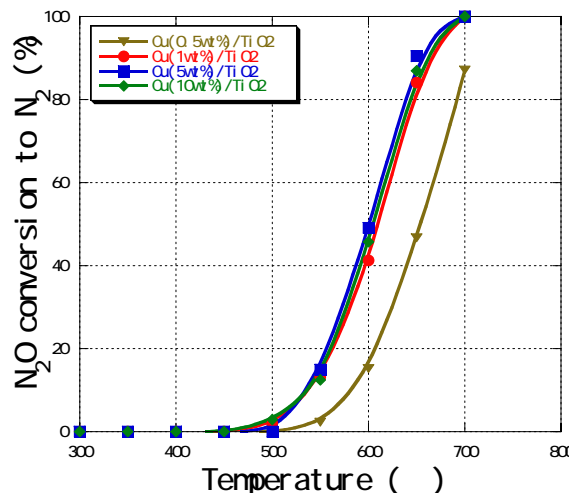


Fig.3 The catalytic activity for the decomposition of N<sub>2</sub>O over Cu/TiO<sub>2</sub>

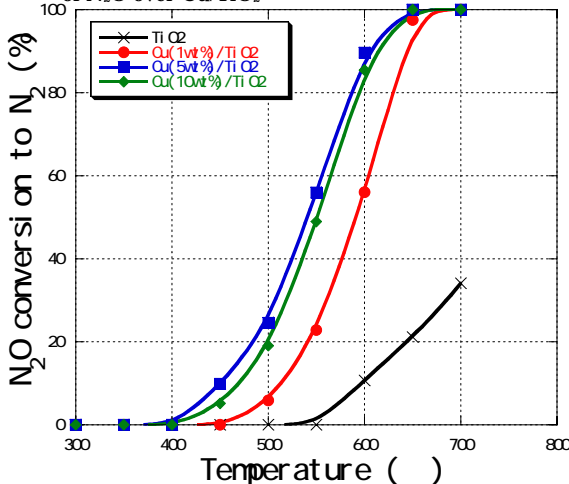


Fig.4 The catalytic activity for the decomposition of N<sub>2</sub>O over Cu/TiO<sub>2</sub>

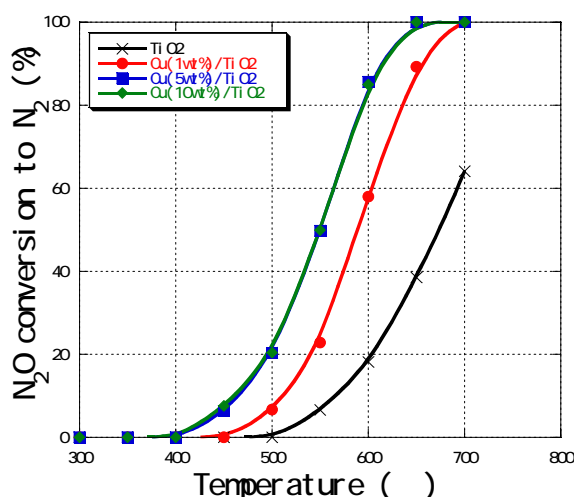


Fig.5 The catalytic activity for the decomposition of  $N_2O$  over  $Cu/TiO_2$

The BET specific surface areas of JRC-TIO-1, 2, 4, 5 and 6 were  $82.0m^2/g$ ,  $15.9m^2/g$ ,  $52.9m^2/g$ ,  $1.24m^2/g$  and  $73.0m^2/g$ , respectively. The projected area of one molecule of  $CuO$  on the surface of  $TiO_2$  was calculated by using the radius of  $Cu^{2+}$  ion and  $O^{2-}$  ion and the bonding distance of  $Cu-O$  molecule ( $Cu^{2+} : 0.69$  ,  $O^{2-} : 1.40$  ,  $Cu-O : 1.95$  ). The projected area of one molecule of  $CuO$  on the surface of  $TiO_2$  was calculated to approximately  $7.59 \text{ \AA}^2$  by using the geometrical equation in Eq.1.

$$S = \int_{-1.40}^{1.355} \sqrt{1.40^2 - x^2} dx + \int_{1.355}^{2.64} \sqrt{0.69^2 - (x-1.95)^2} dx \quad (\text{Eq.1})$$

However, during impregnation, it was  $Cu(NO_3)_2$  rather than  $CuO$  that was dispersed and loaded on the surface of  $TiO_2$ . Therefore the projected area of  $Cu(NO_3)_2$  on  $TiO_2$  surface was also calculated. When the surface of  $TiO_2$  was assumed to be uniform and, covered with  $CuO$  or  $Cu(NO_3)_2$  monolayer, the necessary amount of  $CuO$  or  $Cu(NO_3)_2$  molecule to make one full layer on the  $TiO_2$  surface could be calculated.

Table 1 Relationship between specific surface area of  $TiO_2$  and optimum Cu loading level for the decomposition of  $N_2O$

Support	Specific surface area ( $m^2/g$ )	Optimum Cu loading level (wt%)		
		Experimental data	Geometrical calculation of $CuO$	Geometrical calculation of $Cu(NO_3)_2$
JRC-TIO-1	82.0	10	11.4	2.25
JRC-TIO-2	15.9	1	2.21	0.436
JRC-TIO-4	52.9	5	7.35	1.45
JRC-TIO-5	1.24	0.5	0.172	0.0340
JRC-TIO-6	73.0	5	10.1	2.00

Table 1 shows the relationship between the BET specific surface area of  $TiO_2$  and the optimum Cu loading level of  $Cu/TiO_2$  from the catalytic activity experiments for  $N_2O$  decomposition and geometrical calculation from  $CuO$  and  $Cu(NO_3)_2$  projected area.

The results from Table 1 indicate that the optimum Cu loading level of  $Cu/TiO_2$  obtained from the catalytic activity experiments was agreed well with on the calculated value from the projected area of  $CuO$ . Therefore, when the  $TiO_2$  surface was covered with  $CuO$  molecule completely, the catalytic activity for the decomposition of  $N_2O$  reached the highest value. If the amount of  $CuO$  loaded exceeded the optimum loading, the catalytic activity remained the same or declined because of sintering of copper.

Figure 6 shows comparison of the catalytic activities over  $Cu/TiO_2$  prepared from JRC-TIO-1, 2, 4, 5 and 6. The Cu loading level for each sample here was selected from loading level of the sample with the best performance result.

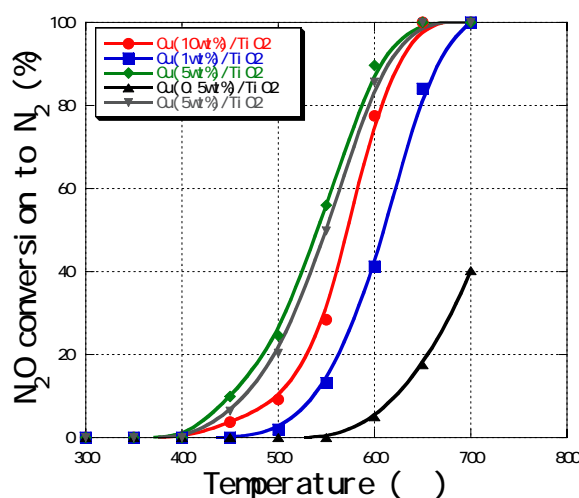


Fig.6 The catalytic activity for the decomposition of  $N_2O$  over  $Cu/TiO_2$  prepared from each  $TiO_2$

The catalytic activity of Cu(1wt%)/TiO<sub>2</sub> and Cu(0.5wt%)/TiO<sub>2</sub> for the decomposition of N<sub>2</sub>O were the lower than the other catalysts in this experiment. The small specific surface area and the low Cu loading level were considered as the causes of the low activity of Cu(1wt%)/TiO<sub>2</sub> and Cu(0.5wt%)/TiO<sub>2</sub>.

Cu(5wt%)/TiO<sub>2</sub> and Cu(5wt%)/TiO<sub>2</sub> had higher catalytic activity than Cu(10wt%)/TiO<sub>2</sub>.

Figure 7 shows the results of XRD patterns of Cu/TiO<sub>2</sub> catalyst with the optimum loading level.

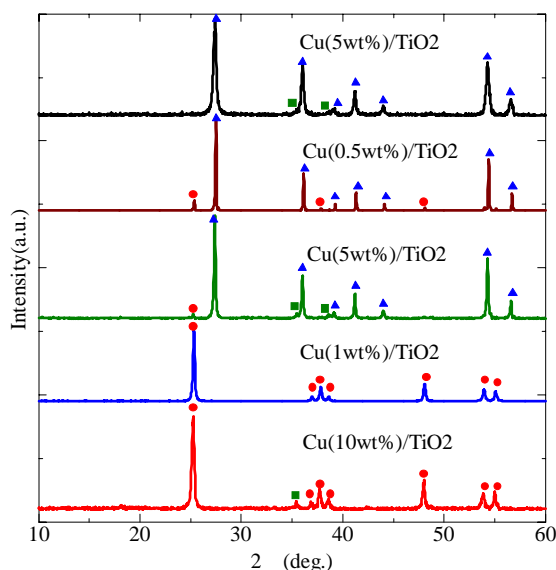


Fig.7 XRD patterns of Cu/TiO<sub>2</sub> prepared from each TiO<sub>2</sub> ( □ : anatase, △ : rutile, ○ : CuO)

It can be seen from figure 6 and figure 7 that both Cu(5wt%)/TiO<sub>2</sub> and Cu(5wt%)/TiO<sub>2</sub> that constitute of rutile structure exhibited higher activity for N<sub>2</sub>O decomposition than Cu(10wt%)/TiO<sub>2</sub> that constitutes of anatase.

Therefore, the rutile structure was considered to be more effective for the decomposition of N<sub>2</sub>O than anatase structure.

### 3.3 The influence of water vapor

Figure 8 shows the influence of water vapor on the catalytic activity of Cu(5wt%)/TiO<sub>2</sub> for N<sub>2</sub>O decomposition. The difference of the catalytic activity for N<sub>2</sub>O decomposition was not observed at all. Even though many catalysts for the decomposition of N<sub>2</sub>O were reported to show lower activity in the presence of water vapor, this result indicates that the presence of water vapor did not influence this catalytic

system of Cu/TiO<sub>2</sub>.

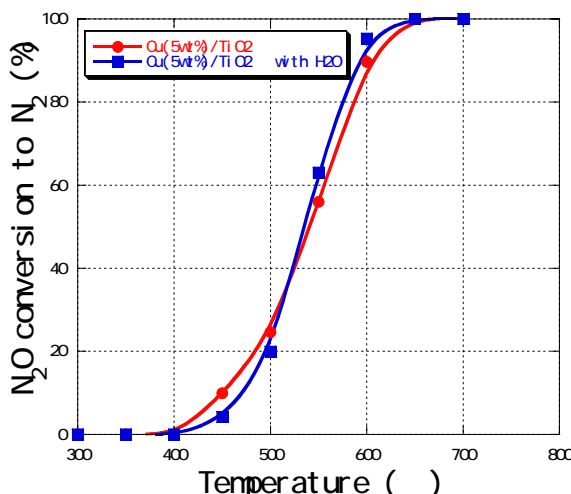


Fig.8 The influence of water vapor on the catalytic activity of Cu(5wt%)/TiO<sub>2</sub> for N<sub>2</sub>O decomposition

### 4. Conclusion

Cu(5wt%)/TiO<sub>2</sub> and Fe(1wt%)/TiO<sub>2</sub> exhibited the catalytic activity for N<sub>2</sub>O decomposition. N<sub>2</sub>O was decomposed completely at 650.

If the BET specific surface area of TiO<sub>2</sub> support was larger, the optimum Cu loading level of Cu/TiO<sub>2</sub> was higher. When TiO<sub>2</sub> surface was covered with CuO completely, the catalytic activity for the decomposition of N<sub>2</sub>O reached the highest value.

The rutile structure was considered to be more effective for the decomposition of N<sub>2</sub>O than anatase structure.

The presence of water vapor did not influence this catalytic system of Cu/TiO<sub>2</sub> for N<sub>2</sub>O decomposition.

### Reference

- [1] J.Haber, et al., Catal. Today, 90 (2004) 15.
- [2] A. Dandekar and M.A. Vannice, Appl. Catal. B, 22 (1999) 179.
- [3] J. Lin, et al., Appl. Surf. Sci., 103 (1996) 307.
- [4] Javier Perez-Ramirez and Freek Kapteijn, Cat. Com., 4 (2003) 333.
- [5] Shin-ichi Tanaka, et al., Catal. Today, 63 (2000) 413.
- [6] T. Chaki, et al., J.Catal., 218 (2003) 220.
- [7] C. Pophal et al., Appl. Catal. B, 16 (1998) 177.
- [8] Liang Yan et al., Appl. Catal. B, 45 (2003) 85.
- [9] J. Mitadera and H. Hinode, Appl.Catal. B, 39 (2002) 205

## Investigation of Natural Zeolite-based Catalyst Activity toward Soot Oxidation

Winarto KURNIAWAN (04M18200)

Research Advisor: Prof. Hirofumi HINODE

### 天然ゼオライト系触媒の煤酸化活性に関する研究

#### Abstract

インドネシア産天然ゼオライト、ベントナイト及び両者を修飾した試料（塩基処理、ナトリウム担持、硝酸ナトリウム担持）の煤酸化に対する活性について熱重量分析による最高酸化温度低下量（ $\Delta T$ ）によって検討した。触媒のキャラクタリゼーションは ICP、XRD、SEM-EDX で行った。天然ゼオライト及びベントナイトは  $\Delta T$  がそれぞれ約 10 及び 20 と活性は低かったが、修飾することにより活性が向上した。最も活性が高く安定性もある触媒は 4M 及び 6M の水酸化ナトリウムで処理したベントナイトであり、両者は 185 の  $\Delta T$  を示した。触媒の中に含まれているアルカリ金属がその高い活性に貢献したと考えられる。

#### 1. Introduction

Soot from diesel engine exhaust can cause severe health problems. Soot can penetrate into lung and gives rise to carcinogenic effects<sup>[1]</sup>. Due to its harmful property, it is essential to develop improved pollution control equipment that can address soot emission problem from diesel engines, for example by using catalyst to oxidize soot into carbon dioxide.

Removal of soot by means of oxidation requires high temperature because typical soot oxidation starts from around 650°C. On the other hand, diesel engine exhaust gas temperature is in the range of 150 to 400°C<sup>[2]</sup>. Therefore, an active catalyst to lower soot oxidation temperature down to diesel engine exhaust gas temperature range is required.

One of the promising materials that can be used as catalyst is zeolite. Compared to other materials, zeolite possesses several advantages, i.e. it is resistant to thermal recursion and the spent catalyst presents less disposal problem. On the other hand, zeolite also has disadvantage, which is its low hydrothermal stability<sup>[3][4][5]</sup>.

In Indonesia, natural zeolite exists in abundance throughout wide area. Although the utilization of this natural zeolite in the area of catalysis has been examined deeply, so far there is no research performed

to investigate its activity toward soot oxidation. Based on the facts above, it is necessary to investigate the potentiality of zeolite as catalyst for soot oxidation.

In this research, the catalytic activities toward soot oxidation of Indonesian natural zeolite (Zeolite Lampung) and also natural bentonite (Bentonite Bandung), which often be found together with zeolite, were investigated. Both were tested for their activity before and after treatment. Treatment methods used were alkali treatment, NaNO<sub>3</sub> loading, and Na loading methods.

#### 2. Materials and Methods

##### 2.1 Materials

Catalyst materials were Zeolite Lampung (mainly consists of clinoptilolite) and Bentonite Bandung. Alkaline solution for alkali treatment method was NaOH (Wako Pure Chemical Industries Ltd.). Precursor for NaNO<sub>3</sub> loading and Na loading methods was NaNO<sub>3</sub> (Wako Pure Chemical Industries Ltd.). BP3700 (Cabot Chemical Company Ltd.) was used as model soot.

##### 2.2 Catalyst Preparation

###### *Alkali treatment method*

Materials were stirred into alkaline solution for 24 hours at room temperature. Materials were then

washed, dried, and calcined at 600°C for 3 hours in air.

#### *NaNO<sub>3</sub> loading method*

Materials were impregnated in NaNO<sub>3</sub> solution for 24 hours, and then dried at 80°C for 24 hours.

#### *NaNO<sub>3</sub> loading method*

Materials were impregnated in NaNO<sub>3</sub> solution for 24 hours. Materials were then dried at 80°C for 24 hours and calcined at 600°C or 750°C for 5 hours in air.

### **2.3 Activity Test**

The activity tests were carried out inside thermobalance (Thermoplus TG-8210, Rigaku Corp.). The samples were prepared by mixing soot and catalyst in tight mode (soot and catalyst were grinded together in agate mortar to achieve close contact<sup>[6]</sup>), with soot to catalyst ratio of 1:10. Platinum crucible was used for sample container. Samples were heated to 750°C with temperature increase rate of 10°C/min. To give an oxidizing atmosphere, air was flowed through the thermobalance at flow rate of 100 mL/min.

Activities of developed catalysts were evaluated from thermogravimetry data in terms of the decrease of soot oxidation temperature ( $\Delta T$ ), which is the difference between the temperature of peak of catalyzed soot oxidation and that of uncatalyzed one.

### **2.4 Catalyst Characterization**

Catalyst characterization was performed using powder X-ray diffraction (XRD, Multiflex X-ray Diffractor, Rigaku Co.), Inductively Plasma Spectroscopy (ICP, SPS7800, Seiko Instruments Inc.), and Energy Dispersive X-ray Spectroscopy (EDX, SEM-EDS JSM-5310LV, JEOL Ltd.).

## **3. Result and Discussion**

### **3.1 Activity Test**

The activity of developed catalysts is shown in Fig. 1 and 2. Horizontal axis indicates temperature, while vertical axis corresponds to differential thermogravimetry (DTG, weight loss of sample per unit time). Peak of DTG curve corresponds to the

temperature at which soot oxidation at the fastest. It can be seen that raw natural zeolite and bentonite showed a low activity toward soot oxidation, with  $\Delta T$  of 10°C and 20°C, respectively. Treatment with alkaline solution has proven to increase the activity of the catalysts. In the case of zeolite, the concentration of NaOH used did not influence activity of catalysts significantly. Zeolites treated with 0.1 M, 1 M, and 2 M of NaOH exhibited similar activity. In the case of bentonite, an increase in NaOH concentration used resulted in the increase of activity of catalysts. However, as the concentration of NaOH reached 4 M, increase in concentration did not influence the activity. It was thought that the activity of bentonite has reached its maximum value after treatment with 4 M of NaOH.

The catalysts that showed the highest activity while still exhibiting good stability at high temperature were bentonite treated with 4 M and 6 M of NaOH. Both catalysts showed  $\Delta T$  of 185°C.

Na-loaded zeolite with loading level of 20% showed a  $\Delta T$  of 205°C, higher than the former two catalysts. However, this catalyst was found to have melted concurrently with soot oxidation.

NaNO<sub>3</sub>-loaded zeolite and bentonite (for both loading levels of 10% and 20%) showed  $\Delta T$  of 240°C, the highest  $\Delta T$  in this research. However, it was found that the catalysts were also exhibited weight loss during catalytic process, which showed that these catalysts have low stability at high temperature.

### **3.2 Catalyst Characterization**

The XRD patterns of selected catalysts are shown in Fig. 3. It can be seen that bentonite treated with 4 M and 6 M of NaOH exhibited weaker spectra compared to bentonite treated with lower concentration NaOH. These weak spectra were thought to be caused by destruction of some bentonite structure in the catalyst. Data from EDX analysis supports this hypothesis, in which the weight fraction of Al and Si decreased in both materials. EDX analysis also shows higher Na

weight fraction on these materials, which was thought to contribute to the increase of their catalytic activity.

NaNO<sub>3</sub>-loaded zeolite and bentonite show additional XRD spectra, which belong to NaNO<sub>3</sub>.

Therefore, it can be concluded that NaNO<sub>3</sub> exists on the surface of these catalysts and that high activity and low thermal stability of these catalysts could be attributed to the existence of this compound.

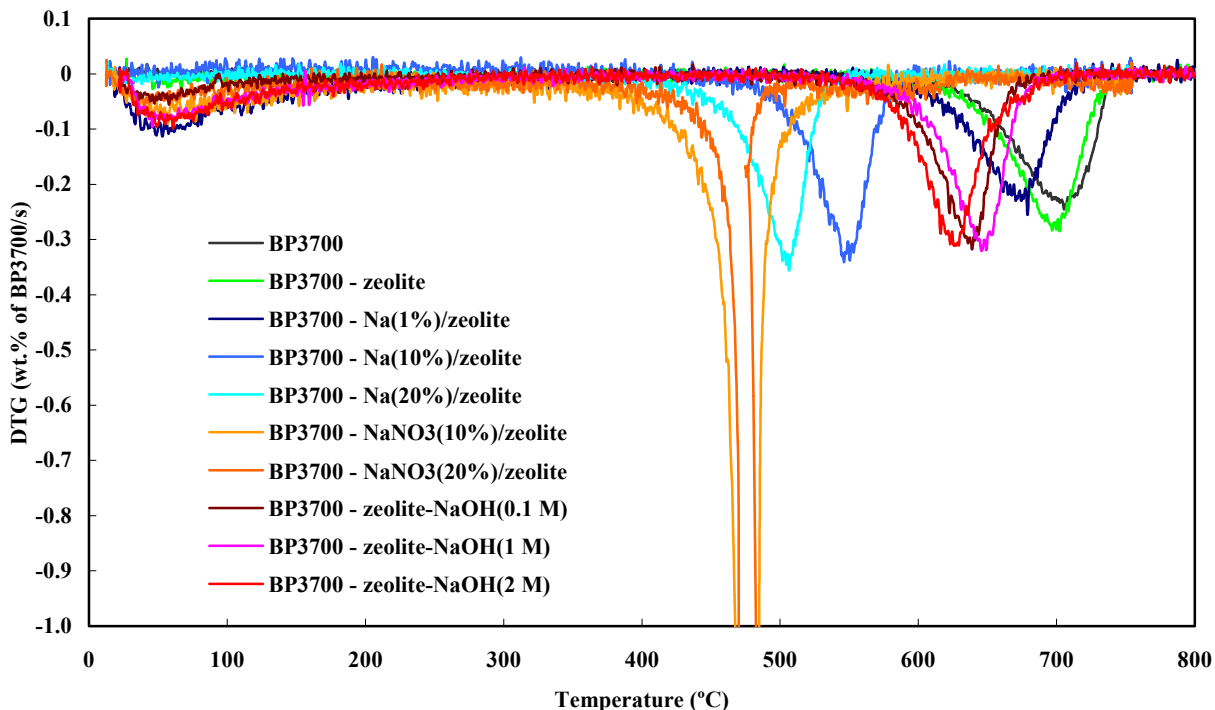


Fig. 1 Comparison of zeolite-based catalysts activity toward soot oxidation

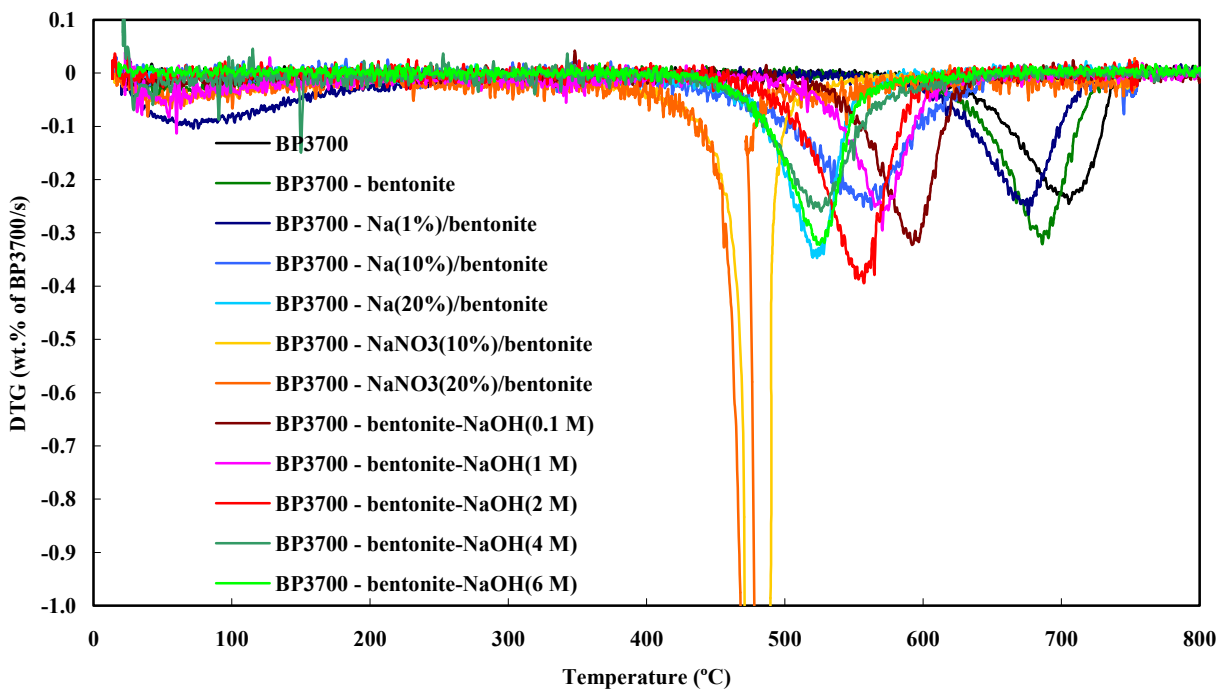


Fig. 2 Comparison of bentonite-based catalysts activity toward soot oxidation

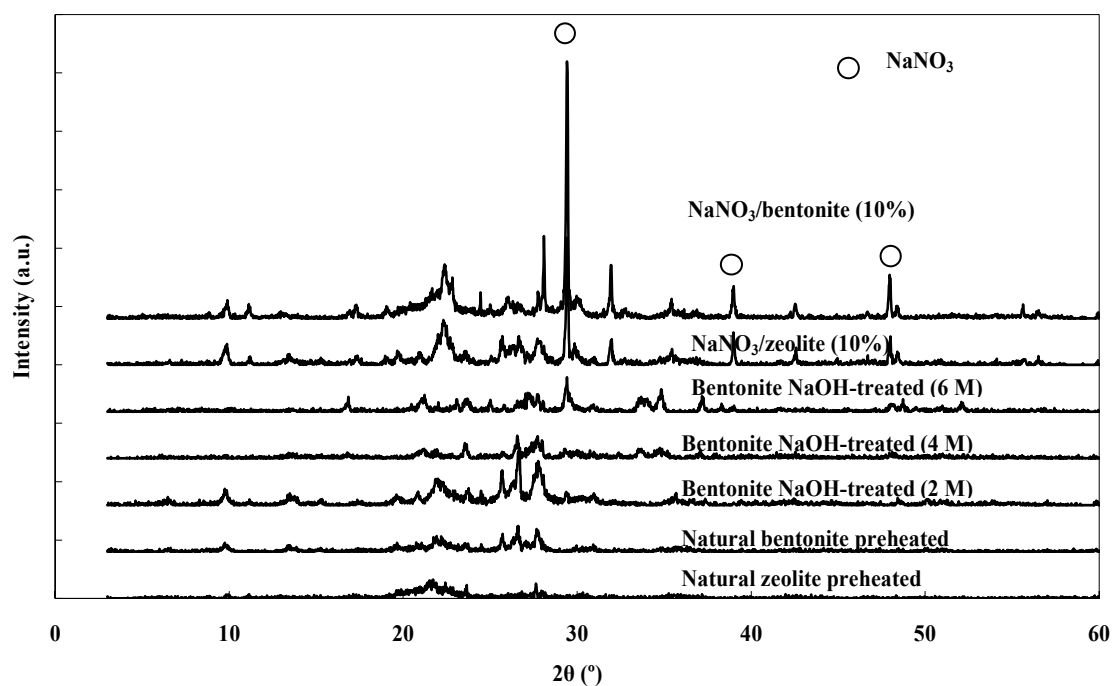


Fig. 3 XRD spectra of selected catalysts

#### 4. Conclusion

Indonesia natural zeolite and bentonite showed low activity toward soot oxidation. Treatment with alkali treatment,  $\text{NaNO}_3$  loading, and Na loading methods successfully increased the activity of natural zeolite and bentonite. The catalysts with the highest activity that still possessed stability at soot oxidation temperature were bentonite treated with 4 M and 6 M of NaOH, with  $\Delta T$  of 185°C. Na-loaded zeolite (loading level of 20%) showed an even higher activity with  $\Delta T$  of 205°C. However, this catalyst was found to melt simultaneously with soot oxidation. The highest activity was shown by  $\text{NaNO}_3$ -loaded zeolite and bentonite with  $\Delta T$  of 235 °C. However, these catalysts were found to decompose simultaneously with soot oxidation, making the catalysts unsuitable for practical applications. These high activities were attributed to the presence of Na species on the surface of catalysts.

#### References

- [1] Wang S., Haynes B.S.; "Catalytic combustion of soot on metal oxides and their supported metal chlorides", *Catal. Comm.*, **4**:591-596 (2003)
- [2] Galdeano N.F, Carrascull A.L., Ponzi M.I., Lick I.D., Ponzi E.N.; "Catalytic combustion of particulate matter. Catalysts of alkaline nitrates supported on hydrous zirconium", *Thermochim. Acta*, **421**:117-121 (2004)
- [3] Wallin M., Karlsson C.J., Skoglundh M., Palmqvist A.; "Selective catalytic reduction of  $\text{NO}_x$  with  $\text{NH}_3$  over zeolite H-ZSM-5: Influence of transient ammonia supply", *J. Catal.*, **218**:354-364 (2003)
- [4] Stevenson S.A., Vartuli J.C., Sharma S.B.; "The effects of steaming and sodium exchange on the selective catalytic reduction of NO and  $\text{NO}_2$  by  $\text{NH}_3$  over HZSM-5", *J. Catal.*, **208**:106-113 (2002)
- [5] Pieterse J.A.Z., van den Brink R.W., Booneveld S., de Bruijn F. A.; "Durability of ZSM5-supported Co-Pd catalysts in the reduction of  $\text{NO}_x$  with methane", *Appl. Catal. B*, **39**:167-179 (2002)
- [6] Stanmore B.R., Brillhac J.F., Gilot P.; "The oxidation of soot: a review of experiments, mechanisms and models", *Carbon*, **39**:2247-2268 (2001)

# A study on the selective catalytic reduction of NO by metal oxides supported on titania

Student Number: 04M18239 Name: Cunfu TANG Supervisor: Hirofumi HINODE

チタニア担持金属触媒による NO 選択還元

湯 存福

本研究では、炭化水素を還元剤としたチタニア担持金属(Fe、Mn)触媒による NO 選択還元反応において、触媒の調製方法が触媒還元活性に与える影響を検討した。その中で、Fe<sub>2</sub>O<sub>3</sub> と Mn/TiO<sub>2</sub> の機械的混合触媒の場合、Mn/TiO<sub>2</sub> 触媒単独のときと比べ、触媒活性が向上した。Fe/TiO<sub>2</sub> 及び Mn/TiO<sub>2</sub> の二層式触媒においては、触媒層の設置順序の違いが触媒活性に大きな影響を与え、Mn/TiO<sub>2</sub> 触媒を二層目にした場合、低温側で二種の触媒の相乗効果が得られた。

## 1. Introduction

Nitrogen oxides (NO, NO<sub>2</sub>) are major sources of air pollution. Since they cause photochemical smog and acid rain. And almost all NO<sub>x</sub> come from automobiles (49%) and power plants (46%) [1]. To reduce the emission of nitrogen oxide the catalytic technologies are quite attractive because of their low cost and high efficiency [1]. Among these technologies, the selective catalytic reduction of NO<sub>x</sub> with hydrocarbons (HC-SCR) has attracted much attention, because of its potential ability to eliminate NO<sub>x</sub> emission from the oxygen-rich exhaust.

It was suggested by many researchers that the HC-SCR reaction is carried out by the reaction to generate NO<sub>2</sub> followed by the reaction of NO<sub>2</sub> with hydrocarbons [2].

In the case of HC-SCR of NO, propene also performed high reduction activity [3]. As for the generation of CO<sub>2</sub>, generally the following two reactions are considered:



Mn/TiO<sub>2</sub> and Fe-Mn/TiO<sub>2</sub> have been reported that they were active for the reduction of nitrogen

monoxide by ammonia in the presence of oxygen [4].

In this paper, we investigate the activities of the M/TiO<sub>2</sub> (M=Fe, Mn) catalyst for the HC-SCR of NO with propene. And we also investigated the influences of the catalyst preparation method on the catalytic reduction activity.

## 2. Experimental

M/TiO<sub>2</sub> (M=Fe, Mn) were prepared by impregnation method. TiO<sub>2</sub> (JRC-TIO-4) and Fe(NO<sub>3</sub>)<sub>3</sub> · 9H<sub>2</sub>O (or MnCO<sub>3</sub> · nH<sub>2</sub>O) were mixed in 300 ml of ion exchange water. The mixtures were then stirred at room temperature for one day. The solutions were dried up at 70 °C for 24 hrs. Then they were calcined at 600 °C in air for 5 hrs. Finally, the samples were crushed and sieved to 0.71-1.00 mm. TiO<sub>2</sub> (JRC-TIO-4) was supplied from the Catalysis Society of Japan. Fe(NO<sub>3</sub>)<sub>3</sub> · 9H<sub>2</sub>O and MnCO<sub>3</sub> · nH<sub>2</sub>O were purchased from Wako Pure Chemicals Industries, Ltd.

For the catalyst preparation method, co-impregnation method, consecutive impregnation, mechanical mixing method, and two levels type catalyst were mainly employed. The co-impregnation indicated as (M1+M2)/TiO<sub>2</sub> is a method to impregnate two kinds of metals (Fe, Mn) to TiO<sub>2</sub>

simultaneously. The consecutive impregnation is a method to impregnate two kinds of metals (Fe, Mn) to TiO<sub>2</sub> one by one. This method is indicated as M1-M2/TiO<sub>2</sub> where metal M2 is supported firstly. The mechanical mixing method which indicated as M1+M2/TiO<sub>2</sub> is a method to grind M2 mechanically after M1/TiO<sub>2</sub> had been prepared. Two-level type catalyst indicated as M1/TiO<sub>2</sub>+M2/TiO<sub>2</sub> is a method to pack two kinds of catalysts into quartz glass tube without mixing.

The SCR activity measurement was carried out in a fixed-bed flow reactor which was equipped with an electric furnace kept at desired temperature under atmospheric pressure. 1.0 gram of the catalyst sample was packed into a 6 mm inner diameter quartz glass tube. The reactant gas composition was as follows: 1500 ppm NO, 1500 ppm C<sub>3</sub>H<sub>6</sub>, 10% O<sub>2</sub>, and He as a balance gas. The total flow rate was about 4 ml/s, which correspond to 13000 h<sup>-1</sup> of space velocity. The temperature range of reaction was from 150 to 600 .

NO and NO<sub>2</sub> concentrations were analyzed by NO<sub>x</sub> analyzer (Shimadzu, NOA-305A). N<sub>2</sub>O was analyzed by gas chromatograph (Shimadzu, GC-8A). CO<sub>2</sub> and CO concentrations were analyzed by gas chromatograph (GL Science, GC-390). Catalysts are characterized by TG-DTA, SEM-EDS, XRD and, BET.

### 3. Results and discussion

#### 3.1 Catalyst activity

From the activity test result on the effect of metal loading to the catalytic activity, it was known that the highest conversion of NO to N<sub>2</sub> was shown at metal loading of 0.5wt.%. The highest conversions of Fe(0.5)/TiO<sub>2</sub> catalyst and Mn(0.5)/TiO<sub>2</sub> were 28% and 26% respectively. Thus, this optimal metal loadings of Fe(0.5)/TiO<sub>2</sub> catalyst and Mn(0.5)/TiO<sub>2</sub> catalyst were employed for catalyst preparation mentioned below.

Figure 1 shows the effect of different packing configuration of two-level type catalyst on catalyst activity. The conversion of N<sub>2</sub> slightly

increased compared to that of single catalyst Fe(0.5)/TiO<sub>2</sub> or Mn(0.5)/TiO<sub>2</sub>, and when Mn(0.5)/TiO<sub>2</sub> was used as the first level catalyst, the maximum conversion reached 32%. And the maximum conversion increased to 40% when Fe(0.5)/TiO<sub>2</sub> was used as the first level catalyst. Therefore, it can be concluded that the catalytic reduction activity improved when a Mn/TiO<sub>2</sub> catalyst used as the second level catalyst.

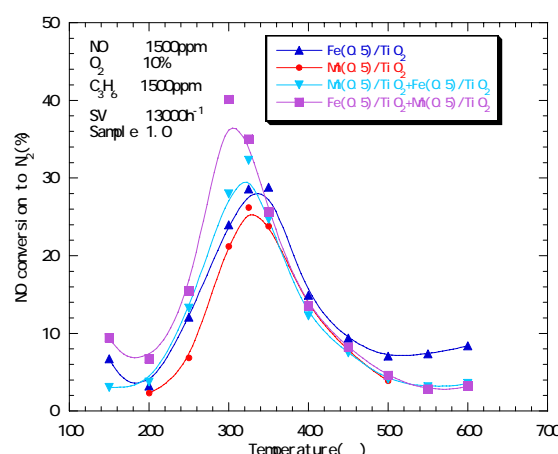


Fig.1: Catalytic activity of two-level type catalyst (M1/TiO<sub>2</sub>+M2/TiO<sub>2</sub> (M=Fe, Mn)) for the reduction of NO to N<sub>2</sub> using C<sub>3</sub>H<sub>6</sub> as a reducing agent

Table 1 and Table 2 show the conversion to N<sub>2</sub> and CO<sub>2</sub> respectively for two-level type catalyst, and the total value of single catalysts of Mn/TiO<sub>2</sub> and Fe/TiO<sub>2</sub> is additionally shown.

Table 1: The comparison of two-level type catalyst activity for the reduction of NO to N<sub>2</sub>

T ( °C )	Total value (%)	Mn/TiO <sub>2</sub> at the first level (%)	Fe/TiO <sub>2</sub> at the first level (%)
200	5.51	3.73	6.74
250	18.97	13.26	15.47
300	45.18	27.98	40.11
325	54.81	32.29	35.04
350	52.66	24.72	25.67
400	28.66	12.25	13.59
450	17.23	7.50	8.25
500	10.97	4.13	4.60

In the low temperature regions, the two-level

type catalyst that uses Fe/TiO<sub>2</sub> catalyst at the first level, showed similar degree of conversion of N<sub>2</sub> and CO<sub>2</sub> as that of single catalysts of Mn/TiO<sub>2</sub> and Fe/TiO<sub>2</sub> added together at the same temperature. It can be thought that reduction of NO to N<sub>2</sub> occurred in the two level of catalytic beds together. Therefore, it can be concluded that the synergy effect of two catalysts was observed in the low temperature regions.

**Table 2: The comparison of two-level type catalyst activity for the reduction of C<sub>3</sub>H<sub>6</sub> to CO<sub>2</sub>**

T( )	Total value (%)	Mn/TiO <sub>2</sub> at the first level (%)	Fe/TiO <sub>2</sub> at The first level (%)
200	2.57	4.65	4.85
250	11.90	8.64	10.48
300	53.18	31.17	49.78
325	97.05	57.98	75.19
350	(100.00)	74.55	84.67
400	(100.00)	93.41	98.40
450	(100.00)	99.02	100.00
500	(100.00)	100.00	100.00

Figure 2 shows the conversion of N<sub>2</sub> for various catalysts prepared by different preparation method that used in this experiment.

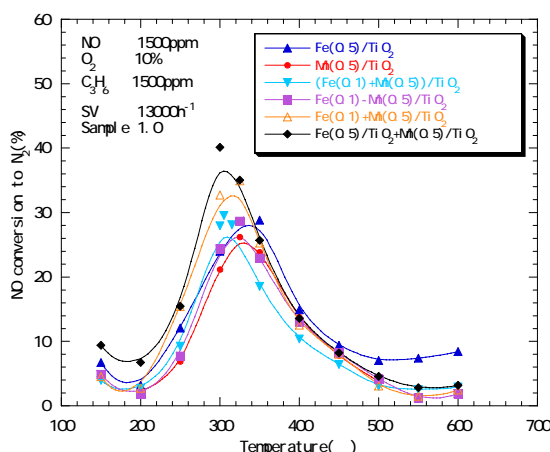


**Fig.2: Catalytic activity of catalysts with different preparation method for the reduction of NO to N<sub>2</sub> using C<sub>3</sub>H<sub>6</sub> as a reducing agent**

The catalytic activity slightly increased when the co-impregnation method was used. In the case of a consecutive impregnation catalyst, the

influence on the catalytic activity was insignificant. In the case of a mechanical mixing catalyst and a two-level type catalyst, the catalytic activity significantly increased. Two-level type catalyst showed the highest activity among the catalysts developed in this research.

The conversions of NO<sub>2</sub> and CO<sub>2</sub> are shown in Fig.3 and Fig.4.

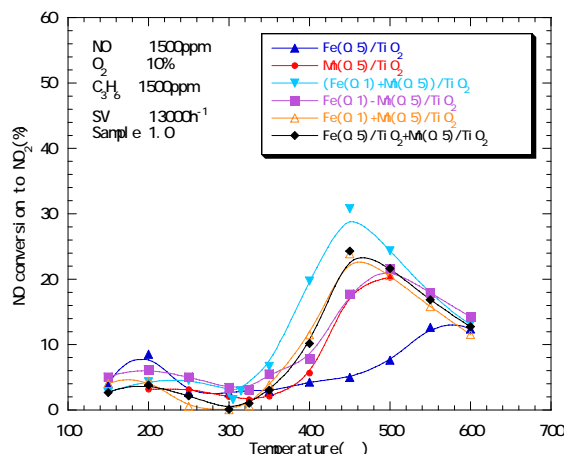


**Fig.3: Catalytic activity of catalysts with different preparation method for the reduction of NO to NO<sub>2</sub> using C<sub>3</sub>H<sub>6</sub> as a reducing agent**

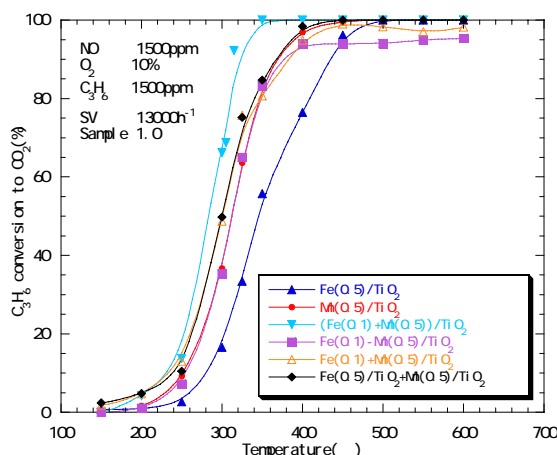


**Fig.4: Conversion of C<sub>3</sub>H<sub>6</sub> to CO<sub>2</sub> over catalysts with different preparation method under oxidizing atmosphere**

The highest conversion to NO<sub>2</sub> was achieved in the case of co-impregnation catalyst. However, NO conversion was low in the low temperature region because the combustion of HC, which is the reducing agent, rapidly occurred according to the reaction (2). Therefore, the conversion to N<sub>2</sub>

did not increase. When the mechanical mixing method catalyst or two-level type catalyst was used, the conversion to  $\text{NO}_2$  slightly increased compare to  $\text{Mn}/\text{TiO}_2$  catalyst only. In these cases, the combustion of HC also occurred similar to the case of  $\text{Mn}/\text{TiO}_2$  catalyst. Therefore, the conversion to  $\text{N}_2$  was thought to increase. In the case of consecutive impregnation, the degree of conversion to  $\text{NO}_2$  and  $\text{CO}_2$  were the same as that of  $\text{Mn}/\text{TiO}_2$  catalyst. Thus it can also be supposed that in this case there was no change in conversion to  $\text{N}_2$  either.

### 3.2 Characterization of Catalysts

The BET surface areas of iron catalysts and manganese catalysts are summarized in Table 3.

**Table 3: Specific surface area of various catalysts**

Catalysts	Specific Surface Area [ $\text{m}^2/\text{g}$ ]
$\text{TiO}_2$ (JRC-TIO-4)	49.1
$\text{Fe}_2\text{O}_3$	5.3
$\text{Mn}_2\text{O}_3$	54.2
$\text{Fe}(0.5)/\text{TiO}_2$	41.8
$\text{Mn}(0.5)/\text{TiO}_2$	23.4
$(\text{Fe}(0.1)+\text{Mn}(0.5))/\text{TiO}_2$	43.6
$\text{Fe}(0.1)-\text{Mn}(0.5)/\text{TiO}_2$	33.6
$\text{Mn}(0.5) + \text{Fe}(0.1) / \text{TiO}_2$	33.2
$\text{Fe}(0.1)+\text{Mn}(0.5)/\text{TiO}_2$	38.3

The surface area of the  $\text{TiO}_2$  support was 49.1  $\text{m}^2/\text{g}$ . After impregnation with iron or manganese, the surface area decreased. For the mixture catalysts of Fe and Mn, it was found that addition of iron oxide increased the surface area of catalyst. Therefore, it can be concluded that iron enhanced the dispersion of manganese on  $\text{TiO}_2$ .

Figure 5 shows the XRD patterns of the sample which calcined at 600 in  $\text{Fe}(\text{NO}_3)_3 \cdot 9\text{H}_2\text{O}$  and  $\text{MnCO}_3 \cdot n\text{H}_2\text{O}$ . The samples were identified as  $\text{Fe}_2\text{O}_3$  and  $\text{Mn}_2\text{O}_3$ . Therefore, it can be estimated that the oxidation states of the catalysts used in this study were  $\text{Fe}_2\text{O}_3$  and  $\text{Mn}_2\text{O}_3$ , because they

were calcined at the same temperature.

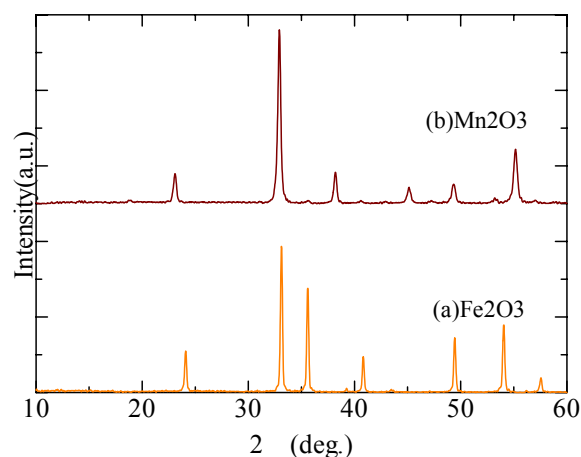


**Fig.5: XRD pattern of various metal oxides**

## 4. Conclusions

In the case of two-level type catalyst, the packing order influenced on the catalytic activity. An active synergy effect two catalysts was obtained in the low temperature regions when  $\text{Mn}/\text{TiO}_2$  catalyst was used at the second level.

The rank of the activity of catalysts developed in this research is as follows:

$$\text{Fe}(0.5)/\text{TiO}_2 + \text{Mn}(0.5)/\text{TiO}_2 > \text{Fe}(0.1) + \text{Mn}(0.5)/\text{TiO}_2 > (\text{Fe}(0.1) + \text{Mn}(0.5))/\text{TiO}_2 > \text{Fe}(0.1) - \text{Mn}(0.5)/\text{TiO}_2.$$

**The oxidation states of the catalysts used in this study were  $\text{Fe}_2\text{O}_3$  and  $\text{Mn}_2\text{O}_3$ . Iron was found to enhance the dispersion of manganese on  $\text{TiO}_2$ .**

## References

- [1] H.Schneider, U.Scharf, A.Wokaun, A.Baiker, *J.Catal.* 147, 545 (1994)
- [2] H. Hamada, Y. Kintaichi, M. Sasaki and T. Ito and M. Tabata, *Appl. Catal.*, 70, L15 (1991)
- [3] R.Burch, T.C.Watling, *Appl. Catal.B*, 11, 207 (1997)
- [4] Gongshin Qi, Ralph T. Yang, *Appl. Catal.*, 217, B44 (2003)

# A Study on New Approach to Prepare CoMo / Al<sub>2</sub>O<sub>3</sub> Catalyst for Deep Hydrodesulphurization

Student Number: 04M18245 Name: Haibo ZHANG Supervisor: Hirofumi HINODE

## 深度水素化脱硫 CoMo/Al<sub>2</sub>O<sub>3</sub> 触媒の新たな調製方法の研究

張 海波

石油精製における水素化脱硫触媒 CoMo/Al<sub>2</sub>O<sub>3</sub> において活性種と考えられている CoMoS 相の新たな合成法を目指し、Mo の先駆物(NH<sub>4</sub>)<sub>2</sub>MoS<sub>4</sub> (ATTM) の導入および調製方法を検討した。チオフェン脱硫反応により水素化脱硫活性を評価した結果、調製試料が市販触媒より高い活性を示した。ATTM を真空焼成してから、Co を還元雰囲気中で担持する方法で調製した試料は金属担持量の増加とともに活性が上昇の傾向を示し、Mo 担持量 15wt% で 96.5% のチオフェン転化率を示した。生成物質分布の考察により調製試料の脱硫選択性が高いことが分かった。XRD、XAFS、TEM などの解析により、多層化した CoMoS 相の存在が確認された。調製試料表面の CoMoS 相の積層数が市販触媒より多いことが水素化脱硫活性および脱硫選択性が高い原因であると考えられる。

### 1 INTRODUCTION

To meet the need of deep desulphurization of transportation fuels, researches and developments of hydrodesulphurization(HDS) processes and catalysts have been carried out. It is considered to be difficult to get super-low sulfur level liquid fuels (e.g. Japanese stand: less than 10 ppm) by exiting hydrotreating technology alone, therefore, the present approaches such as increasing reactor size, operating in more severe conditions (e.g. high pressure and high temperature), and new designs in desulfurization process are considered to be good solutions<sup>[1]</sup>.

CoMo/ Al<sub>2</sub>O<sub>3</sub> catalyst is widely used in the HDS of naphtha, paraffin oil, and light oil. Researches and developments of CoMo / Al<sub>2</sub>O<sub>3</sub> HDS catalysts are being carried out in every aspect, such as supports and interactions between active metals. The known active site for this catalyst is a kind of CoMoS interacted by each element. The promotion of HDS activity is linked to Co atoms present as CoMoS in the CoMo/Al<sub>2</sub>O<sub>3</sub> catalyst<sup>[2]</sup>.

In the conventional preparation process, Al-O-Mo bond and CoMoO<sub>4</sub> compound are produced during calcination and it had been found that these bond and compound do not contribute to the production of active sites<sup>[3]</sup>. For this reason, the conventional method of catalyst preparation is facing a limitation in the way of improving efficient utilization of active metals.

New route for catalyst preparation process was proposed in this research in order to investigate the new approach to prepare the catalyst for deep HDS. This new route is expected to efficiently improve utilization of active metals in catalyst in order to produce CoMoS phase.

### 2 EXPERIMENTAL

#### 2.1 Catalysts preparation

##### 2.1.1 Materials used in preparation of catalysts

Precursors of the catalysts were Co(NO<sub>3</sub>)<sub>2</sub> · 6H<sub>2</sub>O (Wako Pure Chemical Industries, Ltd., purity = 99.5%) and (NH<sub>4</sub>)<sub>2</sub>MoS<sub>4</sub> (Aldrich Chem. Co., purity = 99.97%). JRC-ALO-2 (Al<sub>2</sub>O<sub>3</sub>, Reference Catalyst, The Catalysis

Society of Japan) was used as support. As reference HDS catalyst, commercial CoMo/Al<sub>2</sub>O<sub>3</sub> catalyst was used after pre-sulfidation treatment.

### 2.1.2 Preparation of catalysts

Consecutive impregnation method was used in the preparation of catalysts. The loading of Mo was varied in a range of 10~15wt% and the molar ratio of Co /Mo was fixed at 0.27. There were three preparation routes investigated in this research. The prepared samples were named by prepared route and the loading of Mo, for example, R1-10 means that the sample prepared by Route1 and the loading of Mo is 10wt%.

Route 1 (R1) includes impregnation of Co(NO<sub>3</sub>)<sub>2</sub> · 6H<sub>2</sub>O, calcination under H<sub>2</sub> atmosphere, and impregnation of ATTm, vacuum calcination at 500 and 700 .

Route 2 (R2) includes impregnation of Co(NO<sub>3</sub>)<sub>2</sub> · 6H<sub>2</sub>O, calcination under air atmosphere, and impregnation of ATTm, vacuum calcination at 500 .

Route 3 (R3) includes impregnation of ATTm, vacuum calcination at 500 , and impregnation of Co(NO<sub>3</sub>)<sub>2</sub> · 6H<sub>2</sub>O, calcination under H<sub>2</sub> atmosphere.

Pre-sulfidation was carried out at 400 in a H<sub>2</sub>S/H<sub>2</sub> (10%) gas stream for all samples.

### 2.2 Activity measurement

The reaction was carried out in a fixed-bed reactor under atmospheric pressure. The catalyst was palletized, crashed and sieved to 0.71~1.00mm. 0.2g of the sample was packed in the reactor and the total flow rate of the feed mixture gas was fixed at 20ml/min.. The concentration of thiophene in the feed stream was maintained at 2.1mol%. The reaction temperature was selected at 300 to 350 .

Thiophene and reaction products such as butane and butene were quantitatively analyzed by GC-MS (Shimadzu Co. QP5050A) equipped with capillary column (Chrompack, CP-Porabond Q Fused Silica,

0.25mm × 30m).

### 2.3 Characterization

The samples were characterized by powder X-ray diffraction (XRD), X-ray absorption fine structure (XAFS), transmission electron microscope (TEM), and Brunauer-Emmett-Teller method (BET).

## 3 RESULTS AND DISCUSSION

### 3.1 HDS activity and selectivity

Fig.1 showed thiophene conversions of samples prepared by three routes at 350 .

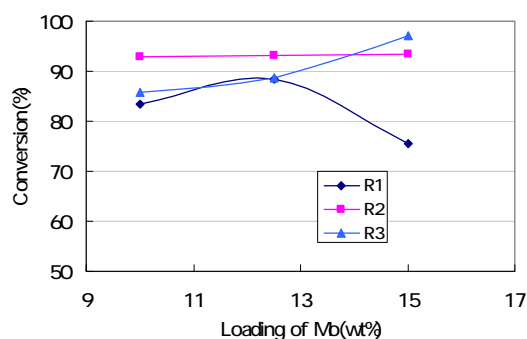


Figure 1: Thiophene conversions of prepared samples

In route 1, sample with a Mo loading of 10% showed thiophene conversion of 83.6%, when the Mo loading increased to 12.5%, the sample exhibited a approximately the same thiophene conversion as that of commercial catalyst (88.5%), while the thiophene conversion decreased to 77.5% when the Mo loading was increased to 15%. There was an optimum Mo loading in this preparation route approximates to 12.5%. More than this value, the agglomeration caused by calcination at 700 was considered to be the reason of resulting in the decreasing of catalytic activity.

In route 2, all prepared samples showed thiophene conversion more than 93%, and there was no apparent difference found among three samples. The active site formation by MoS<sub>2</sub> and Co is considered to be easier formed through CoO than through Co<sup>[4]</sup>, but the formation of CoMoS active site was limited to generate only on the surface of Al<sub>2</sub>O<sub>3</sub> because Co impregnated

previous to ATTMM could only access to the  $\text{MoS}_2$  located on the  $\text{Al}_2\text{O}_3$  surface, not to the part of  $\text{MoS}_2$  extending from the surface. This is the reason that samples prepared by route 2 had high activity, however, there is a limitation on in increasing the catalytic activity by increasing Mo loading.

In route3, samples showed a tendency that the thiophene conversion increased together with the increasing of Mo loading. Mo loading of 10% and 12.5% showed thiophene conversion of 85.3% and 88.5% respectively, and the sample with a 15% Mo showed the highest thiophene conversion of 96.5%(8% higher than commercial catalyst) in all samples. ATTMM was introduced to  $\text{Al}_2\text{O}_3$  before the impregnation of Co, and then decomposed to  $\text{MoS}_2$ . After that, precursor of Co was absorbed on the surface of both  $\text{Al}_2\text{O}_3$  and  $\text{MoS}_2$  during the impregnation. Co and  $\text{MoS}_2$  create CoMoS phase (interacted by each element<sup>[2]</sup>) in the active treatment and promoted catalytic activity of HDS.

Table 1 showed comparison between sample R3-15 and commercial catalyst on the product distributions at 325 . 1-butene, trans-2-butene, n-butane, cis-2-butene were detected as reaction products. The conversion to n-butane(defined as moles of n-butane in the products per mole of thiophene in the feed) can represent the hydrogenation (HYD) ability of catalyst during thiophene HDS reaction<sup>[5]</sup>. During the process of deep desulphurization, the HYD function of catalyst performs saturation of olefins, and for example in the case of gasoline desulphurization, this causes loss of octane number in the final products<sup>[6]</sup>, meanwhile low HYD ability directly contributes to low  $\text{H}_2$  consumption. Therefore, catalysts with high desulfurization ability and low hydrogenation ability are desirable.

The conversions to n-butane of the prepared samples (43% for sample R3-15) were less than that of commercial catalyst (50%). The prepared samples have high HDS ability but lower HYD ability.

Table 1: Comparison of product distributions

Specific Area ( $10^{-6}$ )	1- butene	Trans-2- butene	n- butane	Cis-2- butene	Thiophene
R3-15	7.7	215.2	728.0	418.0	248.1
Commercial	4.1	215.2	809.0	365.7	227.7

Reaction conditions:325 , Thiophene concentration in feed: 2.1mol%,GHSV 5800h<sup>-1</sup>

Thiophene conversion of R3-15:81.9%

Thiophene conversion of commercial catalyst: 82.5%

### 3.2 Characterization

The XRD patterns of prepared samples (Fig.2) showed characteristic peaks of  $\text{MoS}_2$  at  $2\theta=14.2^\circ(002)$ ,  $33.6^\circ(100)$ ,  $39.5^\circ(103)$ ,  $58.5^\circ(110)$ , and characteristic peaks of  $\text{Al}_2\text{O}_3$  at  $2\theta=46.3^\circ(400)$ ,  $66.9^\circ(440)$ . No characteristic peaks of Co or Co sulfide was detected. This means that during the Co addition, Co does not undergo a reconstruction of  $\text{MoS}_2$  crystallite, although  $\text{MoS}_2$  acts as a support to provide Co desirable location for the formation of CoMoS active site<sup>[7]</sup>.

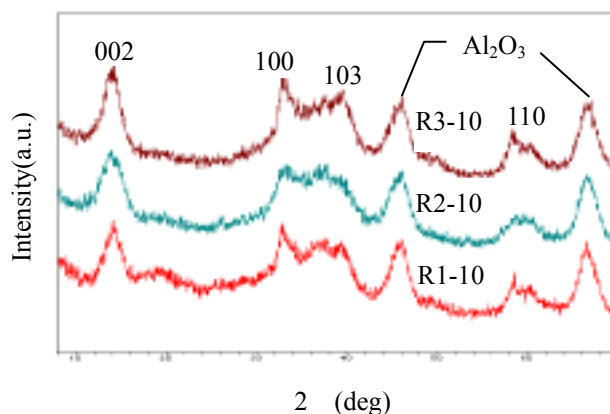


Figure 2: XRD patterns of prepared samples

As shown in Fig.3, in TEM micrographs  $\text{MoS}_2$  crystallite can be clearly seen in the form of groups of parallel dark lines with a space of about 6 . The number of  $\text{MoS}_2$  layers in the prepared sample seems to range from 5 to 20 slabs more than that of commercial catalyst with 2 to 7 slabs. This can be considered to give promotions to the catalytic activities of HDS reaction<sup>[8]</sup> and to reduce steric hindrances for large molecular (such

as 4,6-dimethyldibenzothiophene) to approach active site<sup>[3]</sup>.

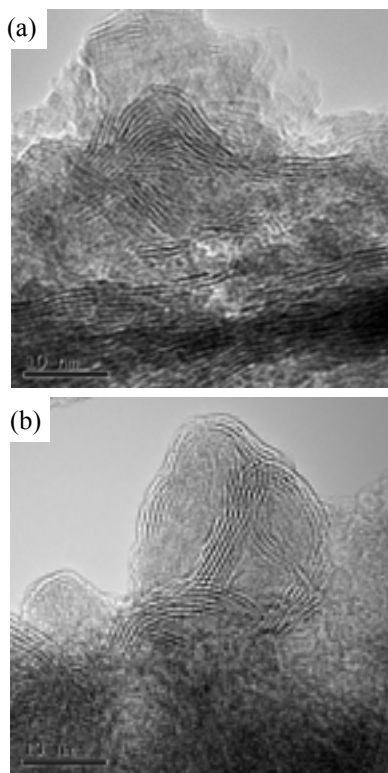


Figure 3: TEM images of (a) R3-15 and (b) commercial catalyst

XAFS spectra provided electronic structure information of prepared sample that Co has a coordination number (CN) of 5.3 with S, and a CN=1.6 with Mo. This result agreed well with the reported electronic structure of CoMoS (Type 2) phase, which has a CN=5.2 of Co-S, a CN=1.5 of Co-Mo<sup>[9]</sup>. CoMoS (Type 2) phase is generally considered to be the active site for HDS reaction.

#### 4 CONCLUSION

The introduction of ATTMM as the precursor of Mo with appropriate preparation method showed great promotion to catalytic activity of CoMo/Al<sub>2</sub>O<sub>3</sub> HDS catalyst. The prepared samples showed high activity during thiophene HDS reaction (thiophene conversion of 96.5%, 8% higher than commercial catalyst). The prepared samples with higher HDS ability exhibited a relatively lower hydrogenation ability compare to commercial catalyst. XRD, XAFS, TEM, and BET gave information that

promotions in the CoMoS structure contributed to the promotions of catalytic activity and selectivity.

#### References

- [1] Song C. "An overview of new approaches to deep desulfurization for ultra-clean gasoline, diesel fuel, and jet fuel", *Catal. Today*. 86(2003)211-263.
- [2] Topsøe H., Clausen B.S., Active sites and support effects in hydrodesulfurization catalysts", *Appl. Catal.* 25(1986)273-293.
- [3] Whitehurst D.D., Isoda T., Mochida T.I., "Present state of the art and future challenges in the hydrodesulfurization of polyaromatic sulfur compounds" *Adv.Catal.*42(1998)345-471.
- [4] Li Jiapeng, "catalytic Hydrogenation Technology", Fushun Research Institute of Petroleum and Petrochemicals of SINOPEC, pp.254-266, Jan.1990 (in Chinese)
- [5] Klimova T., Casados D.S., Ramirez J., "New selective Mo and NiMo HDS catalysts supported on Al<sub>2</sub>O<sub>3</sub>-MgO(x) mixed oxides", *Catalysis Today* 43(1998)135-146
- [6] Yin C., Liu C., "Hydrodesulfurization of cracked naphtha over zeolite-supported Ni-Mo-S catalysts", *Appl. Catal. A:General* 273(2004)177-184
- [7] Inamura K., Prins R., "The Role of Co in Unsupported Co-Mo Sulfides in the Hydrosulfurization of Thiophene" *J.Catal.* 147(1994)515-524
- [8] Okamoto Y., Ishihara S., Kawano M., Satoh M. and Kubota T., "Preparation of Co-Mo/ Al<sub>2</sub>O<sub>3</sub> model sulfide catalysts for hydrosulfurization and their application to the study of the effects of catalyst preparation" *J. Catal.* 217(2003)12-22
- [8] Bouwens S.M.A.M., van Zon F.B.M., van Dijk M.P., van der Kraan A.M., de Beer V.H.J., van Veen J.A.R., and Koningsberger D.C., "On the Structural Differences between Alumina-Supported CoMoS Type and Alumina-,silica-,and Carbon-Supported CoMoS phases Studied by XAFS, MES, and XPS" *J.Catal.* 146 (1994)375-393

# Improvement of Rubberwood Process Using the Thermally Treated Products from Wood Residue

Student ID#:04M18110

Name:KONISHI, SHUNSUKE

Supervisor:EGASHIRA, RYUICHI

## 残材の熱処理生成物を用いたゴム木材プロセスの改良

小西 俊介

ゴム木材の家具製造プロセスにおける有害防腐剤による排水汚染と大量の残材投棄が問題となっている。本研究では残材を熱処理することで木酢液、木炭、および可燃性気体に分離し、それぞれ低有害防腐剤、廃水処理用吸着剤、および熱源として再利用することでの問題の改善を考えた。ゴム木材おが屑を原料として温度や雰囲気等条件を変えて熱処理実験を行い、結果を用いてプロセス全体での物質収支および熱収支計算を行った。木酢液と木炭は十分な量得られ、出入り口でのエンタルピー差を熱処理の必要熱量としたとき、可燃性気体と吸着で余った木炭の発熱量により約半分の熱を回収できることが分かった

### 1. Introduction:

In Southeast Asia Countries, various forms of residues are discharged from the process of rubberwood manufacturing. In this process, a portion of wood residues are being thrown away to isolated country site and are burned illegally. These disposal methods do cause environmental problems, such as accidental forest burning, release of hazardous gases, and soil contamination by toxic preservatives. Besides, the issue of wood preservative has also been paid attention because of the toxicity of present wood preservative products. These problems are considerably serious in these countries.

Wood can be thermally decomposed into useful materials such as pyrolygneous acid (PA), char and fuel off-gas. PA from wood can be used as a substitute for the ordinary toxic wood preservative<sup>[1,2,4]</sup>. The char was studied to have a high adsorption capacity to remove unfavorable components from waste water<sup>[3,5]</sup>. Off-gas contains some flammable gases such as, H<sub>2</sub>, CO, CH<sub>4</sub>.

In this study, we are trying to improve the existing rubberwood process. Thermal decomposition of rubberwood was conducted to obtain the useful products. The yield and characteristic of the products were estimated. We proposed a rubberwood process in which the products is utilized as a preservative, adsorbent and gas energy. The balance of heat energy as well as material balance in the whole process was estimated based on the experimental data.

### 2. Thermal treatment of rubberwood and characterization of the products:

#### 2.1, Experimental Thermal treatment

Rubberwood sawdust was treated thermally to obtain crude pyrolygneous acid (CPA), char, and off-gas in the various conditions. **Table 2.1** shows the experimental conditions, specified temperature, steam flow rate and holding time at specified temperature. The CPA was distilled into PA and tar at 413K. The apparatus of thermal treatment and distillation are figured in **Figure 2.1**.

#### Characterization of the products

The CPA, PA and off-gas were analyzed by GC to know the concentration of main components. Elementary analysis of the char and rubberwood were also conducted. Preservative efficiency of PA was estimated by comparing the composition of phenolic compounds in PA with that in the previous preservative. Phenols are known to have the preservative effect. The calorific value of the gas, char and wood were calculated from enthalpy difference between before and after burning.

#### Adsorption

The char produced at 700K was used in the adsorption experiment. The char was mixed with various concentrations of aqueous phenol and the mixtures were put in the agitator at 303K for 120 hours enough for the adsorption equilibrium. After the adsorption experiment, the aqueous phenols were separated from the char by the filtration. The initial and separated phenol solutions were analyzed by GC. The adsorption mass of phenol on the unit mass of the char was estimated.

Table 2.1 Experimental condition in the thermal treatment

Run No	Experimental condition
A-700	700K, 0.03m <sup>3</sup> -steam/h, hold time 1hour
A-900	900K, 0.03m <sup>3</sup> -steam/h, hold time 1hour
A-1092	1092K, 0.03m <sup>3</sup> -steam/h, hold time 1hour
A-1292	1292K, 0.03m <sup>3</sup> -steam/h, hold time 1hour
B-700	700K, 0.03m <sup>3</sup> -steam/h, hold time 0.5hour
B-900	900K, 0.03m <sup>3</sup> -steam/h, hold time 0.5hour
B-1092	1092K, 0.03m <sup>3</sup> -steam/h, hold time 0.5hour
B-1292	1292K, 0.03m <sup>3</sup> -steam/h, hold time 0.5hour
C-1092	1092K, 0.015m <sup>3</sup> -steam/h, hold time 1hour
C-1292	1292K, 0.015m <sup>3</sup> -steam/h, hold time 1hour

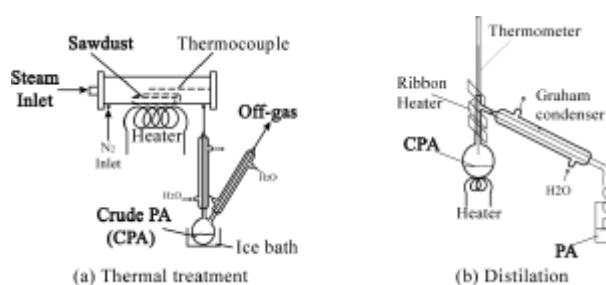


Figure 2.1 Schematic diagram of experimental apparatus

#### 2.2, Results and Discussion

##### Thermal treatment

The yield of each product in the thermal treatment was expressed as,

$$Y_i = \frac{W_i}{W_{\text{sawdust}}} \quad (2-1)$$

The yield of each product is shown in **Figure 2.2**. It was studied that char is completely produced around 600K and the produced char is gradually consumed by steam above 800K. In this study, the char yield decreased with increasing the treatment temperature due to the high consumption of carbon by steam. No char remained in the thermal treatments at 1292K. The char was consumed more in the experiment A than the others due to the more steam provided. As for CPA, the yield was not influenced by the temperature. It is because the wood is

completely decomposed into CPA by 600K and in the higher temperature range, the yield of CPA does not change any more. The CPA is composed of the volatile components from the wood and the water from the feed steam. The yield of CPA is determined by not only feed wood but also feed steam mass. The yield of CPA was higher in the Experiment A than the others. It is because that more steam was provided in the apparatus and the unreacted steam was directly condensed to the CPA. Contrary, the yield of the off-gas increased with increasing temperature. In the range of higher temperature, more char and steam were reacted and more off-gas was produced. The produced gas contained many inflammable components such as, H<sub>2</sub> and CO above 1092K. The reactions are written below,



**Distillation**

The CPA produced at each thermal treatment condition was distilled around same temperature, 413K. The yield of each product in the distillation was expressed as,

$$Y_i = \frac{W_i}{W_{CPA}} \quad (2-4)$$

The yield of interested components in the PA was defined as,

$$y_i = x_i \cdot Y_{PA} \quad (2-5)$$

The yield of PA and tar is shown in **Figure 2.3**. It was very difficult to control the distillation temperature which influences strongly the yield of products. The higher distillation temperature, the higher yield of PA and the lower yield of tar. As a result, the yield varied in the distillation of each CPA due to the unstable distillation conditions. However, the variation range of PA yields was between 0.7~0.9 and these values were enough for a wood preservative.

The concentration of phenols in PA is shown in **Figure 2.4**. All the PA contained larger phenols, preservative components, than the previous PA which was confirmed to have preservative effect. The result indicated that all the PA of this study had high preservative effect and could be used as a preservative.

**Adsorption capacity of the char**

**Figure 2.5** shows the adsorption isotherms of phenol by the char. The char treated with steam atmosphere at 700K was prepared in this study. The adsorption by the char of 1292K was not conducted because the char was not obtained in the thermal treatment as mentioned above. The adsorptions by the char of 900 and 1092K were conducted in the previous studies<sup>[1,3,5]</sup>. The amount of adsorption of phenol increased with increasing temperature of thermal treatment. It means that the char treated at higher temperature has higher adsorption capacity. The adsorption capacities of char with steam were somewhat smaller than that of the chars with CO<sub>2</sub>. However, the char with steam above 873K had enough adsorption capacity for an adsorbent of waste water. The Langmuir isotherm equation was used to quantify the adsorption capacity of each char. Product of the adsorption coefficient and the maximum adsorption amount of char, K·q, represents the relative adsorption capacity in a dilute solution. **Table 2.2** shows K·q of each char and also the relative adsorption capacity on CO<sub>2</sub>-1073 basis.

**Heating value of Off-gas**

**Figure 2.6** shows the mass production of components in the Off-gas at left axis, and the heating value at right side. The off-gas mainly contained Hydrogen, Carbon oxide, Carbon dioxide and Methane. The flammable gas, Hydrogen and Carbon oxide, increased with treatment temperature due to the

active reactions of carbon and steam. These reactions were shown above at equation (2-2),(2-3). At higher temperature, these reactions were more active, and Hydrogen and Carbon oxide were produced more. These high production of flammable gases resulted in the increase of the heating value of Off-gas. At low temperature, 700 and 900K, the off-gas contained little flammable gas and had low heating value as a heat recovery for the thermal treatment. On the other hand, the off-gas produced at 1092 and 1292K had high heating value and these were useful for the heat recovery.

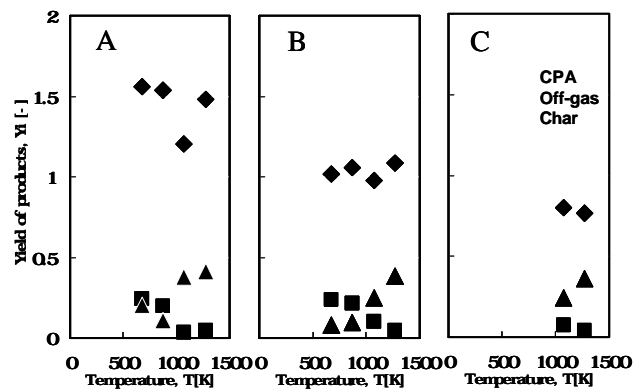


Figure 2.2 Yield of the products in the thermal treatment

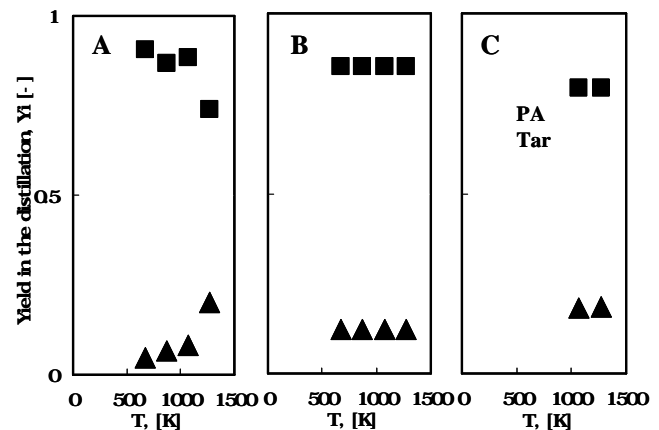


Figure 2.3 Yield of PA and tar in the distillation

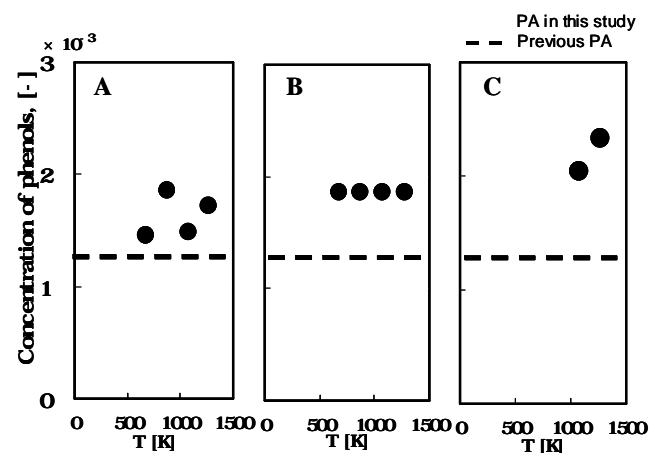


Figure 2.4 Composition of phenols in PA

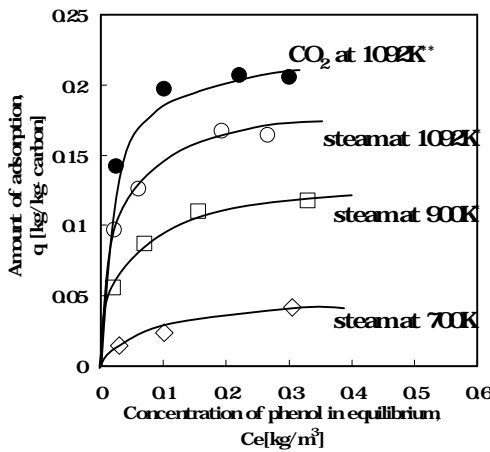


Figure 2.5 Adsorption isotherms of phenol in the model solution

Table 2-2 Adsorption capacity of each char produced

	$q_s \times K_L$ [m³/kg-carbon]	Adsorption capacity [-]
CO <sub>2</sub> -1092	20.3252	1
steam-1092	8.2645	0.4066
steam-900	4.5290	0.2228
steam-700	0.5293	0.0260

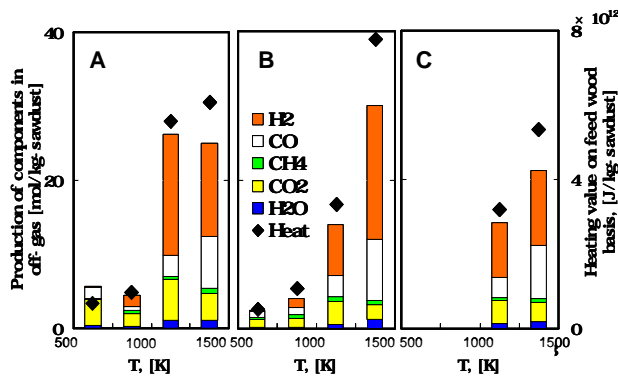


Figure 2.6 Mass production of each component in Off-gas (left) and heating value of Off-gas (right)

### 3. Balance of material and heat in the process:

#### 3.1. Proposed rubberwood process

We proposed an improved rubberwood process utilizing the thermal treated products, PA, char, and off-gas, from wood residue as shown in **Figure 3.1**. Some waste wood are burned to generate the heat for Drying. A portion of the remaining waste wood, wood residue1, is decomposed into the useful products in Thermal treatment. The other wood residue, wood residue2, is burned to recover the heat for the proposed process. After PA is put on the surface of wood product for preservation, it is washed out into the wastewater. This wastewater is contacted with the char adsorbing the phenols derived from PA. The Off-gas is also burned with wood residue2 in Burning and produces the heat for Thermal treatment and Distillation.

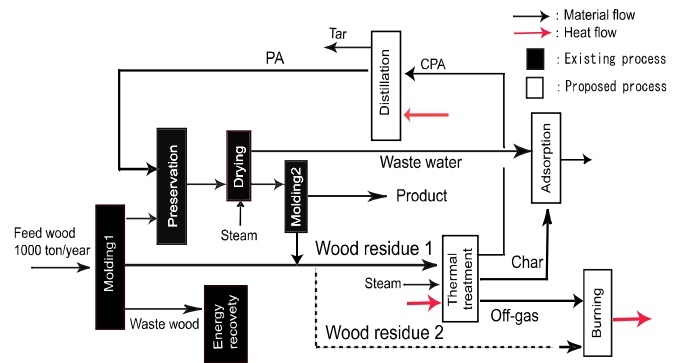


Figure 3.1 Proposed process flow

#### 3.2. Calculation condition and assumptions

Feed wood of 1000 ton/year is provided to Molding1. It is molded into wood product, wood residue and waste wood. The wood product of 200 ton/year is treated with preservative by PA of constant rate, 33.4 ton/year. Flow rates of thermally decomposed products are calculated using the results of yield in the experimental section. The PA produced in Distillation are directly used as a preservative. All the PA components are assumed to be washed out into waste water during Drying. The flow of char requirement for adsorbent is determined from the results of adsorption experiment to meet the regulation of waste water. The flow of PA requirement for preservation is calculated from the reference data and it is constant, 33.4 ton/year. It is estimated the flow rate of required wood residue1 to obtain the requirement of PA and char. The flow of each material is defined as flow rate, ton/year.

The heat consumption in the thermal treatment was estimated from the difference between the enthalpy of inlet and outlet materials. The enthalpy of the inlet materials, sawdust and water, were calculated at room temperature and that of the outlet, Char, CPA and Gas, were calculated at the specified temperature of apparatus. We assumed the composition of each material, that the char was pure carbon, and CPA was composed of only water, acetic acid, methanol and phenol, and off-gas contained only H<sub>2</sub>, CO, CO<sub>2</sub>, CH<sub>4</sub> and H<sub>2</sub>O. The same enthalpy calculation was conducted in the distillation. The flow of each heat is defined as heat flow, J/year.

#### 3.3. Results and discussion

**Figure 3.2 (a)** shows the flow rates of the PA produced and preservative requirement against flow rate of wood residue1. The flow rate of the PA increased with wood residue1 and these were larger than that of requirement in all the cases. **Figure 3.2 (b)** shows the flow rates of the char produced and adsorbent requirement. The char treated at 900K were satisfied the requirement for the process at all the flow of wood residue1. The char treated at the other temperatures were less than the requirement at low flow of wood residue1. As the flow of wood residue1 increased, these char products increased and reached the requirement at a flow rate of wood residue1. **Figure 3.3** shows the minimum flow rate of wood residue1 at which the either PA or char meets the requirement. The flow rate for char requirement was always larger than that for PA. We defined the residue1 flow for char as a required residue1 flow rate to meet both PA and char requirement.

**Figure 3.4** shows the heat consumption in Thermal treatment and Distillation, and also heat recovery from off-gas and wood residue2 at the each defined residue1 flow. The heat consumption increased with increasing the defined residue1. When the residue was treated at 700K, the defined residue1 was high and then the heat consumption was also high. We estimated how much wood residue2 was burned for heat recovery. **Figure 3.5** shows the flow rate of the total required

wood residue, which is sum of the wood residue1 to obtain PA and char, and the wood residue2 to recover the heat. At the present process, wood residue is discharged at various flow rates. This flow rate depends on the situation. From the reference data, we estimated that the wood residue could be discharged from 66 to 374 ton/year. This range is shown as a red line in Figure 3.5. When the wood residue was treated at A-900, B-900, B-1092 and C-1092, the flow rates of the total required residue were below this range. The result means that in these conditions, the PA and char were satisfied the requirement and the heat is also recovered completely.

**4. Conclusion :**

We confirmed that the useful materials were produced by thermal treatment of wood. The PA had high preservative effect. The char had high adsorption capacity. The off-gas had high heating value and the heat recovery from off-gas was 10-40% of the heat consumption in the proposed process. The result of the process calculation showed that, when the wood residue was treated at 900 or 1092K, the total requirement of the residue was lowest. In these conditions, the useful products were obtained enough for the preservative and adsorbent, and the heat consumption for the proposed process was also recovered.

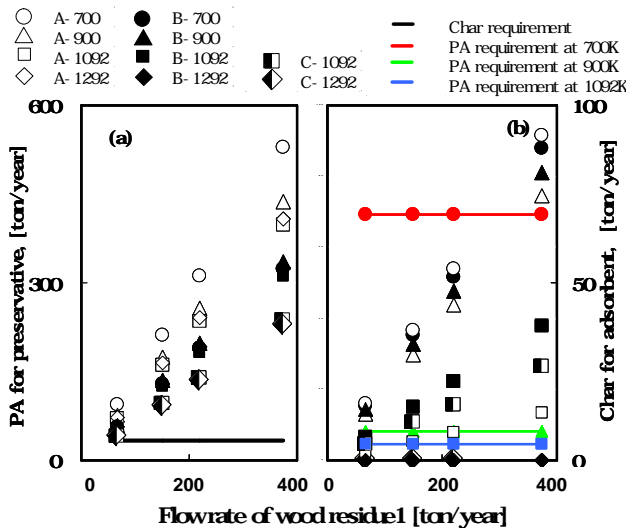


Figure 3.2 Flow rates of PA(a) and Char(b) against flow rate of wood residue1

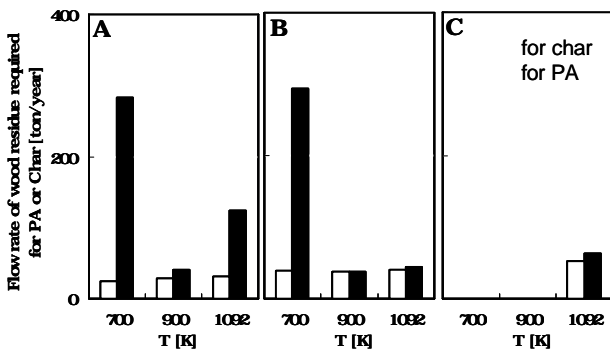


Figure 3.3 Flow rate of wood residue1 required for PA and char

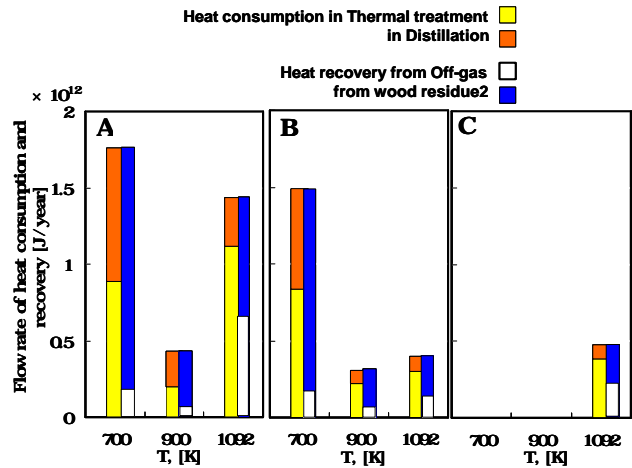


Figure 3.4 Flow rate of heat consumption and heat recovery at the defined flow rate of wood residue1

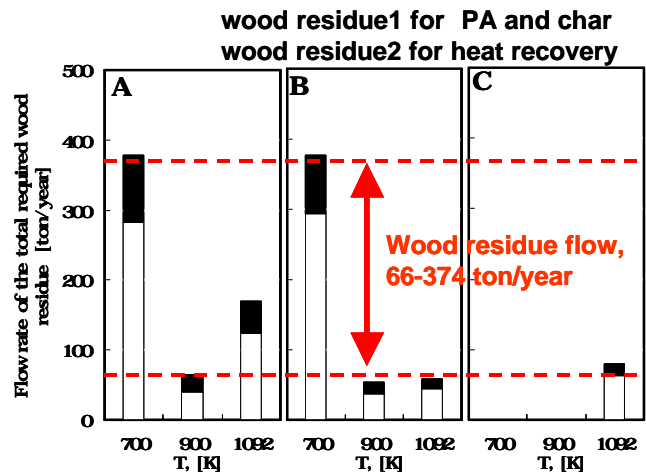


Figure 3.5 Flow rate of the total required wood residue

**Nomenclature**

W	Mass of material	[g]
T	Specified temperature in the thermal treatment	[K]
$Y_i$	Yield of product	[-]
$y_i$	Yield of component	[-]
$x_i$	Composition of component	[-]
q	Amount of adsorption	[m <sup>3</sup> /kg-carbon]
q	Saturated amount of adsorption	[m <sup>3</sup> /kg-carbon]
Ce	Equilibrium concentration	[kg/m <sup>3</sup> ]
$K_L$	Langmuir adsorption coefficient	[m <sup>3</sup> /kg]

**References**

- [1] Sato, M., Bachelor thesis, Tokyo Institute of Technology, Japan, March (2005)
- [2] Lim, K.G., Master thesis, Tokyo Institute of Technology, Japan, March (2004)
- [3] Konishi, S., Bachelor thesis, Tokyo Institute of Technology, Japan, March (2004)
- [4] Lim, K.G., et al.; RSCE 2004, ES-257 (2004 Bangkok)
- [5] Sato, M., et al.; SCEJ 70th annual meeting S117 (2005 Nagoya)

# Enzymatic treatment of phenol waste water with thermo-responsive chitosan

Student Number:04M18096 Name: Shuichi KAWATOKO Supervisor: Ryuichi EGASHIRA, Sachio HIROSE

熱応答性キトサンを用いたフェノール排水の酵素的処理

川床 修一

本研究では、熱応答性キトサン（ヒドロキシブチルキトサン，HBC）のゲル化特性を利用して、フェノール排水処理に使用した酵素（ペルオキシダーゼ、HRP）をリサイクルする方法を提案する。

実験では、HBC 溶液のゲル化温度、ゲル収縮特性、HRP 活性、HBC 存在下でのフェノール重合反応の反応率を調べた。これらの結果より、反応操作条件を 30℃、pH 5.9、HBC 1.6 w/w%、HRP 5 mg/L と決定して、各操作において物質収支をとった。その結果、リサイクルを行わない場合と比べ 1.0-1.7 倍の効果が得られた。

## 1. Introduction

Phenol-polluted waters are widely produced as wastes of several industrial and agricultural activities. Phenolic compounds and their derivatives are considered primary pollutants because they are harmful toward living organisms, even at low concentrations [1]. If released into the environment, they may accumulate in soil, ground water, or surface water, thus representing an issue of great environmental concern.

Removal of phenols from wastewater can be performed by conventional remediation methods (e.g., solvent extraction, chemical oxidation and adsorption on activated supports) [2]. Some of these methods may present a number of disadvantages, such as high costs, time-consuming procedures and formation of toxic residues although it is effective. Biological technologies dealing with the use of oxidoreductive enzymes, for instance, laccases, peroxidases, and tyrosinases, may represent an efficient, alternative way to address the clean-up of phenol-polluted wastewater from low to high density. Phenol reaction formula by enzyme was shown in below.



A: C<sub>6</sub>H<sub>4</sub>-OH

Enzyme figures as high reactivity, substrate specificity, biodegradability, and can be operates at mild conditions of temperature, pressure, and pH. However, there are a number of practical problems in the use of enzymes. It costs for isolation and purification of enzyme, the instability of their structures.

In this study, we suggested the enzyme recycle method by using thermo-responsive chitosan (hydroxybutyl chitosan, HBC)(Fig.1). In this method after phenol polymerization by horseradish peroxidase (HRP) and hydrogen peroxide, the solvent was gelated. From this step, treated water drains from shrinking HBC gel. In the next step, HBC gel returns solvent with cooling, polyphenol was removed as precipitation.

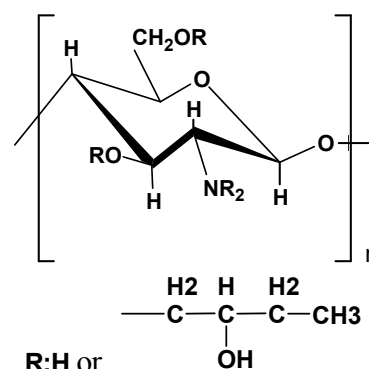


Fig.1 HBC structure.

## 2. Experimental

### 2.1 Materials

HBC was provided from Dainichiseika Ltd., Japan. HRP was purchased from Biozyme Laboratelies (South Wales, UK). All other chemicals were the highest purity available and purchased from Wako Pure Chemicals Co., Japan.

Two types of buffer solution were prepared, 0.1 M phosphate buffer (pH 5.7-7.0) from sodium dihydrogenphosphate and disodium hydrogenphosphate, 0.1 M acetate buffer (pH 5.4-5.6) from acetic acid and sodium acetate.

### 2.2 Measurement of HBC gelation temperature

HBC solutions (pH 5.4-7.0, 1.0-2.0 w/w%) were prepared, and measured their gelation temperature by inverting test tube [3].

### 2.3 HPLC analysis

HPLC analysis was performed with a Shimazu instrument equipment with a wavelength absorbance detector set at 280nm. A wakoshi II 4.6 mm×10 mm column was used. Isocratic solution was performed at a flow rate of 1mL min<sup>-1</sup> with mobile phase composed of water, acetic acid and acetnitrile (39.6: 0.8: 60.0 %; v/v)

### 2.4 Measurement of shrinking ratio

HBC solution(pH 5.9, 1.6 w/w%) was heated in

incubation bath at 33°C, moved another incubation bath (at 40, 45, 50°C) and measured their ratio of shrinking after each times(10, 30, 60 min). Ratio of shrinking was measured by weight of HBC gel after removal of water and HBC solution before galation. And phenol and HRP concentration after gel shrinking were determined by the HPLC method of analysis for phenol concentration

2.5 HRP Activity

HRP activity was assayed by measuring absorbance (450nm) intermediate product of phenol and 4-aminoantipyrine (4-AAP) as the substrate.

To investigate effect of pH and temperature to HRP activity, phenol (10.6 mM final concentration), 4-AAP(2.6 mM final concentration), HRP (5.4 × 10<sup>-1</sup> mg/L final concentration) and H<sub>2</sub>O<sub>2</sub>(0.22 mM final concentration) as initiation reagent were prepared in 0.1 M phosphate buffer (pH 5.4-7.0), and the absorbance was measured after 5 min at 25-37°C by microplate reader.

To investigate thermostability, HRP activity was measured, after 10 mM HRP solution was incubated in each incubation bath (33-60°C). Thermostability was defined the following equation as relative activity (RA).

$$RA = A_t / A_0$$

A<sub>t</sub> [-]: HRP activity with t minutes heating

A<sub>0</sub> [-]: HRP activity with no heating

2.6 Phneol polymerization in the presence of HBC

To determine HRP concentration in the reactor, phenol polymerization tests by HRP and H<sub>2</sub>O<sub>2</sub> as initiation reagent was carried out at with 1000 mg/L phenol in 0.1 M phosphate buffer (pH 5.9) with out HBC. Samples were analyzed for phenol concentration by HPLC at each times (10-120 min). And phenol polymerization tests by HRP (5 mg/L final concentration) and H<sub>2</sub>O<sub>2</sub> was carried out at phenol concentrations ranging from 50-500 mg/L with or without HBC on the same condition of previous tests. Samples were analyzed for phenol concentration by HPLC at each times (10-120 min).

2.7 Material balance

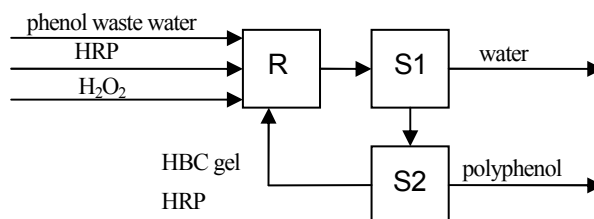
Using the values from experiments, material balance for the method was calculated. As the modeling assumption, the followings were assumed. i ) The reaction related on material balance would be phenol polymerization at R and HRP deactivation at S1, ii ) Polyphenol was separated completely at S1, iii) HRP added to R had no deactivated HRP, iv) HBC and polyphenol were not included in treated water, and additive solvent to R.

Material balance calculations showed that all flows and concentrations shown in Fig.2 were expressed by the relation using the rate of reaction, RA, rate of shrinking, phenol ratio in HBC, HRP ratio in HRP, initial phenol concentration, initial phenol feed, and reaction HRP concentration. To evaluate the proposed model (Fig.2), HRP recycle effect (RE) was defined as below;

$$RE = C_{Ea, no\ recycle} / C_{Ea, recycle}$$

C<sub>Ea, no recycle</sub>[mg/L]: Additive enzyme concentration on no recycle method

C<sub>Ea, recycle</sub>[mg/L]: Additive enzyme concentration on this recycle method



R: phenol polymerization reaction

S1: separation by heating

S2: separation by cooling

Fig.2 Outline of enzyme recycle model.

3. Results and Discussion

3.1 HBC gelation temperature

Fig.3 shows the relationship between gelation temperature and pH in various HBC concentrations. From this graph, HBC solution had a tendency to be gel at higher pH, temperature and HBC concentration. These gelation behaviors can be attributed to the protonation of amino groups in HBC and the property of hydroxybutyl bond in HBC. The pK<sub>a</sub> of chitosan is approximately 6.5. Hence chitosan is dissolved under pH 6.5 due to protonated amino group of chitosan. Above pH 6.5, chitosan is tendency to turn into gel because the amino groups in chitosan were deionized. HBC turn to gel at high temperature because of lower critical solution temperature (LCST) derived from hydroxybutyl bond. In addition, HBC with high concentration tune to gel because the cross linkage points of molecule entanglement and the hydrophobic binding increase.

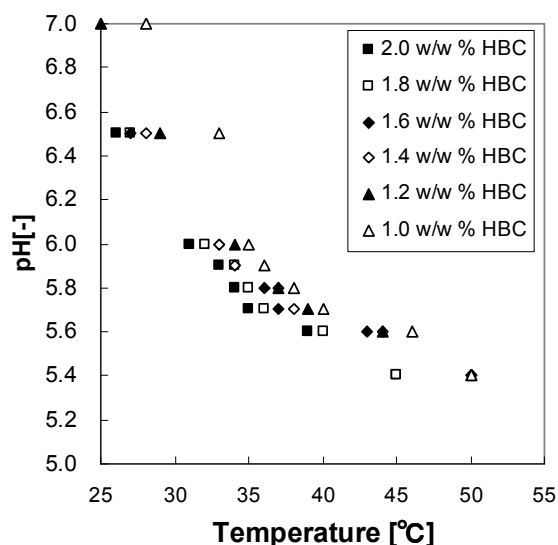


Fig.3 Relationship between gelation temperature and pH in various concentrations of HBC.

3.2 shrinking ratio

Time causes of HBC shrinking ratio is shown in Fig.4. The ratios of phenol and HRP in HBC gel after gel shrinking were also shown in Fig.5 and Fig.6. In each case, HBC gels were rapidly shrinking within 10 min. HRP and phenol ratios in HBC decreased with increasing time and the concentrations of them increased due to HBC gel shrinking. Relationship between phenol ratio in HBC and phenol concentration is linear as shown in Fig.5, and those equations were summarized in Table 1.

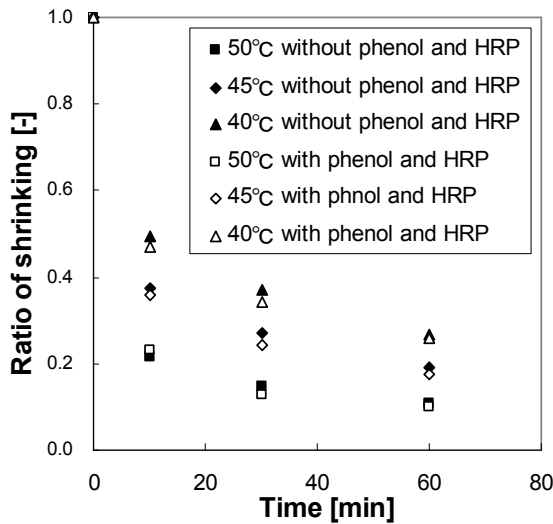


Fig. 4 Time courses of HBC shrinking ratio in pH 5.9.

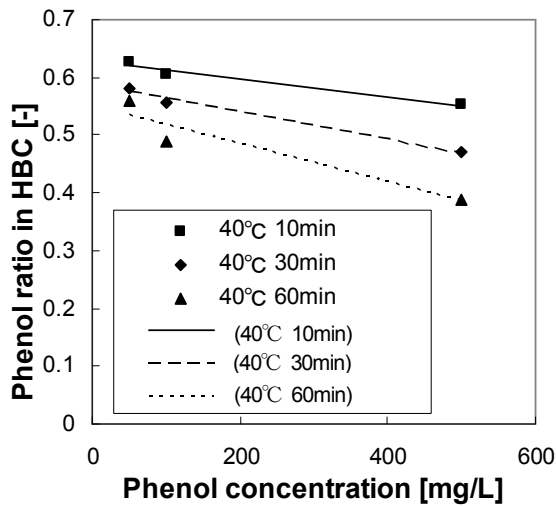


Fig.5 Relationship between phenol ratio in HBC and phenol concentration in pH 5.9 at 40°C.

3.3 HRP activity

From HRP activity measurement, HRP activated at pH 6.5 in the range of pH 5.4-7.5 and at higher temperature in the range from 25°C to 37°C. HRP activity after 60 min heating retained over 60% RA at up to 50°C(Fig.7).

In consideration of above results, phenol polymerization condition was decided as described below: pH 5.9, 30°C, 1.6 w/w% HBC.

Table1 Relationship between phenol ratio ( $\xi_2$  (Temperature [°C], Time [min])) in HBC and phenol concentration

$$\begin{aligned} \xi_2(40, 10) &= -1.5 \times 10^{-4} \times C_{P2} + 0.63 \\ \xi_2(40, 30) &= -2.4 \times 10^{-4} \times C_{P2} + 0.59 \\ \xi_2(40, 60) &= -3.3 \times 10^{-4} \times C_{P2} + 0.55 \\ \xi_2(45, 10) &= -3.1 \times 10^{-4} \times C_{P2} + 0.62 \\ \xi_2(45, 30) &= -4.2 \times 10^{-4} \times C_{P2} + 0.60 \\ \xi_2(45, 60) &= -4.9 \times 10^{-4} \times C_{P2} + 0.59 \\ \xi_2(50, 10) &= -3.5 \times 10^{-4} \times C_{P2} + 0.54 \\ \xi_2(50, 30) &= -4.2 \times 10^{-4} \times C_{P2} + 0.53 \\ \xi_2(50, 60) &= -5.9 \times 10^{-4} \times C_{P2} + 0.59 \end{aligned}$$

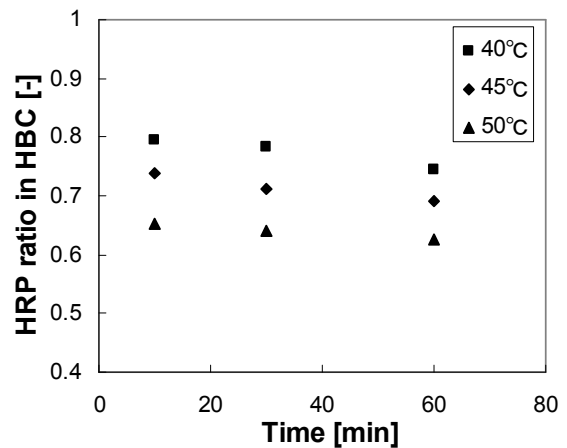


Fig. 6 Time courses of HRP ratio in HBC in pH 5.9 at different temperatures.

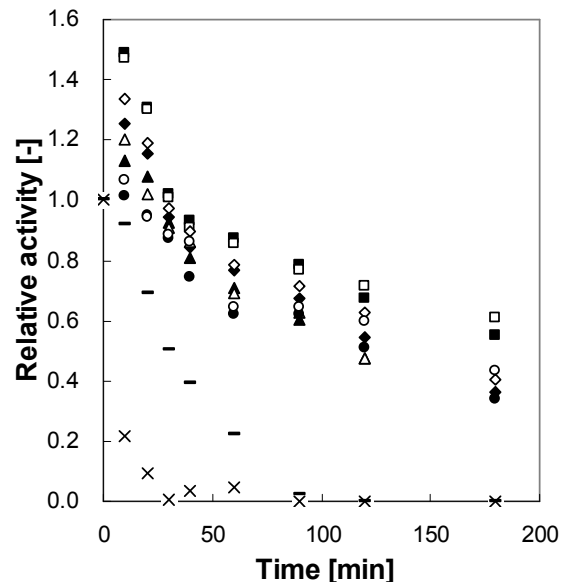


Fig. 7 The relationship between time and relative activity in various pHs and temperatures. (■:pH 5.7, 35°C, □:pH 5.9, 35°C, ◆:pH 5.7, 40°C, ◇:pH 5.9, 40°C, ▲:pH 5.7, 45°C, △:pH 5.9, 45°C, ●:pH 5.7, 50°C, ○:pH 5.9, 50°C, ×:pH 5.7, 60°C, —:pH 5.9, 60°C)

### 3.4 Phenol polymerization in the presence of HBC

Fig.8 shows time course of phenol concentration in various HRP concentrations. This graph indicates that polymerization reaction rate increase with increasing HRP concentration. However, it's more economic to use less HRP. Therefore HRP concentration in polymerization process was decided to 5 mg/L. Time courses of phenol concentration in the condition with or without HBC are shown in Fig.9. This result indicates that phenol polymerization could occur in the presence of HBC.

### 3.5 Material balance

RE was shown in Fig.10. From calculation results, the proposed recycle model turns out to be effective compared to no recycle method. And it was also found that recycle solution had approximately 3 times HRP concentration to initial HRP concentration when HBC solution was shrank for 30 min at 50°C.

## 4. Conclusion

In this study, we suggested the HRP separation method from aqueous solution by using HBC gelation process. Gelation temperature of HBC in various conditions, gel shrinking ratio, phenol and HRP ratio in HBC gel, HRP activity, thermostability of HRP, and phenol polymerization reaction were investigated. And 10-500 mg/L phenol wastewater in HBC was treated. The result showed possibility of decrease up to environmental criteria of phenol concentration was implied.

Material balances in each process were calculated using obtained data. In the results, the proposed HRP recycle method showed 1.0-1.7 times effect defined as additive HRP concentration compared to the condition of no recycle process.

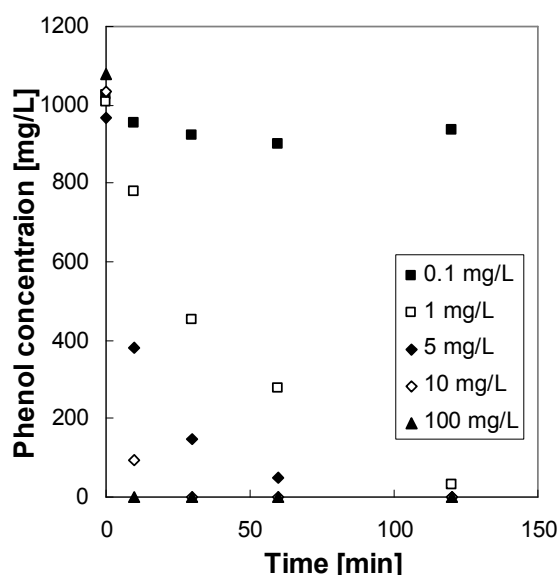


Fig.8 Time course of phenol concentration in the conditions of various HRP concentrations.

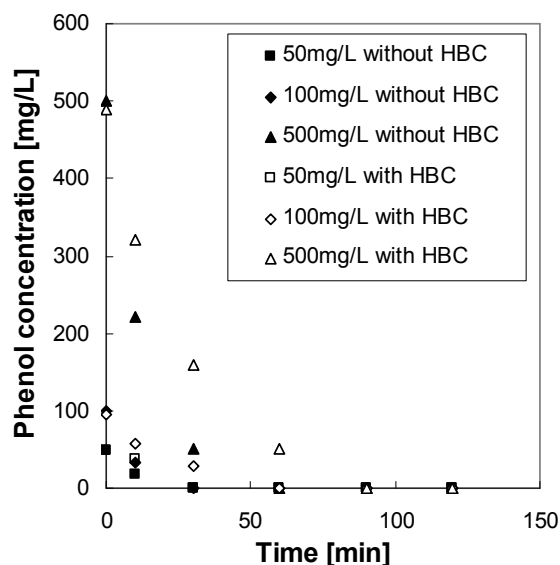


Fig.9 Time courses of phenol concentration in the conditions with or without HBC.

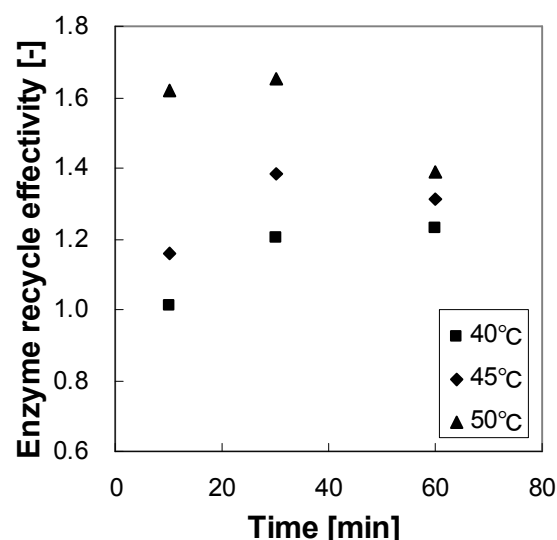


Fig. 10 Enzyme recycle effect of various times and temperatures.

## Acknowledgement

We are grateful to T. Kajiuchi Prof. Emeritus at Tokyo Institute of Technology for his helpful discussion. We wish to thank Dainichiseika Ltd., for providing HBC.

## References

- [1] L. Gianfreda *et al*, *Water research*, **37**, 3205-3215 (2003)
- [2] Miguel A Duarte-Vazquez *et al.*, *Chem. Technol. Biotechnol.*, **78**, 42-47 (2002)
- [3] 長田義仁, 梶原莞爾: 普及版ゲルハンドブック, エヌ・ティー・エス (1997) in Japanese

## EXTRACTION OF COAL TAR ABSORPTION OIL BY A CONTINUOUS COUNTER CURRENT SPRAY COLUMN

Student Number: 04M18127 Name: Saito Jun Supervisor: Egashira Ryuichi

### 連続式向流接触スプレー塔によるコールタール吸収油の抽出分離 齋藤 潤

コールタール蒸留留分の一つである吸収油中の含窒素成分（キノリン，イソキノリン，インドール）とその他の成分（同素環式化合物など）の抽出分離に対しスプレー塔型接触装置を適用した。溶媒の組成，両相の流量，などの条件を変化させて，原料吸収油（重液，分散相）と溶媒であるメタノール水溶液（軽液，連続相）を向流に接触させ定常状態に至らせた。良好な向流接触操作が可能であり，含窒素成分の収率および他の成分に対する分離の選択性は，それぞれ最大で 0.3 および 30 程度であった。また，物質移動抵抗は連続相側が支配的であった。

### 1. Introduction

Coal tar, one of the byproducts from coal carbonization, contains many useful compounds to chemical industry. First, coal tar is separated into several fractions by distillation. Absorption oil (abbreviated to AO) which is one of these fractions (b.p.=470~550K) contains nitrogen heterocyclic compounds (nitrogen compounds) such as quinoline (Q), isoquinoline (IQ), indole (IL), etc, and the other compounds such as naphthalene (N), 1-methylnaphthalene (1MN), 2-methylnaphthalene (2MN), biphenyl (BP), dibenzofuran (DBF) etc. Generally, the current method mainly used to separate these compounds in AO is reactive extraction by acid and/or base. However, this process is relatively costly because the acid and base used as solvent are very difficult to be recovered and cause corrosion of the equipments. For the separation problems, the solvent extraction with aqueous methanol (MeOH aq.) etc<sup>1-8)</sup> has been suggested. The process proposed is based on the liquid-liquid equilibriums of the components and there are no studies concerning about practical contactors and mass transfer rates. Spray columns are the simplest differential-contact devices in laboratory studies. Their advantages are that the throughput is large and the interfacial area is directly measurable. In this study, a countercurrent spray column was applied to separation of AO as a continuous apparatus in practical use and operability, separation performances including mass transfer rates, and so forth were examined.

### 2. Experimental

Schematic diagram of the apparatus used in continuous operation is shown in Fig. 1. The column is made of pyrex glass and behavior in the column can be observed. Figure 2 shows details of distributors. The distributor of dispersed phase has 8 needle nozzles. The distributor of continuous phase has outlets on side of cylinder to pretend falling disperse drops entering in it. The experimental procedure is below. First, feed

(AO) and solvent (MeOH aq.) were stocked in the tanks. The column top and bottom were continuously fed with AO as the dispersed phase and MeOH aq. as the continuous phase respectively and the two fluids were contacted countercurrently. The inlet flow rates were kept constant by checking the flow indicators and the level of the interface between the continuous phase and accumulated raffinate phase at the bottom was maintained by adjusting the drain valve of raffinate phase. The inlet and outlet flow rates were determined by weighing outlet mass per unit time, respectively. The holdup of dispersed phase in the column was obtained by measuring the ascent of interface between continuous phase and accumulated raffinate phase at the bottom when the AO inlet and drain were closed at the same time. AO, solvent, raffinate, and extract phase were

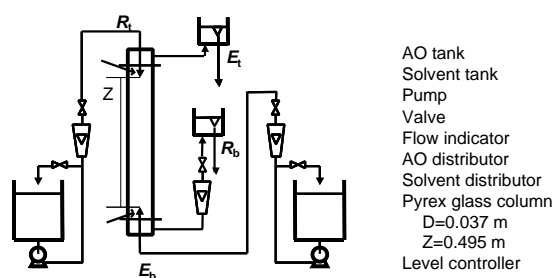


Fig.1 Schematic diagram of the experimental apparatus

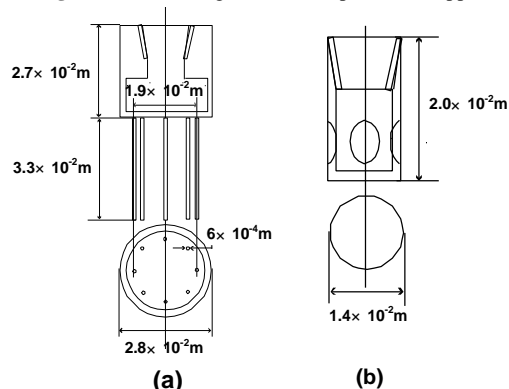


Fig. 2 Details of distributors;

(a) for dispersed phase; (b) for continuous phase

analyzed by GC<sup>6)</sup> and Karl Fischer's titration was conducted to give the water content. The densities of these phases were measured with the pycnometers. The principal experimental conditions are summarized in **Table 1**. Water content in the solvent,  $y_{w,b}$ , and inlet flow rates,  $E_b$ , and  $R_t$ , were changed.

**Table.1** Experimental conditions

No	feed:absorption oil $R_t$ [kg·hr <sup>-1</sup> ·m <sup>-2</sup> ]	solvent:aqueous methanol $y_{w,b}$ [-]	$E_b$ [kg·hr <sup>-1</sup> ·m <sup>-2</sup> ]
EC1	$4 \times 10^2 \sim 3 \times 10^3$	0.3	$1 \times 10^3$
EC2	$5 \times 10^2 \sim 5 \times 10^3$	0.5	$1 \times 10^3$
EC3	$4 \times 10^2 \sim 4 \times 10^3$	0.3	$2 \times 10^3$
EC4	$4 \times 10^2 \sim 5 \times 10^3$	0.5	$2 \times 10^3$

The liquid-liquid equilibrium relationships were measured for estimating the mass transfer rates.

### 3. Result and discussion

#### 3.1. Basic results

##### 3.1.1. Liquid-liquid equilibrium

The liquid-liquid equilibrium relationships obtained in this study were equal to those in the previous study<sup>6)</sup>.

##### 3.1.2. Density

The densities of materials are summarized in **Table 2**. The density of dispersed phase was larger than that of extract phase. The density changes did not effect seriously on continuous operation. The density of continuous phase in the runs with  $y_{w,b} = 0.5$  was larger than that in those with 0.3.

**Table.2** Densities of the materials

Materials	Density [kg·m <sup>-3</sup> ]
absorption oil	$1.1 \times 10^3$
methanol	$7.9 \times 10^2$
aqueous methanol ( $y_{w,b} = 0.3$ )	$8.7 \times 10^2$
aqueous methanol ( $y_{w,b} = 0.5$ )	$9.2 \times 10^2$
raffinate phase	$1.1 \times 10^3$
extract phase ( $y_{w,b} = 0.3$ )	$8.8 \sim 8.9 \times 10^2$
extract phase ( $y_{w,b} = 0.5$ )	$9.2 \sim 9.3 \times 10^2$

#### 3.2. Numerical relationships

The holdup of dispersed phase in the column,  $H$ , was defined by

$$H = V_d / V \quad (1)$$

The  $V_d$  and  $V$  in the equation were the volume of disperse phase in the column and the column volume, respectively. One can write the material balance relationship in terms of the mass change rates of constituents  $i$  in respective phases with the mass fractions, as follows:

$$R_t \cdot x_{i,t} - R_b \cdot x_{i,b} = E_t \cdot y_{i,t} - E_b \cdot y_{i,b} \quad (2)$$

The yield,  $Y_i$ , and separation selectivity relative to 2MN of component  $i$ ,  $\beta_{i/2MN}$ , were defined by,

$$Y_i = E_t \cdot y_{i,t} / R_t \cdot x_{i,t} \quad (3)$$

$$\beta_{i/2MN} = (y_{i,t} / y_{2MN,t}) / (x_{i,b} / x_{2MN,b}) \quad (4)$$

The overall coefficient of mass transfer based on the

concentration in continuous phase,  $K_{c,i}$ , was calculated by,

$$d(R \cdot x_i) / dz = -K_{c,i} \cdot a \cdot (y_i^* - y_i) \quad (5)$$

with the boundary conditions of top and bottom of the column.  $y_i^*$  in this equation was estimated from  $x_i$  with using the equilibrium relationships.  $a$  and  $z$  were specific interfacial area between continuous phase and disperse phase and distance from top of the column, respectively.

#### 3.3. Behavior in the column

In all the runs, entrainment of the dispersed phase particles into the continuous phase and flooding were not observed and then countercurrent contact could be carried out favorably. The diameters of dispersed phase drops were larger in the runs with  $y_{w,b} = 0.5$  than in those with 0.3 because the differences of densities between continuous and dispersed phase were smaller (see Table 2). The drop diameters decreased, as the flow rate of dispersed phase,  $R_t$ , increased (see **Fig. 3**). The coalescence of the dispersed phase and axial mixing were observed in the range of higher  $R_t$ . Holdup of dispersed phase in the column,  $H$ , shows in **Fig. 4**.  $E_b$  and  $y_{w,b}$  had no effect on  $H$ . Therefore the flow rates of both phases were under the loading point. **Figure 5** shows the specific interfacial area,  $a$ , plotted against  $R_t$ .

#### 3.4. Composition

The compositions of feed AO are shown in **Table 3**. **Figure 6** shows the extract compositions,  $y_{i,t}$ , plotted against  $R_t$ . The substantial mass transfers of studied compounds could be detected with this bench scale column of which effective contact height was 0.495 m. In all the runs,  $y_{i,t}$  increased with increasing  $R_t$ . The nitrogen compounds transferred from feed into extract phase preferentially to the other compounds and the separation between these compounds could be achieved. In the low range of  $R_t$ ,  $y_{i,t}$  were smaller in the runs with  $E_b=2000$  than in those with 1000, but the differences became small with increasing  $R_t$ . It was because two phases in the column almost reached equilibrium in the high range  $R_t$ ,

**Table 3** Compositions of feed oil

Composition in mass fraction			
quinoline	$x_{Q,t}$	[-]	0.05 ~ 0.09
isoquinoline	$x_{IQ,t}$	[-]	0.02 ~ 0.03
indole	$x_{IL,t}$	[-]	0.04 ~ 0.06
naphthalene	$x_{N,t}$	[-]	0.02 ~ 0.03
1-methylnaphthalene	$x_{1MN,t}$	[-]	0.09 ~ 0.1
2-methylnaphthalene	$x_{2MN,t}$	[-]	0.2 ~ 0.3
biphenyl	$x_{BP,t}$	[-]	0.06 ~ 0.09
dibenzofuran	$x_{DBF,t}$	[-]	0.06 ~ 0.1
water	$x_{w,t}$	[-]	0 ~ 0.004
methanol	$x_{MeOH,t}$	[-]	0 ~ 0.04

#### 3.5. Yield and selectivity

**Figure 7** shows the yields  $Y_i$  against  $R_t$ .  $Y_i$  were bigger in the runs with  $y_{i,w} = 0.3$  than in those with 0.5 for the equilibrium relationship. In the range of this work,  $Y_i$  of the nitrogen compounds were about 0.4 at maximum with this column,

while those of the other components were below 0.1. **Figure 8** shows the separation selectivity,  $b_{i/2MN}$  against  $R_t$ .  $b_{i/2MN}$  of the nitrogen compounds were larger in the run with  $y_{w,b} = 0.5$  than in those with 0.3 and about 30 at maximum.

**3.6. Overall mass transfer coefficient**

**Figure 9** shows the overall volumetric mass transfer coefficients based on the concentration in continuous phase,  $K_{c,i}a$ , against  $R_t$ .  $K_{c,i}a$  increased with  $R_t$ , mainly due to the decrease of diameter of dispersed phase drops and then that of the increase of specific interfacial area,  $a$ . The effects of  $R_t$  on the overall mass transfer coefficient based on the concentration in the continuous phase,  $K_{c,i}$ , are shown in **Fig. 10**. The axial mixing was observed in the high range of  $R_t$ .  $K_{c,i}$  decreased with increasing  $R_t$  because concentration differences became smaller compared with the case to assume the plug flow in the column.  $K_{c,i}$  in the case of higher solvent flow rate,  $E_t$ , was larger than those at the lower  $E_t$ . Therefore, the laminar film in continuous phase controlled the mass transfers.

**4. Conclusion**

The extraction separation of absorption oil with the continuous apparatus was carried out favorably under the conditions in this study. The yields,  $Y_i$ , and selectivity,  $\beta_{i/2MN}$ , of them were about 0.4 and 30 at maximum, respectively. The mass transfers were explained in term of mass transfer coefficients. The overall mass transfer coefficient based on the concentration in the continuous phase,  $K_{c,i}$ , decreased with increasing  $R_t$  because axial mixing occurred in the column. The mass transfer resistance existed mainly in continuous phase. Consequently, the useful information for the process design was provided.

**Acknowledgment**

AO was provided by JFE Chemical Corporation.

**Nomenclatures**

- $a$  : specific interfacial area [m<sup>2</sup>·m<sup>-3</sup>]
  - $E$  : superficial mass flow rate of aqueous phase [kg·hr<sup>-1</sup>·m<sup>-2</sup>]
  - $H$  : holdup of the dispersed phase [-]
  - $K_c$  : overall mass transfer coefficient based on the concentration in continuous phase [kg·hr<sup>-1</sup>·m<sup>-2</sup>]
  - $R$  : superficial mass flow rate of oil phase [kg·hr<sup>-1</sup>·m<sup>-2</sup>]
  - $V$  : volume in the column [m<sup>3</sup>]
  - $x$  : mass fraction in oil phase [-]
  - $y$  : mass fraction in aqueous phase [-]
  - $Y$  : yield [-]
  - $z$  : distance from top of the column [m]
  - $Z$  : effective contact height of column [m]
  - $b_{i/2MN}$  : separation selectivity of component  $i$  relative to 2-methylnaphthalene [-]
- <Subscripts>  
 1MN : 1-methylnaphthalene  
 2MN : 2-methylnaphthalene

- b : at bottom of the column
- BP : biphenyl
- DBF : dibenzofuran
- IL : indole
- IQ : isoquinoline
- $i$  : component  $i$
- MeOH: methanol
- N : naphthalene
- Q : quinoline
- t : at top of the column
- W : water

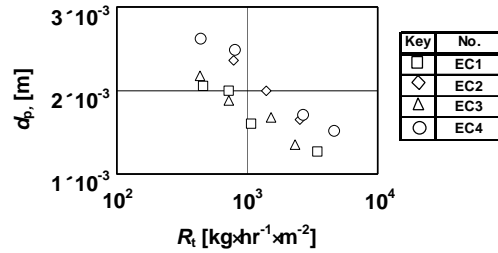


**Fig. 3** Diameters of the dispersed phases

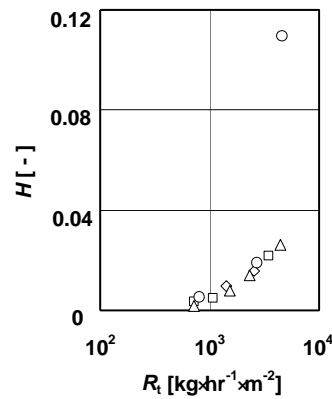


**Fig. 4** Holdup of the dispersed phase,  $H$ : (the keys are the same as Fig. 3)

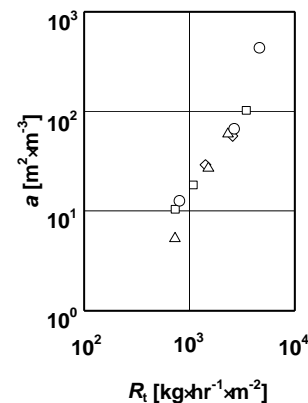


**Fig. 5** specific interfacial area,  $a$ : (the keys are the same as Fig. 3)

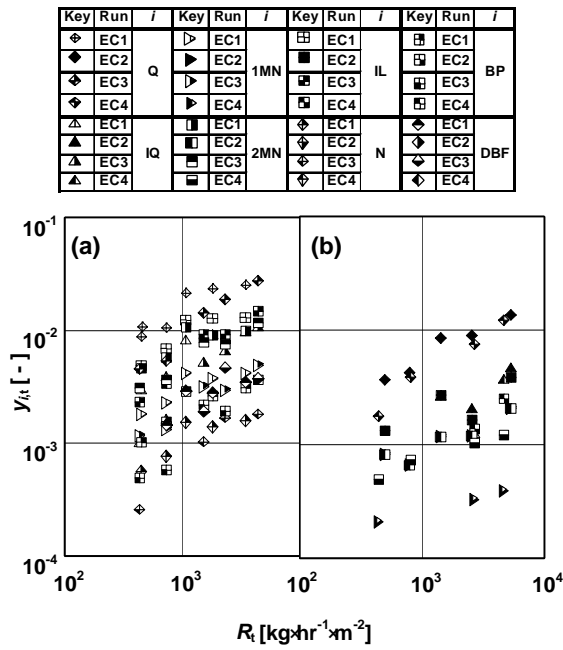


Fig. 6 Extract compositions,  $y_{it}$ :(a) in EC1 and 3; (b) in EC2 and 4

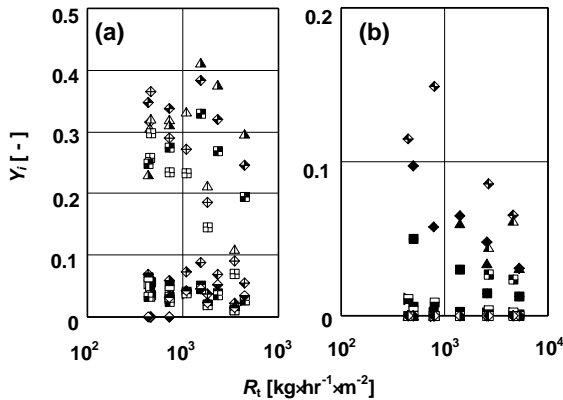


Fig. 7 Yields,  $Y_i$ :(a) in EC1 and 3; (b) in EC2 and 4 (the keys are the same as Fig. 6)

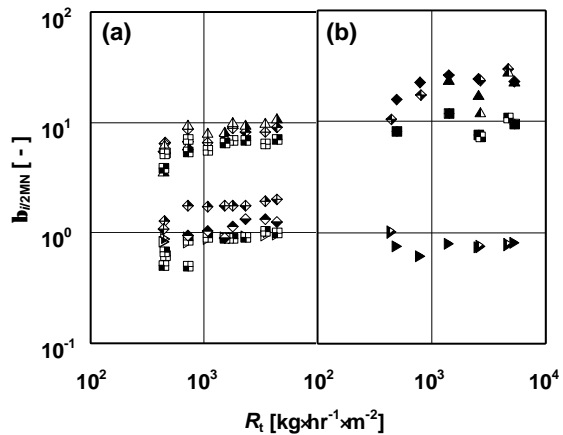


Fig. 8 Separation selectivity,  $b_{i/2MN}$ :(a) in EC1 and 3; (b) in EC2 and 4 (the keys are the same as Fig. 6)

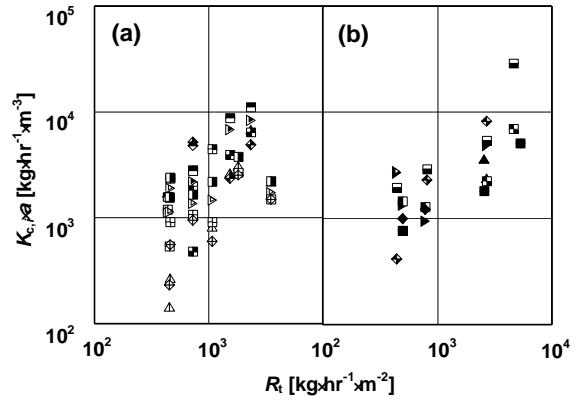


Fig. 9 Overall volumetric mass transfer coefficients based on the concentration in continuous phase,  $K_{c,i}α$ :(a) in EC1 and 3; (b) in EC2 and 4(the keys are the same as Fig. 6)

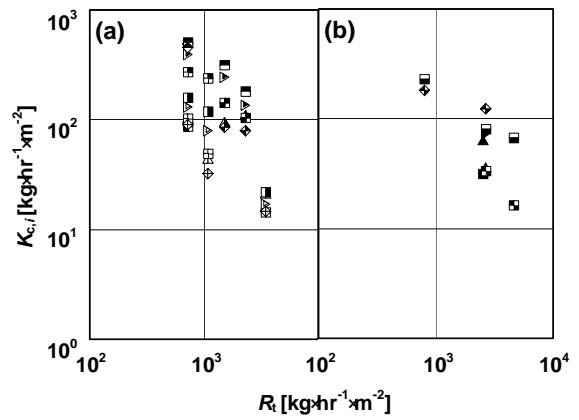


Fig. 10 Overall mass transfer coefficients based on the concentration in continuous phase,  $K_{c,i}$ :(a) in EC1 and 3; (b) in EC2 and 4 (the keys are the same as Fig. 6)

Reference

- 1) Ukegawa, K., Matsumura, A., Kodera, Y., Kondo, T., Nakayama, T., Tanabe, H., Yoshida, S., Mito, Y., *Sekiyu Gakkaishi (J. Jpn. Petrol. Inst.)*, **33**, (4), 250 (1990).
- 2) Kodera, Y., Ukegawa, K., Mito, Y., Komoto, M., Ishikawa, E., Nagayama, T., *Fuel*, **70**, (6), 765 (1991).
- 3) Matumura, A., Kodera, Y., Kondo, T., Ukegawa, K., Tanabe, H., Yoshida, S., Mito, Y., *Shigen to Kankyo (Journal of NIRE)*, **4**, (2), 147 (1995)
- 4) Egashira, R., Nagai, M., *Sekiyu Gakkaishi (J. Jpn. Petrol. Inst.)*, **43**, (5), 339 (2000)
- 5) Egashira, R., Salim, C., *Sekiyu Gakkaishi (J. Jpn. Petrol. Inst.)*, **44**, (3), 178 (2001)
- 6) Salim, C., Saito, J., Egashira, R., *Journal of the Japan Petroleum Institute*, **48**, (1), 60 (2005)
- 7) Watanabe, K., Egashira, R., 34th Japan Petroleum Institute meeting, (2004)
- 8) Salim, C. Dissertation for a doctoral degree of engineering, Tokyo Institute of Technology (2005)

## Preparation and Structure Control of Plasma Polymerized Films by Utilizing Afterglow Region in Atmospheric Non-thermal Plasma

Student Number: 03M18236 Name: Takuo MIURA Supervisor: Hidetoshi SEKIGUCHI

大気圧非平衡プラズマのアフターグロー領域を利用した重合膜の作製とその構造制御

三浦 拓生

本研究では、大気圧下の非平衡プラズマにおいて、アフターグロー領域を活用した技術に着目し、アセチレンから有機系の重合膜の作製するとともに、その構造制御を試みた。様々なパラメータを操作して生成した膜の赤外分光スペクトルを比較した結果より、アルゴンの活性種が気相中で  $sp^2$  結合の生成を促進し、基板温度によって水素の結合が進む重合モデルを提示した。

### 1. Introduction

Plasma assisted chemical vapor deposition (PACVD) technology by using atmospheric non-thermal plasma has a potential use in a film deposition on a substrate which is easily affected by heat, such as plastics. In our laboratory, we have succeeded to prepare the carbon related thin films by using atmospheric glow discharge (APGD) [1]. The carbon related films prepared by the PACVD can form as amorphous hydrogenated carbon ( $a-C:H$ ), diamond like carbon (DLC) and organic thin films [2]. The organic thin films have various applications in mechanics, electronics and optics [3]. In particular, the organic films prepared by plasma, so called plasma polymer, have unique structure represented by the irregular three-dimensional crosslinked network [4].

However, the structure control of the plasma polymer has not been achieved due to a variety of active species produced in the plasma region [5]. It causes a difficulty to design the molecular structure of the polymer and its properties.

Therefore, this work will exhibit the significant factors in the structure of the plasma polymer under atmospheric conditions. The afterglow region of the APGD is utilized because it can reduce the impact of highly active species in bulk region which can dissociate monomer gas into a various species. Besides, pulsed plasma which is known as a technique to reduce input power is also used to investigate the effect of pulse parameters.

### 2. Experimental

Experimental set-up is shown in Figure 1. Cylindrical quartz torch (diameter: 6 mm, thickness: 1 mm) has a copper tube (diameter: 2 mm, thickness: 0.5 mm) as inside high voltage electrode and aluminum foil (width: 15 mm) as outside ground electrode. Acetylene gas (in some

cases ethylene is used as a monomer) is introduced through the inside of the copper tube while argon gas flows between the copper tube and the quartz torch. Three types of power supply with different frequency range at 13.56 MHz, 200 – 1999 kHz and 0.1 – 10 kHz are employed to generate plasma. Carbon related thin films are deposited on mono-crystal silicon wafer substrates which are open to the atmosphere. The voltage and the current are measured with an oscilloscope and the power is calculated by numerical integration. In this torch, the monomer gases are led into the afterglow region of the plasma, so that the bulk plasma can be generated with only argon gas at low power [6]. In the case of pulsed plasma, pulsed condition is achieved by connecting a function generator to the power supply.

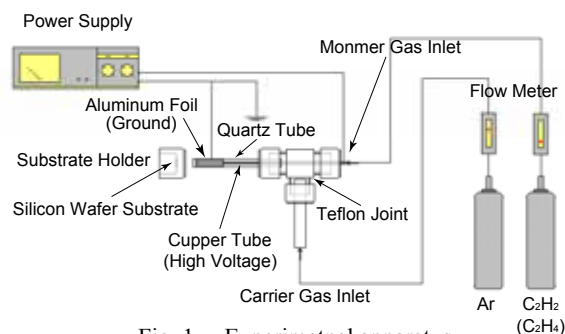


Fig. 1. Experimental apparatus

Deposited films are analyzed by Fourier Transfer Infrared Spectroscopy (FT-IR). In this work, the  $sp^2/sp^3$  ratio and  $CH_3/CH_2$  ratio of the carbon bond is measured by peak fitting of the FT-IR spectra. The peaks between  $2800\text{ cm}^{-1}$  and  $3100\text{ cm}^{-1}$  assign C-H bond. The details of the assignments are shown in Table I.

The integrated intensity is applied for the peak ratio.  $R(sp^2/sp^3)$  is defined as the ratio between  $sp^2$  bond and  $sp^3$  bond while  $R(CH_3/CH_2)$  indicates the ratio between terminal carbon and chained carbon.

Table I. Assignments of C-H bonds between 2800 cm<sup>-1</sup> to 3100 cm<sup>-1</sup> in IR spectrum (possibly shift in a few Kayser)

Wavenumber [cm <sup>-1</sup> ]	Assginment
2840	-CH <sub>2</sub> sp <sup>3</sup> sym
2870	-CH <sub>3</sub> sp <sup>3</sup> sym
2890	-CH sp <sup>3</sup>
2920	-CH <sub>2</sub> sp <sup>3</sup> asym
2960	-CH <sub>3</sub> sp <sup>3</sup> asym
3000	=CH sp <sup>2</sup>
3025	=CH <sub>2</sub> sp <sup>2</sup> olef
3055	=CH sp <sup>2</sup> arom
3080	=CH <sub>2</sub> sp <sup>2</sup> asym
3300	≡CH sp <sup>1</sup>

(sym: symmetric, asym: asymmetric, olef: olefinic, arom: aromatic)

Experimental conditions are shown in Table II. Three different power supplies are used in order to change the frequency range. Pulse parameters are available under pulsed plasma conditions.

Table II. Experimental conditions

Frequency	13.56 MHz
	600 – 800 kHz
	6 – 10 kHz
Voltage	1 – 3 kV
Power	2 – 40 W
Argon flow rate	20 – 50 sccm
Acetylene flow rate	2 – 10 sccm
Deposition time	10 min
Period (pulse)	1 – 20 ms
Duty (pulse)	20 – 60 %

### 3. Results and Discussion

#### 3.1. FT-IR spectra at the different frequency range

In this work, plasma polymerized films were prepared mainly from acetylene monomer by using three different frequency range; 13.56 MHz, 600 – 800 kHz and 6 – 10 kHz. Figure 2 shows those typical FT-IR spectra at each frequency.

Firstly, a peak around 3400 cm<sup>-1</sup> observed at 6 – 10 kHz frequency is noticeable compared to the other spectra. The peak indicates hydroxyl bond having -OH functional groups. Although it is not likely for oxygen to get involved in the polymerization with argon and acetylene, there are a few possibilities such as ion etching of quartz tube and air contamination in the afterglow region. The major difference between 6 – 10 kHz and the other two cases is the voltage which is much higher at low frequency. Thus, it is suggested that the

higher voltage at low frequency can produce higher energy electrons and different excited argon species which can cause quartz tube sputtering and oxygen dissociation. The hypothesis can be supported by the optical emission spectra (OES) of argon plasma at the different power supply shown in Figure 3. Some peaks get strong or weak by changing the frequency.

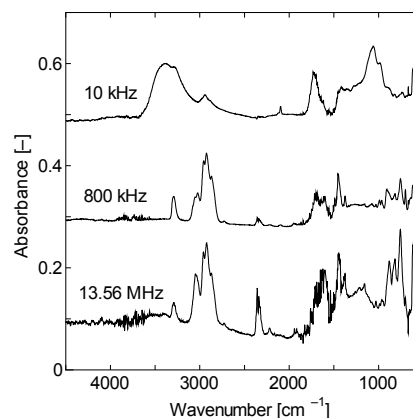


Fig. 2. FT-IR spectra with different frequency

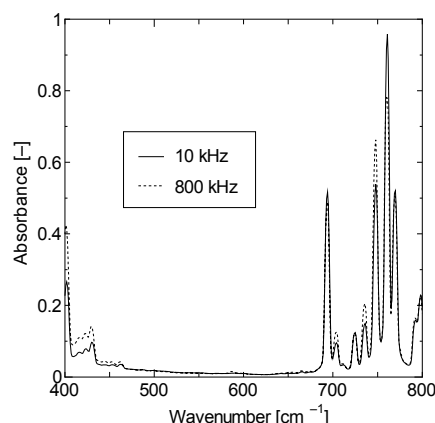


Fig. 3. OES spectra with different frequency

Secondly, comparing the two spectra at 13.56 MHz and 600 – 800 kHz, the peak intensity around 3000 – 3080 cm<sup>-1</sup> assigning =CH with 13.56 MHz seems to be higher than that with 600 – 800 kHz. In fact,  $R(sp^2/sp^3)$  is 0.3 – 0.7 with 13.56 MHz while it is 0.1 – 0.3 with 600 – 800 kHz in various conditions. This is considered to be due to the power difference because 13.56 MHz power supply consumes much larger power than 600 – 800 kHz. Large power can cause the high argon radicals concentration and raise the energy level of the argon radicals. It also increases the temperature of the reaction field. The effect will be discussed further in Section 3.3.

### 3.2. Correlation between the monomers and the film structure

Acetylene and ethylene were employed as monomer gases at 800 kHz. Figure 4 shows that there are three distinctive differences between the films prepared by acetylene and ethylene as follows:

- (1) Carbon triple bond assignment at 3300  $\text{cm}^{-1}$  can not be observed in the case of ethylene.
- (2) The stronger peak around 3000 – 3080  $\text{cm}^{-1}$  is observed under acetylene use conditions.
- (3) Ethylene monomer makes the 2960  $\text{cm}^{-1}$  peak stronger than the peak at 2920  $\text{cm}^{-1}$  while acetylene makes the opposite.

These characteristic differences are identical to the report with low pressure plasma.

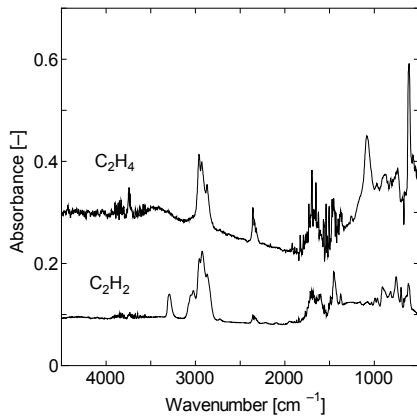


Fig. 4. FT-IR spectra of the films with different monomers; acetylene ( $\text{C}_2\text{H}_2$ ) and ethylene ( $\text{C}_2\text{H}_4$ )

### 3.3. Effect of the argon and acetylene flow rates and the input power

$R(\text{sp}^2/\text{sp}^3)$  and  $R(\text{CH}_3/\text{CH}_2)$  were measured with different argon and acetylene flow rates and input power by using 13.56 MHz power supply.

As shown in Figure 5 and 7,  $R(\text{sp}^2/\text{sp}^3)$  slightly increases with argon flow rate, however it does not change with acetylene flow rate. Figure 9 shows  $R(\text{sp}^2/\text{sp}^3)$  rises as the input power increases. The increase of the argon flow rate causes intense interference between argon and the other species, such as acetylene and its polymerized particles. On the other hand, the acetylene flow rate cannot affect  $R(\text{sp}^2/\text{sp}^3)$ .

Therefore, the argon species including radicals and ions are considered to have an increase effect on the  $\text{sp}^2$  bond. It is supported by the power dependence because higher power can increase the effect of the activated argon species in terms of the concentration and the energy level.

As to  $R(\text{CH}_3/\text{CH}_2)$ , it declined with argon flow rate while being constant with acetylene flow rate in Figure 6 and 8. In Figure 10,  $R(\text{CH}_3/\text{CH}_2)$  increased with the input power. The different tendency with argon flow rate from  $R(\text{sp}^2/\text{sp}^3)$  proposes a different mechanism.

In this case, the temperature has an effect on  $R(\text{CH}_3/\text{CH}_2)$  because the temperature decreased with argon flow rate but did not change with acetylene flow rate. Similarly, it increased with the input power. Thus, it is suggested that high temperature promotes hydrogen addition on the film as  $\text{CH}_3$  is mainly produced by a reaction between activated carbon and dissociated hydrogen.

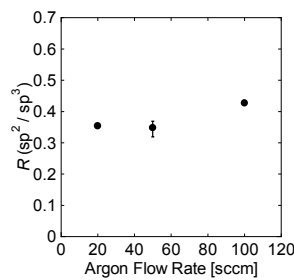


Fig. 5.  $R(\text{sp}^2/\text{sp}^3)$  with different argon flow rate

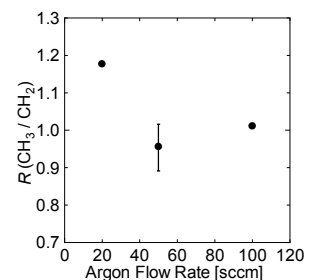


Fig. 6.  $R(\text{CH}_3/\text{CH}_2)$  with different argon flow rate

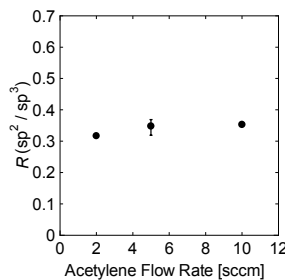


Fig. 7.  $R(\text{sp}^2/\text{sp}^3)$  with different acetylene flow rate

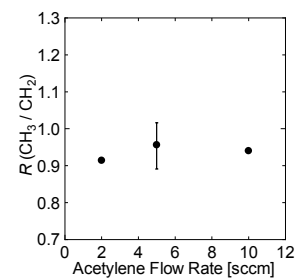


Fig. 8.  $R(\text{CH}_3/\text{CH}_2)$  with different acetylene flow rate

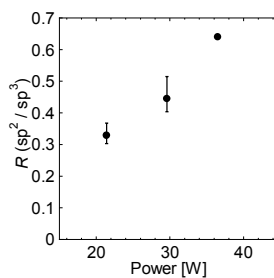


Fig. 9.  $R(\text{sp}^2/\text{sp}^3)$  with different power

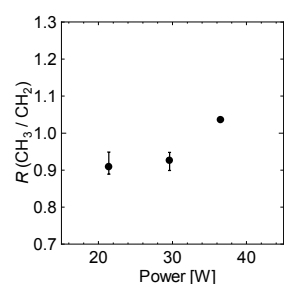


Fig. 10.  $R(\text{CH}_3/\text{CH}_2)$  with different power

### 3.4. Reaction mechanism with respect to $R(\text{sp}^2/\text{sp}^3)$ and $R(\text{CH}_3/\text{CH}_2)$

According to the discussion above,  $R(\text{sp}^2/\text{sp}^3)$  is affected by argon radicals and ions. As for

$R(\text{CH}_3/\text{CH}_2)$ , temperature has a significant effect on the ratio. From a complementary experiment shown in Figure 11 and 12, it was found that the post treatment of the prepared film by heat shows significant decline of  $R(\text{sp}^2/\text{sp}^3)$  and  $R(\text{CH}_3/\text{CH}_2)$  while argon plasma has little effect on them. Considering the results of the plasma effects that increase both ratios, the post treatments is not the same with the plasma effects.

These results indicate the activated argon species promote  $\text{sp}^2$  increase in the gas phase not on the substrate. Besides, hydrogen addition can be occurred at high temperature in the presence of hydrogen radicals.

The reaction model proposed above is visualized in Figure 13.

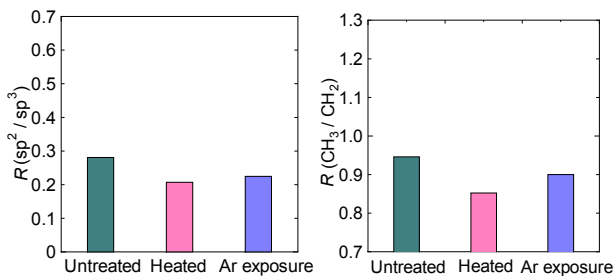


Fig 11. Effect of heat and argon plasma on  $R(\text{sp}^2/\text{sp}^3)$

Fig 12. Effect of heat and argon plasma on  $R(\text{CH}_3/\text{CH}_2)$

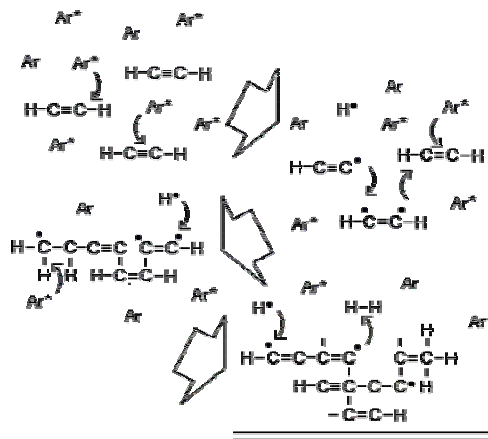


Fig 13. Polymerization mechanism

### 3.5. Pulsed plasma conditions

Under the pulsed plasma conditions at 800 kHz frequency,  $R(\text{sp}^2/\text{sp}^3)$  and  $R(\text{CH}_3/\text{CH}_2)$  were measured by changing period and duty.

From the results shown in Figure 14 and 15, both of the  $R(\text{sp}^2/\text{sp}^3)$  and  $R(\text{CH}_3/\text{CH}_2)$  decreased with period. On the other hand, both ratios increased with duty as described in Figure 16 and 17. Compared to the results with continuous

wave power supply (CW), low  $R(\text{sp}^2/\text{sp}^3)$  is observed at long period and short duty, and high  $R(\text{CH}_3/\text{CH}_2)$  is observed at short period and large duty.

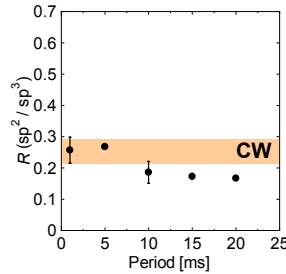


Fig 14.  $R(\text{sp}^2/\text{sp}^3)$  with different period

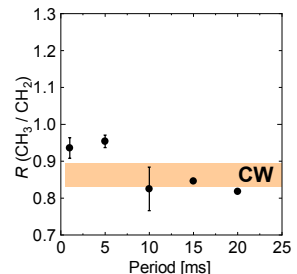


Fig 15.  $R(\text{CH}_3/\text{CH}_2)$  with different period

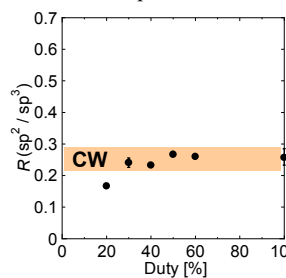


Fig 16.  $R(\text{sp}^2/\text{sp}^3)$  with different duty

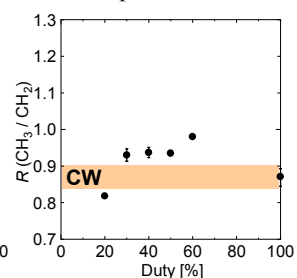


Fig 17.  $R(\text{CH}_3/\text{CH}_2)$  with different duty

Even though no satisfactory mechanism can be proposed through these experiments, these results show the potential of the pulsed plasma to control the plasma polymer structure.

## 4. Conclusions

In this research, plasma polymerized films were prepared using afterglow region and the film structure was analyzed by FT-IR at different conditions. From the behaviors of  $R(\text{sp}^2/\text{sp}^3)$  and  $R(\text{CH}_3/\text{CH}_2)$ , the reaction mechanism was proposed in relation to argon and hydrogen radicals. Besides, we found the potential of pulsed plasma to control the plasma polymer structure.

## 5. References

- [1] Miura, T., Sekiguchi, H., Transactions of the Materials Research Society of Japan, **29** (2004) 3411
- [2] Robertson, J., *Phil.Mag.*, **76** (1997) 335
- [3] Frank F.S., *Surf. Coat. Technol.*, **82** (1996) 1
- [4] Tibitt, J.M., Shen, M., Bell, A.T., *J. Macromol. Sci., Chem.* **A10** (1976) 1623
- [5] Biederman, H., Osada, Y., *Advances in Polym. Sci.*, **95** (1990) 57
- [6] Leveille, V., Cooulombe, S., *Plasma Sources Sci. Technol.*, **14** (2005) 467

# NUMERICAL ANALYSIS FOR SOLIDIFICATION OF MELT PLASTIC WITH A SPECTRAL FINITE DIFFERENCE SCHEME

04M18179 Aya FUJITA Supervisor: Yoshihiro MOCHIMARU

## スペクトル差分法を用いた溶融高分子の凝固解析

藤田 文

プラスチックは今日、工業において必要不可欠な材料で、使用分野は多岐に渡る。金型内で溶融高分子を冷却することによって成形されるプラスチックの流動過程は、溶融高分子が液体から固体に相変化するため、非常に複雑な現象であり、実験室的に実現することが難しく、数値計算によって解析を行うことが求められている。本研究では、計算精度の高いスペクトル差分法を用いて計算を行い、形状内の温度場と流れ場の特性を明らかにすることができた。

### 1. Introduction

Plastics contribute to improvement of human life, for example as parts of electrical or medical appliances, elements of automobiles, casing of food, and housing elements. Thus, demand for plastics has been increasing year by year for refinement on production process, and alternatives of the materials to reduce product weight. Also, with expansion of industries in which plastics are used, higher molding technique than ever has been needed.

Phenomena in plastic molding are very complicated, since the flow in the process is non-isothermal and unsteady with phase change from liquid to solid. Moreover, melt plastic is non-Newtonian with visco-elasticity. These characters of the fluid and flow make it difficult to predict the flow and thermal fields analytically. Many researchers had studied the behavior of non-Newtonian fluid and solidification problem of water or other Newtonian fluid. However, the problem of solidification of non-Newtonian fluid has not been investigated very much, so far. Therefore, in this study, numerical analysis for solidification of melt plastic with phase change was performed to the shape which has right angle branch, where a spectral finite difference method was used as a computational scheme with higher accuracy.

### 2. Numerical analysis

#### 2-1. Governing equations

Governing equations are the equation of continuity, the equation of motion and the equation of energy, which can be expressed as

$$\nabla \cdot \mathbf{V} = 0 \quad (2-1)$$

$$\rho \frac{D\mathbf{V}}{Dt} = -\nabla p + \nabla \cdot \boldsymbol{\tau} + \rho \mathbf{g} \quad (2-2)$$

$$\rho C_p \frac{DT}{Dt} = k \nabla^2 T \quad (2-3)$$

where  $t$ : time,  $\boldsymbol{\tau}$ : extra stress tensor,  $p$ : pressure,  $\mathbf{V}$ : velocity vector,  $\rho$ : density,  $C_p$ : specific heat,  $T$ : temperature,  $k$ : thermal conductivity,  $\mathbf{g}$ : acceleration vector of gravity. It was assumed that the flow was incompressible and laminar, and that the thermo-physical properties were constant in each phase except for viscosity. For the above governing equations, the effect of natural convection was taken into account.

In case of formulating with the stream function-vorticity method, vorticity transport equation obtained from the equation of motion and the equation of relationship between vorticity and a stream function in a Cartesian coordinate are given in a dimensionless form as,

$$\begin{aligned} & \frac{\partial \zeta}{\partial t} + \frac{\partial \psi}{\partial y} \frac{\partial \zeta}{\partial x} - \frac{\partial \psi}{\partial x} \frac{\partial \zeta}{\partial y} \\ & = Pr \left( \frac{\partial^2 \tau_{xy}}{\partial x^2} - \frac{\partial^2 \tau_{xy}}{\partial y^2} - \frac{\partial^2 \tau_{xx}}{\partial x \partial y} + \frac{\partial^2 \tau_{yy}}{\partial x \partial y} \right) + Pr Ra \frac{\partial \theta}{\partial x} \end{aligned} \quad (2-4)$$

$$\zeta = - \left( \frac{\partial^2 \psi}{\partial x^2} + \frac{\partial^2 \psi}{\partial y^2} \right) \quad (2-5)$$

where  $\zeta$ : vorticity,  $\psi$ : stream function,  $Pr = \nu/a$ : Prandtl number,  $Ra = g\beta\Delta TH^3/\nu\alpha$ : Rayleigh number,  $\nu = \mu/\rho$ : kinematic viscosity,  $\mu = \mu_0 \exp(\hat{H}/R(1/T - 1/T_0))$ :

viscosity,  $\Delta\hat{H}$ : activation energy,  $R$ : universal gas constant,  $a$ : thermal diffusivity,  $H$ : characteristic length,  $\beta$ : coefficient of volume expansion. Buoyancy in the vorticity transport equation is expressed with adopting Boussinesq approximation.

## 2-2 Modeling of solidification

If high temperature melt plastic is cooled, the phase of plastic changes from liquid phase to transition phase at melting temperature ( $T_m$ ). Then, as plastic is cooled more, the phase changes to solid at solidification temperature ( $T_s$ ). The gradient of heat capacity between  $T_m$  and  $T_s$  is very large since latent heat is emitted between  $T_m$  and  $T_s$ . Therefore, during solidification, there exists three phases in the mold, which requires three types of energy equation. Specific heat was assumed to be of the form,

$$\rho C_p' = \begin{cases} \rho_s c_{ps} & (T \leq T_s) \\ \bar{\rho} c_p + \frac{\rho L}{T_m - T_s} & (T_s < T < T_m) \\ \rho_l c_{pl} & (T_m \leq T) \end{cases}$$

where  $L$ : latent heat,  $C_p'$ : apparent specific heat. Thus, the phase change problem is expressible in a single energy equation, which is in the stream function – vorticity formulation in a Cartesian coordinate.

$$C_p' * \left( \frac{\partial \theta}{\partial t} + \frac{\partial \psi}{\partial y} \frac{\partial \theta}{\partial x} - \frac{\partial \psi}{\partial x} \frac{\partial \theta}{\partial y} \right) = \left( \frac{\partial^2 \theta}{\partial x^2} + \frac{\partial^2 \theta}{\partial y^2} \right) \quad (2-6)$$

where  $C_p'$ : dimensionless apparent specific heat,  $\theta$ : dimensionless temperature.

## 2-3 Constitutive equation

In this study, Maxwell model was used as a constitutive equation. Components of the Maxwell model equation are

xx component:

$$\tau_{xx} + We \left\{ \frac{\partial \tau_{xx}}{\partial t} + \frac{\partial \psi}{\partial y} \frac{\partial \tau_{xx}}{\partial x} - \frac{\partial \psi}{\partial x} \frac{\partial \tau_{xx}}{\partial y} - 2 \left( \frac{\partial^2 \psi}{\partial x \partial y} \tau_{xx} + \frac{\partial^2 \psi}{\partial y^2} \tau_{xy} \right) \right\} = 2 \frac{\partial^2 \psi}{\partial x \partial y} \quad (2-7)$$

xy component:

$$\tau_{xy} + We \left\{ \frac{\partial \tau_{xy}}{\partial t} + \frac{\partial \psi}{\partial y} \frac{\partial \tau_{xy}}{\partial x} - \frac{\partial \psi}{\partial x} \frac{\partial \tau_{xy}}{\partial y} - \left( -\frac{\partial^2 \psi}{\partial x^2} \tau_{xx} + \frac{\partial^2 \psi}{\partial y^2} \tau_{yy} \right) \right\} = \left( -\frac{\partial^2 \psi}{\partial x^2} + \frac{\partial^2 \psi}{\partial y^2} \right) \quad (2-8)$$

yy component:

$$\tau_{yy} + We \left\{ \frac{\partial \tau_{yy}}{\partial t} + \frac{\partial \psi}{\partial y} \frac{\partial \tau_{yy}}{\partial x} - \frac{\partial \psi}{\partial x} \frac{\partial \tau_{yy}}{\partial y} + 2 \left( \frac{\partial^2 \psi}{\partial x^2} \tau_{xy} + \frac{\partial^2 \psi}{\partial x \partial y} \tau_{yy} \right) \right\} = -2 \frac{\partial^2 \psi}{\partial x \partial y} \quad (2-9)$$

where  $\tau_{xx}$ ,  $\tau_{xy}$ ,  $\tau_{yy}$ : components of extra stress,  $We$ : Weissenberg number. In case of  $We = 0$ , the equations just express a Newtonian fluid.

## 2-4 Coordination transform

For applying the spectral finite difference scheme to a right angle branch shape, the following conformal mapping from Cartesian coordinate ( $x, y$ ) to a boundary - fitted conformal coordinate ( $r, \beta$ ) was applied.

$$r = \exp \alpha \quad (2-10)$$

$$f = e^{\alpha+i\beta} = (1+i\eta)/(1-i\eta) \quad (2-11)$$

$$\eta = -cz_1^2 + z_1 + 1/z_1 \quad (2-12)$$

$$z_1 = z_2 + b_1^2/(z_2 - 1) + b_2^2/(z_2 + 1) \quad (2-13)$$

$$w = \frac{2}{\pi} \left( H_1 \tan^{-1} \frac{z_2}{\sqrt{a_H^2 - z_2^2}} + H_2 \tanh^{-1} \frac{H_2}{H_1} \frac{z_2}{\sqrt{a_H^2 - z_2^2}} \right) \equiv x + iy$$

$$a_H^2 = 1 + H_2^2 / H_1^2 \quad (2-14)$$

Where  $c, H_1, H_2$ : constant and  $0 \leq r \leq 1, -\pi \leq \beta \leq \pi$ . Figure 1 shows the coordinate system for analysis at  $c = 1.0, H_1 = H_2 = 1.0$  and  $b_1 = b_2 = 1.0 \times 10^{-3}$ . In this coordinate, the space was divided into a suitable number,  $M$ , in  $r$  direction and  $r_M$  was defined at the boundary and  $r_0$  ( $r = 0$ ) at the center of coordinate.

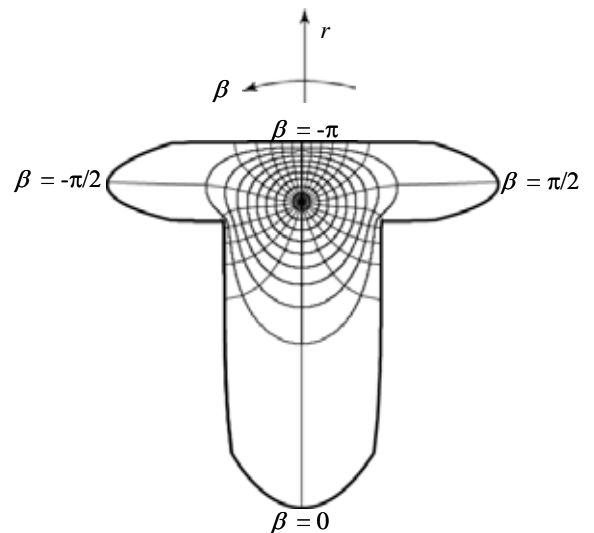


Fig.1 The coordinate system for analysis.

### 2-5 Spectral finite difference formulation

The spectral expressions of variables by using Fourier series are

$$\begin{bmatrix} \psi \\ \zeta \\ \theta \\ \tau \end{bmatrix} = \sum_{k=0}^{\infty} \begin{bmatrix} \psi_{ck}(r,t) \\ \zeta_{ck}(r,t) \\ \theta_{ck}(r,t) \\ \tau_{ck}(r,t) \end{bmatrix} \cos(k\beta) + \sum_{k=1}^{\infty} \begin{bmatrix} \psi_{sk}(r,t) \\ \zeta_{sk}(r,t) \\ \theta_{sk}(r,t) \\ \tau_{sk}(r,t) \end{bmatrix} \sin(k\beta) \quad (2-15)$$

$\psi_{ck}$  and  $\psi_{sk}$ ...are Fourier coefficients that are the function of  $r$  and  $t$ . Then, substituting these variables to Eq. (2-4) - (2-9), the equations are generally formed as follows:

$$\sum_{n=0}^{\infty} F_{cn}(r,t)\cos(n\beta) + \sum_{n=1}^{\infty} F_{sn}(r,t)\sin(n\beta) = 0 \quad (2-16)$$

The spatial variable  $\beta$  is separated and a system of simultaneous partial differential equations (with respect to one spatial variable  $r$  and time  $t$ ) is obtained.

### 2-6 Boundary conditions

The fluid was assumed to be substantially incompressible, so that no slip flow at the boundary was assumed. The conditions become  $\psi = 0$ ,  $\partial\psi/\partial r = 0$  and  $\theta = 0$  at the boundary. Also, auxiliary conditions at  $r = 0$  ( $r = r_0$ ) were introduced. The conditions of extra stress were obtained from the conditions of stream function.

### 3. Results and discussion

The material was assumed to be polyethylene. The properties of polyethylene are shown in Table 1.

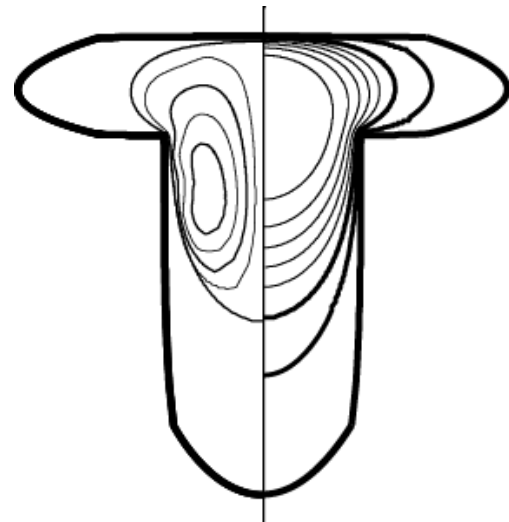
Table 1 The properties of polyethylene.

Property	Value
$\rho$ [kg/m <sup>3</sup> ]	954
$k$ [W/(mK)]	0.182
$L$ [kJ/(kg)]	135.3
$\Delta\hat{H}/R$ [K]	$4.5 \times 10^3$

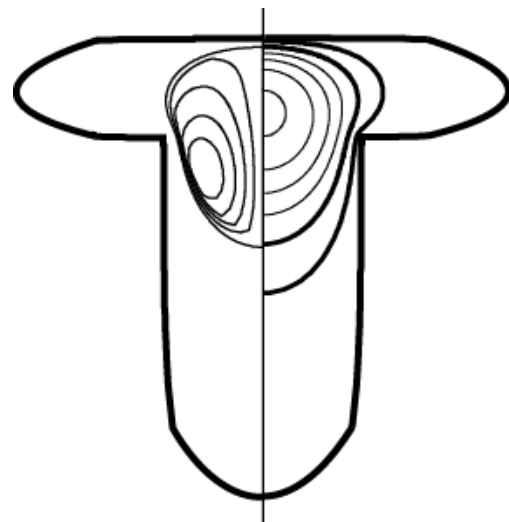
Fluid in the shape was assumed to be at rest before the computation starts and the initial temperature and the wall temperature were assumed to be 450K and 303 K respectively.  $Pr$  was fixed at  $2.2 \times 10^6$  and  $We$  was order of  $10^{-2}$

#### 3-1 Flow and temperature field

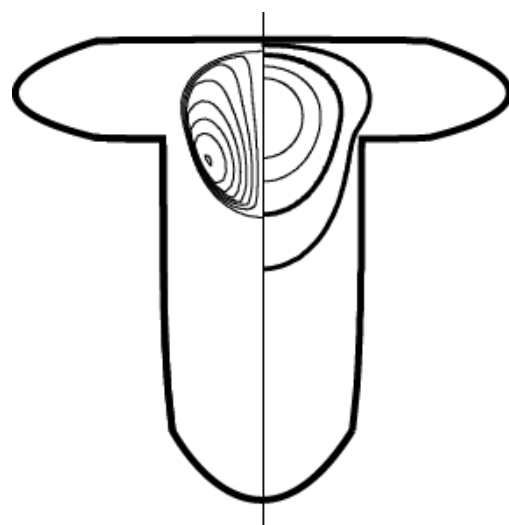
Figure 2 shows streamlines and isotherms in the left half and in the right half respectively. Among the isotherms, the temperature of the thick ones is under



(a) Time step = 200 ( $\Delta\psi = 1.0 \times 10^{-1}$ ,  $\Delta\theta = 5.0 \times 10^{-1}$ ).



(b) Time step = 600 ( $\Delta\psi = 1.0 \times 10^{-1}$ ,  $\Delta\theta = 5.0 \times 10^{-1}$ ).



(c) Time step = 1000 ( $\Delta\psi = 1.0 \times 10^{-2}$ ,  $\Delta\theta = 5.0 \times 10^{-1}$ ).

Fig.2 The streamlines and isotherms at  $PrRa = 1.0 \times 10^5$ .

dimensionless solidification temperature,  $\theta_s$ . From these figures, the process of cooling of high temperature melt plastic can be observed. At the beginning of the computation, the distance between isotherms near the right angle is small, which shows that the temperature gradient is large there. The direction of flow (in the left of the figure) is counterclockwise. The distance between streamlines is small near the boundary of the phase since the temperature difference is large there.

### 3-2 Cooling curve

Figure 3 shows cooling curves near the wall at the right angle. The thick line shows the temperature next to the wall,  $r_{M-1}$ , and the thin line,  $r_{M-2}$ . Dimensionless melting temperature,  $\theta_m$  is 1.7 and  $\theta_s$  is 1.0. This result has the characteristic tendency which the cooling curve of material without phase change does not have. In Fig.3, the temperature behavior changes at  $\theta_m$  and  $\theta_s$  since the latent heat is emitted between  $\theta_m$  and  $\theta_s$ .

### 3-3 Nusselt number changes with time

Local Nusselt number, the dimensionless heat transfer coefficient, was calculated at  $r = r_{M-1}$  as,

$$Nu = -\frac{\partial\theta}{\partial r} \quad (3-1)$$

Figure 4 gives the comparison of the change of  $Nu$  with locations shown in Fig. 4. At the right angle, point C in Fig. 4,  $Nu$  is the largest all the time, since the temperature gradient is largest at this point, which is found in Fig. 2. Figure.5 shows the comparison of  $Nu$  with  $PrRa$  at the right angle. As  $PrRa$  is larger, the change of  $Nu$  with time becomes sharper, since cooling of the melt plastic is advanced more at higher  $PrRa$ .

### 4. Conclusion

In this study, using the spectral finite difference scheme to solidification phenomenon of the melt plastic, the characteristics of the flow and thermal fields in the right angle branch were explained.

### References

- [1] Yoshihiro MOCHIMARU, Effectiveness of a spectral finite difference scheme, Comput. Fluid Dyn. Rev., 1998, 1(1998), pp. 563-568
- [2] Esam M. Alawadhi, Phase change process with free convection in a circular enclosure: numerical simulations, Comp. & Fluids, 2004, 33(10), pp. 1335-1348

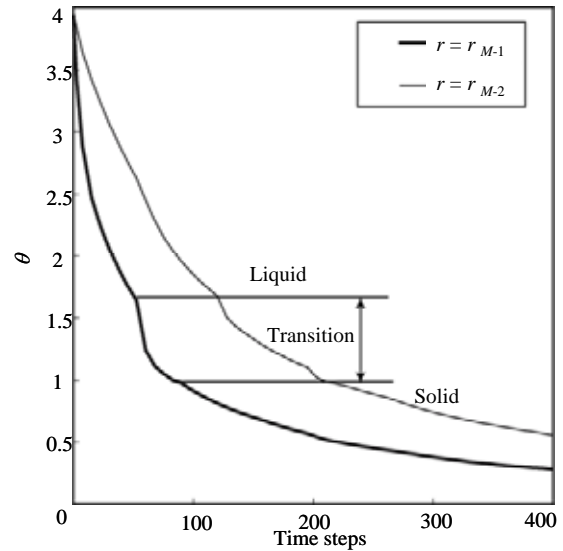


Fig.3 The cooling curve at  $PrRa = 1.0 \times 10^5$ .

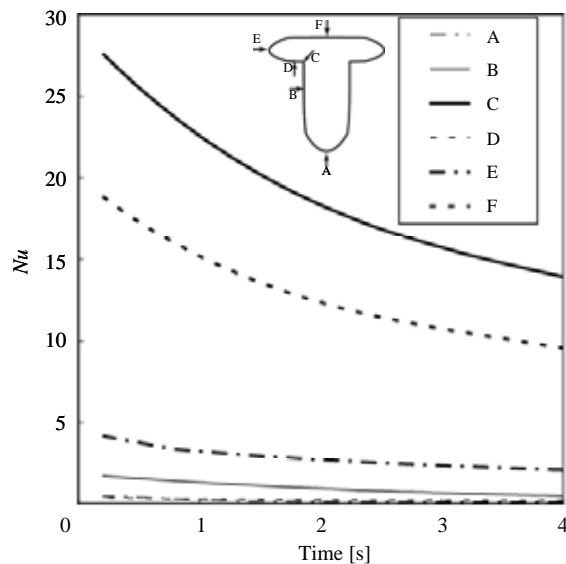


Fig. 4 Local Nusselt number at  $PrRa = 1.0 \times 10^5$ .

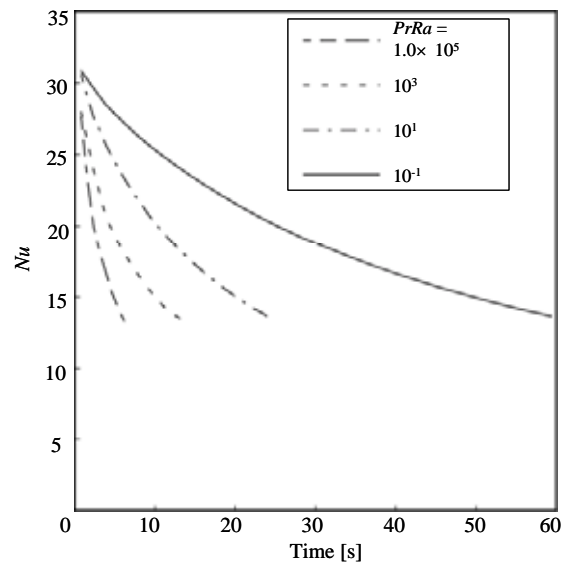


Fig.5 Comparison of Nusselt number with  $PrRa$ .

## The effect of probe shape and wettability

### for expanding applicability of micromanipulation using capillary force

Student Number: 04M18067 Name: Kenichi J. OBATA Supervisor: Kunio TAKAHASHI

#### 操作プローブの先端形状と材質が 液架橋力マイクロマニピュレーションの適用範囲拡大に及ぼす影響

尾畑 賢一

現在、高機能材料やマイクロデバイスの開発を目的に、微小構造物を精緻に操作・組立する技術が求められている。微小環境では凝着力が支配的なため、凝着現象を考慮したマニピュレーション手法が必要である。液架橋力を用いる手法は対象物を傷つけない点などで優れており、実用化が期待されている。ところが従来提案された手法では、液体体積に対して液架橋力の制御可能範囲が小さいことが問題であった。そこで本研究では、液体体積制御による微小物体操作の適用範囲を拡大するために、捕捉時には液架橋を大きく、配置時には液架橋力が小さくなるようなプローブ形状を提案し、液架橋力の理論解析と実証実験を通して、その実現可能性を検証した。

## 1 Introduction

Recently, micromanipulation techniques have been in demand to fabricate highly functional micro-devices or micro-electro-mechanical-systems (MEMS). In micromanipulation, the influence of adhesional force is extremely large compared to gravitational force [1,2]. Furthermore, adhesional force has large dispersion because of its dependence on surface condition such as surface roughness, at each contact point. Thus, in order to realize reliable micromanipulation, we need a force that is controllable and greater than the adhesional force, or some mechanism to avoid the dispersion of adhesional force. Saito *et al.* have investigated the mechanical force required to slip and roll an object in considering the adhesional effect [3]. The mechanical method, however, might damage the object. Takahashi *et al.* have evaluated the force generated by Coulomb interaction [4], although the electrostatic method might cause a discharge or melt an object [5]. In order to avoid damaging the manipulated object, use of capillary force is considered effective if use of liquid is allowed. Actually, Tanikawa *et al.* have picked/placed an object with a micro-hand and a micro-drop [6], but they have not provided any analysis of the capillary force involved. We have proposed a scheme for micromanipulation based on capillary force by regulation of the liquid volume [7]. In our previous

scheme, it is assumed that the object shape is spherical, and the probe and substrate surfaces are flat. The profile of a liquid bridge between two solids was analyzed based on Orr's theory [8], and the force generated for the profile was presented clearly. These analyses have indicated the feasibility of the proposed scheme. The range of the force, however, never seems large enough for practical/reliable micromanipulation.

In this study, we propose a probe with a concave-tip as shown in Figure 1. The concaved probe-tip would generate greater capillary force than a flat probe-tip so that it can expand the possibility of picking up manipulation. If a large amount of liquid was supplied, liquid must overflow to a flat surface, and capillary force would be equivalent to the flat probe-tip case for successful placing. Through both numerical estimation and its experimental verification, the magnified range of capillary force is presented as a function of concavity radius, wettability, and liquid volume.

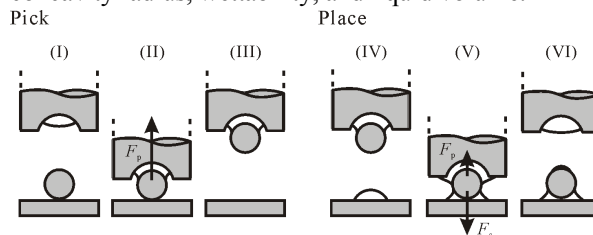


Figure 1: Schematic illustration of manipulation procedure: (I) positioning, (II) lowering, (III) picking up, (IV) positioning, (V) lowering, and (VI) placing.

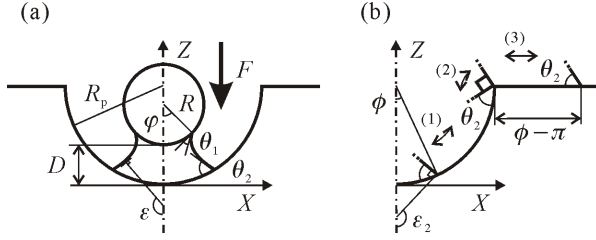


Figure 2: Liquid bridge between a spherical object and a concave probe-tip: (a) whole menisci and (b) menisci end at probe surface.

## 2 Analysis of capillary force

Figure 2 shows an axisymmetric model for the analysis of a liquid bridge between a spherical object and a concave probe-tip, where  $R$  is the radius of the object,  $R_p$  is the radius of the concave curvature,  $D$  is the distance from the concave probe-tip to the object,  $\varphi$  is the filling angle of the object,  $\phi$  is the filling angle of the probe-tip,  $F$  is the attractive force acting on the object, and  $V$  is the volume of the liquid between two solids. The meniscus forms contact angles  $\theta_1$  at the object and  $\theta_2$  at the probe-tip. The profile of the liquid bridge is expressed by the coordinates  $(X, Z)$ . The value of  $\varepsilon$  expresses the angle between the normal to the meniscus and the vertical axis. We make the following assumptions. (i) The influence of gravity is negligible and the profile of the liquid bridge follows Young-Laplace equation [8]; (ii) the dynamic flow of the liquid is negligible; (iii) the volume of the liquid is conserved; (iv) the contact angles are determined by Young's equation [2]; (v) The object and the probe are ideally rigid. The capillary force acting on the object is the sum of the pressure difference and the axial component of the surface tension, i.e.,

$$F = -\Delta P \pi X_1 + 2\pi \sigma X_1 \sin \varepsilon_1, \quad (1)$$

where  $\Delta P$  is the Laplace pressure which is pressure difference between inside and outside of meniscus,  $\sigma$  is the surface tension of the liquid, and  $X_1$  and  $\varepsilon_1$  is the  $X$  coordinate and the  $\varepsilon$ -angle, respectively, at the meniscus end of sphere side.

The Laplace pressure can be expressed by Laplace equation, which relates the pressure difference to the meniscus profile;

$$\Delta P = 2H\sigma, \quad (2)$$

where  $H$  is the local mean curvature which can be written by the meniscus geometry [8];

$$2H = \frac{d}{dX} (\sin \varepsilon) + \frac{\sin \varepsilon}{X}. \quad (3)$$

Since the Laplace pressure  $\Delta P$  is hydrostatic, and thus, constant at any local point, the local mean curvature  $H$  is also constant anywhere on the meniscus. Therefore, this equation can be solved as a two-point boundary-value problem. The boundary conditions are written as

$$\begin{cases} \varepsilon_1 = \varphi + \theta_1, & X_1 = \sin \varphi, \\ \varepsilon_2 = \pi + \phi - \theta_2, & X_2 = R_p \sin \phi. \end{cases} \quad (4)$$

Once the profile is obtained,  $H$  is determined from equation (3), and  $F$  is obtained from equation (1). For generalization, some parameters are normalized as the following equation:

$$x = \frac{X}{R}, \quad z = \frac{Z}{R}, \quad d = \frac{D}{R}, \quad f = \frac{F}{\pi R \sigma}, \quad v = \frac{V}{R^3},$$

$$\text{and } r_p = \frac{R_p}{R}. \quad (5)$$

Figure 3 shows a relation between the normalized maximum capillary force and the normalized concavity radius for  $v = 0.10$ . Both horizontal and vertical scale is logarithmic. Note that the variable horizontal axis is not  $r_p$  but  $r_p - 1$ . Maximum value of the capillary force is the critical value of the object detachment from the concaved probe-tip. This figure suggests that as the radius of concavity approaches to the sphere, the maximum capillary force increases drastically. If the object and probe have smaller contact angles, capillary force becomes much larger than that for relatively large contact angles.

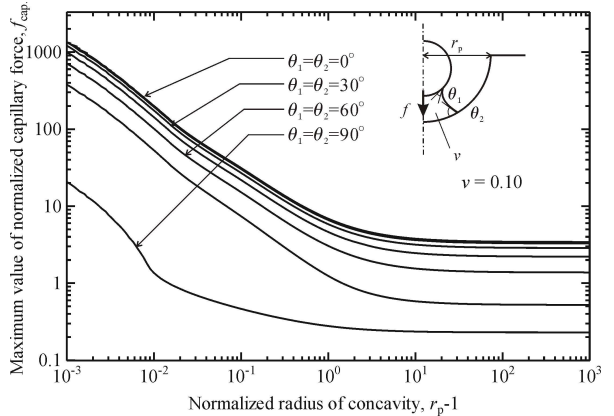


Figure 3: The effect of the probe-tip curvature on the maximum capillary force for  $v = 0.10$ .

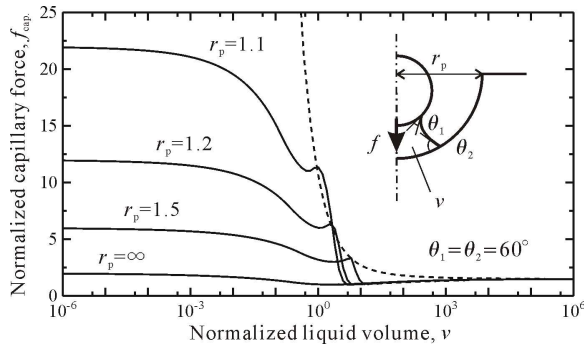


Figure 4: Relation between the normalized maximum capillary force and the normalized liquid volume for  $\theta_1 = \theta_2 = 60^\circ$ .

On the other hand, the capillary force should be reduced for placing manipulation. The solid lines in Figure 4 shows a relationship between the normalized maximum capillary force and the normalized liquid volume for  $\theta_1 = \theta_2 = 60^\circ$  and  $r_p = 1.1, 1.2, 1.5,$  and  $\infty$ . The infinite value of  $r_p$  means the sphere-plate model. As approaching  $r_p$  to 1, the force difference regulated by the liquid volume can be expanded. This means that the force control by the liquid volume is valid for reliable micromanipulation.

### 3 Measurement of capillary force

Figure 5 shows the experimental system used. The experiment was performed in atmosphere. The order of the object size was determined according to the Bond Number ( $\rho g R^2 / \sigma$ , where  $\rho$  is the density of the fluid and  $g$  is the gravitational acceleration). Since the influence of gravity is negligible as long as the Bond Number is small enough, we adopted  $R = 1.984\text{--}3.175 \times 10^{-3}$  [m] for the object radii corresponding to the bond number  $\rho g R^2 / \sigma = 0.53\text{--}1.35$ , which might shift the capillary force due to the gravity no more than 10%. The liquid used was purified water with  $\sigma = 0.073$  [N/m], which was refined through ion-exchange membrane process. A micro-pipette with a volume resolution of  $2 \cdot 10^{-11}$  [m<sup>3</sup>] was used to determine the volume of the liquid. An electronic balance (Sartorius, TE153S) with a resolution of  $10^{-5}$  [N] was used to measure the force between the object and the probe-tip. Automated precise stages (Suruga Seiki, K701-20LMS) with a resolution of  $5 \times 10^{-8}$  m were used to adjust the position of the object and the probe. Probes having concave tips were fabricated with  $R_p = 3.1 \times 10^{-3}$  m and  $3.3 \times 10^{-3}$  m (of glass and

polytetrafluoroethylene: PTFE); with  $R_p = 3.1 \times 10^{-3}$  m (of stainless steel). Spherical objects of several sizes were attached to steel rods. With the combination of the radii, the value of  $r_p$  can be set to 1.033–1.562. Contact angles for the materials were determined by observing the edge of a water-drop deposited on a plate using a video microscope:  $50^\circ$  for glass,  $75^\circ$  for stainless steel, and  $85^\circ$  for PTFE.

Figure 6 shows the measurement value of the capillary force as a function of the distance  $d$  for the liquid volume  $v = 0.08$ . The experimental value of the capillary force is obtained as square marks in an approaching process, and as triangle marks in a detaching process. Such hysteresis occurs due to the inequality of the contact angle between these processes. The broken line and the dotted line denote the theoretical value of the capillary force for the fixed contact angle  $\theta_1 = \theta_2 = 60^\circ$  and  $75^\circ$  (Sliding Mode [9]). The solid line denotes the value of the force for the contact angle transition from  $60^\circ$  to  $75^\circ$  (Pinning Mode [9]). Note that the maximum value of the capillary force never achieves the theoretical maximum during Pinning Mode.

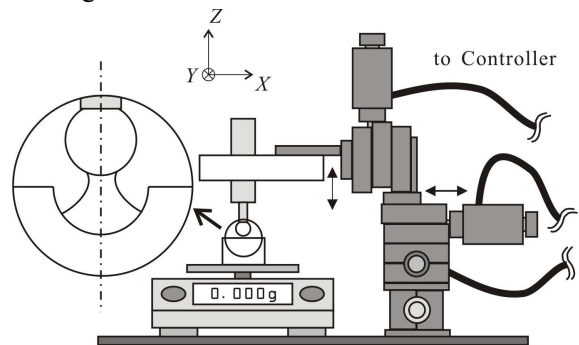


Figure 5: Schematic illustration of experimental system used.

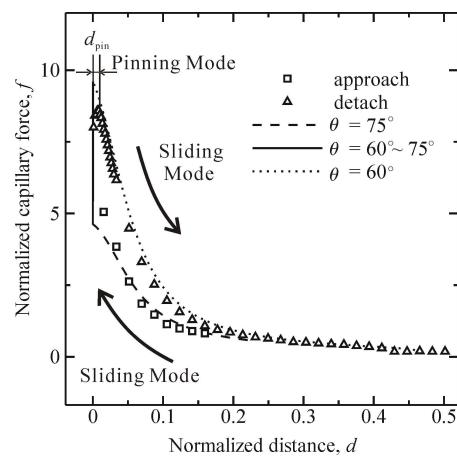


Figure 6: Capillary force-curve for glass specimen for  $r_p = 1.19$  and  $v = 0.08$ .

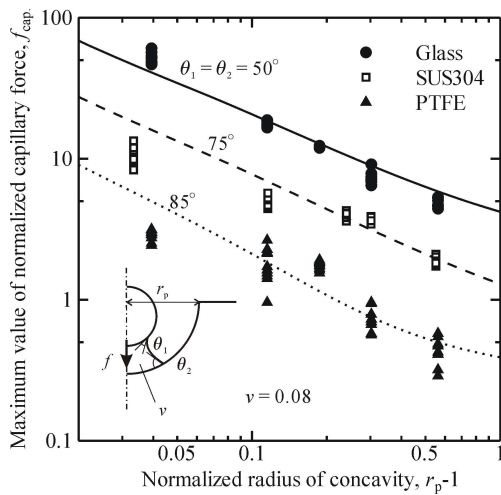


Figure 7: The effect of concavity radius and wettability.

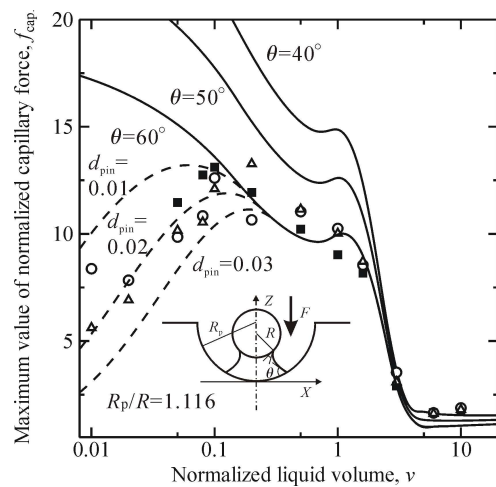


Figure 8: Relation between the normalized maximum capillary force and the normalized liquid volume for glass specimen and  $R_p/R = 1.116$ .

The relations between the normalized maximum capillary force  $f_{cap}$  and the normalized radius of concaved curvature  $r_p$  for a given normalized liquid volume  $v = 0.08$  are shown in Figure 7. Lines denote the values estimated from the numerical analysis for contact angles  $\theta_1 = \theta_2 = 50^\circ$ ,  $75^\circ$ , and  $85^\circ$ . Circle, square, and triangle marks denote the values actually measured in the experiment. The experimental results are in good agreement with the theoretical predictions for all three materials. The force  $f_{cap}$  drastically increases as  $r_p$  approaches 1. Probes made of the material with small contact angle generate much larger capillary force.

As shown in Figure 8, magnified capillary force can be controlled by the regulation of liquid volume. Circle, triangle, and square marks are expressing the experimental values. These are in good agreement with theoretical predictions for the range of the liquid

volume  $v > 0.1$ . In the case of  $v < 0.1$ , the experimental value of capillary force and the calculation considering contact angle hysteresis (broken lines) are almost the same. Assuming transition distance  $d_{pin}$  is constant, the capillary force is reduced with decreasing liquid volume. This means that too small supply of liquid causes less capillary force generated. In order to realize efficient and reliable manipulation, the normalized liquid volume should be controlled from 0.1 to 10.

## 4 Conclusion

This study clarifies the most important factors for reliable capillary micromanipulation by concave probe, i.e. the material wettability, the concave shape and dimension, and the amount of liquid supply. The shape of the probe-tip can be designed as shown in Fig. 1 so that the range of the capillary force can be extended due to the change of the apparent contact angle for a given liquid volume. If the outer flat part of the glass probe, for instance, is coated with large-contact-angle material such as PTFE, the expanded range of the capillary force can be expected. This suggests that micromanipulation by capillary force has a great potential for a wide range of applications.

## References

- [1] K. L. Johnson, K. Kendall, and A. D. Roberts, Proc. R. Soc. London, Ser. A, vol. 324, pp.301, 1971.
- [2] J. Israelachvili, "Intermolecular and Surface Forces", Academic, New York, 1985.
- [3] S. Saito, H. T. Miyazaki, T. Sato, and K. Takahashi, Journal of Applied Physics, vol. 92, pp.5140, 2002.
- [4] K. Takahashi, H. Kajihara, M. Urago, S. Saito, Y. Mochimaru, and T. Onzawa, Journal of Applied Physics vol. 90, pp.432 2001.
- [5] S. Saito, H. Himeno, and K. Takahashi, Journal of Applied Physics, vol. 93, pp.2219, 2003.
- [6] T. Tanikawa, Y. Hashimoto, and T. Arai, Proceedings, 1998 IEEE International Conference on Intelligent Robots and Systems IEEE, Piscataway, NJ, pp. 776, 1998.
- [7] K. J. Obata, T. Motokado, S. Saito, and K. Takahashi, J. Fluid Mechanics, vol. 498, pp.113 2004.
- [8] F. M. Orr, L. E. Scriven, and A. P. Rivas, J. Fluid Mechanics vol. 67, pp.723, 1975.
- [9] Oliver Pitois and Xavier Chateau, Langmuir vol. 18, pp.9751-9756, 2002.

# A manipulation method of a dielectric micro-particle by electrostatic force

Student Number: 04M18216 Name: Min HAN Supervisor: Kunio TAKAHASHI

## 静電気力による微小誘電体操作法

韓 敏

本研究では、静電場数値解析によって、静電気力を用いた微小誘電体操作の可能性を示し、その検証実験を行った。異なる材料の誘電体微小球に対して、再現性を調べた。さらに、実験現象に基づき、操作メカニズムを解明した。以上より、静電気力を用いた微小誘電体操作を実現させることを目的とする。

## 1 Introduction

In micro-manipulation, the adhesional force is dominant since the adhesional force is proportional to the first power of the object size<sup>[1]</sup>, whereas the gravitational force is proportional to the third power of the object size. In order to manipulate a micro-particle, it is necessary to generate the force which is larger than the adhesional force between objects.

It is generally known that electrostatic force can be easily controlled and is effective for the generation of a large force. In recent years, many researches with regard to electrostatic methods for manipulating a conductive micro-particle have been carried out. Takahashi *et al.* used the boundary element method (BEM) to analyze the applied voltage required for detachment in electrostatic micro-manipulation<sup>[2]</sup>. Based on the analysis results, Saito *et al.* did the experiments to determine the voltage required for detachment. The results of experiment are in good agreement with the analysis. Simultaneously, the kinetic control of the detached particle has been recognized to be indispensable to place the particle on the substrate plate without any excessive impact<sup>[3]</sup>. By considering the total work to the particle during the flight, Saito *et al.* clarified the condition of voltage and time for the non-impact manipulation of a particle<sup>[4]</sup>. Kurihara did the experimental verifications Based on the results of Saito *et al.*<sup>[5]</sup>.

However, no research has been done to investigate the detachment of a dielectric micro-particle. "Can we use the electrostatic micro-manipulation to detach a dielectric micro-particle?" Even the possibility of manipulation by electrostatic force is still unknown.

In the present research, the boundary element method (BEM) is used to evaluate the Coulomb forces

to show the possibility of manipulation. Based on the analytical results, we do the experimental study using two different types of dielectric spherical micro-particles to verify the reproducibility of manipulation. In addition, the mechanism of the manipulation is clarified according to the experiment phenomena. Therefore, the purpose of the present research is to realize the dielectric micro-particle manipulation by electrostatic force.

## 2 Analysis of static electric field

### A. Analysis Model

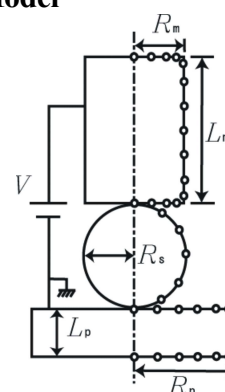


FIG. 1. A schematic illustration of the model used.

Figure 1 shows a schematic illustration of the model used. The system consists of three objects: A conductive manipulation probe, a dielectric spherical particle, and a conductive substrate plate. The manipulation probe is assumed to be cylindrical with a length  $L_m$  and a radius  $R_m$ . The spherical particle with a radius  $R_s$  is right under the center of the probe tip. The plate is assumed to have an infinite plate. Thus, the system has axial symmetry. The calculations are carried out through the use of the mirror images of the objects.

The charge density is assumed to be linear between the  $i$ th nodal  $P_i$  and the  $(i+1)$ th nodal point  $P_{i+1}$ ; the

charge density at point  $P$  between  $P_i$  and  $P_{i+1}$  is assumed to be

$$q = (1-s)q_i + sq_{i+1} \quad (1)$$

where  $q_i$  is the charge density at  $P_i$ .

The voltages  $V_1-V_N$  can be written as a linear combination of charge densities  $q_1-q_N$ ; i.e.,

$$V = A \cdot q \quad (2)$$

where  $A$  is the matrix whose elements are determined from the size of the objects.

Normal directions of the static electric fields  ${}_nE_k$ - ${}_nE_l$  of the sphere can be written as a linear combination of charge densities  $q_1-q_N$ ; i.e.,

$${}_nE_{\text{sphere}} = D_{\text{sphere}} \cdot q \quad (3)$$

where  $D$  is the matrix whose elements are determined from the size of the objects.

Using the boundary condition of dielectric surface, formula (4) can be gotten.

$$0 = B_{\text{sphere}} \cdot q \quad (4)$$

where  $B$  is the matrix whose elements are determined from the size of the objects and the dielectric constant of the micro-particle.

The voltages of the manipulator and the plate are given, and the charge densities at the nodal points can be calculated by the written Equations [6].

## B. Results of analysis

### ● Pick-up

Consider the case where the spherical Polystyrene particle is in contact with the center of the probe tip. In Figure 2, the force is plotted as a function of the normalized radius of the manipulation probe.

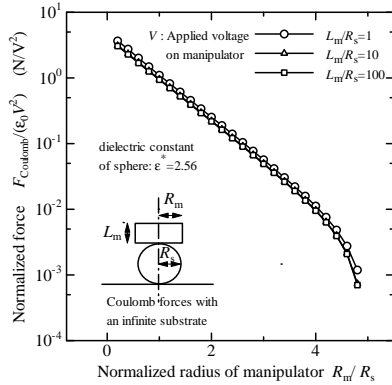


FIG. 2 Effects of the radius of the manipulation probe  $R_m$  on the force.

On the other hand, the force required to pick-up the adhered particle from the substrate can be written as

$$F_{\text{adhesion}} = \frac{3}{2} \pi \Delta \gamma R_s, \quad (1)$$

where  $\Delta \gamma$  is the work of adhesion, which is the energy change from the surface to the interface per unit area [1].

The voltage required for pick-up can be obtained from

$$F_{\text{Coulomb}} > F_{\text{adhesion}}. \quad (2)$$

Therefore, the voltage for pickup can be plotted as Figure 3. In Figure 3, the required voltage is obtained as a function of the normalized radius of the manipulation probe.

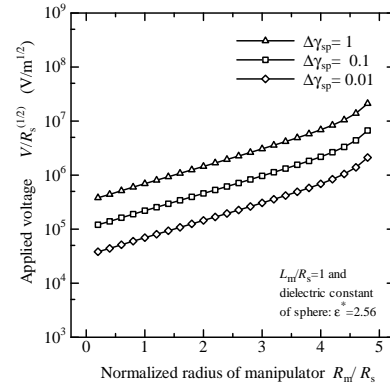


FIG. 3 Voltage required to pickup a particle from the substrate.

According to the results of analysis, it is possible to pick-up a dielectric micro-particle from a substrate by electrostatic force. By applying a DC voltage between the probe and the substrate, an electrostatic force which is larger than the adhesional force can be generated for picking.

### ● Detachment

Consider the case where the spherical Polystyrene particle adheres to the center of the probe tip. In Figure 4, the force is plotted as a function of the normalized gap (the distance between the sphere and the plate).

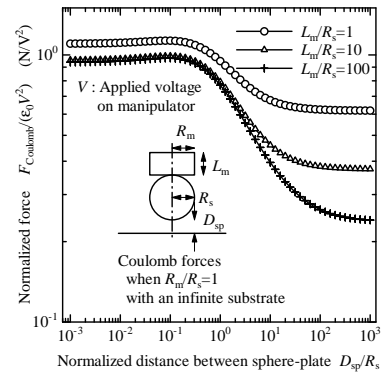


FIG. 4 Effects of the gap  $D_{sp}$  on the force.

According to the results of analysis, it is impossible to detach a dielectric micro-particle which is adhering to the tip of the probe. Because the electrostatic force generated by the applied voltage is always upward. So a repulsive force for detaching can not be generated.

However, in an actual manipulation, a dielectric micro-particle is probably not completely insulated. The effect of this phenomenon is difficult to estimate. In the next session, we show the experimental verifications

### 3 Experimental verifications

#### A. Experimental system

Figure 5 shows the experimental system used. The experiment was performed in atmosphere. The manipulation part consisted of a probe, a dielectric spherical micro-particle, and a substrate plate. The axial direction of the probe was set vertical to the plate.

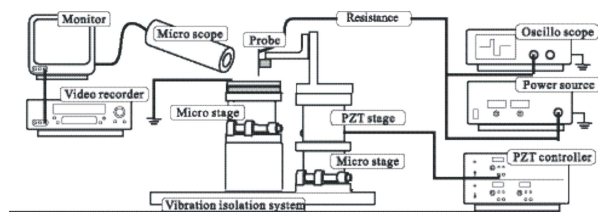


FIG. 5 Illustration of the experimental system used.

A stainless-steel needle with approximately a 14.3- $\mu\text{m}$  tip radius was used as the manipulation probe. Polystyrene micro-balls with a 60- $\mu\text{m}$  diameter and Phenol micro-balls with a 54- $\mu\text{m}$  diameter were

used as the dielectric spherical micro-particles. A stainless-steel plate with a 50 mm $\times$ 10 mm area and 0.1-mm thickness was used as the substrate plate. The plate was polished with emery papers to have surface roughness similar to that of a mirror. As for the translational stages, triaxial translational stages with a 0.05-mm resolution were manually used to adjust the position of the objects. A piezoelectric actuator stage with a 1-nm resolution (Jena, Tritor 3D, custom made) was used to control the gap between probe and the substrate plate. The substrate plate was attached to one of the manual stages. The manipulation probe was attached to the piezoelectric actuator stage on another manual stage. An optical video microscope (Hirox, KH-2200) was used to observe the manipulation probe, the spherical micro-particle, and the substrate plate. The power supply (Nihon matsusada, HJPM-3R5-L2) was used to apply a voltage between the probe and the plate. An oscilloscope (Tektronix™, TDS-2012) was used to monitor the actual voltage between the probe and the plate.

#### B. Results of the experiments

##### ● Manipulation of a Phenol micro-ball with a 54- $\mu\text{m}$ diameter

When a DC voltage is applied to the probe, the particle which was arranged right under the probe (Figure 6) is able to be caught by the probe (Figure 7). Afterwards, even if the probe is brought close to the substrate side, the particle still adheres to the tip of the probe without detachment (Figure 8).



FIG. 6. Photo obtained before micro-particle pickup.



FIG. 7. Photo obtained after micro-particle pickup.



FIG. 8. Photo obtained after trying to detach micro-particle.



FIG. 9. Photo obtained before micro-particle pickup.



FIG. 10. Photo obtained after micro-particle pickup.



FIG. 11. Photo obtained after micro-particle detachment.

● **Manipulation of a Polystyrene micro-ball with a 60- $\mu$ m diameter**

When a DC voltage is applied to the probe, the particle which was arranged right under the probe (Figure 9) is able to be caught by the probe (Figure 10). Afterwards, when the probe is brought close to the substrate side, the particle is able to detach from the probe and be placed on the substrate (Figure 11).

● **A reciprocal motion phenomenon of a Polystyrene micro-ball**

When a DC voltage is applied to the probe and the distance between the probe and the substrate is kept at a constant, the particle which was arranged right under the probe shows a reciprocal motion between the probe and the substrate.

**C. The mechanism of manipulation of dielectric micro-particle**

● **Phenol micro-particle**

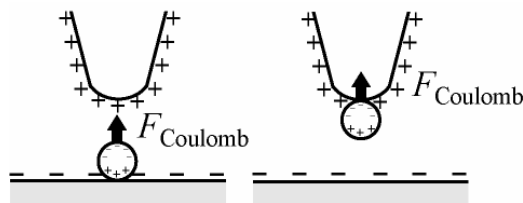


FIG. 12. Generated electrostatic force of a Phenol micro-particle.

As the result of the experiments, Phenol micro-particle can be picked up and can not be detached by electrostatic force. It is in agreement with the analysis result. We thought the Phenol micro-particle used in the research is similar to complete insulation.

When a static electric field is given between the probe and the substrate, the field is concentrated on the probe side which has a smaller surface area. The polarization in the dielectric micro-particle generated by the static electric field should bias to the probe side. Therefore, an attraction force by the probe is able to be generated. It is possible to pickup the particle by the attraction force and it is impossible to detach the particle adhered to the tip of the probe because there is no repulsion force will be generated (Figure 12).

● **Polystyrene micro-particle**

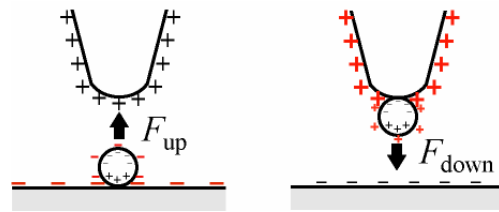


FIG. 13. A reciprocal motion of a Polystyrene micro-particle.

As the result of the experiments, Polystyrene micro-particle can be picked up and detached by electrostatic force. It is not in agreement with the analysis result. The reason for the movement of the polystyrene micro-particle can be explained as follows: A particle should be polarized by the static electric field. Because of the incomplete insulation of the dielectric micro-particle, the surface of the particle has the same charges as those of the substrate. Then, the polarized particle is attracted by the probe. Once the particle reaches the probe, its polarization would be kept, but the charges on the surface of the particle would be the same as those of the probe. Then, the particle should detach from the probe by the repulsion force generated by the same charge of the probe and particle (Figure 13). Consequently, the particle bounces back and forth between the probe and the substrate.

**4 Conclusions**

The manipulation mechanisms for dielectric particles are discussed with both theoretical and experimental approaches. Electrostatic force on ideal dielectric materials is analyzed theoretically with numerical simulation. The geometry of the probe effects on the dielectric force. The ideal dielectric materials can be picked up, however, can not be placed. The dielectric interaction is investigated also experimentally. Phenol micro-particle is verified to have the features of the ideal dielectric material. However, Polystyrene micro particle is proved to be able to be picked up and placed, because it has both the feature of the dielectric and the conductive materials.

**References**

[1] K. L. Johnson, K. Kendall, and A. D. Roberts, Proc. R. Soc. London, Ser. A 324 (1971)  
 [2] K. Takahashi, H. Kajihara, M. Urigo, S. Saito, Y. Mochimaru, and T. Onzawa, J. Appl. Phys. Vol. 90, No.1 (2001)  
 [3] S. Saito, H. Himeno and K. Takahashi, J. Appl. Phys. Vol. 93, No. 4, (2003)  
 [4] S. Saito, H. Himeno and K. Takahashi, Applied Physics Letters. Vol. 83, No. 10, (2003)  
 [5] K. Kurihara, Master thesis, (2005)  
 [6] M. Han, Bachelor thesis, (2004)

**BENEFICIAL 2-WAY INTERNATIONAL COOPERATION BETWEEN  
JAPAN AND DEVELOPING COUNTRIES IN ASIA:  
TECHNOLOGY TRANSFER OF WELDING TECHNOLOGY CASE STUDY**

Student Number: 04M18280

Name: Braga Bruno Martins

Supervisor: Takahashi Kunio

援助国及び被援助国双方の利益となる国際技術協力のあり方  
—溶接技術に関する国際協力を例として—

ブラガ・ブルーノ・マルチンス

現在行われている日本による開発途上国に対する国際協力は、日本および対象国の要求と実状に合ったものであるべきである。基礎教育だけでなく専門学術教育を支援する事は基礎教育だけの支援より早く貧困を撲滅する事に繋がる。技術に裏打ちされた経済的な発展に繋がるからである。本研究では、溶接技術を例に取り、国際協力を通じた日本の従来技術移転のあり方を検討している。国内外の溶接技術に関する組織と実際に連携し、実際に技術移転支援に協力しながら国際技術協力のあり方を提案している。

## 1 Introduction

“Knowledge is like light. Weightless and intangible, it can easily travel the world, enlightening the lives of people everywhere. Yet billions of people still live in the darkness unnecessarily.”<sup>[1]</sup>

The influence of the globalization in the world affects all areas, especially those related to development and technology. The transfer of technology to developing countries as international cooperation has been also influenced by the velocity of the worldwide changes. Developed countries are practically competing with each other for opportunities of cooperation with developing countries<sup>[2]</sup>. Japanese Official Development Assistance (ODA) has, however, decreased for 5 consecutive years, as shown in Figure 1. Some measures are being considered for this issue, under validation process by the Japanese government<sup>[3]</sup>.

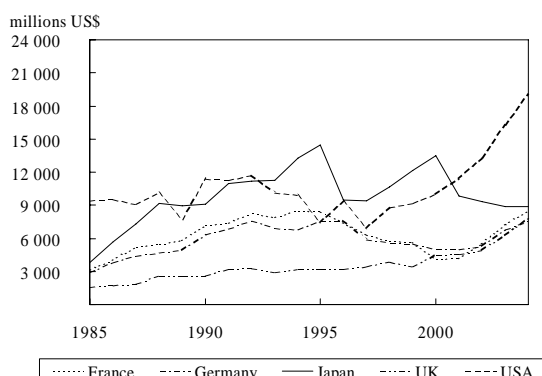


Figure 1: Trends in ODA for the last 20 years<sup>[4]</sup>

However, the needs of developing countries vary. While some live in poverty, others have access to

high-level education. Due to this lack of balance, it is necessary to better evaluate the priority of aid programs, which may occur in many ways. Without discharging the importance of basic and fundamental aid programs such as poverty eradication, the action of international cooperation between developed and developing countries has to be optimized according to each country's interests, considering also specific programs such as professional education.

Regardless the fact that international cooperation with developing countries means “help”, the actions from developed countries seem clear, attracted by trade facilitations, implementation of industry due to low cost of labor and raw material, and finally standardization<sup>[5]</sup>. The repercussion of fixing own standards internationally is obvious and beneficial for both sides, in many aspects. The technical cooperation of professional education requires, however, matching the demand and supply, which means the developing countries' needs for specific/applicable knowledge and developed countries' potentials for technology transfer.

This research aims to clarify the present situation in international cooperation between Japan and developing countries in Asia taking welding technology as case study, and to understand the effectiveness of current aid mechanisms.

## 2 Japanese welding technology

Welding technology is the case study took for this research because of its large applicability in almost every areas of industry. Despite the difficulty to measure the strength of a country in a world of technology competition, the high quality of Japan is still recognized worldwide<sup>[6]</sup>, and has a strong participation in scientific communities. The figure 2 presents the number of papers published at the International Institute of Welding (IIW), organization which congregates almost all welding

societies in the world [7].

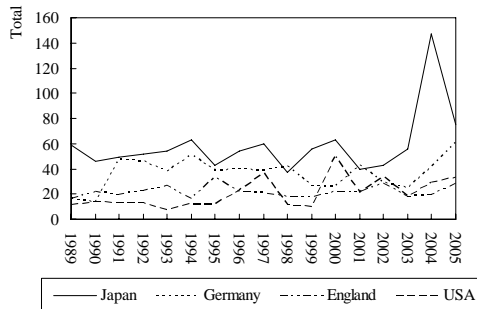


Figure 2: Publications in IIW for the last 15 years

It is worth to mention that there is no research investigation in the present bibliography which analyzes the present situation in international cooperation between Japan and developing countries in Asia in welding technology.

### 3 Methodology

To verify the present situation in international cooperation between Japan and developing countries in Asia, taking welding technologies as example of professional level education, this research has collected data using questionnaire for welding related professionals: during Asian Welding Federation (AWF) meetings in Philippines (2004/10), Malaysia (2005/3), and India (2005/10), since its establishment in 2004; and at the Japan International Cooperation Agency (JICA) Welding Technology Training Course (2005/6). Although the amount of data gathered was limited as shown in table 1, the respondents were participating of international scale events for welding community. Therefore, we consider it as very useful for this research's purpose.

Location	Total of respondents
Philippines	47 (29%)
Malaysia	64 (40%)
JICA Course	9 (6%)
India	41 (25%)
<b>Total:</b>	<b>161</b>

Table 1 : Respondents by location

Since the evaluation was not actually part of the program at AWF meetings neither JICA Course, it was advised to build a compact questionnaire, focusing only on the major interests of this research, to not become an inconvenience to the main activities. The figure 3 represents an example of the questionnaire used in this research, divided in respondent's characteristics and main questions, which aimed at the following:

- impression of welding technology in Japan and own country;
- past and future priorities for welding technology in own country;
- future needs in welding technology;
- use of aid resources in welding technology;

東京工業大学大学院 理工学研究科 国際開発工学専攻  
Tokyo Institute of Technology  
Graduate School of Science and Engineering  
Dept. of International Development Engineering

Questionnaire on Welding Technology

---

**Instructions**

This questionnaire will not take more than 5 minutes.

- Please, fill in this form with CAPITAL letters and "X" for the questions.
- Your answer will be used only for research purposes. There is no need to identify yourself.
- We appreciate your kindness on helping us with this valuable research.

**Part I - Personal Data**

Country:

Field (Work, Study or Research):

Entity (Company, University or Institute):

**Part II - Questions**

① How is your impression about the Welding Technology in Japan?

great    good    not so good    poor    very poor

Please, fill in the back too. ↩

Ref.007-01 Braga, BRUNO (Takahashi Lab.)

---

Questionnaire on Welding Technology

② How would you rate the Welding Technology in your Country?

great    good    not so good    poor    very poor

③ In your opinion, which kind of Welding Technology should have priority in your Country for the next 5 years?  
(You may choose more than one item, if applies)

MMA (Manual Metal Arc)    GMAW (Gas Metal Arc Welding)    FCW (Flux Cored Welding)  
 SAW (Submerged Arc Welding)    Other (\_\_\_\_\_)

④ Which kind of Welding Technology has received more investments in your Country for the last 5 years?  
(You may choose more than one item, if applies)

MMA    GMAW    FCW    SAW    Other (\_\_\_\_\_)

⑤ Do you think that a program to help the development on Welding Technologies would be an important benefit for your Country?

Yes    No    will not change    no opinion

⑥ In your opinion, how should the aid organizations use their resources on Welding Technologies in your Country?

monetary funding    knowledge supply    Other (\_\_\_\_\_)

⑦ Write here your comments or opinions, if necessary.

We're done! Thanks for your cooperation. ✓

Ref.007-01 Braga, BRUNO (Takahashi Lab.)

Figure 3: Questionnaire used in this research

### 3.1 Data Results

The analysis of the questionnaire revealed that the Japanese welding technology is also very recognized among developing countries. In a 1-5 scale from very poor to very good, the average rating for Japan was 4.6, against 3.7 for own country. The objective however is not necessarily to compare these results, but understand the impression that technicians from developing countries have regarding Japan as well as their own country's welding technology. The results also confirm that the gap of technology level from developed and developing countries is not completely understood. In the case of JICA course, the participants were unanimous in choosing their impression as 5 (very good) for Japan, and as 3 (not so good) for their own countries. The possible reason is the fact that they had direct contact with the Japanese welding technology. Further, since the JICA course participants are considered the top researchers from their countries, their opinion should be emphasized.

Also, the average tendencies for the future use of welding techniques are presented in figure 4, clarifying the continuous decrease of Manual Metal Arc (MMA) usage; a tenuous increase of interest in Submerged Arc Welding (SAW) and Flux Cored Welding (FCW); and the Gas Metal Arc Welding (GMAW) still remaining as the most used technique. There were some hand-writing comments about interest on latest and top technologies, such as laser welding (13%).

The last question of the questionnaire registered comments and suggestions, most of them regarding the necessity of international cooperation for development of welding and strengthening the Asia's influence worldwide.

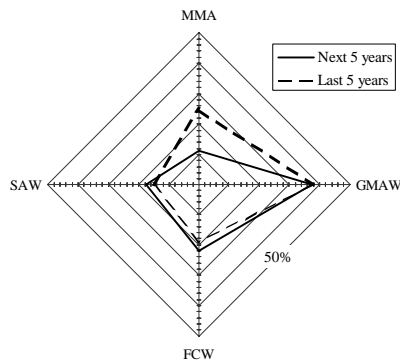


Figure 4: Shift of priorities by welding technique

Comparing the data obtained from the questionnaire to the values from developed countries [8], as presented in figure 5, we notice that the tendencies of use of welding techniques are about the same. Since there is no such information for developing countries, the questionnaire aimed to capture the same concept from the professional's opinions.

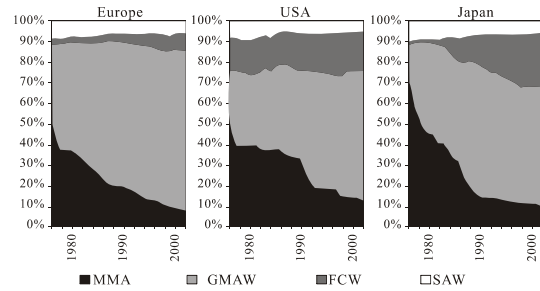


Figure 5: Usage of welding for the last 15 years

The welding professionals also expect more education and know-how related aid support, rather than only financial support in international cooperation programs, as presented in table 2, clarifying that there is demand for education focused aid programs in welding technology. In average, 71% of the respondents opted for knowledge supply. Some of them also chose both answers, representing around 15% of all respondents.

Location	Preferred aid resources	
	Monetary Funding	Knowledge Supply
Philippines	15 (31%)	34 (69%)
Malaysia	22 (29%)	55 (71%)
JICA Course	4 (31%)	9 (69%)
India	11 (28%)	29 (73%)
<b>Total:</b>	<b>52 (29%)</b>	<b>127 (71%)</b>

Table 2 : Preferred aid resources by location

The figure 6 express the fact that practically all respondents agree that the international cooperation programs for the development of welding technology can be an important benefit for their countries. The respondents who opted "no opinion" did not add any comment, consequently the reason for choosing this answer is unknown.

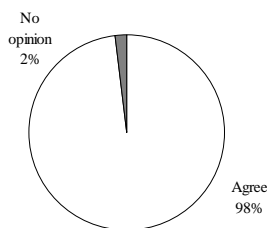


Figure 6: Can programs to help development of welding technology be an important benefit for your country?

### 3.2 Findings

The major findings from this analysis are as follows:

- Respondents are more interested in knowledge supply, rather than financial support;
- The high level of Japanese welding technology is well recognized;
- Despite tenuous differences between each group of respondents, GMAW remains as priority;
- International cooperation in welding technology can be a good benefit for developing countries;
- There is also interest in latest and top technologies as well;

## 4 Conclusion

This research clarified that the Japanese welding technology can contribute to developing countries, also being well recognized worldwide. The welding professionals are willing to obtain know-how through education related aid programs, showing that there is demand for educational related cooperation in welding technology. Finally, a beneficial 2-way international cooperation should be considered, focusing on the needs of developing countries and the needs of Japan as well, for promoting a sustainable cooperation. For Japan, the benefits are establishing standards through the world and creating better environment for Japanese industry allocated overseas, among others, but not as direct and immediate as the benefits for developing countries.

## 5 Future prospect

This paper also presents some key factors to suggest a future project, which is an alternative for Japan to transfer welding technologies, especially widely applicable techniques such as GMAW, which has been used in majority both in Japan and in developing countries in Asia. Instead of concentrating all tasks for Japanese government agencies (figure 7), the alternative is to use AWF as intermediate, in a multilateral cooperation (figure 8). The major points of this proposal are as follows:

- *Key technology:* Emphasize on more applicable technologies, such as GMAW;
- *Method of Transfer:* Focus on training and professional education, rather than financial support only;
- *Form of Cooperation:* From bilateral to multilateral cooperation (e.g.: intermediation of AWF);

The expected outcome of this proposal is as follows:

- Increase & strengthen professional network;
- Increase visibility of welding technology field in international cooperation;
- Contribute in regional cooperation & standardization in Asia;
- Possible simplification on Japan side's administration;

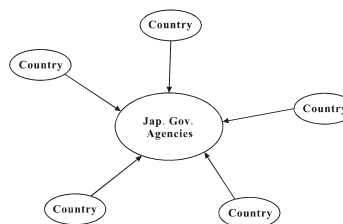


Figure 7: Illustrative scheme of bilateral cooperation procedure (present model)

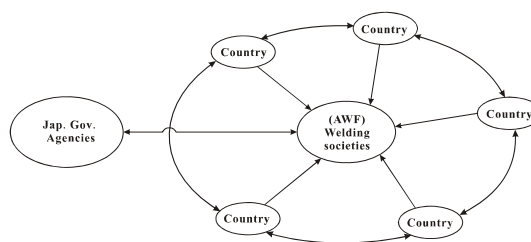


Figure 8: Illustrative scheme of multilateral cooperation procedure (alternative model)

## References

- [1] World Bank, "World Development Report: Knowledge for Development" (Open Statement), p.4, 1998/99
- [2] Evans, P.C.; Oye, K.A., "International Competition: Conflict and Cooperation in Government Export Financing", 2004/4/29, p.113-158
- [3] 日本経済新聞, 「外務省の来年度予算概算要求, ODA11.9%増」, 総合 p.3, 2005年8月30日
- [4] OECD-DAC, "Net ODA from DAC countries from 1950 to 2004", 2005/12/15 (Last Access: 2005/12/30) <<http://www.oecd.org/dataoecd/43/24/1894385.xls>>
- [5] Soesastro, H., "Sustaining East Asia's Economic Dynamism: The role of Aid", PRI-OECD Research Project, 2004/5, p.4
- [6] Eagar, T. W., "Technology Transfer and Cooperative Research in Japan", AWS Welding Journal, 1989/1, p.39~43
- [7] IIW, "IIW Technical Documents Database" (Last Access: 2006/01/02) <[http://www.iw-iis.org/iw/iw\\_databases/technical/index.cgi](http://www.iw-iis.org/iw/iw_databases/technical/index.cgi)>
- [8] Svensson, E.; Elvander, J., "Challenges for welding consumables for the new millennium", Svetsaren No.1-1999/2, p.3-11

# A STUDY ON PLASTIC DEFORMATION MECHANISM WITHOUT DISLOCATIONS IN METALS BY TRANSMISSION ELECTRON MICROSCOPY

Student Number :04M18162 Name: Hidetoshi Fujii Supervisor:Satoshi Kojima

透過型電子顕微鏡を用いた金属の非転位塑性変形機構の研究

藤井英俊

金属の高速変形時に転位によらない変形機構が存在する可能性は、近年の研究を通じて極めて濃厚になっている。本研究では純金を用いて引っ張り破断実験を行い、亀裂進展部位に発生するボイドに特に注目し、その挙動から転位によらない新しい変形機構の存在可能性を検証するものである。

## 1. Introduction

In the recent studies by Kiritani et al, many experimental results which imply the existence of deformation mechanism without dislocation were reported [1]. In this deformation, many unique features can be seen which cannot be observed in usual deformation. For example, no dislocations are observed and a large number of vacancy clusters like SFT are observed at the fractured tip. Kiritani et al proposed "Glide Element Model" as the new deformation mechanism but the detail of the deformation is still unknown.

Kojima revealed a new interesting fact in the tensile fracture experiment in pure gold. Several numbers of voids were observed at the leading part of the fractured region [2]. Such topics about voids in pure metal have not yet been discussed before. Thus, this result has possibility that suggest new deformation mechanism of metals.

In this study, we have paid an attention to the generation and behavior of voids during deformation in tensile fracture experiment of pure gold through TEM (transmission electron microscope). At the same time, we have observed behavior of other clustered defects (mainly dislocations) and their relationship with voids. Finally, we will discuss the results of the observation, and propose a new deformation mechanism of metal.

## 2. Experimental Procedure

### 2-1 Tensile specimen, holder for electron microscopy utilizing Piezo devise

For this study, we prepared particular holder for electron microscopy made by K.Hamada of Hokkaido University to achieve more precise experiment. Piezo devise has peculiar property that length change by changing applied voltage. This holder enabled us to perform fine tensile fracture experiment at the range of nano meter in electron microscope. The experiment was always started from same voltage, because Piezo devise has a property of hysteresis.

To operate this holder, electric power source, control devise and PC were set. We connected each other, and controlled the voltage of Piezo devise using VBA (Visual Basic for Applications).

### 2-2 Specimen

Pure gold (99.99%) was rolled to the thickness of 50  $\mu$  m. They were annealed in Hiroshima Institute of Technology and cut to the pieces of 15mm  $\times$  3mm. At the middle of the specimen, a notch cut was introduced in order to provide a starting point for the tensile fracture. The specimen was set to the specimen holder with Piezo devise for electron microscopy.



Fig1. Specimen holder for microscope

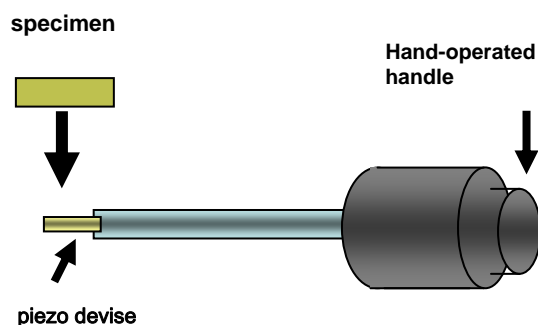


Fig2. Specimen and specimen holder

### 2-3 In-situ tensile experiment

In order to investigate the tensile velocity dependence to void reactions, in-situ tensile experiments were performed.

Observation 1 was made by decreasing voltage for Piezo device from 100v to 90v taking 100 seconds. In this observation, real velocity of tensile at specimen is about 1nm/s. Observation 2 was performed as well as observation 1. In this case, the tensile velocity is 100nm/s on an average. Observation 3 and 4 are different from 1 and 2. We used hand-operated handle attached specimen holder instead of Piezo device in these observations. If the handle is rotated by 10 degrees, then real displacement of specimen is about  $5 \mu\text{m}$ . Observation 3 was made by rotating this handle 5 degrees per second. Actual tensile velocity is  $3 \mu\text{m/s}$ .

Observation 4 was made by rotating 90 degrees per second. Velocity is about  $50 \mu\text{m/s}$ . In each experiment, both bright and dark field observation for TEM image were made before and after deformation, and recorded the behavior of defects during deformation by movie.

## 3 Experimental Results

### 3-1 Deformation Process

Through the observation 1 and 2, it could be found that two types of deformation exist just before fracture.

Case 1: Fracture tips glide each other along glide line of dislocations, and reach to fracture. In this case, the shape of saw-tooth portions is almost well-shaped triangle. Their tops are directed toward  $\langle 100 \rangle$  direction.

Case 2: First, tangled dislocations move to base portion, and all the dislocations disappear at the elongated region. In this region, elastic strain reach to 10~20% [3]. The saw-tooth portion shows a shape like trapezoid, and the top directs toward  $\langle 112 \rangle$  direction. The result of observation 2 is almost the same as observation 1, but there was a different point. In this case, almost all the observation results of showed abnormal high strain deformation process (case2 of observation1)

These results suggest the possibility that non-dislocation deformation mechanism is appeared.

### 3-2 Generation of voids

In observation 3, several numbers of voids were observed at the thick part of deformed regions. The shape of voids was almost sphere. In observation 3 and observation 4, since the tensile velocity was too fast to take a movie, the observation during deformation was not made. However, because the top of all saw-tooth portion which generated voids directed toward  $\langle 112 \rangle$  direction, there is a possibility that these deformation have been proceeded under abnormal high strain.

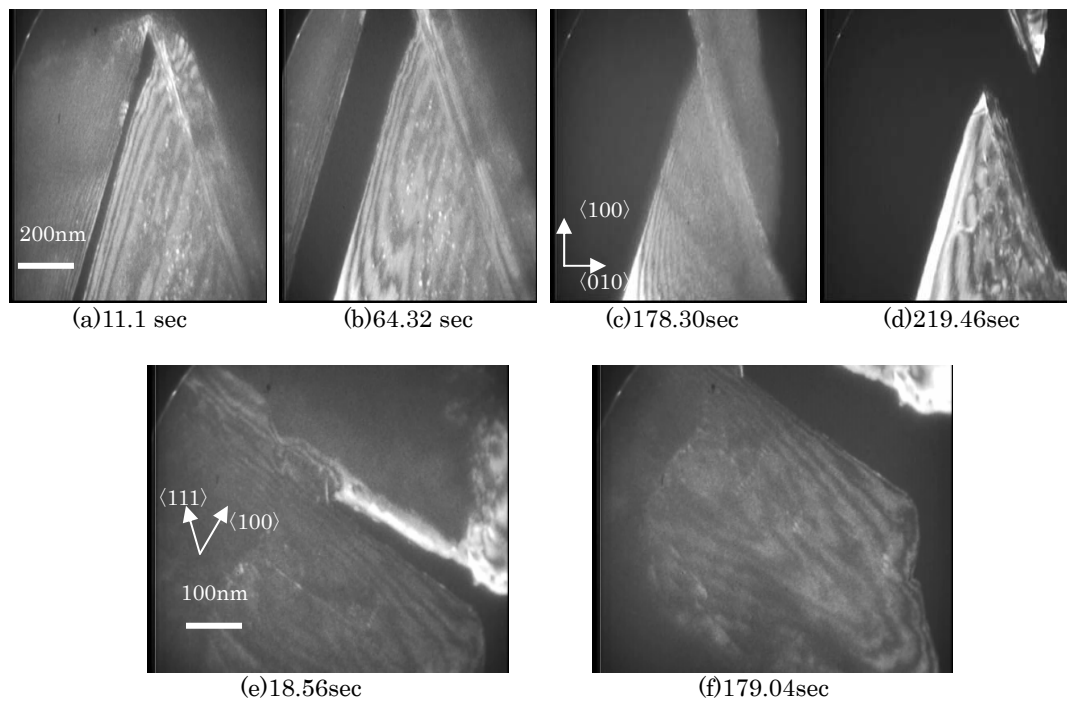


Fig3. deformation process observed in observation1 ,case1 {(a)~(d) } ,case2 {(e),(f)}

### 3-3 Distribution of voids in high speed deformation

In observation4, a large number of voids are observed in both the fracture region and saw-tooth portion.

In this deformation, lots of oval-shaped voids as if extended were observed. An interesting fact was also found. Voids remained in saw-tooth portion were arranged in a line. From the micrographs, we cannot understand the 3 dimensional direction, however, it is considered that these lines are arranged toward  $\langle 110 \rangle$  direction. This direction is not the same as tensile direction, thus this result may show how vacancy clusters act during deformation.

## 4 Discussions

### 4-1 Deformation Process

From the observed results of the deformation process, it is considered that a deformation mechanism without dislocation appears after all the dislocations disappeared from the elongate part. In this deformation, very high elastic strain occurred just

before the fracture. Calculating the stress in this area from Young's Module, the value reaches to about 15Gpa. In usual deformation in metals, such phenomena cannot happen.

### 4-2 Generation of Voids

In these experiments, voids were observed in observation 3 and 4. These results mean that voids start to appear at the velocity of more than  $0.1 \sim 1 \mu /s$ . From this value, strain rate can be calculated to about  $1 s^{-1}$ .

It is considered that this velocity dependence of void nucleation is caused by the high internal stress in this area This phenomenon can be explained as follows. As the strain rate become high, the production rate of vacancy clusters also increase. Since this concentration in material become high, the possibility of vacancy clusters reaching into nano-crack increase.

This high stress also prevents the nuclei of vacancy clusters from collapsing, unless vacancy clusters become dislocation loops or SFT (stacking fault tetrahedra).

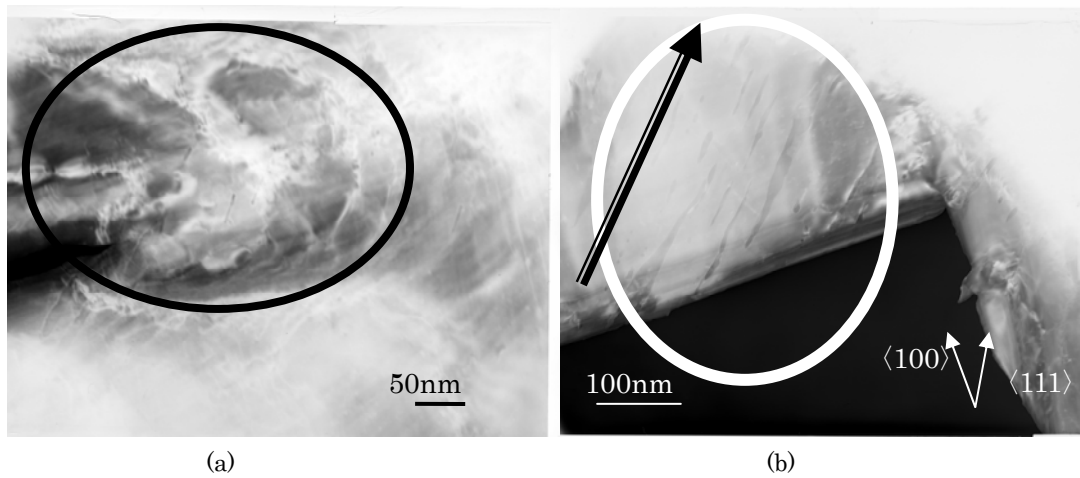


Fig4. Voids remained in fracture region (a) observation3, (4) observation4, line- shaped distribution

### 4-3 One dimensional motion of vacancies

In observation4, line shapes of voids were observed. These lines directed toward  $\langle 110 \rangle$ . This observation result suggests 1-dimensional motion of vacancy clusters.

### 4-4 Proposal of new deformation mechanism— Nano crack deformation

From these observation results and discussion, we propose new deformation mechanism (Nano crack deformation mechanism) in metal. This mechanism is explained by the motion of vacancy clusters in specimen.

Fig.5 shows the process of nano-crack deformation. First, High stress open the lattice space, nano-crack generate { (a) }. Then, the nano-crack breaks into two, and move to the direction  $\langle 110 \rangle$  each other { (b) }. When a pair of separated nano-crack moves apart each other, new atomic plain is created in the x direction { (c) }. This process is necessary in order elongate a material.

Finally, these broken nano-cracks reach to the surface, metal deformation progress { (d) }. This hypothesis can explain all the observation results. Nucleation of voids is explained as the result of gathering vacancies into nano-cracks in the specimen. And the arrangement of voids toward  $\langle 110 \rangle$  direction can be also explained by 1 dimensional nano-crack action.

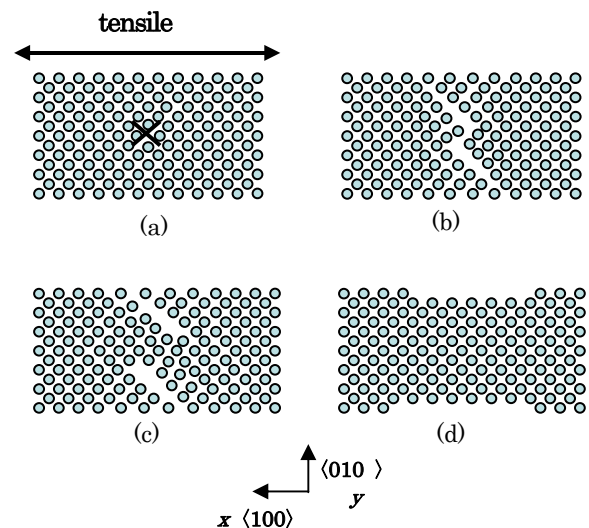


Fig.5 Nano-crack deformation mechanism

### References

- [1] M.Kiritani “Dislocation free plastic deformation under high stress” *Maters. Science &Engineering A350* (2003) 1-7.
- [2] S.Kojima, H.Fujii “Formation of Voids in Thin Foil Pure Gold during Plastic Deformation” *Maters. Trans.* 47 (2006) to be published.
- [3] Y.Matsukawa, Yasunaga, M.Komatsu and M.Kiritani “Dynamic observation of dislocation-free plastic deformation in gold thin foils.” *Materials Science &Engineering A350* (2003) 8-16.

## STUDY OF MAHALANOBIS METRIC

Student Number: 04M18044 Name: Naoya Inoue Supervisor: Yukihiro Yamashita

### Mahalanobis 計量に関する研究 井之上 直矢

パターン認識などではデータ間の距離を Mahalanobis 距離など確率的距離で用いることで単なる Euclid 距離を使うよりも認識精度や解析精度が向上することが知られている。Mahalanobis 距離を更に拡張した Mahalanobis 計量が提案されているが、それを与える Mahalanobis 計量方程式を十分な精度で計算することが出来なかった。そこで本研究では、Mahalanobis 計量を高速に高い精度で求める方法を開発した。

## 1 Introduction

The pattern recognition and the statistical analysis are actively researched. In many cases, there exists the correlation in pattern data. There are a lot of researches who measure them by a probabilistic distance.

Mahalanobis distance is a well-known probabilistic distance.[7](Fig.1)

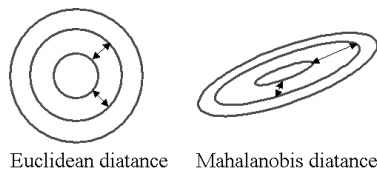


Fig.1: Probability density contour map

However, Mahalanobis distance cannot correspond to a non-normal probability distribution. Actual probability distribution is not normal. Here we research on Mahalanobis metric that is an extension of Mahalanobis distance. However Mahalanobis metric equation cannot solved in enough efficiency. So, we designed a method to obtain Mahalanobis metric accurately and efficiently in this research.

## 2 Mahalanobis distance

Mahalanobis distance measures a probabilistic distance between two vectors. Therefore, even if their Euclidean distance is small, the Mahalanobis distance may be large.

Mahalanobis distance is given by changing inner product of  $\mathcal{R}^n$  from  $\langle x, y \rangle$  to  $\langle R^{-1}x, y \rangle$ . Mahalanobis distance between  $x, y \in \mathcal{R}^n$  is shown as

$$l^2 = \langle x - y, R^{-1}(x - y) \rangle \quad (1)$$

The normal distribution of which average is 0 and covariance matrix is  $R$  is given by

$$p(x) = \frac{1}{\sqrt{(2\pi)^n \det R}} \exp(-\langle R^{-1}x, x \rangle / 2). \quad (2)$$

A normal distribution is transformed to the standard normal distribution with the coordinate transform  $x' = R^{-1/2}x$ . And, Mahalanobis distance is the pullback of  $\langle x', y' \rangle$  by the transform.

In general, Mahalanobis distance provide more accurate result than Euclidean distance. Mahalanobis distance depends only on covariance matrix. Therefore, for example, the part where distribution bends are not accurately measured. However, there are a lot of data according to a non-normal distribution. So, it is necessary to extend Mahalanobis distance.

### 3 Mahalanobis Metric

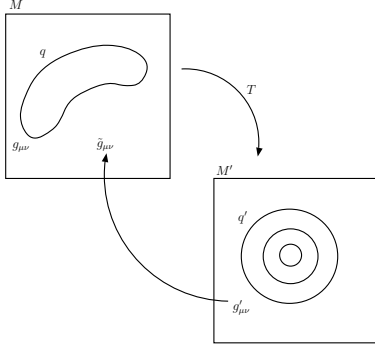


Fig.2: Transformation of probability density function

We define Mahalanobis metric on manifold.  $M$  and  $M'$  are two manifolds, and  $T : M \rightarrow M'$  is a diffeomorphism. We assume that probability density function  $p$  is transformed to a normal distribution in  $M'$  by  $T$ . (Fig.2) Then, we have

$$\nabla'_\mu \nabla'_\nu \log q' = f g'_{\mu\nu}. \quad (3)$$

$\nabla'_\mu$  is the covariant differentiation decided by metric tensor  $g'_{\mu\nu}$ .  $\tilde{g}_{\mu\nu}$  is define by the pull back of metric in  $M$  by  $T$ .  $(x, \tilde{g}_{\mu\nu})$  and  $(x', g'_{\mu\nu})$  become the relations of coordinate transformation. Therefore, we have

$$\tilde{\nabla}_\mu \tilde{\nabla}_\nu \log \frac{q(x)}{\sqrt{\tilde{g}}} = f \tilde{g}_{\mu\nu}. \quad (4)$$

$\tilde{g}_{\mu\nu}$  is rewritten with  $g_{\mu\nu}$  and we define the following formulary.

$$\nabla_\mu \nabla_\nu \left( \log p - \frac{1}{2} \log g \right) = f g_{\mu\nu} \quad (5)$$

It is called Mahalanobis metric equation of metric tensor  $g_{\mu\nu}$  and probability density function  $p$  with a certain scalar  $f$ . Where  $\nabla$  is a covariant differentiation and  $g$  is determinant of metric tensor  $g_{\mu\nu}$ .

The terms which depend on the original metric do not appear in the Mahalanobis metric equation.

Thus, Mahalanobis metric equation does not depend on the metric of an original space. This is extension of independence that Mahalanobis distance does not depend on the original inner product of the space[8].

When we rewrite the expression (5), it becomes

$$\nabla_\mu \nabla_\nu \log p - \frac{\partial}{\partial x^\nu} \Gamma_{\alpha\mu}^\alpha + \Gamma_{\nu\mu}^\eta \Gamma_{\alpha\eta}^\alpha = f g_{\mu\nu}. \quad (6)$$

Because  $f$  is an unknown scalar, the number of unknowns is more than the number of equations, and the equation cannot be solved directly.

The necessary and sufficient condition that a normalized probability density function  $q$  is isotropic independent is given by expression(7) with a certain scalar  $f$ .

$$\nabla_\mu \nabla_\nu \log q = f g_{\mu\nu} \quad (7)$$

By this theorem, when  $M'$  is  $\mathcal{R}^n$ , the scalar  $f$  was to be the constant of less than 0. Therefore, we can assume  $f = -1$ . And, the Mahalanobis metric is given as a solution of this equation.

### 4 Numerical analysis

Mahalanobis metric equation have to solved by the numerical method since it is complex. Here we explain two numerical analysis methods.

The first one is the method of steepest Descent. The method of Steepest Descent is the simplest gradient methods, and searches the direction that a ball tumbles down when we search for the lowest point. The direction is given by  $-\text{grad}f(x)$ . The advantages of the method are that computational complexity of each step is low and convergence is guaranteed. However, it takes very long time to convergence and it may converge not global but a local minimum point.

The second one is Newton's method. First Initial point  $x$  is provided, and draw the tangential line of  $y = f(x)$  at  $f(x, f(x_1))$ . Then,  $x_2$  is the

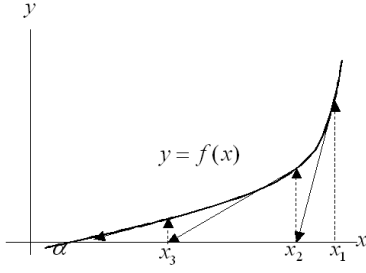


Fig.3: Newton's method

intersection of this tangential line and  $x$  axis. We repeat the procedure. The update rule is described as

$$x \leftarrow x - \frac{f(x)}{f'(x)}. \quad (8)$$

The advantage of Newton's method is very fast convergence, and drawbacks are there is no guarantee for convergence and it may converge not a global but a local minimum point.

## 5 Experiment

We solve Mahalanobis metric equation by the computer, and calculate the metric tensor. The Mahalanobis metric equation in the 2D is described as

$$\begin{aligned} & \partial_\mu \partial_\nu \log p - \Gamma_{\mu\nu}^1 \partial_1 \log p - \Gamma_{\mu\nu}^2 \partial_2 \log p \\ & + \Gamma_{\mu\nu}^1 (\Gamma_{11}^1 + \Gamma_{21}^2) + \Gamma_{\mu\nu}^2 (\Gamma_{12}^1 + \Gamma_{22}^2) \\ & - \partial_\nu (\Gamma_{1\mu}^1 + \Gamma_{2\nu}^2) + g_{\mu\nu} = 0 \end{aligned} \quad (9)$$

Let  $F_{\mu\nu}$  denotes the left-hand-side of equation(9).

$$\begin{aligned} F_{11} = & \partial_1 \partial_1 \log p - \Gamma_{11}^1 \partial_1 \log p - \Gamma_{11}^2 \partial_2 \log p \\ & + \Gamma_{11}^1 (\Gamma_{11}^1 + \Gamma_{21}^2) + \Gamma_{11}^2 (\Gamma_{12}^1 + \Gamma_{22}^2) \\ & - \frac{\partial}{\partial x^1} (\Gamma_{11}^1 + \Gamma_{21}^2) + g_{11} \end{aligned} \quad (10)$$

$$\begin{aligned} F_{12} = & \partial_1 \partial_2 \log p - \Gamma_{12}^1 \partial_1 \log p - \Gamma_{12}^2 \partial_2 \log p \\ & + \Gamma_{12}^1 (\Gamma_{11}^1 + \Gamma_{21}^2) + \Gamma_{12}^2 (\Gamma_{12}^1 + \Gamma_{22}^2) \\ & - \frac{\partial}{\partial x^2} (\Gamma_{11}^1 + \Gamma_{22}^2) + g_{12} \end{aligned} \quad (11)$$

$$\begin{aligned} F_{22} = & \partial_2 \partial_2 \log p - \Gamma_{22}^1 \partial_1 \log p - \Gamma_{22}^2 \partial_2 \log p \\ & + \Gamma_{22}^1 (\Gamma_{11}^1 + \Gamma_{21}^2) + \Gamma_{22}^2 (\Gamma_{12}^1 + \Gamma_{22}^2) \\ & - \frac{\partial}{\partial x^2} (\Gamma_{12}^1 + \Gamma_{22}^2) + g_{22} \end{aligned} \quad (12)$$

$F_{\mu\nu}$  have to be vanished.  $\Gamma_{ij}^k$  is connection coefficients and a function of  $g_{\mu\nu}$ . Then  $F_{\mu\nu}$  is a function of only  $g_{\mu\nu}$ .

Approximation is used for solving Newton's method. Our experiment, we use 51times51 mesh.

Fig.4(a) and (b) illustrate calculated  $g_{11}$  and  $g_{22}$  with ideal  $g_{11}$  and  $g_{22}$ , when  $x_1$  and  $x_2$  are changed while  $x_2 = 0$  and  $x_1 = 0$ , respectively.

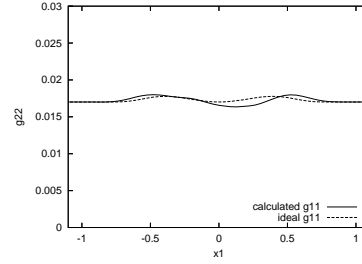
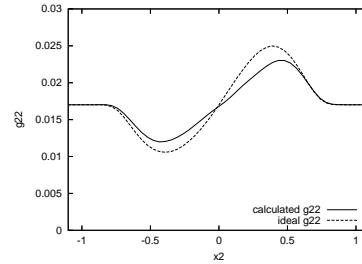
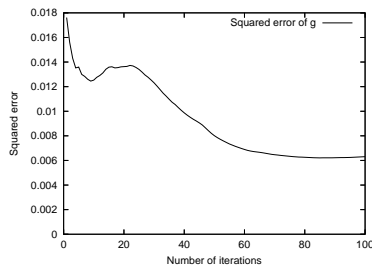

 (a) Metric tensor  $g_{11}$  ( $x^2 = 0$ )

 (b) Metric tensor  $g_{22}$  ( $x^1 = 0$ )

Fig.4: result(2/2)

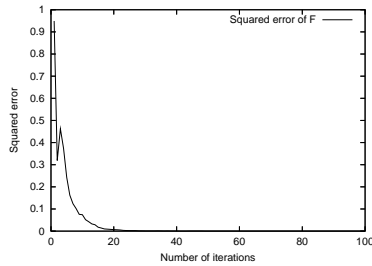
Fig.5(a) and(b) illustrate the convergence of squared error of  $F_{\mu\nu}$  and  $g_{\mu\nu}$ , respectively.

## 6 Summary

Compared to the previous result by Steepest descent method.(Fig.6). We cannot obtain enough accurate solution by Newton's method. However for Steepest descent method, 100000 iterations and the calculation of several days were necessary for convergence. On the other hand, for Newton's method, only 100 iterations and several hours were necessary.



(a) convergence of squares of error of  $g_{\mu\nu}$



(b) convergence of squares of error of  $F_{\mu\nu}$

Fig.5: Trial frequency and convergence of error

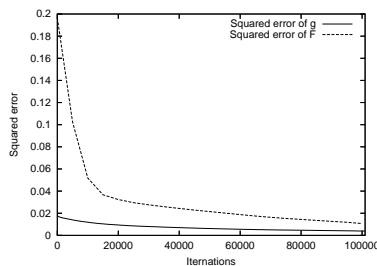


Fig.6: Trial frequency and convergence of error by Steepest descent method

Convergence is not enough since it converges to local solution. It is a problem to be solved. We will add the condition of the curvature, and search for the parameter by which Newton's method converges to the global solution.

## References

[1] Maistrov, L.E., *Probability theory, a historical sketch* (Translated and Edited by Kotz, S.), Academic Press, New York and London, 1974.  
 [2] Feller, W., *An introduction to probability theory and its application*, third edition, **vol.1**, John Wiley & Sons, New York, 1968.

[3] Tien, C.L. and Lienhard, J.H., *Statistical Thermodynamics*, Revised Printing, Hemisphere Publishing Corporation, Washington, 1985.  
 [4] Amari, S., "Defferencial geometrical method in statistics," Springer-Verg, Berlin Heidelberg, 1985.  
 [5] Fry. T.C., *Probability and its engineering uses*, second edition, D. Van Nostrand Company, Princeton, New Jersey, 1965.  
 [6] Spivak, M., *A comprehensive introduction to differential geometry*, second edition, **vol.1-5**, Publish or Perish, Inc., Houston, Texas, 1979.  
 [7] Mahalanobis, P.C., "Normalization of statistical variates and the use of rectangular co-ordinates in the theory of sampling distributions," *Sankhay*, vol. 3, no. 1, pp.1-40, Jan. 1937.  
 [8] Yukihiro Yamashita, Hidemitsu Ogawa, "Phase and optimal image restoration filter of image space," *Electronic information communication society thesis magazine(D-II)*, vol. 75-D-II, no. 2, pp.306-313, Feb. 1992.  
 [9] Yukihiro Yamashita, "Consideration concerning normal distribution on manifold," *The Technical Report of the Institute of Electronics Information and Communication Engineers of Japan*, no. PRMU 2000-174, Jan. 2001.  
 [10] Yukihiro Yamashita, "Consideration concerning normal distribution on manifold to which characterization of Maxwell distribution is enhanced," *The 2002 Japanese Joint Statistical Meeting Lecture papers*, pp.136-137, Sept. 2002.  
 [11] Yukihiro Yamashita, "Consideration concerning normal distribution on manifold to which characterization of Maxwell distribution is enhanced," *The 2002 Japanese Joint Statistical Meeting Lecture papers*, pp.136-137, Sept. 2002.  
 [12] Mariko Numakami, "Mahalanobis Metric on vector space," *The 2004 Tokyo Institute of Technology Department of Communications and Integrated Systems master's thesis*, pp.1-47, Mar. 2005.

## Study of Improvement of Kernel Sample Space Method

Student Number: 04M18251 Name: Chenghan Piao Supervisor: Yukihiro Yamashita

### カーネル標本空間射影法の高精度化に関する研究

朴成漢

パターン認識におけるカーネル法とは、得られたサンプルデータの情報をそのまま使うのではなく、特徴空間と呼ばれる非常に高次元の空間へ非線形に写像してから識別を行う手法である。本論文の目的は KSP (カーネル標本空間射影法) を改良し、その認識精度を向上させることである。一般のカーネル法では、カーネル関数は同じ非線形写像の内積で与えられていることを前提としている。本研究ではカーネル法を拡張し、内積の右辺と左辺に代入する非線形写像を異なるものとした理論を KSP に適用する。また訓練データに対して有効なカーネルパラメータを与える方法を開発するとともに、計算機実験によりその有効性を確かめる。

## 1 Introduction

Pattern recognition is a process to make an input pattern correspond to one of two or more concepts. recognition process consists of observation, preprocessing, feature extraction, classification. Our research is focused on classification. The kernel-based learning machines, e.g. Support Vector Machines (SVMs)[9], Kernel Principal Component Analysis (KPCA)[8] and Kernel Fisher Discriminant (KFD) [4], have been proposed, and achieved very low error rate. However, the kernel function was not able to be used freely for the limitation that the kernel function must be symmetry. To solve this problem, we propose the variable kernel sample space projection method, and show its effectiveness by experiments.

## 2 Kernel Based Method

In kernel-based methods, an N-dimensional input vector  $f \in R^N$  is mapped to a high dimensional space  $\mathcal{F}$  by a nonlinear map  $\Phi$ .

$$\Phi : R^N \rightarrow \mathcal{F}, f \mapsto \Phi(f) \quad (1)$$

We call this high dimensional space  $\mathcal{F}$  'feature space.' The inner product in a feature space is calculated by a positive definite kernel function  $k$  as

$$\langle \Phi(x), \Phi(y) \rangle = k(x, y), \quad (2)$$

where  $\langle \cdot \rangle$  denotes inner product. The function  $k$  is a "Mercer kernel function."

Mercer kernel functions which are widely used are as follows

$$k(x, y) = \langle x, y \rangle : \text{Identical} \quad (3)$$

$$k(x, y) = (\langle x, y \rangle + 1)^d : \text{Polynomial} \quad (4)$$

$$k(x, y) = \exp\left(-\frac{\|x - y\|^2}{2\sigma^2}\right) : \text{Gaussian} \quad (5)$$

If eq.(3) is chosen as a kernel function, the map  $\Phi$  is an identity operator. If the polynomial function eq.(4) and the Gaussian kernel function eq.(5) are used, an N-dimensional input vector is mapped into a  $(N+d)C_d - 1$ -dimensional and infinite dimensional space, respectively.

By using a mapping  $\Phi$ , linear or quadratic discriminant in a feature space is equivalent to more complex discriminant in the input space.

## 3 Kernel Sample Space Projection Classifier

We consider training samples  $f_1^i, f_2^i, \dots$ , and,  $f_{L_i}^i$  of class  $i$ , where  $L_i$  is the number of samples in the class. We define an operator as

$$S_i = [\Phi(f_1^i) \ \Phi(f_2^i) \ \dots \ \Phi(f_{L_i}^i)]. \quad (6)$$

We call the space spanned by samples in the feature space "kernel sample space."  $\mathcal{R}(S_i)$  is a kernel sample space, where  $\mathcal{R}(S_i)$  is the range of  $S_i$ .

In kernel-based methods, an input vector is mapped to a very high or infinite dimensional space. Its dimension is almost much larger than the number of samples  $L_i$ . Therefore a kernel sample space is non-dense space and expresses the feature of a class.

In KSP, the similarity between an unknown input vector and a class  $i$  is evaluated by the norm of its projection onto kernel sample space of the class. An unknown input vector is classified to the class of which norm is maximum(fig1)[10].

Now we describe it mathematically. Let

$$K_i = S_i^* S_i \quad (7)$$

$$= \begin{pmatrix} k(f_1^i, f_1^i) & \dots & k(f_1^i, f_{L_i}^i) \\ \vdots & \ddots & \vdots \\ k(f_{L_i}^i, f_1^i) & \dots & k(f_{L_i}^i, f_{L_i}^i) \end{pmatrix}, \quad (8)$$

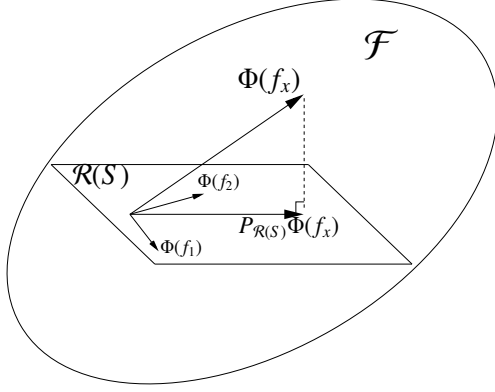


Figure 1: kernel sample space projection method

where  $S_i^*$  denotes an adjoint operator of  $S_i$ .  $K_i$  is called “kernel gram matrix.”

Let  $A^\dagger$  be a Moore-Penrose generalized inverse operator of an operator  $A$  satisfies

$$\begin{aligned} AA^\dagger A &= A \\ A^\dagger AA^\dagger &= A^\dagger \\ (AA^\dagger)^* &= AA^\dagger \\ (A^\dagger A)^* &= A^\dagger A. \end{aligned}$$

If  $A$  is a nonsingular operator,  $A^\dagger = A^{-1}$ .

A projection operator to  $\mathcal{R}(A)$  is given as

$$P_{\mathcal{R}(A)} = AA^\dagger \quad (9)$$

$$= A(A^*A)^\dagger A^*. \quad (10)$$

Let  $f_x$  be an unknown input vector, and  $h(f_x)$  be

$$\begin{aligned} h(f_x) &= S_i^* \Phi(f_x) \\ &= (k(f_1^i, x) \ k(f_2^i, x) \ \dots \ k(f_{L_i}^i, x)). \end{aligned}$$

Then, the projection operator  $P_{\mathcal{R}(S_i)}$  and the norm of the projection of  $\Phi(f_x)$  onto  $\mathcal{R}(S_i)$  are given as

$$P_{\mathcal{R}(S_i)} = S_i K_i^\dagger S_i^* \quad (11)$$

$$\|P_{\mathcal{R}(S_i)} \Phi(f_x)\|^2 = \langle h(f_x), K_i^\dagger h(f_x) \rangle. \quad (12)$$

An unknown input vector  $f_x$  is classified to the class of which projection norm is maximum.

$$\begin{aligned} \|P_{\mathcal{R}(S_i)} \Phi(f_x)\|^2 &> \|P_{\mathcal{R}(S_j)} \Phi(f_x)\|^2 \quad \forall j \neq i \\ &\Rightarrow f_x \in \Omega_i \end{aligned} \quad (13)$$

In KSP, an orthogonal projection can extract the features of each category. Thus, the projection norm of an unknown input vector  $\Phi(f_x)$  onto  $\mathcal{R}(S_i)$  stands for the similarity between  $f_x$  and class  $i$ . However, KSP may extract features that belong to more than one class. Such features cannot be used for classification, since they may be as harmful as noise. They can be suppressed using an oblique projection which in used Suppressed KSP(SKSP), they can be suppressed, and we expect higher performance.

## 4 Regularization

Generally, a set of learning samples will include outliers or noisy samples. Thus, the generalization capability of classifiers may not be high, even if they can classify finite learning samples correctly. This problem is the over-fitting or over-learning problem, and it can be avoided by using regularization or model selection. For example, [1] and [6], introduced a soft margin for SVM and AdaBoost technique. In KSP, the learned patterns are always classified correctly as long as the Gram matrix is non-singular. Thus, the over-fitting problem may occur when it is used.

The over-fitting problem occurs when the classifier has a too complex decision boundary. If the classifier has a discriminant function, the complexity of its decision boundaries is measured using the variation of the function with respect to a very small variation in the input vector. Let  $\Delta$  be the former variation,  $\delta f_x$  be a small variation of  $f_x$  and  $d : R^N \rightarrow R$  be a discriminant function. Then  $\Delta$  is expressed as

$$\Delta = \frac{(d(f_x + \delta f_x) - d(f_x))/d(f_x)}{\|\delta f_x\|/\|f_x\|}. \quad (14)$$

For KSP,  $\Delta_{KSP}$  is expressed as

$$\Delta_{KSP} \leq \frac{\|P_{\mathcal{R}(S_i)} \Phi(f_x + \delta f_x) - P_{\mathcal{R}(S_i)} \Phi(f_x)\|}{\|\delta f_x\|} \quad (15)$$

$$\frac{\|f_x\|}{\|P_{\mathcal{R}(S_i)} \Phi(f_x)\|}. \quad (16)$$

To suppress  $\Delta_{KSP}$  directly is difficult because  $\Phi$  is non-linear. Instead of  $\Delta_{KSP}$ , we introduce  $\Delta'_{KSP}$ , which is a variation of the feature with respect to a very small variation  $\delta \Phi(f_x)$  of  $\Phi(f_x)$ . Then we have

$$\Delta'_{KSP} = \frac{\|P_{\mathcal{R}(S_i)} \delta \Phi(f_x)\|}{\|\delta \Phi(f_x)\|} \cdot \frac{\|\Phi(f_x)\|}{\|P_{\mathcal{R}(S_i)} \Phi(f_x)\|}. \quad (17)$$

Suppression of  $\Delta$  has been discussed in reference to ill-posed problems and regularization ([2]). Most ill-posed problems are caused by the first part of  $\Delta$ ,  $\frac{d(f_x + \delta f_x) - d(f_x)}{\|\delta f_x\|}$ . If  $d(f) = \|Af\|$ , the maximum value of the first part of  $\Delta$  is given by its operator norm which is defined as  $\|A\| = \sup_{\|f\|=1} \|Af\|$ .

Tikhonov's regularization avoids ill-posed problems ([7]). It suppresses the Frobenius norm, which is defined as  $\|A\|_2 = \sqrt{\text{tr}[A^*A]}$ . Since  $\|A\| \leq \|A\|_2$ , we can avoid ill-posed problems by suppressing the Frobenius norm.

We define the regularized KSP as follows. [Regularized KSP] Regularized KSP is defined by the solution of following optimization problem.

$$\begin{aligned} \min : \quad J[X_i] &= \frac{1}{L_i} \sum_{s=1}^{L_i} \|\Phi(f_s^i) - X_i \Phi(f_s^i)\|^2 \\ &+ \mu \|X_i\|_2^2, \end{aligned} \quad (19)$$

$$\text{subject to : } \mathcal{N}(X) \supset \mathcal{R}(S_i)^\perp, \quad (20)$$

where  $\mu > 0$  is a regularization parameter. A solution of Regularized KSP is

$$\tilde{P}_{\mathcal{R}(S_i)} = S_i(K_{S_i} + \mu L_i I)^{-1} S_i^*, \quad (21)$$

where  $I$  denotes the identity matrix. If  $K_{U_i}$  is nonsingular,  $P'_{\mathcal{R}(S_i)}$  is a projection operator onto  $\mathcal{R}(S_i)$ .

If  $K_{U_i}$  is nonsingular,

$$P'_{\mathcal{R}(S_i)} P_{\mathcal{R}(U_i)} = P'_{\mathcal{R}(S_i)}, \quad (22)$$

$$P_{\mathcal{R}(U_i)} P'_{\mathcal{R}(S_i)} = P'_{\mathcal{R}(S_i)}, \quad (23)$$

where  $P_{\mathcal{R}(U_i)}$  is the orthogonal projection operator onto  $\mathcal{R}(U_i)$ .

If  $K_{U_i}$  is nonsingular,  $P'_{\mathcal{R}(S_i)} v = 0$  for all  $v \in \mathcal{R}(T_i)$ .

$P'_{\mathcal{R}(S_i)} \Phi(f_x)$  can be considered as follows. First,  $\Phi(f_x)$  is orthogonally projected onto  $\mathcal{R}(U_i)$ , after it is projected onto  $\mathcal{R}(S_i)$  along  $\mathcal{R}(T_i)$ . The similarity between  $f_x$  and  $\Omega_i$  against  $\Psi_i$  is given as  $\|P'_{\mathcal{R}(S_i)} \Phi(f_x)\|$ . If  $\Psi_i = \phi$ ,  $P'_{\mathcal{R}(S_i)} = P_{\mathcal{R}(S_i)}$ . Thus, SKSP is an extension of KSP.

In actual problems, KSP can extract necessary features by itself. Thus we do not have to use all samples of other classes, only the samples that are similar to  $\Omega_i$  have to be included in  $\Psi_i$ . Since the similarity of an input vector is evaluated using the projection norm onto  $\mathcal{R}(S_i)$ , it is sufficient that samples whose projection norms are large are included in  $\Psi_i$ .

We also introduce a Tikhonov's regularization term to SKSP as well as KSP. Regularized SKSP is defined as

min :

$$J[X_i] = \frac{1}{L_i} \sum_{s=1}^{L_i} \|\Phi(f_s^i) - X_i \Phi(f_s^i)\|^2 \quad (24)$$

$$+ \frac{\alpha}{M_i} \sum_{t=1}^{M_i} \|X_i \Phi(g_t^i)\|^2 + \mu \|X_i\|_2^2 \quad (25)$$

$$\text{subject to: } \mathcal{N}(X_i) \supset \mathcal{R}(U_i)^\perp, \quad (26)$$

where  $\mu > 0$  is the regularization parameter.

Let

$$\tilde{D}_i = \begin{pmatrix} L_i I_{L_i} & 0_{L_i, M_i} \\ 0_{M_i, L_i} & \frac{M_i}{\alpha} I_{M_i} \end{pmatrix}. \quad (27)$$

A solution of Regularized SKSP is

$$\tilde{P}'_{\mathcal{R}(S_i)} = U_i D_i (K_{U_i} + \mu \tilde{D}_i)^{-1} U_i^*. \quad (28)$$

[11]

Let

$$\begin{aligned} \tilde{K}_{U_i} &= K_{U_i} + \mu \tilde{D}_i, \\ h_i(f_x) &= U_i^* \Phi(f_x) \\ &= (k(f_x, f_1^i), \dots, k(f_x, f_{L_i}^i), \\ &\quad k(f_x, g_1^i), \dots, k(f_x, g_{M_i}^i))^\top, \end{aligned}$$

then the similarity between an unknown input vector  $f_x$  and  $\Omega_i$  against  $\Psi_i$  is given as

$$\|\tilde{P}'_{\mathcal{R}(S_i)} \Phi(f_x)\|^2 = \langle h_i(f_x), \tilde{K}_{U_i}^{-1} D_i K_{U_i} D_i \tilde{K}_{U_i}^{-1} h_i(f_x) \rangle \quad (29)$$

## 5 Variable Kernel Method

In a kernel function has to be symmetric. Here, we apply the asymmetric kernel theorem to KSP and SKSP, and propose the variable kernel sample space method (VKSP) and the variable suppressed kernel method (VSKSP).

In the previous kernel method, the kernel function is defined by

$$k(x, y) = \langle \Phi(x), \Phi(y) \rangle. \quad (30)$$

In the variable kernel method, it is defined by

$$k(x, y) = \langle \Phi_1(x), \Phi_2(y) \rangle \quad (31)$$

$$k_1(x, y) = \langle \Phi_1(x), \Phi_1(y) \rangle \quad (32)$$

that is, the kernel function it is given as a product in the result of two the difference mappings to the feature space. The Gauss kernel is used as a kernel function in this thesis. Because test sample is an unknown, the kernel parameter uses a constant parameter about the test sample.

The variable kernel function is given as

$$k(x, y) = \left( \frac{\sigma_0}{\sqrt{\sigma^2(x) + \sigma_1^2}} \right)^K \exp \left( -\frac{\|x-y\|^2}{2(\sigma^2(x) + \sigma_1^2)} \right)$$

and

$$k_1(x, y) = \left( \frac{\sigma_0}{\sqrt{\sigma^2(x) + \sigma^2(y)}} \right)^K \exp \left( -\frac{\|x-y\|^2}{2(\sigma^2(x) + \sigma^2(y))} \right)$$

parameter of the Variable kernel sample space projection (VKSP) is changed according to the density of input pattern. parameters decided by For each training samples the parameter os set to the minimum Euclidean distance to (1) all training sample of the other category or (2) all the other training samples or (3) all the other samples in the own category. Because the kernel function is given by a product in these two vectors, it becomes variable.

Let  $f_x$  be an unknown input vector, and  $h_1(f_x)$  be

$$\begin{aligned} h_1(f_x) &= S_i^* \Phi_1(f_x) \\ &= (k_1(f_1^i, x), k_1(f_2^i, x), \dots, k_1(f_{L_i}^i, x)). \end{aligned}$$

Then, the projection operator  $P_{\mathcal{R}(S_i)}$  and the norm of the projection of  $\Phi(f_x)$  onto  $\mathcal{R}(S_i)$  are given as

$$P_{\mathcal{R}(S_i)} = S_i K_i^\dagger S_i^* \quad (33)$$

$$\|P_{\mathcal{R}(S_i)} \Phi(f_x)\|^2 = \langle h_1(f_x), K_i^\dagger h_1(f_x) \rangle. \quad (34)$$

Regularized KSP is defined by the solution of following optimization problem.

$$\begin{aligned} \min : \quad J[X_i] &= \frac{1}{L_i} \sum_{s=1}^{L_i} \|\Phi_2(f_s^i) - X_i \Phi_1(f_s^i)\|^2 \\ &\quad + \mu \|X_i\|_2^2, \end{aligned} \quad (35)$$

$$\text{subject to: } \mathcal{N}(X) \supset \mathcal{R}(S_i)^\perp, \quad (37)$$

where  $\mu > 0$  is a regularization parameter.

## 6 Experiment

We used several practical data sets that were used in [6], [3] and [5]<sup>1</sup>. It consists of 13 binary classification problems and each dataset consists of 100 or 20 realizations. We also conduct experiments of two-class classification problems. The mean test error rates and their standard deviations are shown in Table 1 and 2. All values are described in percentage and bold font means the better than KSP or SKSP by T-test result in those methods.

Table 1: Results of two-class classification

Name	VKSP	KSP	SVM	KFD
Banana	10.4±0.5	10.4±0.5	11.5±0.7	10.8±0.5
B.Cancer	<b>28.3±4.4</b>	29.7±4.5	26.0±4.7	24.8±4.6
F.Solar	<b>38.5±4.7</b>	39.1±2.4	32.4±1.8	33.2±1.7
German	<b>29.8±2.0</b>	31.3±2.5	23.6±2.1	23.7±2.2
Heart	15.4±3.4	15.4±3.3	16.0±3.3	16.1±3.4
Ringnorm	19.9±1.8	19.9±1.8	1.7±0.1	1.5±0.1
Splice	<b>12.1±0.7</b>	12.6±0.7	10.9±0.7	10.5±0.6
Thyroid	4.2±2.3	4.2±2.3	4.8±2.2	4.2±2.1
Titanic	28.3±9.4	28.3±9.4	22.4±1.0	23.3±2.1
Twonorm	2.4±0.1	2.3±0.1	3.0±0.2	2.6±0.2

Table 2: Results of two-class classification

Name	VSKSP	SKSP	SVM	KFD
Banana	10.4±0.5	10.4±0.5	11.5±0.7	10.8±0.5
B.Cancer	25.8±4.3	26.0±4.5	26.0±4.7	24.8±4.6
F.Solar	<b>36.7±5.3</b>	37.2±4.5	32.4±1.8	33.2±1.7
German	23.5±1.6	23.4±1.6	23.6±2.1	23.7±2.2
Heart	15.6±3.2	15.8±3.1	16.0±3.3	16.1±3.4
Ringnorm	<b>16.4±0.9</b>	18±2.3	1.7±0.1	1.5±0.1
Splice	<b>11.1±0.6</b>	11.2±0.7	10.9±0.7	10.5±0.6
Thyroid	4.2±2.3	4.6±2.2	4.8±2.2	4.2±2.1
Titanic	28.9±12.9	29.4±10.3	22.4±1.0	23.3±2.1
Twonorm	2.4±0.1	2.4±0.1	3.0±0.2	2.6±0.2

## 7 Discussion

The VKSP outperforms the KSP in four kinds of data sets. Besides, almost the same recognition rate as KSP was obtained. The VSKSP exceeded the recognition rate of SKSP in six kinds of data sets. This is because the separating boundary is more correctly expressed by variable kernel functions than by fixed kernel functions.

## 8 Conclusions

We proposed variable kernel sample space projection method (VKSP and VSKSP), the feature and effectiveness were shown by the recognition experiment. For the future work they have to be applied various problems, calculation time has to be reduced and needed about

<sup>1</sup>The data sets were downloaded from 'http://ida.first.fraunhofer.de/projects/bench/benchmarks.htm'.

how to decide the kernel parameter has to be investigated.

## References

- [1] C. Cortes and V. Vapnik, "Support-Vector Networks," *Machine Learning*, vol.20, no.3, pp.273–297, 1995.
- [2] C.W. Groetsch, *Inverse problems in the mathematical sciences*, Vieweg, 1993.
- [3] S. Mika, G. Rätsch, J. Weston, B. Schölkopf, and K.R. Müller, "Fisher discriminant analysis with kernels," *Neural Networks for Signal Processing IX*, ed. Y.H. Hu, J. Larsen, E. Wilson, and S. Douglas, pp.41–48, IEEE, 1999.
- [4] K.R. Müller, S. Mika, G. Rätsch, K. Tsuda, and B. Schölkopf, "An introduction to kernel-based learning algorithms," *IEEE Transactions on Neural Networks*, vol.12, no.2, pp.181–201, 2001.
- [5] G. Rätsch, *Robust Boosting via Convex Optimization*, Ph.D. thesis, University of Potsdam, Neues Palais 10, 14469 Potsdam, Germany, October 2001.
- [6] G. Rätsch, T. Onoda, and K.R. Müller, "Soft margins for AdaBoost," *Machine Learning*, vol.42, no.3, pp.287–320, March 2001. also NeuroCOLT Technical Report NC-TR-1998-021.
- [7] A.N. Tikhonov and V.Y. Arsenin, *Solution of Ill-posed problems*, V. H. Winston and Sons, 1977.
- [8] K. Tsuda, "Subspace classifier in the Hilbert space," *Pattern Recognition Letters*, vol.20, no.5, pp.513–519, 1999.
- [9] V.N. Vapnik, *Statistical Learning Theory*, Wiley, New-York, 1998.
- [10] 鷲沢嘉一 and 山下幸彦, "カーネル標本空間射影法によるパターン認識," 第6回情報論的学習理論ワークショップ IBIS2003 予稿集, pp.149–154, Nov. 2003.
- [11] 鷲沢嘉一 and 山下幸彦, "抑制型カーネル標本空間射影法によるパターン認識," 電子情報通信学会技術研究報告 PRMU2003-270 予稿集, pp.85–90, March. 2004.

## Support vector machine with asymmetric kernels

Student Number: 04M18274 Name: Shen Liu Supervisor: Yukihiko Yamashita

### 非対称カーネルサポートベクターマシン

柳 森

パターン認識におけるカーネル法とは、得られたサンプルデータの情報をそのまま使うのではなく、特徴空間と呼ばれる非常に高次元の空間へ非線形に写像してから識別を行う手法である。本研究の目的はSVM(サポートベクターマシン)を改良し、その認識精度を向上させることである。一般のカーネル法では、カーネル関数は同じ非線型写像の内積で与えられていることを前提としている。本研究ではカーネル法を拡張し、内積の右辺と左辺に代入する非線型写像を異なるものとした理論をSVMに適用する。また訓練データに有効なカーネルパラメータを与える方法とその有効性を計算機実験により確かめる。

## 1 Introduction

Optimal hyperplane classifier (OHC) classifies an input pattern by a hyperplane. Support vector machine (SVM), which is a kernelized version of OHC, attained high classifier accuracy. A nonlinear and complicated boundary can be realized by the kernel method. However, since a kernel function has to be symmetric and positive-definite, the direct realization of SVM with a variable kernel function is a difficult problem. In order to solve this problem, we apply the asymmetric kernel method to OHC, and proposed the SVM with a variable kernel function. Furthermore, we apply it to two-class classification problems and show experimental results.

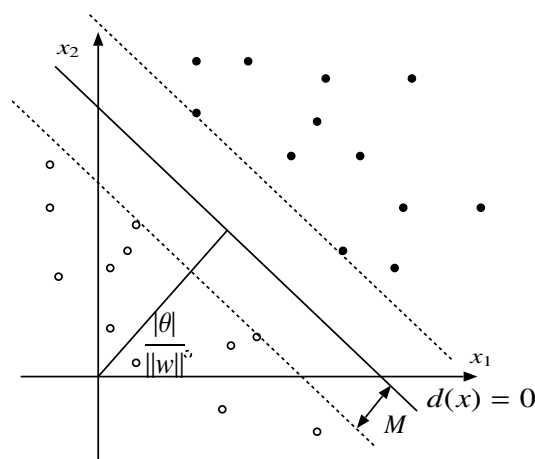


Figure 1: OHC or Margin

## 2 OHC of SVM

### 2.1 Linear Support Vector Machine

#### 2.1.1 The separable case

Assume that patterns are in  $\mathbb{R}^d$ . Let  $\mathbb{Y} = \{+1, -1\}$  be a set of labels. Consider the labeled training data  $\{x_1, y_1\}, \dots, \{x_n, y_n\} \in \mathbb{R}^d \times \mathbb{Y}$ . Suppose we have some hyperplane which separates the positive from the negative examples. The support vector algorithm simply looks for the separating hyperplane with largest margin. It can be formulated as follows: suppose that all the training data satisfy the following constraints,

$$\langle w, x \rangle + b \geq +1 \text{ for } y_i = +1 \quad (1)$$

$$\langle w, x \rangle + b \leq -1 \text{ for } y_j = -1 \quad (2)$$

These can be combined into one set of inequalities:

$$y_i(\langle w, x_i \rangle + b) - 1 \geq 0 \quad (3)$$

Hyperplanes ( $\langle w, x \rangle + b = \pm 1$ ) are parallel and that no training point falls between them. Thus we can find the pair of hyperplanes which gives the maximum margin by minimizing  $\|w\|^2$ , subject to constraints (3).

#### 2.1.2 The non-separable case

The above algorithm for separable data, when applied to non-separable data, will find no feasible solution. SVM is extend these ideas to handle non-separable data. We would like to relax the constraints (1), but only when necessary, that is, we would like to introduce a further cost for doing so. This can be done by introducing positive slack variable  $\xi_i > 0, i = 1, \dots, l$  in the constraints, which then become:

$$\langle w, x \rangle + b \geq +1 - \xi_i \text{ for } y_i = +1 \quad (4)$$

$$\langle w, x \rangle + b \leq -1 + \xi_i \text{ for } y_j = -1 \quad (5)$$

Thus, for an error to occur, the corresponding  $\xi_i$  must exceed unity, so  $\sum \xi_i$  is an upper bound on the number of training errors. Hence a natural way to assign an extra cost for errors is to change the objective function to be minimized from  $\|w\|^2/2$  to  $\|w\|^2/2 + C\sum \xi_i$ , where  $C$  is a parameter to be chosen by the user, a larger  $C$  corresponding to assigning a higher penalty to errors.

### 2.2 Nonlinear Support Vector Machine (Kernel method)

The above methods are generalized to the case where the decision function is not a linear function of the data. Now suppose we first mapped the data to some other (possibly infinite dimensional) Euclidean space  $\mathfrak{R}$ , using a mapping which we will call  $\Phi : \mathbb{R}^d \rightarrow \mathfrak{R}$ . Then of course the training algorithm would only depend on the data through the inner products in  $\mathfrak{R}$ , i.e. on functions of the form  $\langle \Phi(x_i), \Phi(x_j) \rangle$ .

Consider about the identification of two classes  $A$  and  $B$ . The samples of classes  $A$  and  $B$  as figures 2,

$$f_1^A = (1, 1), \quad f_2^A = (-1, -1) \quad (6)$$

$$f_1^B = (1, -1), \quad f_2^B = (-1, 1) \quad (7)$$

are given. In this case, this sample cannot be separated by the linear identification function. In other words, classes  $A$  and  $B$  can not be separated by the straight line. When mapping  $\Phi$

$$\Phi : \mathbb{R}^2 \rightarrow \mathbb{R}^3$$

$$(x_1, x_2)^T \mapsto (x_1^2, x_2^2, 2x_1x_2)^T \quad (8)$$

is used and the samples are

$$\Phi(f_1^A) = (1, 1, 2), \quad \Phi(f_2^A) = (1, 1, 2) \quad (9)$$

$$\Phi(f_1^B) = (1, 1, -2), \quad \Phi(f_2^B) = (1, 1, -2) \quad (10)$$

The new sample are illustrated in figure 3 . As a result, it comes to be able to separate the sample of class  $A$  and  $B$  by the plane. Now if there were a "kernel function"  $K$  such that  $K(x_i, x_j) = \langle \Phi(x_i), \Phi(x_j) \rangle$ , we would only need to use  $K$  in the training algorithm, and would never need to explicitly even know what  $\Phi$  is, The examples of the kernel function are given as

$$k(x, y) = \langle x, y \rangle \quad : \quad \text{Identical} \quad (11)$$

$$k(x, y) = (\langle x, y \rangle + 1)^d \quad : \quad \text{Polynomial} \quad (12)$$

$$k(x, y) = \exp\left(-\frac{\|x - y\|^2}{2\sigma^2}\right) \quad : \quad \text{Gaussian} \quad (13)$$

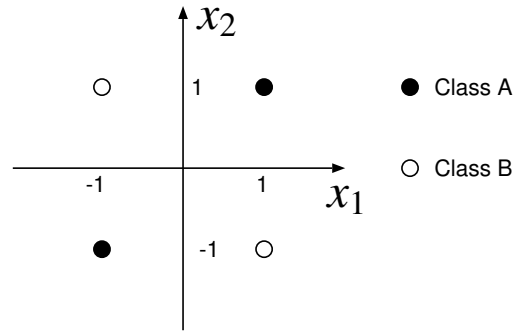


Figure 2: examples of the kernel method:A

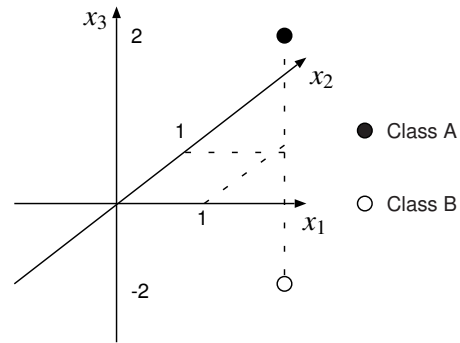


Figure 3: examples of the kernel method:B

### 3 Variable Kernel Method

In the kernel method, the complexity of the boundary depends on the kernel function of SVM that was limited to be a positive definite symmetry function. So it was difficult to make the kernel parameter variable. The complexity of the best boundary for identification varies according to place. So it is necessary to make it variable. In a conventional kernel method,

$$k(x, y) = \langle \Phi(x), \Phi(y) \rangle \quad (14)$$

the kernel function is defined by the inner product between the images by the same mapping  $\Phi$  like expression (14). Therefore, the condition of positive-definite symmetric function was necessary for the kernel function. In the asymmetric kernel,

$$k(x, y) = \langle \Phi_1(x), \Phi_2(y) \rangle \quad (15)$$

the kernel function is assumed the inner product between two images by the two different feature mapping  $\Phi_1$  and  $\Phi_2$  like expression (15). The asymmetric kernel method is applied to SVM. In this research, we use the Gauss kernel. Here, the parameter to the feature space previously gives a changeable nonlinear map, and the kernel function is provided by the map. Let  $\sigma(x)$  be a changeable kernel parameter for the learning pattern, and  $\sigma_1$  be

a fixed kernel parameter for an unknown pattern. Moreover, Let  $\sigma_0$  be a standard kernel parameter, and the value uses the kernel parameter of compared SVM.

Here, the variable nonlinear map  $\Phi_1(x)$  and  $\Phi_2(x)$  to feature space are defined by

$$(\Phi_1(x))(y) = \left( \frac{\sigma_0}{(2\pi)^{1/4}\sigma(x)} \right)^K e^{-\frac{\|x-y\|^2}{2\sigma^2(x)}} \quad (16)$$

$$(\Phi_2(x))(y) = \left( \frac{\sigma_0}{(2\pi)^{1/4}\sigma_1} \right)^K e^{-\frac{\|x-y\|^2}{2\sigma_1^2}} \quad (17)$$

The necessary variable kernel functions are given as

$$k(x,y) = \langle \Phi_1(x), \Phi_2(y) \rangle \quad (18)$$

$$= \int_{R^K} (\Phi_1(x))(z) (\Phi_2(y))(z) dz \quad (19)$$

$$= \left( \frac{\sigma_0}{\sqrt{\sigma^2(x) + \sigma_1^2}} \right)^K e^{-\frac{\|x-y\|^2}{2(\sigma^2(x) + \sigma_1^2)}} \quad (20)$$

and

$$k_1(x,y) = \langle \Phi_1(x), \Phi_1(y) \rangle \quad (21)$$

$$= \left( \frac{\sigma_0}{\sqrt{\sigma^2(x) + \sigma^2(y)}} \right)^K e^{-\frac{\|x-y\|^2}{2(\sigma^2(x) + \sigma^2(y))}} \quad (22)$$

In this research, we choose  $z_l$  from all training patterns  $x_l$  when the distance between the separating hyperplane and  $x_l$  is less than  $1.1 \cdot \|w\|$ . Moreover,

$$\sigma_1 = \sigma_0 \sqrt{\alpha/2} \quad (23)$$

$$\sigma(z_l) = \beta(z_l) \sigma_0 \sqrt{1 - \alpha/2} \quad (24)$$

$\alpha$  is asymmetric parameter.  $\beta(z_l)$  is assumed 0.5 when  $z_l$  is mis-recognized, and, besides, assumed to 1.0.

## 4 Computer Experiment

We also conduct experiments by two-class classification problems. The mean test error rates and their standard deviations are shown in Table 1. All values are described in percentage and bold font means the best result in this method.

## 5 Discussion

The variable kernel SVM was surpassing of the identification rate of the previous SVM. Their advances are also shown by T-test. Besides, almost

Table 1: Results of two-class classification

Name	SVM in thesis	SVM	VSVM
Banana	11.5 ± 0.7	10.85 ± 0.62	<b>10.48 ± 0.52</b>
B.Cancer	26.0 ± 4.7	28.79 ± 4.6	<b>24.8 ± 4.6</b>
Diabetes	23.5 ± 1.73	24.09 ± 1.89	<b>23.26 ± 1.73</b>
F.Solar	32.4 ± 1.8	37.51 ± 2.9	32.4 ± 1.8
German	23.6 ± 2.1	24.07 ± 2.18	23.6 ± 2.1
Heart	16.0 ± 3.3	17.48 ± 3.36	16.0 ± 3.3
Ringnorm	1.7 ± 0.1	1.64 ± 0.12	1.7 ± 0.1
Thyroid	4.8 ± 2.2	5.4 ± 2.41	<b>4.05 ± 2.14</b>
Titanic	22.4 ± 1.0	22.28 ± 1.03	22.4 ± 1.0
Twonorm	3.0 ± 0.2	2.62 ± 0.17	3.0 ± 0.2
Waveform	9.9 ± 0.4	9.88 ± 0.42	9.9 ± 0.4

the same identification rate as SVM was shown. This is because a complex identification boundary is expressed well according to the density distribution. and the feature of the sample is effectively extracted.

## 6 Conclusion

The kernel method was extended, the variable kernel SVM is proposed and effectiveness is shown by the recognition experiment. Moreover, application to a variety of recognition problems are enumerated as a problem in the future. Moreover, a further work is needed about how to decide the parameter.

## References

- [1] C. Cortes and V. Vapnik, "Support-vector networks," Machine Learning, vol.20, no.3, pp.273–297, 1995.
- [2] Y.S. Hwang and S.Y. Bang, "An efficient method to construct a radial basis function neural network classifier," Neural Networks, vol.10, no.8, pp.1495–1503, Nov. 1997.
- [3] J. Mercer, "Functions of positive and negative type, and their connection with the theory of integral equations.," Trans. Lond. Phil. Soc. (A), vol.209, pp.415–446, 1909.
- [4] S. Mika, G. Rätsch, J. Weston, B. Schölkopf, A.J. Smola, and K.R. Müller, "Invariant feature extraction and classification in kernel spaces," Advances in Neural Information Processing Systems 12, ed. M.S. Kearns, S.A. Solla, and D.A. Cohn, pp.526–532, MIT Press, 2000.
- [5] M.T. Musavi, W. Ahmad, K.H. Chan, K.B. Faris, and D.M. Hummels, "On the training

- of radial basis function classifier,” *Neural Networks*, vol.5, no.4, pp.595–603, Aug. 1992.
- [6] B. Schölkopf, A. Smola, and K. Müller, “Non-linear component analysis as a kernel eigenvalue problem,” *Neural Computation*, vol.10, no.5, pp.1299–1319, 1998.
- [7] Koji Tsuda, “Support Vector Machine with Variable Kernel Function,” *Technical Report of Ieice*, no.PRMU98-175, pp.195–202, Dec. 1998.
- [8] Eisaku Maeda and Hiroshi Murase, “Pattern recognition by kernel nonlinear subspace method” *Technical Report of Ieice (D-II)*, vol.J82-D-II, no.4, pp.600–612, April 1999.
- [9] Koji Tsuda, “Subspace classifier in the Hilbert space,” *Pattern Recognition Letters (D-II)*, vol.J82-D-II, no.4, pp.592–599, April 1999.
- [10] C.J. C. Burges, “A Tutorial on Support Vector Machines for Pattern Recognition” *Data Mining and Knowledge Discovery*, vol.J82-D-II, pp.121-167, 1998

Student Number : 04M18133 Name : Takayuki SHINOZAKI Super visor : Yukihiro YAMASHITA

## 画素単位動き補償予測を用いた動画像符号化に関する研究

篠崎 教志

MPEGに代表されるブロック単位の動画像圧縮方式では、復号した画像にブロック歪が現われる問題が生じる。この問題を解決するために「画素単位動き補償予測を用いた動画像符号化」を提案する。この手法はブロック歪を減らすだけでなく、動きベクトルの正確な検出により、より効率的な符号化が期待できる。

### 1 Introduction

In recent years, the information communication technology called IT (Information Technology) is splendidly developed. Not only a document but also picture, a sound, etc. are widely used for communication. However, the amount of information of the multimedia data which generally contains digitized pictures and sounds are huge. Therefore, in order to treat the information, the transmission way and the mass storage medium of a broadband are needed. Then, research on reduction of the information by the data compression of pictures or sounds so-called compression coding came to be popular for the purpose of efficient use. Although the broadband communication can be used in wide area, narrow-band communication is also used. Then, efficiency of image coding has to be increased.

Video coding is the method of compressing by reducing the redundancy included in video. There are two kinds of the redundancy of video data. One is the spatial redundancy and the other is time redundancy. The former is mainly used still picture coding. JPEG (JointPhotographic Experts Group) which is the international standard system of still picture coding is the technique used very widely. And the algorithm called motion compensation prediction is used in the latter reduction. This is used in by MPEG (Moving Picture Experts Group) which is the international-standard system of video coding. It became possible to code and compress video data at high efficiency by these two techniques compared with the former. However, such algorithm had the problem in a decoding picture. Visual degra-

dation called block distortion is produced from process per block.

In order to solve this problem, we propose the moving picture coding with pixel motion compensation prediction. The wavelet coding which reduces block distortion is applied to video coding. Therefore, motion compensation prediction which is a process in a block is conventionally performed per pixel. Thereby, the problem of block distortion is removed. Moreover, various movement toward rotation, expansion reduction, etc. which were not able to respond conventionally can be extracted more correctly. Since correlation of data becomes high, it becomes possible to perform efficient compression. Therefore, it is thought that decoding which suppressed quality-of-image degradation is realizable in small amount of data. This thesis explains the algorithm of the proposal technique. Next, the validity is confirmed by comparing with MPEG which is a general video coding system by using a computer experiment.

### 2 MPEG

An MPEG standard is a standard of the multimedia coding for accumulation media, broadcast, communication, etc. It mainly consists of three regulations, such as the regulation on the coding method of a video signal, the regulation on the coding method of an audio signal, and for both integrated method.

Video data is realized by set of the still picture located in a line on the time-axis generally called a frame. MPEG performs compression coding by reducing those spatial redundancy and time redundancy. Reduction of

spatial redundancy is called the coding in a frame, and performed DCT (discrete cosine transform) quantization, and coding every  $8 \times 8$  [pixel] block. Moreover, reduction of time redundancy is called the coding between frames, and is performed using the technique of motion compensation prediction. This is extracting and treating the motion information on a certain domain in a picture in two near frames in time. More than it reduces only the redundancy in a frame, it is the technique of making it possible to reduce the redundancy of video. Generally, block matching is performed every  $16 \times 16$  [pixel] block. And the motion vector which is motion information is extracted. The general procedure of motion compensation prediction is shown below.

1. Extraction of moving vector by comparing frame for encoding with reference frame
2. Generation of the prediction picture by the motion vector and the reference frame
3. Generation of the picture of the difference by the difference of the prediction picture and the frame for coding
4. Coding of the motion vector and the picture of difference
5. Execution of 1. to the following two frames

The main coding parts of MPEG are realized with the combination of the coding between frames and inside of a frame. First of all as a basic procedure of MPEG, the frame of the beginning of video or the frame used as a starting point performs only the coding in a frame. These frames omit Intra-coded picture and are called I-picture. I-picture which had conversion-quantization performed here is reverse-changed by the local decoder, and is temporarily memorized by the frame memory. Next, frames other than I-picture perform the coding between frames which uses motion compensation prediction. There are P-picture and B-picture in these frames. The obtained prediction picture which is made based on a vector and it, and the picture of the difference of a target frame are coded. This reduces time redundancy and more efficient compression is performed.

### 3 Moving picture coding with pixel motion compensation prediction

TRIDE-2006-01, February 20, 2006 (ISSN 1880-8648)

In the coding using the block matching method represented by MPEG, the problem of producing block distortion which is visual lattice-like degradation was in the reconstructed video. On the other hand, in the field of still picture coding, the coding which reduces block distortion using wavelet transform and subband conversion as a technique has been advocated. Then, in order to control block distortion produced in video, we try to apply the coding (wavelet coding) which used wavelet transform. In order to control block distortion using wavelet, the motion compensation prediction which is used block matching is not efficient. Then, we propose the pixel motion compensation prediction which extracts the information on a motion in a pixel.

#### 3.1 Pixel motion compensation prediction

The reliability of matching is high since motion presumption by the conventional block matching method might use the macro block of  $16 \times 16$  pixel. Comparison of the value of a pixel will realise motion presumption in a pixel unit. However, this lacks in the reliability as a presuming method. Therefore, in order to obtain exact matching of a pixel, by the proposal technique, we use the recursive algorithm which narrows down a target from the rectangle range of a certain amount of size gradually. Moreover, in order to prevent a motion vector coming dispersing, a smooth portion is detected by the picture and processing suitable for the portion is performed. The algorithm of pixel unit motion compensation prediction is as follows.

1. A target block is made to match with a reference frame using the block of  $16 \times 16$ [pixel]. The variance of each pixel value is calculated, and when the value is below fixed, a block is not divided any more.
2. 4 division (it is called a mini block) of the target block is carried out.
3. To four of each, if the length of the neighborhood of a mini block is not 1 pixel, go to Step 3. When a target block becomes 1 pixel (it is called a target pixel), it is to Step 4.

4. It is search within the limits and a mini block is made into a mini block twice. A motion vector can be extracted thereby more correctly. At this time, the search range is the square domain extended by halves of a length of one side of a mini block on the four directions of the place which the mini block was referring to. A mini block is considered as a new target block, and it returns to Step 2.

5. It matches in the corresponding 1-pixel range of the pixel circumference using the block of 2×2 pixel. Then, the pixel which corresponded in the matched block is made into a reference pixel, and a motion vector is calculated.

### 3.2 Wavelet coding

Wavelet coding is used for the compression coding in the case of mainly inclining information for every frequency band. When especially energy inclines toward the low cycle, it is known that coding of very high efficiency is possible. There is the coding method called SPIHT (Set Partitioning In Hierarchical Trees) which is specialized in the tree structure of wavelet. This coding method is used for the coding part of the proposal technique. Correlation will become high supposing the 2-dimensional motion vector obtained by motion compensation prediction of a pixel unit is extracting the motion correctly. Therefore, information inclines toward lower frequency domain. Moreover, the absolute value of the pixel of the picture of the difference becomes very small. Therefore, both information is compressible at high efficiency using the above-mentioned wavelet coding.

### 3.3 Image coding experiment

In an experiment, two frames of the standard video sequence for assessment of are used for I-picture and P-picture, respectively. And coding and decoding were performed by the proposal technique. The example of a frame is shown in Fig. 1. Moreover, it compared with MPEG used as codec of Hi-Vision or standard quality-of-image television. And quality-of-image degradation of a decoding picture was evaluated numerically. PSNR



Fig. 1: Intersection

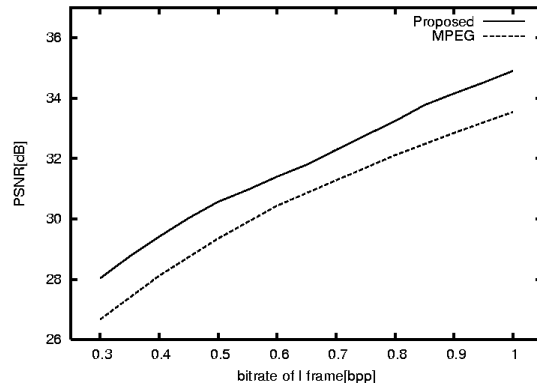


Fig. 2: PSNR for different bitrates (I frame)

is used for numerical assessment. PSNR is given by the following formulas here.

$$PSNR(dB) = 20 \log \frac{255}{MSE} \quad (1)$$

$$MSE = \sqrt{\frac{\sum_{x=0}^{W-1} \sum_{y=0}^{H-1} (f(x,y) - f'(x,y))^2}{WH}} \quad (2)$$

In coding of I-picture, the block distortion of the shape of a lattice produces MPEG which performs block processing in a decoding picture. However, block distortion is not produced by the proposal technique. By comparison by PSNR, it turned out in the amount of marks with the same proposal technique that a picture better than MPEG is obtained. This result is shown in Fig. 2.

In coding of P-picture, The motion vector of the x directions expressed by tone of before and after coding to Fig. 3 and 4 are shown. Moreover, the result of having performed comparison with MPEG by numerical assessment is shown in Fig. 5. In order to carry out assessment, the same bit length used for MPEG, I-picture and P-picture of the proposal technique is taken as the same quantity. This shows that P-picture is surpassing of MPEG at 0.51 [bpp]. However, the proposal tech-

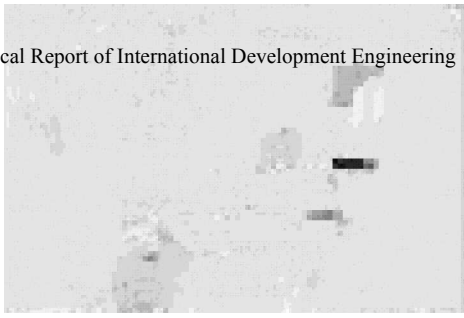


Fig. 3: Before encoding



Fig. 4: After decoding

nique has caused remarkable quality-of-image degradation in the domain which is carrying out regular form like the white line of a crossing paved road or a track in a target frame. This is because matching in a detailed portion is wrong and correlation of a motion vector becomes low in the case of pixel motion compensation prediction.

However, for complicated and high frequency domains, such as persons and characters, matching accuracy is high. Therefore, it turned out that degradation is reduced in such regions. If a motion vector can be correctly extracted by high correlation, distortion will de-

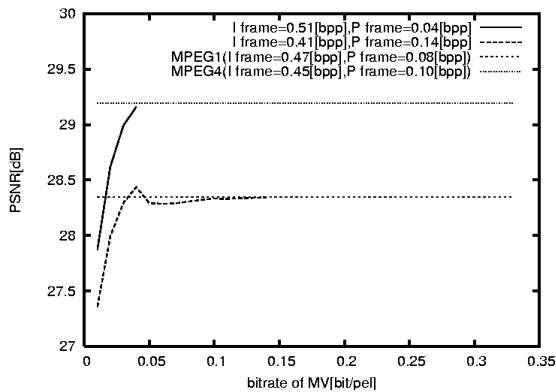


Fig. 5: PSNR for different bitrates (P frame)

crease. Therefore, motion detection method has to be progressed. TRIDE-2006-01, February 20, 2006 (ISSN 1880-8648)

Moreover, there is one more problem in this technique. It is that decoding takes time. The reason is for wavelet transform and SPIHT which codes coefficients to take time. The measurement result of the time concerning these is shown in Table 1. Considering that MPEG processes 30 frames in 1 second, it turns out that this has taken time overwhelmingly.

	SPIHT	wavelet
target frame	3.00	0.51
difference and MV	0.79	1.52

Table 1: decoding time [sec]

## 4 Conclusions

In this paper, the video coding method using pixel motion compensation prediction was proposed, and the computer experiment was conducted. Moreover, the advantage was shown by comparing with MPEG which is an international image coding standard. For future work, we have to develop the pixel motion detection method that provides more highly correlated motion vectors, and a more efficient coding method for the difference image. Furthermore, calculation speed have to be increased.

## References

- [1] Yoshinori Sakai, Toshiyuki Yoshida: "Image information encoding", Ohmsha, 2001.
- [2] Sadayasu Ono, Junji Suzuki: "Achievement method of comprehensible JPEG/MPEG2", Ohmsha, 1995.
- [3] Susumu Sakakibara: "Wavelet beginner's guide", Tokyo Electrical Engineering College Publications Service, 1995.
- [4] Amir Said, William A. Pearlman: "A New Fast and Efficient Image Codec Based on Set Partitioning in Hierarchical Trees", IEEE Trans. Circuits and Systems for Video Technology, vol.6, pp.243-250, June. 1996.

# Propagation Paths Measurement System for Electronic Toll Collection Systems (ETC)

Student Number: 04M18038 Name: Yumihiko ANNAKA Supervisor: Jun-ichi TAKADA

## ETC 電波伝搬パス同定システムの提案

安中 弓彦

自動料金収受システム (Electronic Toll Collection Systems, ETC) は、高速道路料金所において、停車することなく料金の支払いを無線通信によって行うシステムである。このシステムにおいて、マルチバスや隣接レーンからの漏洩などの不要波により、通信障害が発生する。問題が起きうる不要波抑圧のために、料金所では電波吸収体が設置されているが、吸収性能が経年劣化するため、その性能を随時確認出来るシステムが必要となる。このような背景から本研究では ETC の実信号を用い、実時間で電波の伝搬経路を同定できるシステムを提案する。このシステムにより同定された個々の伝搬経路に着目し、個々の劣化した電波吸収体の劣化度を評価することができる。また、伝搬経路を同定するアルゴリズムについても、種々の検討を行った。

## 1 Introduction

### 1.1 Background

Recently, the demand for short range wireless communications has been increasing.

In express ways, the intelligent transport systems (ITS), a new transportation system in order to resolve traffic problems by sharing information networks among people, road, and vehicles [1], is considered. ITS covers several development areas. One of them is the electronic toll collection systems (ETC).

The ETC is a wireless communication system between a transmitter at the toll gate and a receiver attached inside the car. This system executes the automatic payments without stopping at the toll gate.

### 1.2 Problems of radiowave propagation in ETC

In Japan, the ETC has some problems in system operations due to undesired waves via unexpected paths [2]. The undesired waves may cause the communication error, such as a double accounting, crashing to gate, or unexpected accounting.

The Japan Highway Public Corporation (JH) installs the radio absorbers on the whole surfaces of the toll gates to suppress the reflected waves, and also installs the transparent radio absorbers between adjacent lanes in order to suppress the inter-lane interference. However, the function of absorbers may be degraded by aging deterioration, so the function of the absorbers should be regularly maintained for the sustainable usage of the system. Then, the system that can evaluate the performance of the radio absorbers is needed. The propagation paths measurement system can do that. It is impossible to estimate the propagation path directly, instead, we estimate the angles of arrival (AOA) of individual paths and identify the scattering points. The system can resolve the paths to identify each individual contribution of the absorber.

In addition, the measurement at the gates in operation should be finished within a short period of time, because the long time measurements cause traffic congestion. Then, a real time measurement system is required.

For the real time measurement, it is beneficial that the system is installed on a car. When this car passes through a toll gate, it receives the ETC signal and records it.

### 1.3 Objective of the study

From several reasons mentioned in the subsection 1.2, the propagation paths measurement system using a multichannel receiver equipped with an array antenna is proposed in this thesis.

The objective of this study is to propose the propagation paths measurement system for the ETC that can be operated in a real time by using the real ETC signal. The system should be installed on a car, equipping the array antenna.

Also, this thesis develops a new AOA estimation scheme using only amplitude data.

## 2 System Architecture

This section introduces the format of the ETC signal and architecture of the hardware.

### 2.1 Format of the ETC signal

The ETC signal has been standardized by Association of Radio Industries and Businesses (ARIB) [3].

The wireless access method of the ETC signal is TDMA-FDD, which is a method that the frequency of uplink signal is different from that of downlink signal, and different time slots are allocated for different users.

Since the proposed system uses the downlink signal, the ETC signal in this thesis represents the downlink signal. The specification of the ETC signal is shown as Table 1. The modulation scheme is amplitude shift keying (ASK), which uses split-phase encoding.

### 2.2 Hardware of the proposed channel sounding technique

This subsection describes the hardware architecture of the proposed system. Two types of hardware are introduced. One measures both phase and amplitude of the received signal, The other does amplitude only.

Table 1: Specification of the ETC signal (downlink)

Multiple-access	TDMA-FDD
Frequency	5.795, 5.805GHz
Bit rate	1024kbps
Modulation	ASK
Flame length	Less than 900 bytes
Polarization	Right hand circular polarization

### 2.2.1 Hardware to measure phase and amplitude

Figure 1 illustrates the hardware to measure amplitude and phase of the received signal. The structure is similar to the conventional channel sounders, such as [4]. It consists of several heterodyne receivers, and all receivers share the common local oscillator (LO) in order to synchronize themselves for measuring phase.

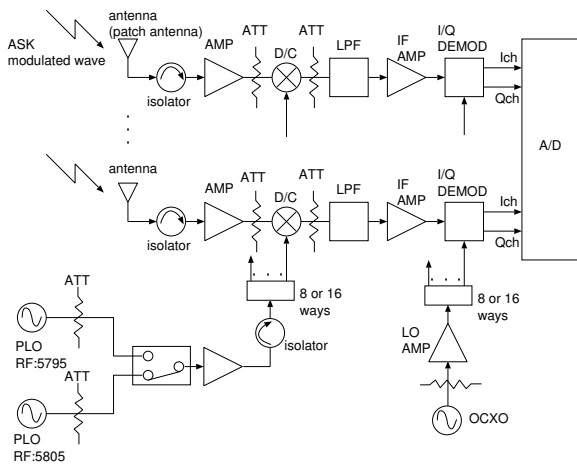


Figure 1: Hardware to measure phase and amplitude of the received signal

### 2.2.2 Hardware to measure only amplitude

Figure 2 illustrates the hardware to measure only amplitude of received signal. The system has a simpler structure than the system described in the section 2.2.1, because the synchronization among channels is not necessary. Therefore it costs lower.

Two types of the hardware architectures for measuring only the amplitude of the received signal can be considered. One is to use RF PIN switch and a single receiver, shown as Figure 2. The other is to prepare multiple receivers, just like Figure 1, but it is not necessary to use common LO.

## 3 AOA estimation scheme using only amplitude

In this chapter, two novel AOA estimation schemes using only the amplitude data of array output are pre-

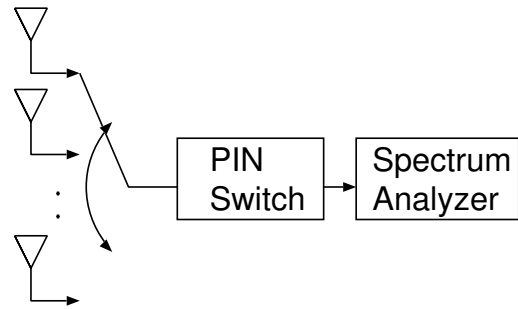


Figure 2: Hardware to measure only amplitude of the received signal

sented. The first scheme is to estimate phase by Hilbert transform and reconstruct received signal. The second scheme is to use the power spectrum to jointly estimate the cross spectra for all the AOAs simultaneously.

The parameters to be estimated are amplitude  $a_l$  and angle of arrival  $\phi_l$ , where  $l$  is the index of the path. Figure 3 shows the coordinates to define  $\phi_l$ . Let us assume a linear array aligned on  $x$  axis.  $H(x)$  denotes the voltage of the received signal at position  $x$ , and is expressed as

$$H(x) = \sum_{l=1}^L a_l \exp(jk_c x \cos \phi_l) \quad (1)$$

where  $k_c$  is a wavenumber  $2\pi/\lambda$ ,  $L$  is the number of arrival waves,  $\lambda$  is a wavelength.

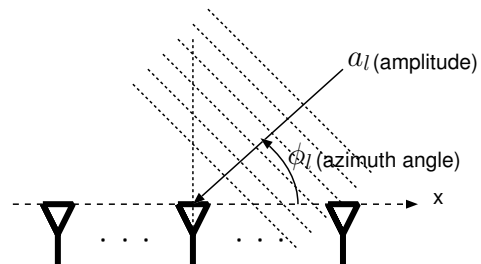


Figure 3: The definition of coordinate and parameters

### 3.1 Phase reconstruction scheme assuming maximum-phase system

This scheme requires the following 2 conditions.

- Measurement environment shall be line-of-sight (LOS).  
The arrival angle  $\theta_d$  of the strongest wave, i.e. direct wave shall be known prior to the signal processing.
- Two linear arrays shall be used.  
These base-lines shall not be in parallel, such as a V-shaped array depicted in Figure 4.

The key point of this algorithm is the phase estimation from  $|H(x)|$  with an assumption that  $H(x)$  is the

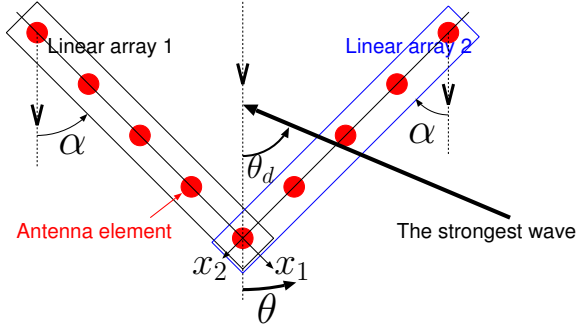


Figure 4: V-shaped array

maximum-phase. The estimation is carried out in the following steps:

1. Obtain the amplitude of  $|H_1(x_1)|$  by the linear array 1 defined in Figure 4, where  $H_1(x_1)$  is a received signal by the linear array 1, and  $x_1$  axis is an array axis of the linear array 1.
2. Estimate the corresponding phase of  $|H_1(x_1)|$  by using Hilbert transform by assuming  $H_1(x_1)$  is the maximum-phase [5],

$$\arg H_{m1}(x_1) = \Psi [\log |H_1(x_1)|], \quad (2)$$

where  $H_{m1}(x_1)$  is an estimated complex signal assuming the maximum-phase condition,  $\Psi[\cdot]$  denotes the Hilbert transform.

3. Reconstruct the received signal  $H_{m1}(x_1)$  by

$$H_{m1}(x_1) = |H_1(x_1)| \exp(j \arg H_{m1}(x_1)). \quad (3)$$

4. Transform  $H_{m1}(x_1)$  to the wavenumber space by the Fourier transform as

$$h_1(k) = \int_{-\infty}^{\infty} H_1(x_1) e^{-jkx_1} dx_1. \quad (4)$$

Where  $h_1(k)$  satisfies the causality in the space domain  $h_1(k) = 0; k < 0$ . Due to the limitation of the amplitude measurement, the waves that has negative and positive  $k$  cannot be distinct. The former is projected to the latter. The peak at  $k = k'(> 0)$  has an ambiguity whether its true peak is at  $k = k'$  or  $k = -k'$ .

5. Turn back the wavenumber spectrum  $h_1(k)$  at  $k = 0$ ,

$$h'_1(k) = \begin{cases} h_1(k) & k \geq 0 \\ h_1(-k) & k < 0 \end{cases} \quad (5)$$

6. Shift  $h'_1(k)$  so much as  $+k_c \cos(\theta_d - \alpha)$  along  $k$  axis,

$$h''_1(k) = h'_1(k - k_c \cos(\theta_d - \alpha)). \quad (6)$$

7. Transform  $h''_1(k)$  to the angular domain,

$$\tilde{h}_1(\phi) = h''_1(k_c \cos \phi), \quad (7)$$

$$\tilde{h}'_1(\theta) = \tilde{h}_1(\theta - \alpha). \quad (8)$$

8. Derive the angular spectrum  $\tilde{h}'_2(\theta)$  in the linear array 2 by the same process from 1 to 7.
9. Compare  $\tilde{h}'_1(\theta)$  with  $\tilde{h}'_2(\theta)$  and the peaks appeared in the same angles are determined as the true waves.

These procedures are shown as a flowchart in Figure 5.

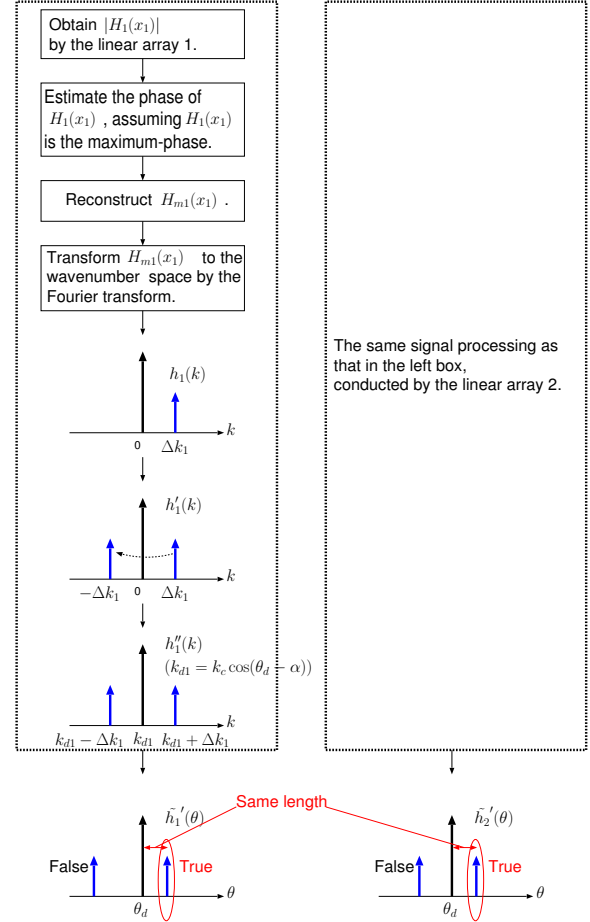


Figure 5: Flowchart of AOA estimation assuming the maximum-phase

### 3.2 Direct AOA estimation from power spectrum

The algorithm also requires the knowledge about the AOA of the strongest wave. The received spatial power spectrum  $P(x) = |H(x)|^2$  is

$$P(x) = \sum_{n=1}^L \sum_{m=1}^L a_n a_m^* \exp(j(k_n - k_m)x). \quad (9)$$

The Fourier transform of  $P(x)$  is

$$p(k) = \sum_{n=1}^L \sum_{m=1}^L a_n a_m^* \delta(k - (k_n - k_m)). \quad (10)$$

The peaks of  $p(k)$  are at  $\{\Delta k_{n,m} = k_n - k_m\}_{n,m=1}^L$ . The implementation flow of this algorithm is following:

1. Obtain the spatial power spectrum  $P(x)$  by array antenna.
2. Calculate  $p(k)$  by the Fourier transform of  $P(x)$ . The maximum  $k$  value of the peak position is  $\Delta k_{1,L}$ , assuming the condition  $k_1 > k_2 > \dots > k_L$ .
3. Choose any  $(L-1)$  peak positions of  $p(k)$  except  $\Delta k_{1,L}$ , and let the value of  $k$  at these chosen  $(L-1)$  peaks be  $\Delta \hat{k}_{2,L}, \Delta \hat{k}_{3,L}, \dots, \Delta \hat{k}_{(L-1),L}$ .
4. Estimate  ${}_L C_2$  peak positions  $\{\Delta \hat{k}_{n,m}\}_{n,m=1}^L$  by chosen  $(L-1)$  peak positions as
 
$$\Delta \hat{k}_{n,m} = \Delta \hat{k}_{n,L} - \Delta \hat{k}_{m,L} \quad (11)$$
5. Confirm if  ${}_L C_2$  peak positions estimated in the previous step match the original  ${}_L C_2$  peak positions.
6. If they match, they are final estimates of  $\Delta k_{n,L}$ . If not match, come back to step 3 and other  $L$  peaks are chosen again.
7. The maximum peak value among these  $L$  peaks corresponds to the peak of the direct wave, and its position can be  $k_M - k_L$ . Then, it is possible to estimate  $k_1, k_2, \dots, k_L$ .

From Shannon's sampling theorem, the length  $d$  between antenna elements must satisfy  $d < \lambda/4$ , which is half a length when the conventional AOA estimation algorithm applies. It means that the angular resolution is half of other conventional methods, because the array size is halved for the same number of elements.

### 3.3 Evaluation of proposed schemes

In this section, two AOA estimation schemes using only the amplitude of array output are presented.

The first one reconstructs the complex signal assuming the maximum-phase condition. Further mathematical investigation revealed that this algorithm can estimate AOAs if and only if all waves but direct wave arrive at only one side with respect to the direct wave. If more than 2 waves arrive at the both sides, AOAs can not be estimated correctly.

The second one uses the spatial power spectrum. This algorithm can estimate AOAs if all the real peaks can be distinguished from sidelobes. But the angular resolution of this algorithm is worse than the conventional one.

It is concluded that AOA estimation algorithm using only the amplitude is not feasible for the proposed application.

## 4 Conclusion

In this thesis, the radio propagation measurement system for the ETC is proposed. The system is installed

on a car, which equips the array receiver to estimate AOA.

AOA estimation algorithms using only amplitude are discussed. Although they are advantageous in the implementation of the hardware, their performance are poor. The conventional scheme utilizing both amplitude and phase was finally considered for the proposed application. The detail is not described in this abstract, but successive interference cancellation based space-alternating generalized EM (SIC-SAGE) [6][7][8][9] has been considered. The difficulty was the detection of the weak paths, which needs further investigation.

## References

- [1] Road Bureau ITS homepage.  
<http://www.mlit.go.jp/road/ITS/>
- [2] K. Haneda, J. Takada, T. Iwata, Y. Wakinaka, and T. Kunishima, "Experimental Determination of Propagation Paths for the ETC System - Equipment Development and Field Test," IEICE Trans. Fundamentals, Vol. E87-A, No. 11, pp. 3008-3015, Nov 2004.
- [3] "Dedicated Short-Range Communication System, ARIB Standard" Association of Radio Industries and Business.
- [4] K. Sakaguchi, J. Takada, and K. Araki, "A novel architecture for MIMO spatio-temporal channel sounder," IEICE Trans. Electron., Vol. E85-C, No. 3, pp. 436-441, Mar, 2002.
- [5] Y. Annaka, J. Takada, "Direction of arrival estimation based on amplitude-only array output," IEEJ Instrumentation & Measurement Society, IM-05-027, pp. 43-47, June, 2005.
- [6] J. A. Fessler, A. O. Hero, "Space-Alternating Generalized Expectation-Maximization Algorithm," IEEE Transactions on Signal Processing, Vol. 42, No.10, pp. 2664-2677, October, 1994.
- [7] B. H. Fleury, M. Tschudin, R. Heddergott, D. Dahlhaus, and K. I. Pedersen, "Channel Parameter Estimation in Mobile Radio Environments Using the SAGE Algorithm," IEEE Journal on Selected Areas in Communications, vol. 17, No. 3, pp. 434-450, March, 1999.
- [8] B. H. Fleury, D. Dahlhaus, R. Heddergott, Mtschudin, "Wideband Angle of Arrival Estimation Using the SAGE Algorithm," in Proc. IEEE Fourth Int. Symp. Spread Spectrum Techniques and Applications, Mainz, Germany, pp. 79-85, Sept, 1996.
- [9] B. H. Fleury, X. Yin, K. G. Rohbrandt, P. Jourdan, A. Stucki, "Performance of a High-Resolution Scheme for Joint Estimation of Delay and Bidirectional Dispersion in the Radio Channel," in Proc. IEEE 55th Vehicular Technology Conference (VTC 2002/Spring), pp. 522-526, May 2002.

# Analysis of Radio Wave Propagation in Highway Electronic Toll Collection Gate

Student Number: 04M18268 Name: Junsheng Lu Supervisor: Jun-ichi TAKADA

ETC 料金所における電波伝搬経路の解析

陸 俊聖

高速道路料金所の ETC ゲートにおいて、隣接レーンへの電波のもれにより、ETC ゲートの誤動作が問題として挙げられている。その問題を解決するために、本研究は ETC 料金所において実験を行い、電波伝搬経路の解析を行い、解決策を講じた。本研究において、測定に超広帯域信号 (UWB) が使われている。それは広帯域信号を用いて、測定系の時間分解能を向上させ、より詳細な経路の解析が可能となった。さらに、実験結果を補うように実験で測定できなかったポイントにおいてはコンピュータシミュレーションを用いて解析を行った。

## 1 Introduction

The Electronic Toll Collection System (ETC) has been developed in last several years. In March 2001, the ETC service was started. Until March 2004, ETC system had been implemented in more than 900 toll gates across the country [1].

Recently, there were some problems reported on the ETC system. One of the most reported problems is the electronic wave interference happened between two adjacent lanes. As the result, for example, the bar does not open even the toll is collected, or the the toll is collected twice when the automobile passes the toll gate. The reason of the interference is considered to be the reflection and diffraction of the electronic waves.

In this research, where the interference happened in ETC gate was found out by experiment and computer simulations.

## 2 Experiment

### 2.1 Preparing Experiment

In order to see where the measurement point would be set on, the preparing experiment, receiver signal level characteristics experiment, was conducted by Japan Highway. As the result, the receiver signal around 2 meters area is higher than  $-70$ dB, the threshold for malfunction. Hence, the ultrawideband array measurement was conducted around 2 meters area. The receiver signal level characteristics experiment result is shown in Figure 1.

### 2.2 Propagation Path Estimation Experiment

The propagation path estimation experiment was done on February 24th, 2005 in Akiruno toll gate in the central Tokyo Area. The measurement area includes toll gate, two lanes and one spraying lorry. Figure 2 shows the experiment environment.

The propagation path estimation includes two parts. One is Direction of Arrival (DoA) estimation and delay time estimation. Ultrawideband array measurement was conducted for propagation path estimation. The measurement system is shown in Figure 3.

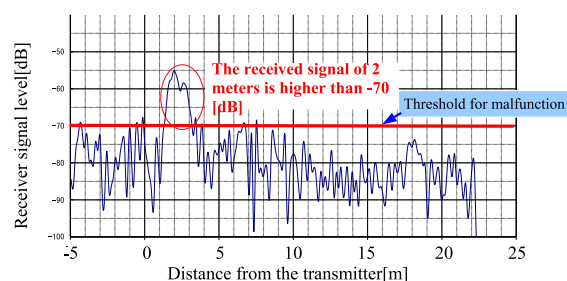


Figure 1: Receiver Signal Level Characteristics Experiment Result



Figure 2: Experiment Environment

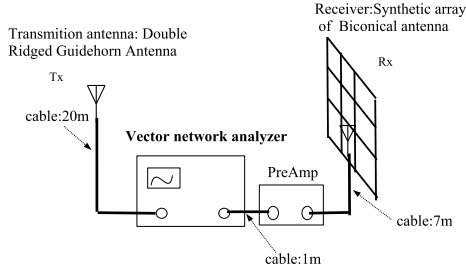


Figure 3: Measurement System

The transmission antenna is double ridged guidehorn antenna, and the receiver is synthetic array of biconical antenna. The synthetic array antenna is formed by a positioner and a biconical antenna. The size of the array antenna is  $7 \times 7 \times 2$ . The reason why array antenna was used is that the DoA can be estimated by array antenna. The experiment result is obtained from vector network analyzer. In this research, ultrawideband (UWB) signals was used because the time resolution is very high. The frequency band is from 3.1GHz to 10.6GHz, hence the delay resolution is 0.13ns.

### 2.3 Signal processing

Space-Alternating Beamforming (SABF) Algorithm is a proposed algorithm to do propagation path estimation [4]. The flow chat of proposed propagation path estimation algorithm is shown in Figure 4.

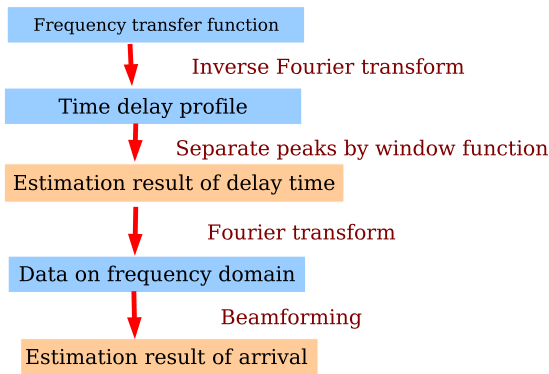


Figure 4: Flow Chat of Space-Alternating Beamforming(SABF)

The data obtained from vector network analyzer is frequency transfer function. The first step of signal processing is to obtain time delay profile after inverse Fourier transform. Each of the peak whose delay time

is longer than that of direct wave is considered to be the delay time of a path. Each peak should be cut out from the delay profile to avoid the interference from other waves. The window function is used to cut out the peaks from time delay profile. Here the delay time of a path is estimated.

The signals of separated peaks are once Fourier transformed to obtain the frequency charateresitcs. The last step of signal processing is beamforming. By using the Fourier transform result of separated peaks, the DoA of the waves can be estimated.

On the other hand, Sapce-Alternatin Generalized Ex-perctation Maximization (SAGE) Algorithm is a well used maximum likelihood based algorithm for angle and delay estimation. Comparing the result of proposed algorithm and that of SAGE algorithm implemented by another member of the group, the latter revealed to be better. Hence, the result by using SAGE algorithm was used in data analysis.

#### 2.3.1 Fourier Transform

Consider about the environment that there are  $L$  input waves whose complex amplitudes are  $(s_1, s_2, \dots, s_L)$ , delay times are  $(\tau_1, \tau_2, \dots, \tau_L)$ . Then the output of antenna  $X(f)$  is

$$X(f) = \sum_{i=1}^L s_i \exp(-j2\pi f \tau_i) \quad (1)$$

It inverse Fourier transform is

$$\begin{aligned} f(\tau) &= \int_{-\infty}^{\infty} X(f) \exp(j2\pi f \tau) df \\ &= \int_{-\infty}^{\infty} \sum_{i=1}^L s_i \exp(-j2\pi f \tau_i) \exp(j2\pi f \tau) df \\ &= \sum_{i=1}^L s_i \delta(\tau - \tau_i) \end{aligned} \quad (2)$$

But, time delay profile is a function to  $\delta$  only when the integral interval is infinite in the frequency domain. In the case of digital signal processing, the bandwidth for integration is limited, so the function is mordified as follows,

$$\begin{aligned} f(\tau) &= \int_{f_0 - \frac{\Delta F}{2}}^{f_0 + \frac{\Delta F}{2}} X(f) \exp(j2\pi f \tau) df \\ &= \sum_{i=1}^L s_i \int_{f_0 - \frac{\Delta F}{2}}^{f_0 + \frac{\Delta F}{2}} \exp(j2\pi f (\tau - \tau_i)) df \\ &= \sum_{i=1}^L s_i \Delta F \exp(j2\pi f_0 (\tau - \tau_i)) \text{sinc}((\tau - \tau_i) \Delta F) \end{aligned} \quad (3)$$

where

$$\text{sinc}(x) = \frac{\sin \pi x}{\pi x} \quad (4)$$

## 2.4 Experiment Result

In this section, the experiment result is introduced.

First of all, the direct path is found in experiment result. The azimuth angle, elevation angle and the delay time of experiment result is nearly as same as the theoretical value, calculated as direct wave. However, the path gain of experiment result is less than the theoretical value, shown in Table 3. The considerable value is a part of array was shadowed by gantry.

Table 1: Experiment Result of Direct Wave

	experiment result	theoretical value
Azimuth angle[deg]	156.2	154.29
Elevation angle[deg]	37.6	36.1
Delay time[ns]	21.64	21.84
Path gain[dB]	-82.4	-64.11

Except the direct path, there are three major single-bounce paths were identified. These three major single-bounce paths are reflected from the roof of driving seat, the sensor and the pole, respectively. The experiment result of single-bounce paths is shown in Figure 5 and Table 3.

The method to identify a single-bounce path is introduced followed. Assume that there is one direction of arrival has been estimated. If the reflection point can be found in the direction of arrival, the distance between reflection point and receiver can be calculated. By the same way, the distance between reflection point and transmitter can be also calculated. Hence, the delay time is known. If the delay time of experiment result is equal or very close to the theoretical value, a single-bounce path can be identified.

Table 2: Experiment Result of Single-Bounce Path

Reflection point	roof of driving seat	sensor	pole
Azimuth Angle[deg]	170.0	245.3	224.8
Elevation Angle[deg]	15.7	17.5	16.9
Path Gain[dB]	-88.0	-87.4	-86.5

On the other hand, if the delay time of experiment result is longer than that of theoretical value of single-bounce path, the estimation result can be considered to be a double or multiple bounce path. As the direction of transmission is unknown, then the double or multiple bounce path can not be uniquely identified. Some double or multiple bounce paths are also found in the experiment, which is shown in Figure 6.

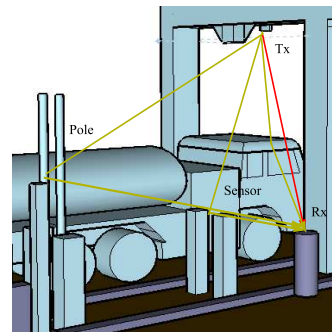


Figure 5: Experiment Result 1

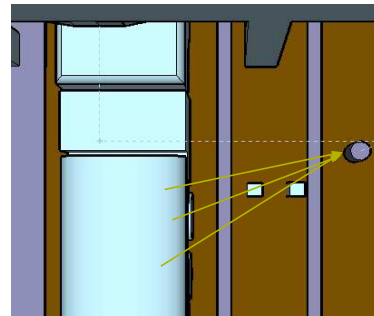


Figure 6: Experiment Result 2

## 3 Computer Simulation

For comparison, a commercial simulation named Raplab by Kozokeikaku Engineering Inc. [5] was used. Raplab is ray-tracing simulator. Geometrical optics (GO) and geometrical theory of diffraction (GTD) are deployed for scattering calculation. Reflection on flat surface and diffraction on edge are modeled [3, Page:745-773].

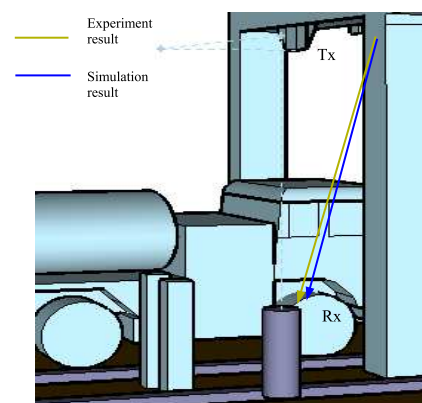


Figure 7: Simulation Result 1

The direct path is found in simulation result, shown in Figure 7. The azimuth angle, elevation angle and delay time of simulation result is nearly as same as those of experiment result. The path gain of simulation result

is close to theoretical value, greater than that of experiment result. The reason was explained previously.

Table 3: Comparison in Reflecion of Pole

	experiment result	simulation result
Azimuth angle[deg]	224.8	225.6
Elevation angle[deg]	16.9	17.3
Delay time[ns]	49.23	48.67
Path gain[dB]	-83.82	106.31

The single paths reflected from the roof of driving seat and the pole are also found in simulation result, shown in Figure 8. the path loss of simulation result is greater than that of experiment result. The considerable reason is modeling method of ray-tracing simulation.

Table 4: Comparison in Reflecion of Roof of Driving Seat

	experiment result	simulation result
Azimuth angle[deg]	170.0	171.3
Elevation angle[deg]	15.7	16.1
Delay time[ns]	32.12	31.80
Path gain[dB]	-88.82	106.68

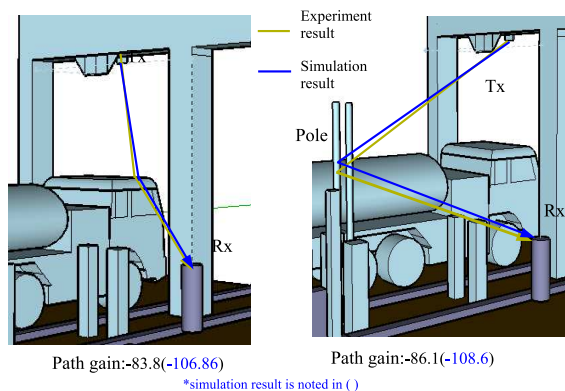


Figure 8: Simulation Result 2

In the ray-tracing simulation, the curved surface was approximately modeled as polyhedren. As the result, the reflected path in experiment becomes diffracted path in simulation, shown in Figure 9. The path loss of diffraction is much more than that of reflection (usually order of 20dB weaker than reflection). In this research, the reflection points of main single bounce paths are the roof of driving seat pole. All of these reflection points are on curved surface. Hence, the reflection happened in these reflection points became diffraction in the computer simulation. As the result, the path gain

of simulation result is greater than that of experiment result.

Curved surface is usually modeled in this way in ray-tracing simulation. However, it is cause great error, which is proved in this research once more.

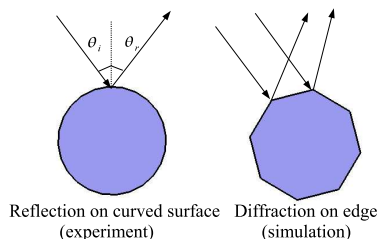


Figure 9: Simulation Analysis

## 4 Conclusion

Experiment has been done to find the paths which cause interference to the adjacent lane in ETC toll gates. Several dominant paths are identified.

On the other hand, simulation has also been done for comparison. The simulator could predict the major paths accurately, but the path gain values were erroneous as the reflection from the curved surface was modeled by the edge diffraction at the polyhedren.

In order to improve the simulator, the reflection of curved surface should also be accurately modeled by geometrical optics.

## References

- [1] Road Bureau ITS homepage. <http://www.mlit.go.jp/road/ITS/>
- [2] K.Haneda, J.Takada, T.Iwata, Y.Wakinaka, and T.Kunishima, "Experimental Determination of Propagation Paths for the ETC System - Equipment Development and Field Test" IEICE Trans. Fundamentals, Vol.E87-A, No.11 Nov 2004.
- [3] Constantine A. Balanis, "Advanced Engineering Electromagnetics," John Wiley & Sons, Inc., 1989.
- [4] Don H. Johnson, Dan E. Dudgeon, "Array Signal Processing Concepts and Techniques," P T R Prentice-Hall, Inc., 1993.
- [5] Raplab Homepage. <http://www.kke.co.jp/raplab/>

# Location Estimation for Wild Animals

Student Number: 04M18021 Name: Jun-ichi ABE Supervisor: Jun-ichi TAKADA

## 野性動物の生態調査用位置推定システムの開発

阿部 順一

今日、様々な開発に伴う野性動物の生態環境の破壊が問題になっている。開発の事前と事後で野性動物の生態環境がどのように変化したか、動物の行動を追跡調査する手段が求められている。現在、動物に小型送信機を取り付け、観測地点の周囲に八木宇田アンテナを備えた受信局を複数配置し、動物からの電波を受信、電波の到来方向を推定し、動物の位置を特定、追跡するシステムが存在する。しかし、電波の到来方向の推定を八木宇田アンテナの回転による電界強度の測定により行っているため、1回の観測に時間がかかり、追跡精度が良くない。本研究では、アレーアンテナを使用した信号処理技術を用いて、高速に方向推定を行うシステムの開発を行い、屋外実験にて評価を行った。

## 1 Introduction

Today, there are a lot of environmental problems. One such problem is the ecosystem of wild animals. Before and after developments, for example river improvement, there is a need to investigate the living area of wild animals. Telemetry system is one of the methods used for tracing animals' movement. A telemetry system uses a small transmitter and attaches it to wild animals. More than one receiver stations with Yagi-Uda antennas are set in the measurement field and the stations receive signals from the wild animals by rotating Yagi-Uda antenna and are searching for the strongest direction of electric field. Then these measured data are collected and the location of animals are estimated by triangulation[1].

Target animals are small wild animals, for example raccon dogs, rabbits, and fish. But it is difficult to use the conventional for fast-moving animals like birds because it takes more than two minutes to rotate the Yagi-Uda antenna and search for its direction, and the target animals may move during this period. The authors have proposed a fast direction of arrival (DOA) estimation system for wild animals by using an array antenna and signal processing. We have aimed at a fast estimation of direction.

In this paper, we first explain the system design and then describe the development of the receiver station and the preliminary experiment to certain the performance of the system.

## 2 Measurement Environment

Telemetry system are required in the following fields.

- grassland
- forest
- river (Figure 1)

At a river, target animals are fishes and birds. In our case, birds live in sandbanks. The measurement field is about a few hundred meters square because these target animals do not move long distances.

In these fields, there are a lot of obstacles e.g. vegetation, and the signal is scattered, diffracted, and reflected by them[2]. Therefore these environment make multipath propagation.



Figure 1: Test field : river (Chikuma river)

## 3 System Design

The proposed system has the following characteristics.

- A small transmitter is attached to wild animals
- More than one receiver stations which estimate direction of signal arrival are set around the measurement field.
- Wireless LAN network connects between receiver stations and data collection PC.
- Radio frequency band is 144MHz to be compatible with conventional system.

Figure 2 shows the whole system and the functions.

1. The transmitter radiates the signal.
2. Receiver stations detect the signal.
3. Receiver stations estimate DOA.
4. Receiver stations send the result to the data collection server using wireless LAN (IEEE 802.11b).
5. Data collection server receives the results.
6. Data collection server estimates the location of wild animals.

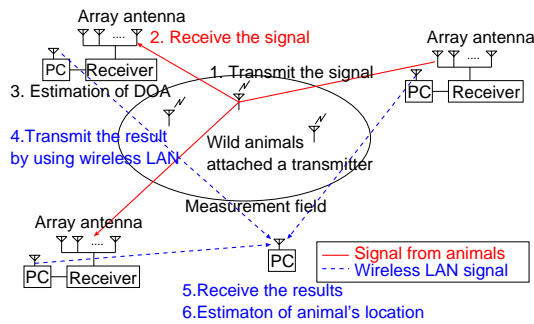


Figure 2: Proposed DOA system

## 4 Transmitter

The transmitter is the “MBFT-7A” which is a small size transmitter[3] manufactured by LOTEK.

This transmitter emits a pulsed signal to save battery power at the frequency band at about 144MHz.

## 5 Receiver station

The receiver station has an array antenna, 8 channel (ch) I/Q receiver, 16ch amplifier, synchronous sampling unit and PC with A/D board and DOA estimation software as depicted in Figure 3.

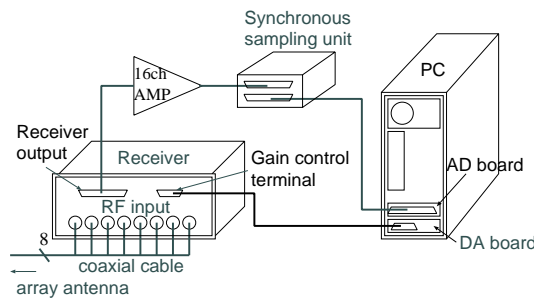


Figure 3: Receiver station

### 5.1 Array antenna

We used the HB9CV type antenna for the array element, which is commonly used among amateur radio. It consists of two linear antenna elements and is unidirectional in order to suppress the influence of multipath from the rear of the array antenna.

### 5.2 Receiver

The receiver is equipped 8 RF input channels (0-7ch). This receiver has a common local oscillator because DOA estimation algorithm requires the phase difference between channels. If each channel has an independent local oscillator, phase information is lost. This receiver converts the signal down from 144.700-144.900MHz to DC-100KHz, and outputs the I/Q signals. According to the specifications of the receiver, input signal level

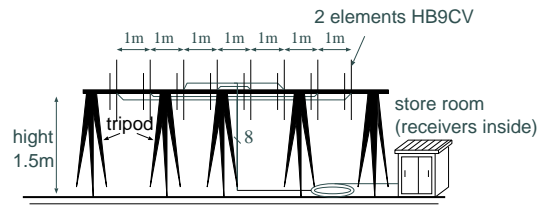


Figure 4: 8 elements of array antenna

must be in the range from  $-50\text{dBm}$  to  $-100\text{dBm}$ . Output signal level must be less than  $250\text{mV}$ .

### 5.3 Baseband Amplifier

The output signal voltage of the receiver is less than  $250\text{mV}$ , but maximum input voltage range of A/D converter is  $10\text{V}$  for sufficient data precision, the output signal of the receiver shall be amplified. Since the output channels of the receiver are 16, a 16ch precise amplifier was fabricated (Figure 5).

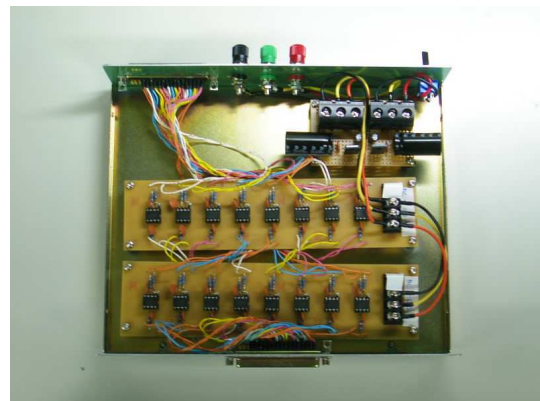


Figure 5: 16ch amplifier

Figure 6 shows an amplifier circuit for a single channel. This circuit is an inverting amplifier and the magnification of the amplifier is 39. Operational amplifier OP37G was used. It has wide-band, low noise and precision characteristics.

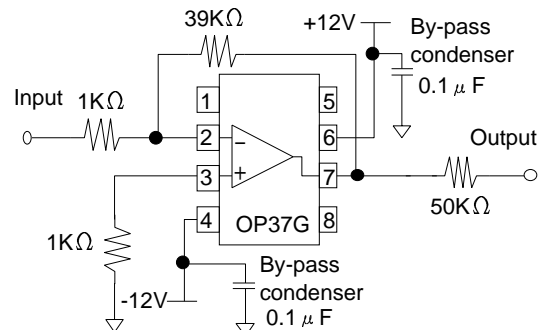


Figure 6: Amplifier circuit

## 5.4 A/D converter and synchronous sampling unit

The A/D converter board converts the output analog signal from the 16ch amplifier to 14bit digital data. I used a commercial A/D converter board “AD681-PCF” manufactured by Microscience.

This A/D converter board has 16 channels but it does not have a function of synchronous sampling because it has only a single channel of A/D converter, and it uses a multiplexer and samples all channels when A/D converter has to sample more than one channel. An optional unit “synchronous sampling unit (SHU-516)” is available and between amplifier and A/D converter board, it can realize pseudo-synchronous sampling.

## 5.5 DOA Estimation Algorithm

There are several types of DOA estimation algorithms. Among them, beamformer and MUSIC algorithm were chosen.

Beamformer algorithm is the most basic DOA estimation algorithm. It is equivalent to the Fourier transform of the array response. This algorithm does not provide super-resolution, but this algorithm may be more robust than subspace-based algorithms such as MUSIC, if the measurement field is a multipath environment.

MUSIC algorithm is a well-known subspace-based super-resolution DOA estimation algorithm. If the measurement field is open and multipath is negligible, super-resolution algorithm can estimate more precise than beamformer algorithm. However if the coherent signals e.g. multipath waves arrive, the spatial smoothing preprocessing(SSP) scheme should be introduced to decorrelate the signals[4].

## 6 Calibration

Array output vector from  $M$ -element array antenna can be modeled as

$$\mathbf{x}(t) = \tilde{\mathbf{a}}s(t) + \mathbf{n}(t). \quad (1)$$

where  $\tilde{\mathbf{a}} = \mathbf{K}\mathbf{a}$ ,  $s(t)$  is an arriving signal with arrival angle  $\theta$ ,  $\mathbf{n}(t)$  is an  $M \times 1$  noise vector,  $\mathbf{a}$  is a steering vector which is expressed as the equation below.

$$\mathbf{a}(t) = \begin{bmatrix} 1 & \exp\left(-j\frac{2\pi d \sin \theta}{\lambda}\right) & \cdots \\ \exp\left(-j\frac{2\pi d \sin \theta}{\lambda}(M-1)\right) \end{bmatrix}^T. \quad (2)$$

$d$  is distance between each antenna element.  $\mathbf{K}$  is an  $M \times M$  error matrix which arise for the impairment of RF channels. The errors cause the phase and amplitude mismatch between channels.

Then the errors have to be cancelled by calibration techniques. The calibration matrix  $\mathbf{C}$  is defined as  $\mathbf{C} = \mathbf{K}^{-1}$ [5].

If the calibration matrix  $\mathbf{C}$  is applied the measured signal, the calibrated signal can be denoted by

$$\tilde{\mathbf{x}} = \mathbf{C}\mathbf{x}(t) = \mathbf{C}\tilde{\mathbf{a}}s(t) + \mathbf{C}\mathbf{n}(t). \quad (3)$$

The calibration matrix  $\mathbf{C}$  can be written as

$$\mathbf{C} = \text{diag} \left[ \frac{\alpha_0}{\alpha_1} \exp(j(\phi_0 - \phi_1)), \cdots, \frac{\alpha_0}{\alpha_M} \exp(j(\phi_0 - \phi_M)) \right], \quad (4)$$

where  $\alpha_0, \cdots, \alpha_M$  and  $\phi_0, \cdots, \phi_M$  refer to as the signal amplitude and phase associated at each array element.

## 7 Field test

Field test was held at Public Works Research Institute (PWRI). A photo of the actual measurement field is shown in Figure 7.



Figure 7: Test Field

We set the 7-element array antenna and a transmitter as Figure 8 since one channel of the receiver was broken at the field test. When the broadside direction of the array antenna is set as 0 degree, we measured the signal from a transmitter in 7 directions, namely,  $-60, -40, -20, 0, 20, 40$  and  $50$  degrees. The distance between Tx and the center of the array antenna is 40m.

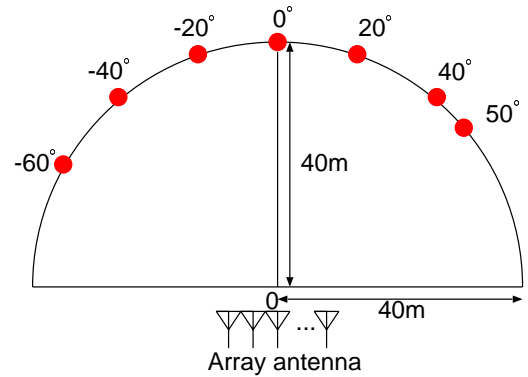


Figure 8: Arrangement measurement

### 7.1 Level diagram

Figure 9 is the level diagram of this measurement. It shows the receiving power margin is 55dB.

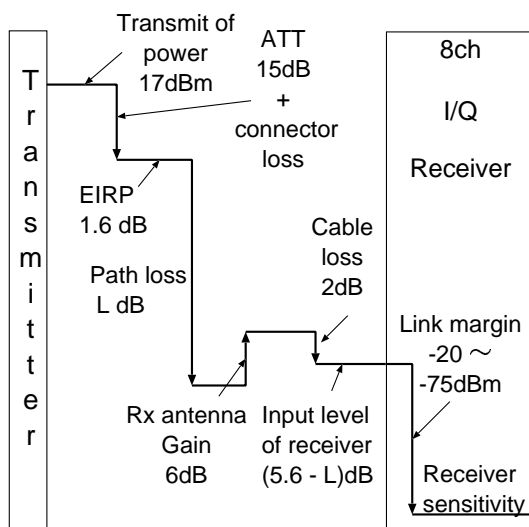


Figure 9: Level diagram

### 7.2 Measurement result

Measurement results are shown in Table 1. The 0 degree measured data were used as the calibration data. The errors between actual angles and estimated angles are less than 3 degree except -60 degree case. In -60 degree case, the estimation error was the biggest. It seems that the error is due to the directivity of HB9CV. A HB9CV has 3dB beamwidth of  $\pm 50^\circ$ , and the antenna is not suitable for estimating angles outside this range.

The dynamic range of the MUSIC spectrum is about 10dB without SSP as shown in Fig 10. But if SSP is applied, it is improved 20 dB. It seems that error of measurement settings e.g. location of array element is randomized by SSP. Detail investigation is required.

Table 1: Measurement result

	MUSIC	MUSIC with SSP
Tx point (degree)	Estimation (degree)	Estimation (degree)
-60	-52.91	-52.87
-40	-39.63	-39.64
-20	-17.59	-17.82
20	18.14	18.06
40	38.00	37.44
50	48.64	48.03

## 8 Conclusion

The DOA measurement system for real time tracing of wild animals' movement was built and was checked in experiment at the open space. This system can not set permanently. And it is required the many improvements e.g. automatic calibration and handling of multipath environment. But it is the first time to show the possibility of real time tracing of wild animals' movement.

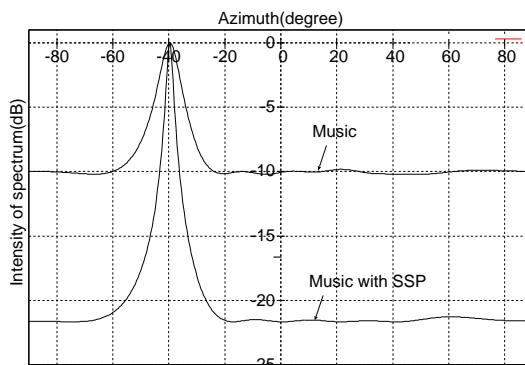


Figure 10: MUSIC spectrum

## References

- [1] M. Denda, K. Shimatani, J. Kukita and S. Iwamoto: "Development of Multi Telemetry Sytem for Monitoring ecosystem of wild animals", Public works research institute.
- [2] NC Rogers: "A Generic Model of 1-60GHz Radio Propagation through Vegetation - Final Report", QinetiQ, 2002.
- [3] Lotek Fish & Wildlife Monitoring Systems, "MBFT Pulsed Radio Tags" <http://www.lotek.com/mbft.htm>
- [4] N. Kikuma: "Adaptive signal processing using array antenna", Science and Technology Publishing Company Inc, 1998.
- [5] G. Sommerkorn, D. Hanpicke, R. Klukas, A. Richter, A. Schneider, R. Thoma, "Reduction of DOA estimation errors caused by array antenna imperfections," in 29th European Microwave Conference, Oct. 1994.

# Investigation of the Wave Scattering Characteristics by using Physical Optics Approximation

Student Number: 04M18297 Name: Navarat LERTSIRISOPON  
Supervisor: Jun-ichi TAKADA

## Abstract

The structure of some scatterer objects in the propagation channel such as signboards and metallic plates are modelled to examine the effects of scattered fields or waves at the observer point. The objective of my research is to utilize Physical Optics (PO) approximation to investigate in more detail the characteristics of wave scattering using a simulation model and to predict the radio wave scattering characteristics. Moreover, polygon meshes are introduced to model scatterer constructions including 2D and 3D geometrical objects and to simplify the complex calculation of the induced current for examining the scattered field. This approach is called “PO using polygon mesh”.

## 1 INTRODUCTION

Propagation mechanisms in urban areas are basically wall reflections, building edges and roof diffractions. Some measurement results however show that scattering from some objects in the environment can have strong impact on the urban propagation channel [1]. Careful analysis of these results reveals that these scattered objects, which can be any surrounding metallic object, such as signboards, street lights, traffic lights and traffic signs, are involved in transferring transmitted signals to the receiver [2].

One of these propagation mechanisms is called scattering, which can be calculated from the electromagnetic fields on the scatterer surface. In the case of a conducting body, the induced currents on the surface must be determined or approximated in order to compute the electromagnetic fields scattered from the scatterer. In [3], PO approximation is utilized to simulate the induced surface current to handle non-specular scattering. The simulation results showed good agreement with the experimental results; therefore, these led the author to continue further studies about the scattering from surrounding objects in urban areas by utilizing the PO approximation method.

## 2 PHYSICAL OPTICS ALGORITHM

PO is a type of high frequency approximation method, meaning the surface of the object is much bigger than the wavelength of the signal. From the field equivalence theorem, the field at an observation point  $P$  is exactly expressed as the sum of contribu-

tions from the source  $\mathbf{E}^i$  and from scattered field  $\mathbf{E}^s$  which can be determined by the equivalent electric and magnetic surface currents  $\mathbf{I}$  and  $\mathbf{M}$  respectively on the surface  $S$  [4].

$$\begin{aligned} \mathbf{E} &= \mathbf{E}^i + \mathbf{E}^s \\ &= \mathbf{E}^i - j\omega\mu\mathbf{A} - j\frac{\nabla\nabla\cdot\mathbf{A}}{\omega\varepsilon} - \nabla\times\mathbf{B} \end{aligned} \quad (1)$$

where,

$$\mathbf{A} = \frac{1}{4\pi} \int_S \mathbf{I} \frac{e^{-jkr}}{r} dS \quad (2)$$

$$\mathbf{B} = \frac{1}{4\pi} \int_S \mathbf{M} \frac{e^{-jkr}}{r} dS \quad (3)$$

are electric and magnetic vector potentials and  $r$  is the distance between the integration point and the observer. Time-harmonic wave is assumed and  $e^{j\omega t}$  omitted. Furthermore,  $\varepsilon$  and  $\mu$  denote the permittivity and permeability of free space, respectively, whereas  $k = 2\pi/\lambda$  is the propagation constant in free space.

In PO approximation, the induced electric current is approximated as the scatterer is replaced by an infinite ground plane, which is tangential to the surface of the scatterer at the point of interest. When the scatterer is a perfect electric conductor (PEC), then the simple image theory is applied. Only the tangential component of magnetic field is doubled, while the normal component is cancelled. The equivalent electric current  $\mathbf{I}$  is given by  $2\hat{n}\times\mathbf{H}^i$  on the illuminated part of the surface  $\mathbf{S}_l$  while on the shadowed part  $\mathbf{S}_s$  of the scatterer, the current  $\mathbf{I}$  is zero,  $\mathbf{H}^i$  is the unperturbed incident magnetic field. For PEC,  $\mathbf{M}$  is always 0, as the tangential

electric field vanishes on the PEC surface. Then

$$\mathbf{I}^{PO} = 2\hat{n} \times \mathbf{H}^i \text{ for illuminated part } \mathbf{S}_1; \quad (4)$$

$$\mathbf{M}^{PO} = 0 \quad (5)$$

In this case, the field in PO is simplified as

$$\mathbf{E} = \mathbf{E}^i - j\omega\mu\mathbf{A} - j\frac{\nabla\nabla \cdot \mathbf{A}}{\omega\varepsilon} \quad (6)$$

Furthermore, if the observer  $P$  is in the far field region of the scatterer, the second term of the scattering field just eliminates the radial component of the first term and the electric field is expressed by using the unit vector  $\mathbf{r}_0$  towards the observer as follows:

$$\mathbf{E} = \mathbf{E}^i - j\omega\mu\mathbf{A} \times \hat{\mathbf{r}}_0 \times \hat{\mathbf{r}}_0 \quad (7)$$

### 3 POLYGON MESHED METHOD

To represent the data structures of scatterers and simplify the calculation, the scatterers should be modelled by polygon structures. Although there are a variety of algorithms available to generate this kind of structure, the triangulation of a polygon is utilized in this research since the curved surfaces being subdivided into triangles can be handled efficiently. The triangulation algorithm is a fundamental operation in computational geometry under the assumption that the polygon is simple, i.e., that the vertices of the polygon are the only points of the plane that belong to two edges, and that no point of the plane belongs to more than two edges.

#### 3.1 Two-Dimensional Geometry

By using a toolbox in MATLAB, the following sequence covers the steps to generate the triangulation and applied in the PO algorithm.

1. Open a drawing tool to draw the basic 2D geometrical objects (circle, rectangle, ellipse or polygon) as shown in Fig.1.

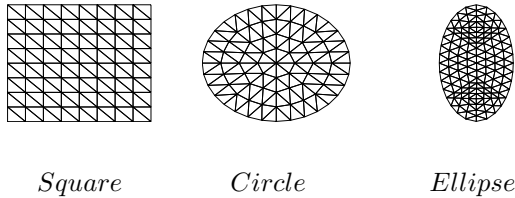


Figure 1: Varieties of scatterer shapes in 2D geometry

2. Initialize the triangular mesh which consists of a Point matrix, an Edge matrix, and a Triangle matrix. In the mesh, minimal regions are triangulated into sub domains, and border segments and boundary segments are broken up into edges.

3. Rearrange all triangular meshes matrix to calculate the normal vector ( $n$ ) at the center point of each triangular mesh by defining two vectors,  $\mathbf{C}$  and  $\mathbf{D}$ , from 3 points ( $P_1$ ,  $P_2$  and  $P_3$ ) of each triangle which is described below.

$$\begin{aligned} \mathbf{C} &= P_2 - P_1 \\ \mathbf{D} &= P_3 - P_1 \\ \text{normal vector } n &= \frac{\mathbf{C} \times \mathbf{D}}{|\mathbf{C} \times \mathbf{D}|} \end{aligned} \quad (8)$$

4. Substitute the normal vector ( $n$ ) in the PO algorithm to obtain  $\mathbf{I}$  and get the scattered field.

#### 3.2 Three-Dimensional Geometry

To generate the triangulation in 3D geometrical objects, the author mapped the triangulation of 2D geometrical objects by adding the height as shown in Fig. 2, while the other sequences are still the same as described in subsection 3.1.

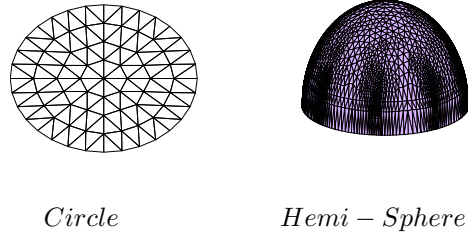


Figure 2: Half sphere produced from circular disk

According to this characteristic, not only the complex scatterer shapes can be represented but the surface integration can also be simplified as the summation of each small area when the size of each triangle mesh is suitable and small enough. Therefore, the surface integration can be represented as the small area summation which is:

$$\mathbf{A} = \frac{1}{4\pi} \sum \mathbf{I} \frac{e^{-jkr}}{r} \Delta s \quad (9)$$

$$\mathbf{B} = \frac{1}{4\pi} \sum \mathbf{M} \frac{e^{-jkr}}{r} \Delta s \quad (10)$$

Moreover, to determine the appropriate size of the polygon mesh, a polygon mesh ratio defined by the following relationship was used.

$$\text{Polygon Mesh Ratio} = \frac{\text{avg}(\text{polygon area})}{\lambda^2} \quad (11)$$

### 4 SIMULATION AND DISCUSSION

To evaluate and demonstrate the effectiveness of using polygon meshes applied in PO, the following simulation parameters were conducted with simulation conditions shown in Table 1.

Table 1: Simulation parameters

Scatterer shape	Square
Size	0.09 m. x 0.09 m.
Frequency	5.2 GHz
Observer distance	20 meters
Transmitted power	40 dBm
Incident $\theta_i$	$60^\circ$
Incident $\phi_i$	$30^\circ$
Scatterer $\phi_s$	$210^\circ$
Polarization	Parallel

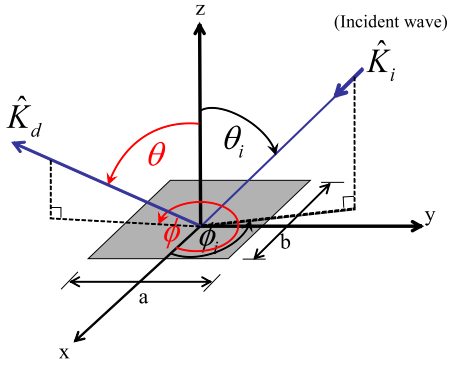


Figure 3: Plane wave scattering from a square plate

Figure 3 shows the scattering of a plane wave by a rectangular plate sized  $a \times b$  in the x-y plane. The incidence propagating in  $\hat{\mathbf{K}}_i$  is coming from  $(\theta_i, \phi_i)$  and has the parallel polarization (only  $\theta_i$  component) while the observer is in the direction of  $\hat{\mathbf{K}}_d$  or  $(\theta, \phi)$ .

Figure 4 illustrates how the polygon mesh method can construct the scatterer when the size of each polygon mesh is varied by the polygon mesh ratio and Fig. 5 illustrates the magnitude of scatterer fields from the rectangular plate with respect to the elevation angle at the observer point. From these figures, it can be seen that when the polygon mesh ratio decreases, the sidelobe also decreases. However, all of them still can construct the signal main reflection beam. As a result, this can be inferred that the signal sidelobe alters proportionally to the polygon mesh ratio.

However, to justify whether the polygon mesh method can be applicable in PO Approximation, we need to compare the results with the PO analytical or conventional model as described in [4]. From this reason, the comparison between PO using polygon mesh method and PO analytical method is illustrated in Fig. 6. A high accuracy for both PO cases in the direction of main radiation ( $\theta = 60^\circ$ ) is observed. This reveals that the PO polygon mesh can perform as well as the PO analytical one. Since the characteristics of PO treats only the portion of the scatterer that can be observed by the source (illu-

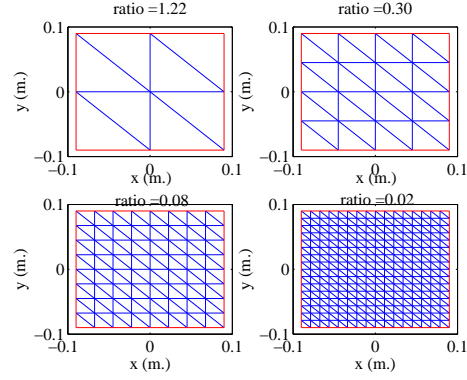


Figure 4: Varying polygon mesh ratio in square plate

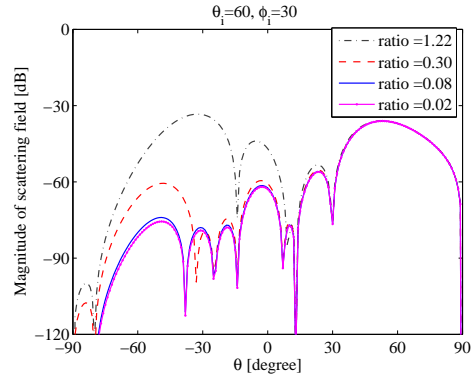


Figure 5: Scattering field corresponding to polygon mesh ratio using PO polygon mesh

minated portion), the simulated scattering field will deviate from MoM as the observer moves away from the illuminated portion and into the shadowed region.

In the real environment, not only the simple construction shape can represent all the obstructions in the channel model, for example, traffic light and its pole, car, etc., the 3D objects should also be simulated in order to implement this algorithm in the real propagation measurement. Therefore, the simulation of the finite cylinder and sphere, which are common 3D objects, were conducted. Nevertheless, only the analytical solution of the scattering from a sphere [5] is known so that PO using polygon mesh for 3D geometrical cases can be evaluated by comparing its output with this analytical result.

The structure of sphere is modelled whose radius is  $5\lambda$  (0.2885 m.) and simulated under the condition that frequency is 5.2 GHz and the incident plane wave impinged at the bottom of the sphere ( $-z$  axis) and with the observer at  $\phi = 0^\circ$ , as shown in Fig 7. In simulating the scattering field, only half of the sphere was used, since in PO, only the illuminated part can be seen which corresponds to half of the sphere centered on the incident wave. To evaluate the accuracy of this approach, the simulation is conducted and compared with the analytical model as shown in Fig.8.

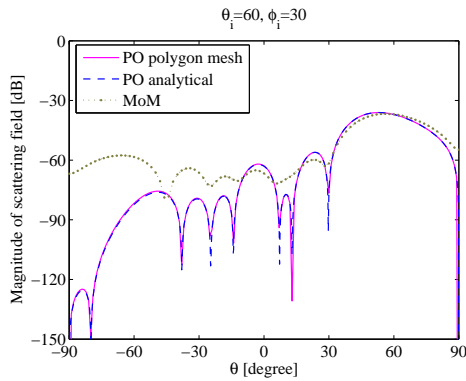


Figure 6: Comparing scatterer fields of PO using polygon mesh method with PO analytical model and MoM

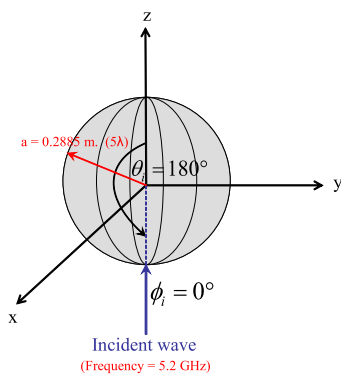


Figure 7: Plane wave scattering from a sphere

The well-known characteristic of PO, in which the accuracy is expected in the region of main direction but degraded in the shadow region was observed in both 2D and 3D geometrical cases. Moreover, a polygon mesh ratio of 0.1 is sufficient for the scattering field to converge.

## 5 CONCLUSION

This study introduced the polygon mesh method applied in PO approximation not only to model the surrounding objects but also to simplify the complex calculation of the induced current in order to examine the scattered field. This approach was called “PO using polygon mesh”.

Simulations of the scattered field from 2D and 3D geometrical objects by either varying the incident directions or varying the observer directions were conducted to evaluate and demonstrate the effectiveness of polygon meshes applied in PO approximation. The relationship between signal wavelength and average area of polygon mesh called “Polygon mesh ratio” is also stated to indicate the proper size of polygon mesh providing a reasonable scattered field.

Furthermore, this approach is verified by comparing it to the PO analytical model and the numer-

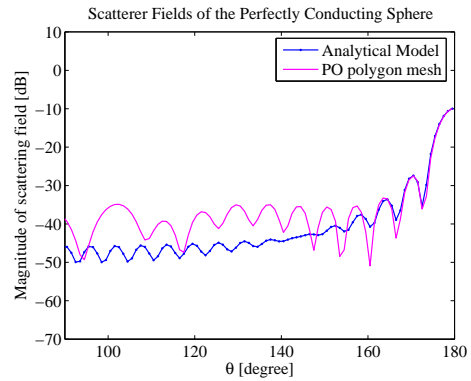


Figure 8: Comparison of the scattered fields from PO polygon mesh and analytical model

ically accurate method of moments (MoM) in the 2D geometrical case. For the 3D geometrical case, the analytical solution of the sphere is used to verify the accuracy of this approach. From the results of both 2D and 3D cases, PO analytical and PO using polygon mesh have great agreement with each other; however, they can perform high accuracy only in the region of main direction and is slowly degraded in the shadow region as a result of PO’s simplification. Therefore, further investigation should be considered to enhance this approach for utilization in the real environment.

## References

- [1] Mir Ghoraiishi, Jun-ichi Takada, and Tetsuro Imai, “Identification of the Scatterers in the Urban Microcell Environments,” *Technical report of IEICE, WBS2004-164, AP2004-345, RCS2004-432, MoMuC2004-215, MW2004-342 (2005-03)*.
- [2] Mir Ghoraiishi, Junichi Takada and Tetsuro Imai, “Investigating Dominant Scatterers in Urban Mobile Propagation Channel,” *IEEE International Symposium on Communications and Information Technologies 2004 (ISCIT 2004), Oct., 2004 (Sapporo, Japan)*.
- [3] Hary Budiarto, Kenshi Horihata, Katsuyuki Haneda, and Jun-ichi Takada, “Experimental Study of Non-specular Wave Scattering from Building Surface Roughness for the Mobile Propagation Modeling,” *IEICE Transactions on Communications, vol. E87-B, no.4, pp. 958-966, Apr. 2004*.
- [4] I. Yamashita, Eikichi, “*Analysis Methods for Electromagnetic Wave Problems. - 2Rev.ed.*” Artech House Inc.1990.
- [5] Nagayoshi Morita, Nobuaki Kumagai, Joseph R. Mautz, “*Integral Equation Method for Electromagnetics*” Artech House Inc, 1990.

## Sorption and flushing characteristic of heavy metal ion response to sand

Student Number : 04M18015 Name : Masatoshi AOKI Supervisor : Hideki Ohta

### 砂質土に対する重金属イオンの吸着洗浄特性

青木雅俊

社会環境の変化と土壤汚染対策法が施行されたことにより、安価な地盤浄化技術の開発がますます強く求められている。そこで、本研究では、「小規模でありながらも経済的な原位置での汚染地盤浄化技術の実用化」を目的として、汚染された砂質土の吸着浄化実験を行った。東京都大田区の砂を用いて、粒度分布を求め、粒径が小さい粒子が土粒子全体の表面積のほとんどを占めていること示した。その後、砂質土の汚染物質に対する吸着・洗浄特性について調べた。

#### 1 Introduction

It has been two years since soil contamination countermeasures law becomes effective. The purpose of this law is to protect the citizen's health. The most important change of this law is responsible. Before 2003 February, the responsible was usually the person who contaminates lands, however now the responsible is the person who owns the land.

The influence of this law, when small and medium size companies close their factories due to economic difficulty, companies must clean the land, if their land is contaminated. However, the cost is so high that they can not sell their land. As a result, the land remains unused. Because of this reason, to clean more cheaply is necessary. Therefore cheap soil wash system in practice is needed. In Ohta Lab., Suga(2005) developed in-situ wash system which is economical and small in scale. In this study, he converted a part of existing boring machine which can excavate by way of running water from tip and circulate stirred water.

In this study, sieve test and sedimentation analysis is carried out and the relationship between grain size and surface area on soil is calculated. The result of sorption and flushing experiment is carried out to know the condition when soils and water are stirred. In this experiment, Bio-surfactant is used. The effect is considered

#### 2 Concept of soil wash system

The soil wash system used in this study focuses that contaminants adhere to surface area of soil particles. The soil wash system eliminates only fine soil deposit. Because fine soil particles consist of only small fraction of total soil weight, it is very easy to eliminate. Fine soil particles consist most of soil surface area.

Therefore, the majority of contaminants stay in fine soil particle's surface area. Eliminating fine soil particles, majority of contaminants can be eliminated from the contaminated ground with relatively small cost.

The following is the concept of soil wash system in this study.

Fig. 2-1 shows that contaminant soils exist in the sandy ground.

Fig. 2-2 shows that a cylinder is set on the ground and a hole is drilled into ground surface area. During drilling, water is filled in the hole; this action means not to collapse the side wall of hole.

Fig. 2-3 shows that the soil particles and water with contaminant is stirred in the hole. In this time, contaminants adhere to the surface area of soil particles because contaminants and soil particles have electric charge.

Fig. 2-4 shows that the hole is left for certain amount of days. Finally, the soil particles sedimented as shown in Fig. 2-5.

Fig. 2-6 shows that fine soil particles in the upper part are taken away after sedimentation, lots of contaminants are eliminated.

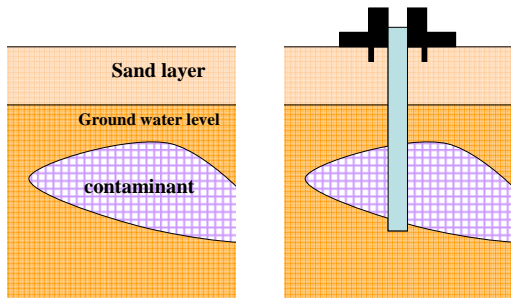


Fig. 2-1 Initial condition

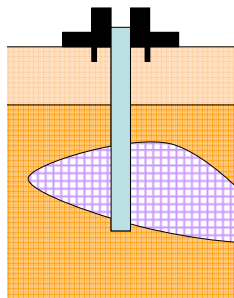


Fig. 2-2 Drilling into ground

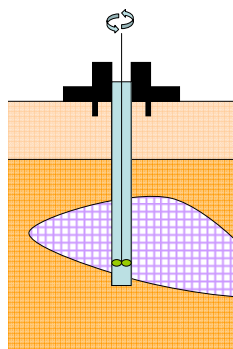


Fig. 2-3 Stirring

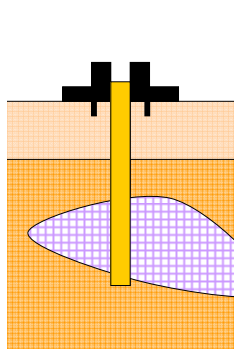


Fig. 2-4 Leaving for a certain period

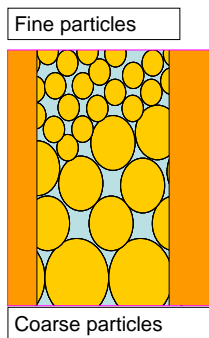


Fig. 2-5 The shape of sedimentation

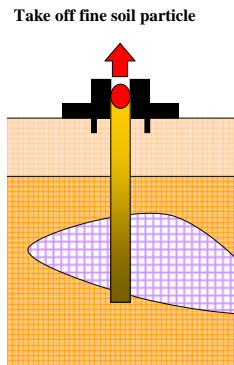


Fig. 2-6 Eliminating fine particle soils

### 3 Physical property of sand

The sand is taken at Ohta district where small and medium size companies exist. Grain size distribution and surface area of sands are investigated. Fig. 3-1 shows the result of grain size distribution. Fig 3-2 shows the relationship between surface area of sand and grain size. Surface areas of sands are calculated by using the concept shown in Fig. 3-3. In the concept shown in Fig.3-3, the author assumed that the soil particles are plain spheres. Fine grain

size sands consist most of surface area in sand. Surface area of fine grain size sands whose diameter is less than 0.1mm are 70% of all soil particles although the weight of fine sands are on the about 10% of total weight of all sands.

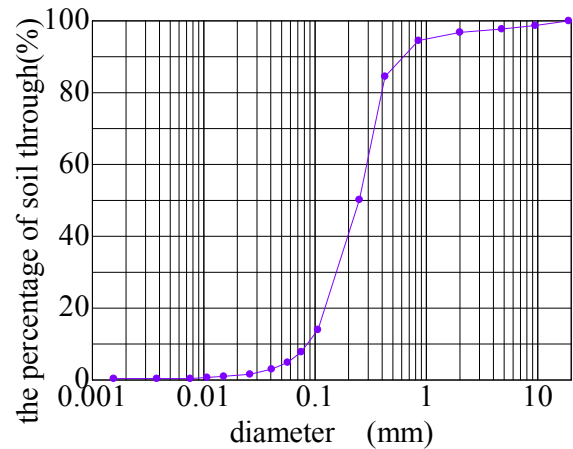


Fig. 3-1 the result of grain size distribution

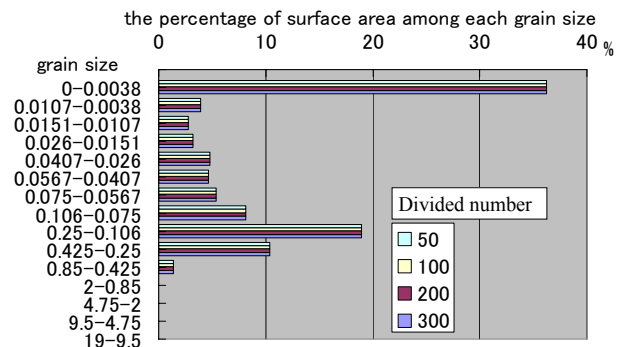


Fig. 3-2 the relationship between surface area of sand and grain size

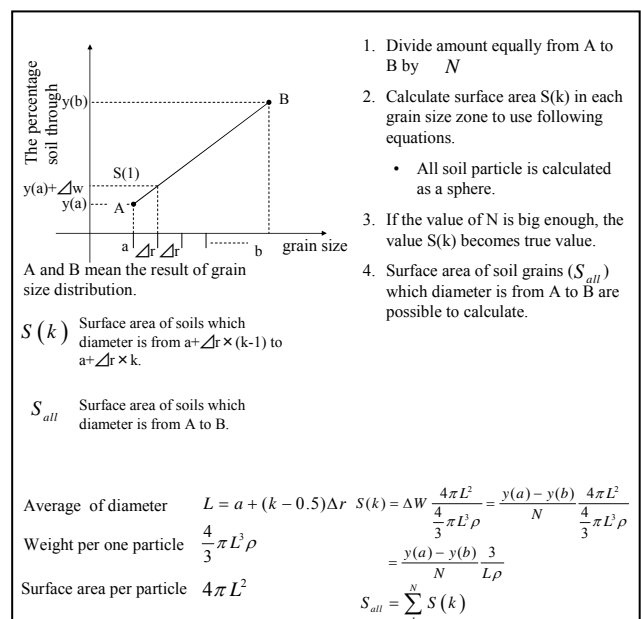


Fig. 3-3 The concept to calculate surface area

#### 4 Sorption and flushing characteristics of heavy metal to soil particles

Before the experiments, contaminants in the sand used in this study are investigated by ICP shown in Fig.4-1. Table. 4-1 shows the result of investigations of contaminants in the sands. It can be seen from Table.4-1 that value of contaminants in the sands are extremely small. In this study, the author assumes that there are no contaminants in the sands. Therefore, to investigate the characteristic of sorption and flushing the sands are contaminated by Cu, Zn, Pb, and Cd. Four contaminants selected in this study

##### (1) sorption experiment

The process of sorption experiment is following,

1. Water, contaminants and soils in bottle is put. The table.4-2 shoes amount of water, contaminants and soils. Fig.4-2 shows the bottles in water, contaminants and soils.
2. The bottles are shaken as shown Fig.4-2. During shaking contaminants adhere to soil grain surface area.
3. Contaminants which adhere to soil grain surface area measured using ICP at 1, 2, 4,6,8,10,16 days.

Fig 4-3 shows that the relationship between concentration of sorption and time and amount of sorption becomes constant values.

This shows that all of cases the concentrations of sorption experience were became equilibrium in seven days. The most absorbent material was Pb, second was Cd, third was Cu the last was Zn.

##### (2) flushing experiment

The process of flushing experiment is following.

1. Water contaminated sands which were used in sorption experiment and Bio-surfactant are put in bottles. Table. 4-3 shows amount of water, contaminated soil and Bio-surfactant.
2. The bottles are shaken as shown Fig.4-2. During shaking the contaminants leave from surface area.
3. Contaminants which adhere to soil grain surface area measured using ICP at 3,17th hours 1, 2, 4, 5, 6,7th days

Fig. 4-4, 5, 6, 7 shows the relationship between the weight of flushing contaminants and time. The concentration of Cd and Zn became equilibrium in one day. The concentration of Pb became equilibrium in two day. However the concentration of Cu did not become equilibrium. From these results, the more concentration of Bio-surfactant, the more contaminant dissolved out.



Fig. 4-1 ICP

Table.4-1 the result of investigations of contaminants

element	result	Minimum concentration	Max concentration
Si	o	26.209	104.836
As	x	0	0.051
Hg	x	0	0.017
Cr	x	0	0.006
Co	x	0	0.008
Mn	o	0.042	0.167
Fe	o	1.604	6.416
Zn	x	0	0.002
Ni	o	0.008	0.033
Cu	o	0.016	0.063
Cd	x	0	0.033
Mo	x	0	0.009
Pb	x	0	0.072
Ag	x	0	0.007

Table 4-2 Amount of water, contaminants and water

Water	1ℓ
Cu	$20 \times 10^{-3}$ mol
Cd	$20 \times 10^{-3}$ mol
Zn	$20 \times 10^{-3}$ mol
Pb	$20 \times 10^{-3}$ mol
Soil	500g

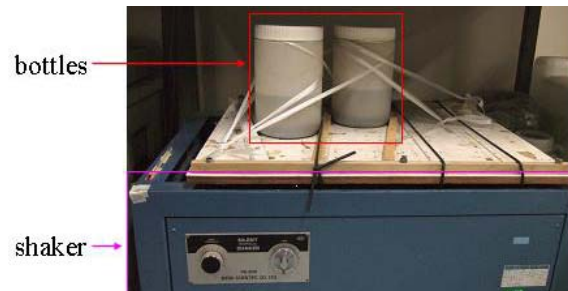


Fig. 4-2 bottles and shaker

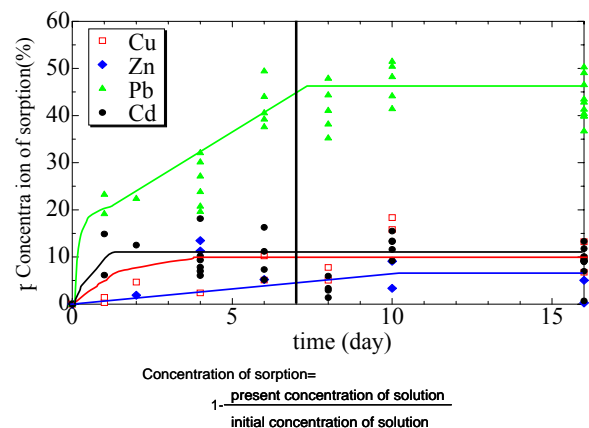


Fig. 4-3 the result of sorption experiment

Table. 4-3  
amount of water, contaminated soils and concentration of Bio-surfactant

Water	0.6l
Contaminated soil	300g
Bio-surfactant	0mg/l
5 cases	5mg/l
	20mg/l
	50mg/l
	100mg/l

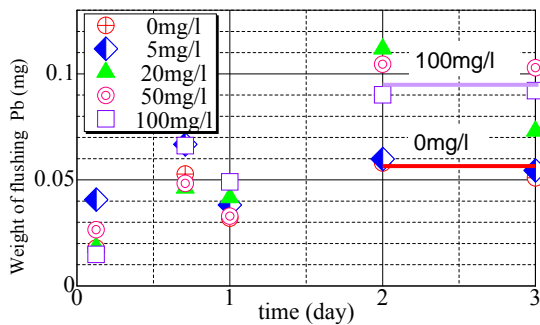


Fig. 4-4 the result of Pb in flushing experiment

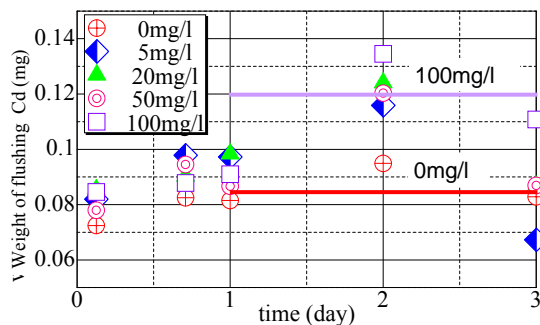


Fig. 4-5 the result of Cd in flushing experiment

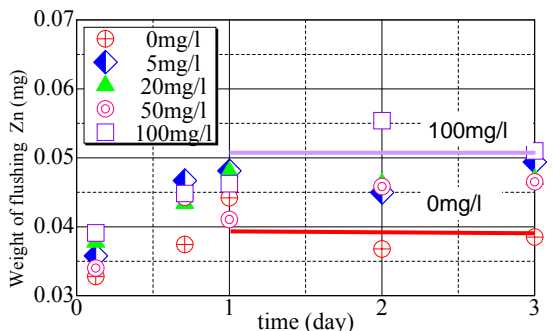


Fig. 4-6 the result of Zn in flushing experiment

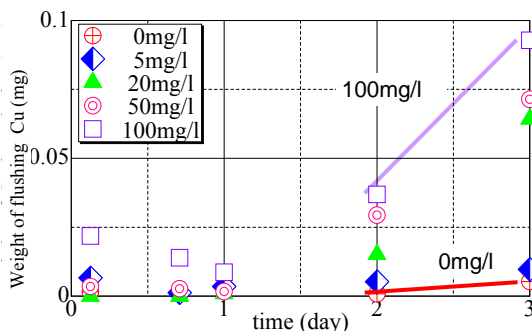


Fig. 4-7 the result of Cu in flushing experiment

## 5 Conclusion

In this study, sorption and flushing characteristics of heavy metal soil particle are investigated to put into practice for new soil washing system developed by Suga(2005). Throughout sorption test, all of cases the concentrations of sorption experience were became equilibrium in seven days. The most absorbent material was Pb, second was Cd, third was Cu the last was Zn. Throughout flushing test, The concentration of Cd and Zn became equilibrium in one day. The concentration of Pb became equilibrium in two day. However the concentration of Cu did not become equilibrium. From these results, the more concentration of Bio-surfactant, the more contaminant dissolved out.

## Reference

- 1) 小澤 英明 (2003): 土壤汚染対策法 pp.16-17
- 2) 佐藤雄也, 土と基礎(2004): 土壤汚染とその対策～土壤汚染対策法の施工から1年余が経過して～,土と基礎 vol.9 pp.2-3
- 3) 平田建正, 土と基礎(2004): 地盤環境汚染のメカニズムの解明から最新技術開発まで vol.10 pp3
- 4) 浅見 輝夫, 「日本土壤の有害金属汚染」 pp.17-21
- 5) Asami,T.(1997): Cadmium pollution of paddy fields and human health in Japan ;in Biogeochemistry of Trace Metals, (Adriano,D.C.,Chen,Z-S.,Yang,S-S, and Iskandar, I.K.ed.), pp.217-264,Science Reviews, Northwood.
- 6) 社団法人 地盤工学会(2002): 土壤・地下水汚染の調査・予測・対策 pp.3、 pp.9-12
- 7) 菅 良一(2005): 汚染された砂質地盤の原位置攪拌洗浄 東京工業大学卒業論文
- 8) 財団法人 地盤工学会(2000): 土質試験の方法と解説(第一回改訂版)
- 9) Kyoung-Jin Hong(2000),Application of Plant-Derived Biosurfactant to Heavy Metal Removal from Fly Ash and Soil, doctor thesis, p66-p87
- 10) Ta Thi Thao(2005), heavy metal content in roadside deposits collected in Tokyo, JAPAN and HANOI, VIETNAM: A CASE STUDY , Dr architect

# POSSIBLE MECHANISM OF HYDRAULIC FRACTURING INITIATION

Student Number:04M18140 Name:Emiko TAKAHASHI Supervisor: Hideki OHTA and Pipatponsa THIRAPONG

ハイドロリックフラクチャリングの発生機構に関する基礎的研究

高橋笑美子

ハイドロリックフラクチャリング(HF)はダム堤体に亀裂を生じ水が浸透する破壊現象であるが、その発生機構は未だ解明されておらず、精密かつ実用的な安全評価法が存在していない。実験的結果によると正しいとされる Seed の HF 発生基準によっては壊れてもおかしくないと評価されたダムのほとんどは破壊せず立っていることも矛盾点である。本研究ではまず、HF と破壊機構において共通点を持つ八王子の斜面崩壊の例を取り上げ、斜面下の低透水層の持つ特性を調べ亀裂ではなくヒービングが起こったことを証明した。また、異なる土の異なる条件下で透水破壊実験を行い HF 発生傾向の評価した。

## 1 Introduction

Hydraulic fracturing (HF) is a failure mechanism in which water pressure generates a formation of crack in low permeable layer of soil, followed by water seepage. Even though dam's HF is a big problem, no precise, practical safety evaluation method based on HF exists today. This is because the details of fracture morphology are poorly known. Previous researchers have observed that when water pressure becomes greater than minimum principal stress, vertical cracks form and seepage failure occurs. However, many dams in Japan that were judged "dangerous" by this HF evaluation method have not failed and still stand today.

Apart from dam, there was failure case sharing the same mechanism. An excavated slope failed after heavy rainfall. It was analyzed that low permeable layer was uplifted by the rise of water pressure in sand layer beneath, but there was no evidence of water spouting nor vertical cracks.

The objective of this study is to investigate further the failure mechanism of the slope and to observe initiation of HF to seek for trend of its mechanism. In order to do so, close investigation on properties of slope site soil was conducted. Then, seepage failure experiment was carried out for different states and different types of soils, simulating the slope site and boundary of dam's core material and sand.

## 2 Background and previous studies

### 2.1 Hydraulic fracturing incidents

On June 5, 1976, Teton dam in Idaho, USA, suddenly broke down at the stage of first filling of the reservoir as shown in **Fig.1**. Piping holes that were discovered on the downstream side surface of the dam body enlarged drastically in few hours as the water overflowed, which then led to the vanishment of nearly the complete dam body. It was a significant event for earth dam geotechnical engineers, because no dam of such a height (about 90 m) had previously

failed in earth dam history.



**Fig.1** Breaching of Teton dam

### 2.2 Proposed mechanism of HF

After the Teton dam failure, H.Seed and J.Duncan (1976) proposed different criteria for HF initiation.

Seed's criterion:  $\Delta u > \sigma_3 + \sigma_t$  (1)

Duncan's criterion:  $\Delta u > \sigma_1 + \sigma_t$  (2)

where  $\Delta u$  is the increase of pore water pressure,  $\sigma_1$  the maximum principal stress,  $\sigma_3$  the minimum principal stress, and  $\sigma_t$  the tensile strength of soil.  $\sigma_t$  is small to be often neglected.

**Fig.2** shows dam body in three dimension. Dam is usually considered that  $\sigma_z$  is largest,  $\sigma_x$  is about half as much as  $\sigma_z$ , which is nearly equal to  $\sigma_y$ . Cracks form in planes perpendicular to each stress. If the effective stress  $\sigma'_y$  becomes 0 or negative, then vertical crack forms on up-down stream direction plane, which is the most critical plane for HF since water can easily penetrate into the crack and seepage failure may begin.

What is minimum or maximum principal stress in a soil varies corresponding to the state of the soil. Referring to **Fig.3**, in  $K_0 < 1$  state (such a condition is usually normally consolidated(NC)) where vertical stress  $\sigma_v$  is greater than horizontal stress  $\sigma_h$ , according to Seed's criterion when the water pressure becomes larger than  $\sigma_h$ , vertical cracks form and water penetrates into a plane perpendicular to  $\sigma_h$ , where  $K_0$  is defined as

$$K_0 = \frac{\sigma_h}{\sigma_v} \quad (3)$$

On the other hand, in  $K_0 > 1$  state, (such a condition is usually overconsolidated(OC)) when water pressure becomes greater than  $\sigma_v$ , horizontal cracks form and water penetrates into a plane perpendicular to  $\sigma_v$ .

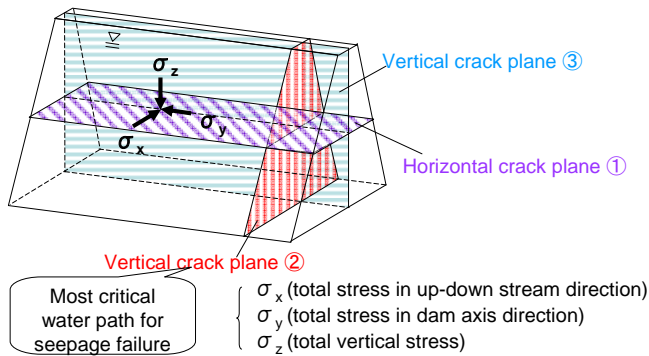


Fig.2 Dam body in 3 dimension

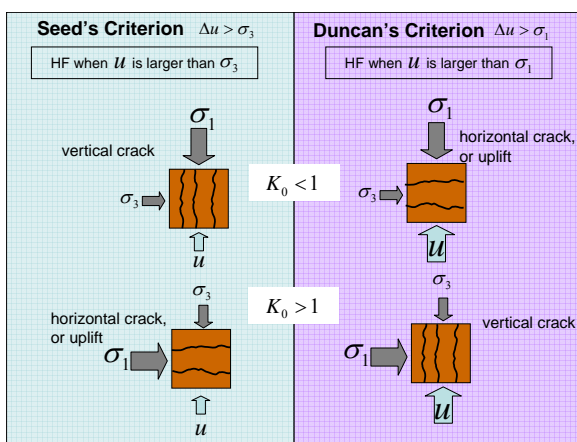


Fig.3 Conceptual diagram of each criterion

### 2.3 Failure of Hachioji slope

Slope of excavated road in Hachioji, Tokyo, failed after one night of intense rain on October 1, 2002. Sidewalk uplifted up to 1.6 m, and cliff fell about 4.0 m as shown in Fig.4 and Fig.5.

Takeyama (2005) focused on geological structure of the site ground. At the bottom laid high permeable Komiya sand layer (Ksg), and on top of it laid low permeable loam layer (Lc). The altitude of the sand layer surface was 10 m below the Tama River which flows nearby. When there was heavy rain, the ground



Fig.4 Sidewalk uplift

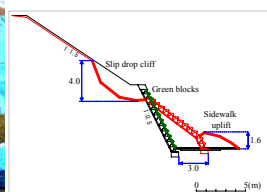


Fig.5 Cross-section

water level in the sand layer suddenly rose up and there was 10m difference of water head in Komiya sand layer. Based on measurements and analysis, Takeyama concluded that due to the heavy rainfall, water pressure in Komiya sand layer became greater than the overburden pressure, and the water pressure

uplifted the loam layer as shown in Fig.6. In conjunction, the area softened by excavation slipped.

Questions remain though, that if the failure was due to water pressure, why did no vertical cracks form nor evidence of water passage exist? According to Seed's criterion, vertical cracks must have formed before such a heaving phenomenon.

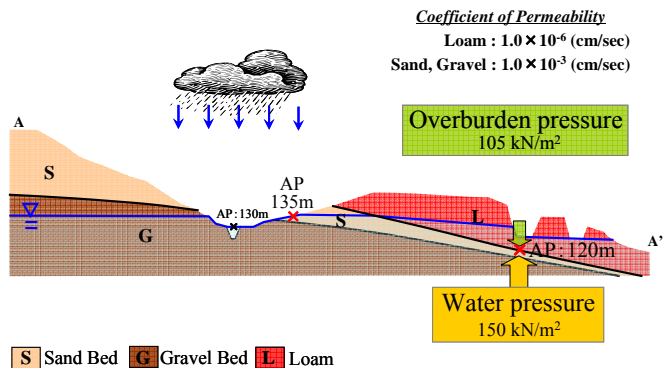


Fig.6 Failure mechanism of Hachioji excavated slope

### 2.4 Previous studies

Previous studies mostly involved cylindrical or cubical specimens, tested under triaxial conditions, in which a small hole allowed the application of water pressure. They compared the pressure necessary to fracture the specimen with the minimum total principal stress and reached a conclusion that Seed's criterion is coherent with their experiment results.

As recent studies, T. Ishiguro(2005) and Y. Arai (2005) each conducted laboratory test and numerical analysis of Kamihikawa dam and Surikiamigawa dam respectively. They prepared specimens using dam's core materials, set in triaxial apparatus, and plotted the relationship between difference in water pressure and minimum principal stress when HF occurred. The experiment result followed Seed's criterion. They also defined HF safety factor based on Seed's criterion:

$$F_{sh} = \frac{\sigma_3}{\Delta u} \quad (4)$$

and evaluated many existing dams in Japan. Most dams in Japan were judged "dangerous" by this safety factor, but these had not failed and still stand today.

## 3 Properties of the object soil

Samples 5-② and 5-③ were extracted from the ground 5 to 6 m below the surface of uplifted sidewalk and the author conducted laboratory tests.

### 3.1 Physical properties

Results of laboratory tests are shown in Table 1.

Oedometer test of undisturbed Hachioji sample was conducted to know the consolidation property and pre-consolidation stress of the soil. Fig.7 shows the e-log  $\sigma_v$  curve.

**Table 1** Physical properties of Hachioji loam

sample name (depth): Hachioji 5-②, 5-③ (5-6m)

water content test		density test	
water content w(%)		density ρ s(g/cm3)	
5-②	56.7	2.664	
5-③	55.1	2.664	
LL/PL test			
liquid limit wL(%)	plastic limit wp(%)	plasticity index Ip	
5-②	91.0	44.3	46.70
5-③			
grain size test			
fine gravel (%)	coarse sand (%)	medium sand (%)	fine sand (%)
5-②	0.1	0.1	1.2
5-③	0.0	0.2	1.3
			4.2
silt (%)	clay (%)	maximum grain size (mm)	50% grain size D <sub>50</sub>
5-②	64.3	32.1	4.75
			0.0243
5-③	60.9	33.4	2
			0.0264

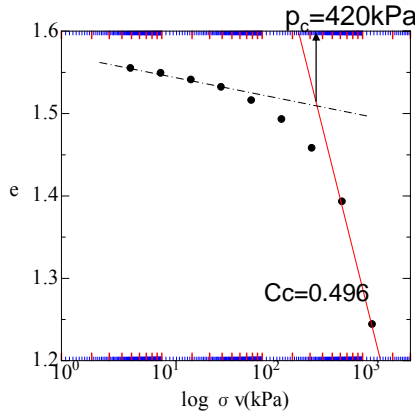


**Fig.7** e-log  $\sigma_v$  curve

By Casagrande's method, pre-consolidation stress  $p_c$  was determined as 420 kPa. From equation

$$\sigma'_v = (\gamma_t - 1)h \cdot \gamma_w \quad (5)$$

vertical effective stress was calculated to lie between 24.5kPa to 29.4kPa in depth of 5 to 6m. Overconsolidation ratio is defined as

$$OCR = \frac{\sigma'_{vmax}}{\sigma'_v} \quad (6)$$

Therefore, OCR of this sample must lie between

$$14 \leq OCR \leq 17 \quad (7)$$

From the result, it was discovered that the loam layer was highly overconsolidated.

### 3.2 $K_0$ load-unload test

$K_0$  load-unload test was conducted for undisturbed Hachioji sample. The specimen was set in  $K_0$  measuring apparatus shown in **Fig.8** and given back pressure, cell pressure, and vertical load. After loading the specimen until it is considered to be normally consolidated, unloading steps were taken by giving extra height of the specimen  $\Delta h$ (cm) and decreasing the cell pressure. When the specimen is at  $K_0$  state, equation

$$\Delta V(\text{cm}^3) = A(\text{cm}^2) \cdot \Delta h(\text{cm}) \quad (8)$$

must be satisfied, where  $\Delta h$  times the area of the specimen equals to the change in water volume  $\Delta V$ .

**Fig.9** shows the result of unloading test. Black plot signifies the specimen is not at  $K_0$  state, while red plot signifies the specimen is in  $K_0$  state. OCR of the plotted values at  $K_0$  state range from 9.7 to 23.7, which include the OCR obtained from oedometer test. Therefore we now know 2 things:  $K_0$  of the loam layer

under Hachioji sidewalk was greater than 1; and same soil of  $OCR=9.7 \sim 23.7$  has  $K_0$  of greater than 1.



**Fig.8**  $K_0$  apparatus

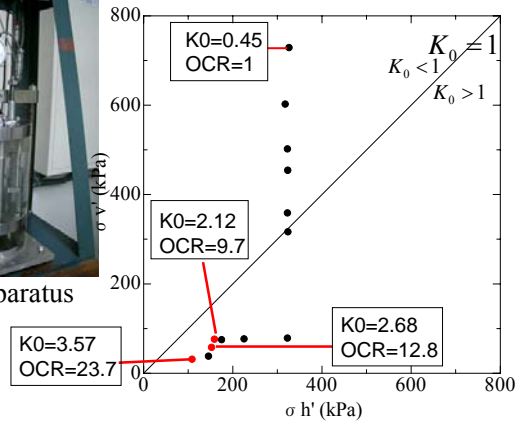


**Fig.9**  $K_0$  state plotted (unload)

## 4 Seepage failure experiment

As stated, most researchers had conducted HF tests in triaxial apparatus which has an advantage in controlling and measuring cell pressure  $\sigma_h$ . However in this study the horizontal deformation is restricted, which expresses the better actual ground and dam condition, which are also horizontally confined by pressure of sideways soil.

The experiment applies water pressure to saturated consolidated soil from the sand layer beneath. The sample is modeled to be uniform. Assuming that the stress conditions do not change, the author discusses Seed's criterion under initial stress conditions. Two states are investigated: NC and OC. Three samples were used: silica flour, Hachioji's loam, and kaolin.

### 4.1 Experiment apparatus and procedure

The diagram of the specimen is shown in **Fig.10**. Dial gauge was set on the loading ram to measure the vertical displacement, water tube was connected to pore water pressure meter, then to a water tank and to a buret to measure the seepage amount. Samples were prepared as slurry by mixing well with water. Air was carefully got rid of inside the specimen and on the way in all tubes and valves. If the apparatus is turned onto the side, the sample can be interpreted as the core material of dam which is given water pressure from left hand side, with the sand layer being filter material of dam.

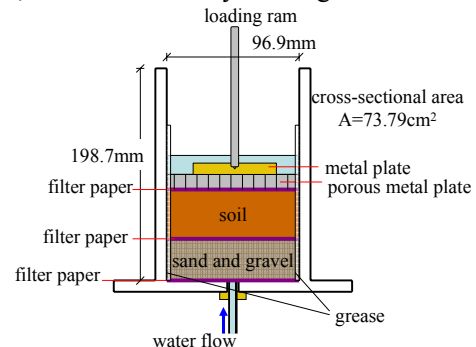


**Fig.10** Diagram of the specimen

### 4.2 Results and discussion

After applying water pressure greater than the vertical load, vertical cracks formed in NC silica flour (Fig.11) while no vertical crack formed in OC silica flour (Fig.12) of OCR=8.

For Hachioji loam sample, vertical displacement *d* (mm) of the sample, applied water pressure *u* (kPa) and seepage amount *q* (cm<sup>3</sup>/s) were recorded and plotted against time (min) in Fig.13.



Fig.11 NC silica flour Fig.12 OC silica flour

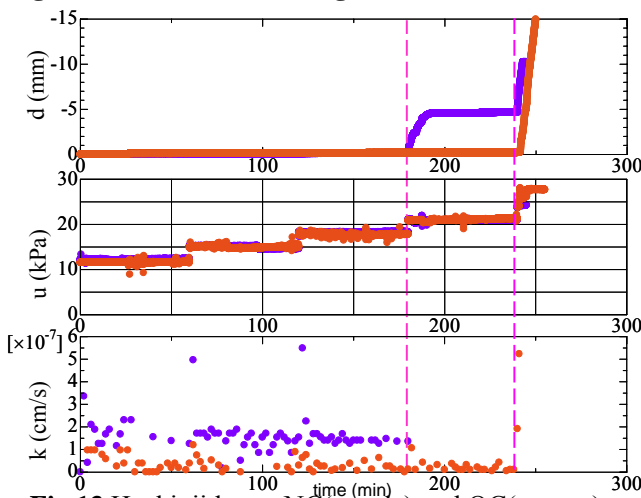


Fig.13 Hachioji loam, NC(purple) and OC(orange)

Coefficient of permeability,  $k=v/i$ (cm/s) was calculated

$$v = \frac{q \text{ (cm}^3\text{/s)}}{A \text{ (cm}^2\text{)}} \tag{9}$$

$$i = \frac{p \text{ (kN/m}^2\text{)}}{h \text{ (m)} \cdot \gamma_w \text{ (kN/m}^3\text{)}} \tag{10}$$

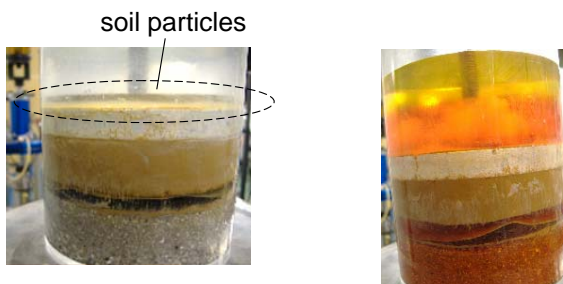


Fig.14 NC Hachioji loam Fig.15 NC Hachioji with ink



Fig.16 OC Hachioji loam Fig.17 NC kaolin with ink

The vertical stress was 20 kPa all cases. In Fig.13, coefficient of permeability of NC abruptly rises at certain points, while it is nearly constant for the OC (OCR=13). This can interpret that in NC, a water path was developed in sample. Vertical displacement rates are also different for NC and OC. NC sample heaves up slowly and nonlinearly possibly because considerable amount of water flowed out through the crack, while OC sample heaves up rapidly and linearly because all water was caught in between the loam layer and sand layer. Evidence of water passing through the NC loam can also be observed in Fig.14 and Fig.15, in which soil particles and red ink were recognized above the porous metal. There was no evidence of such water passage in OC (Fig.16). Safety factor based on Seed's criterion for OC sample at heaving can be calculated by

$$F_{sh} = \frac{20}{24} = 0.83 < 1 \tag{11}$$

Kaolin was tested similarly, and for NC cases coefficient of permeability also changed abruptly, pointing out the possibility of crack formation. As shown in Fig.17, unlike Hachioji sample in which no recognizable crack formed around the perimeter, kaolin formed cracks in the perimeter. The water seemed to target the loosest spot in the sample.

### 5 Conclusions

Hachioji landslide mechanism can be explained by heaving of the loam layer uplifted by water pressure in the sand layer. Because it was overconsolidated, the layer lifted up with no evidence of seepage and hence no vertical cracks. There was an evidence of formation of water path or crack inside NC sample at around  $\Delta u = \sigma_3$ , which follows Seed's criterion. There was no evidence of formation of water path or crack inside OC sample before and after heaving, which follows Seed's criterion. Heaving occurred when the safety factor was lower than 1. The water pressure at HF was different for Hachioji loam and kaolin. Hachioji loam has lower permeability than kaolin, therefore even though they were under the same confined pressure, it can be considered that crack was easier to form in soil with low permeability. Although the crack formation features are different among different samples, all of them followed Seed's criterion.

### References

[1] Ohta,H., Yoshikoshi,Y., Mori,Y., Tomobe,Y., Ishiguro,K., Fujiyama,T.: Safety evaluation of large rockfill dams during first reservoir filling, ICOLD, 2006.  
 [2] Seed,H.B. and Duncan,J.M.: The Teton Dam Failure-A petrospective Review, Proc.,10<sup>th</sup> Int.Conf. S.M.F.E., 1981.  
 [3] Takeyama,Y., Ohta,H.: Slope failures triggered by rise of local ground water level caused by the localized torrential downpour, TITech master thesis, 2005.  
 [4] Murdoch, L.C.: Hydraulic fracturing of soil during laboratory experiments, Geotechnique 43, 1992.

## Proposed Design Method of Cathodic Protection for Reinforced Concrete Member under Chloride Attack

Student Number: 04M18080 Name: Keiyu KAWAAI Supervisor: Nobuaki OTSUKI

### 塩害劣化した鉄筋コンクリート部材に対する電気防食設計手法の提案

河合 慶有

本研究では、鉄筋コンクリート材料の不均一、欠陥および劣化進行過程が電気防食工法の効果に及ぼす影響について実験的および解析的に検討を行った。その結果、以下のことが明らかとなった。防食電流はコンクリートの欠陥部に優先的に流入し、欠陥部の鉄筋部位は過防食になる危険性が示された。なお、この傾向は、いずれの腐食劣化進行過程においても同様であった。多段配筋された鉄筋コンクリート部材では、通電電流密度に関わらず、部材の最深部に配置された鉄筋に流入する防食電流を制御することは困難である。特に、本研究の範囲内では陽極から 250mm 以上離れた鉄筋において所定の防食効果を得ることは困難であることが実験的、解析的に示された。鉄筋コンクリート部材に対する電気防食設計手法が提案された。本手法は、防食基準電位を  $-0.85 \sim -1.0$  (V vs CSE) とした電位制御による防食設計手法とした点に特長がある。

### 1 Introduction

Cathodic protection method has been recognized as one of the most effective corrosion control methods in recent years due to its reliability and effectiveness against steel corrosion in concrete under such as chloride attack.

In order to make use of cathodic protection method effectively, it is necessary to develop a systematic design method for appropriate cathodic protection. As a prerequisite, it is important to design the electric circuit properly in order to provide appropriate current on the steel<sup>1)</sup>. Nowadays, this method is applied to existing reinforced concrete structure using a polarization about 0.1V at each region on the steel bar. Generally, it is very difficult to carry out an optimal corrosion protection to the steel bar in concrete and to evaluate the effectiveness of corrosion protection. This is because the current distribution is affected by the heterogeneity of reinforced concrete, defects in concrete such as cold-joint and crack, and deterioration period of steel bar

such as incubation and propagation on the steel bar. However there are few researches about the influences of these factors on cathodic protection. Therefore, the purposes of this study are as follows: (1) To clarify the influences of the material property of reinforced concrete, defects in concrete, and deterioration period of steel bar on the effectiveness of cathodic protection. (2) To develop a numerical analysis technique using FEM to optimize the cathodic protection to the steel bar in concrete. (3) To propose a systematic design method of appropriate cathodic protection for reinforced concrete members.

### 2 Experimental Procedure

#### (1) Outline of Experiment

There were two types of specimens (case A and B) used in this study as shown in Fig.1 and 2. The size of specimens embedded with divided steel bars as shown in Pic.1 was  $100 \times 100 \times 400$ mm. In the case of case A without cold-joint and case B specimen, concrete was cast at one time. On the other hand, in the case of case A with cold-joint, concrete was cast in the mold half-full and after 24H, new concrete was placed on the top of the hardened concrete. As for the reinforcement used, 14 elements of divided deformed steel bars with the diameter of 13mm were attached together

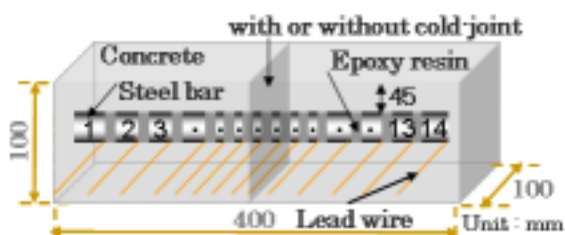


Fig.1 Case A specimen

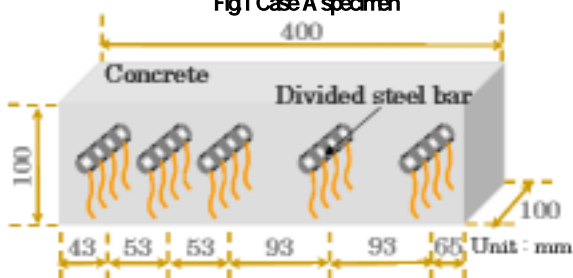
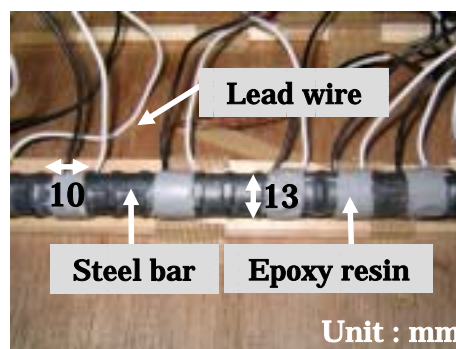


Fig.2 Case B specimen



Pic.1 Divided steel bars

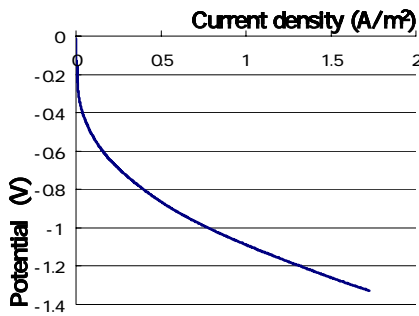


Fig.3 Example of polarization curve

using an epoxy resin to one straight bar. These bars were embedded in case A specimens respectively. In the case of case B specimen, the divided steel bars consisted of 4 deformed steel elements. Each steel element had lead wires soldered on it serving as a connection for the electrical measurement. After demolding, all the specimens were cured in tap water for 28 days. Initial measurements were conducted on the specimens prior to their exposure in Cl<sup>-</sup> acceleration chamber to accelerate corrosion on the steel bar. The acceleration process involved a cycle of subjecting the specimens under wet condition for 36H (40% RH, more than 95% R.H.) and submerged condition for 24H in water containing Cl<sup>-</sup> (3%) during 3 months period.

(2) Outline of Numerical Analysis

The distribution of potential in the concrete complies with the following Laplace's equation<sup>2)</sup>;

$$\nabla(\sigma \nabla \phi) = 0 \tag{1}$$

Where,  $\sigma$  is the conductivity of concrete,  $\phi$  is potential in concrete.

The boundary conditions have two types namely insulation wall and metal electrode surface. At the insulation wall, the current doesn't flow through the wall, and its boundary condition is given by the equation below;

$$n \cdot (\sigma \nabla \phi) = 0 \tag{2}$$

Where,  $n$  is normal vector of the insulation wall.

On the surface of steel and anode, polarization phenomenon occurs under current flows. The polarization behavior is described with an equilibrium potential  $E^0$  and an over potential as a function of current, as follows;

$$E_{steel} = E_{steel}^0 - r_{steel}(j) \tag{3}$$

$$E_{anode} = E_{anode}^0 - r_{anode}(j) + V \tag{4}$$

The measurements of polarization curves give  $E^0$  and  $r(j)$ , and  $V$  is external voltage. Thus, all boundary conditions have been defined and FEM can be used to calculate the current distribution in the steel bar in concrete.

3 Measurement Items

In this study, linear anode system was used as the electric condition. Under this condition, three levels of current density, 10, 20, 30mA/m<sup>2</sup> were investigated. The measurement items considered in this study were as follows: (1) The current distribution, half cell potential and polarization resistance in each steel element were measured using an ammeter and a potentiostat connected with lead wires. Coefficient of variation in the current flowing along the 14 steel elements was calculated to determine the variations of anticorrosive current. (2) Moreover, the polarization curve which was the relationship between current density and potential on the steel bar were measured by using potentiostat (HOKUTO DENKO, HZ-3000) as shown in Fig.3. And the potential scanning rate was 1mV/s with Ag/AgCl serving as a reference electrode. Thus, the potential on each steel element can be calculated by using the current distribution and polarization curve. Furthermore, the relationship was used as a boundary condition on the metal surface, steel and titanium mesh in numerical analysis.

4 Result and Discussion

(1) Influence of materials properties, defects in concrete and deterioration period on the effectiveness of cathodic protection

Fig.4 shows the relationship between current distribution on the steel bars and steel elements in case A specimen without defects during propagation period. From this figure, it can be said that the current distribution in concrete was influenced by materials properties in concrete in each electric current density even if there was no cold-joint in concrete. The Coefficient of variation of current distribution on the steel bars was 25.4%, 25.0%, 26.2% in each electric current density, 10, 20, 30mA/m<sup>2</sup>. This is because electric conductivity was different at each region in concrete due to concrete heterogeneity and shape of steel bar. On the other hand, Fig.5 shows the relationship between current distribution and steel elements in case A specimen with cold-joint at the center part of concrete during propagation period. From this figure, it can be said that

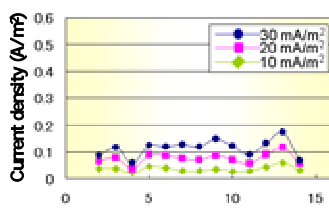


Fig.4 Current distribution, case A Without defects

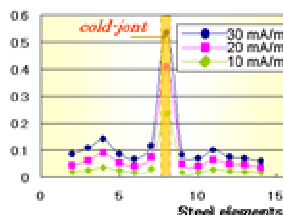


Fig.5 Current distribution, case A With Cold-joint

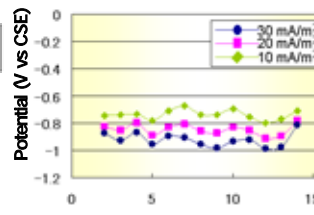


Fig.6 Potential distribution, case A Without defects

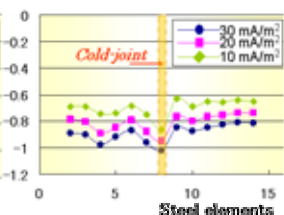


Fig.7 Potential distribution, case A With Cold-joint

current flowed locally into the steel bar at cold-joint in concrete more than any other parts without defect. To compare the result without defects in concrete, the current density which flowed into the steel bar at cold-joint was about 3.3 times than the maximum value obtained in the result in each electric current density.

Fig.6 shows the relationship between potential of the steel bars and steel elements. From this figure, it can be said that the potential distribution on the steel bars varied even if it was under cathodic protection. The coefficient of variation of potential was 6.2%, 6.9%, 7.7% in each electric current density. On the other hand, Fig.7 shows the relationship between potential distribution and steel element. From this figure, the potential on the steel bar at cold-joint was relatively lower than any other parts. According to past research, it is reported that if the potential of steel bar is lower than -1V, the evolution of H<sub>2</sub> occurs on the steel bar and deteriorate the covering concrete<sup>3</sup>. Therefore, the potential of steel bar should be more than -1V, so that the potential of the steel bar at cold-joint was locally over protected as the current density became higher.

This tendency was the same as the result during incubation period. Therefore, the potential of the steel bar at cold-joint in concrete tended to be locally over protected in spite of deterioration period.

(2) Comparison Experimental result and FEM analytical result in the case of case C specimen.

Fig.8 shows the experimental results in the case B

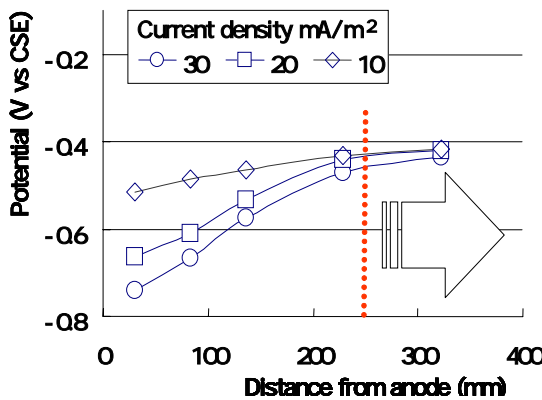


Fig.8 Potential of steel bars case B specimen

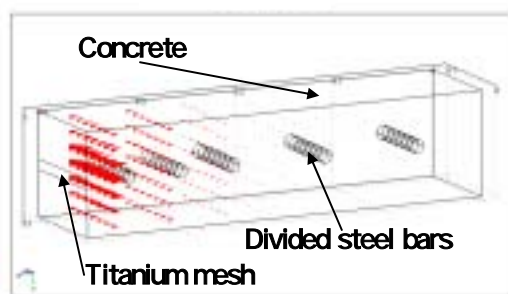


Fig.9 Modeling of case B specimen

specimen during incubation period. This graph shows the relationship between potential of steel bar and each layer of steel bar. From this figure, we can see that the potential of steel bar in the arrangement of steel bars near the distance from the anode became higher as the electric current density became higher. However, it was observed that the potential distribution at a distance over 250mm from the anode was almost constant in spite of electric current density. Therefore, the potential distribution at a distance over 250mm from the anode can not be controlled.

Fig.9 shows the modeling of the case B specimen for numerical analysis technique using FEM. After modeling, the conductivity value was set as  $\sigma = 1/20$  (1/m), and the polarization values of steel bar were set as  $E_{steel}^0 = -0.545$  and  $r_{steel} = -0.61$ . These experimental values were used to define the boundary conditions as shown in Fig.10. Similarly,  $E_{anode} = 0.24$  and  $r_{anode} = 0.846$  were set in the part of anode. The calculated potential distribution of cathodic protection on the steel bar in the case of electric current density, 10mA/m<sup>2</sup>, as shown in Fig.11 (before ). From this figure, it can be said that the analytical result using the technique obtained from past researches, had a good correlation with the experimental results. However, the analytical result obtained from the potential distribution in the steel bar at a distance about 150mm from anode was relatively lower as compared with experimental results. This is because approximate linear polarization curve considered consisted only of one linear component. Thus, the calculated potential distribution was lower than the actual value especially in the case of

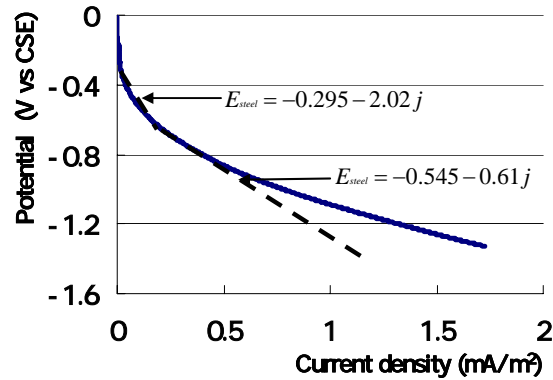


Fig.10 Boundary condition (part of cathode)

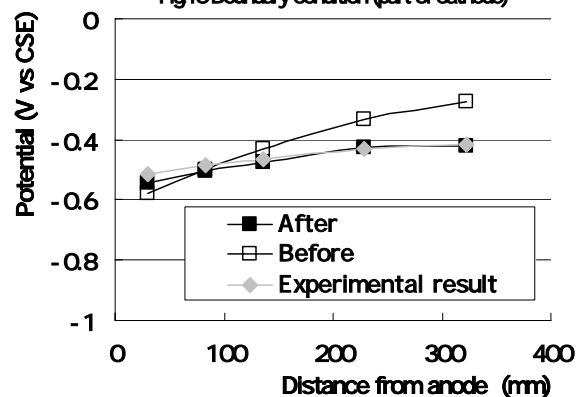


Fig.11 Comparison (FEM vs Experimental result)

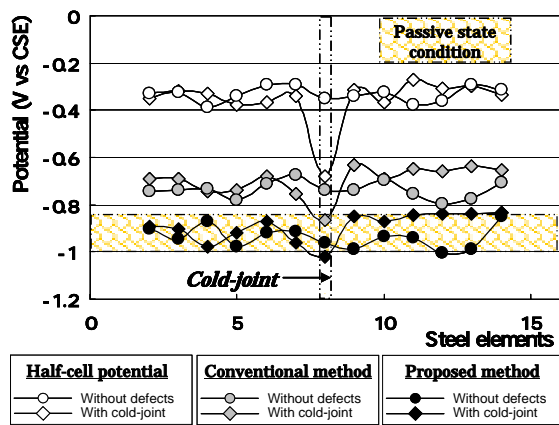


Fig.12 Comparison (Conventional vs Proposed)

applying low electric current density in the steel bar.

Therefore, the boundary condition should be evaluated appropriately. In order to do this, two components were used in approximating the linear polarization curve as shown in Fig.10. The second polarization values were  $E_{steel}^0 = -0.295$  and  $r_{steel} = -2.02$ . From Fig.11 (after ), it can be said the re-calculated potential distribution has better correlation with experimental results. Consequently, this FEM analytical method was applicable for the practical and complex 3-D member.

(3) Proposed design method of cathodic protection

Nowadays, cathodic protection method is applied to existing reinforced concrete structure using a polarization about 0.1V at each region on the steel bar. However, it was confirmed in this study that the potential of the steel bars varied even if it was under cathodic protection during propagation period. It meant that corrosion still occurred under cathodic protection. Therefore, the cathodic protection method should be applied to reinforced concrete structure appropriately during propagation period. In order to do this, a design method was proposed in this study. Proposed method was to control the potential of steel bar between -0.85V and -1V. Based on the guideline for corrosive protection of marine structures, the potential in the steel bar should be less than -0.85V in order to maintain a passive state condition. It means that under this condition corrosion may not occur on the steel bar.

Fig.12 shows the results using conventional and proposed method for case A specimen with or without cold-joint. This graph shows the relationship between potential of steel bars and steel elements. The white dots in graph show the half-cell potential which is initial potential. The gray dots in graph show the potential distribution using this method during propagation period. Electric current density 10 mA/m<sup>2</sup> was applied in each case. From this figure, the potential of steel bar in the specimen without cold-joint lied on the range between -0.6 and -0.75V. On the other hand, in the case of specimen with cold-joint, except for the part where there is cold-joint, the result obtained was similar as

in case A specimen without cold-joint. From these graphs, it can be said that the potential distribution resulted in each case using the conventional method was not enough for appropriate cathodic protection. Therefore, it is necessary to keep the potential of the steel bar less than -0.85V. Moreover, if the concrete member has cold-joint it is also necessary to keep the potential of the steel bar at the cold-joint less than -1V based from the result in (1). Fig.12 shows the results obtained using the method proposed in this study. Electric current density 30mA/m<sup>2</sup> was applied in each case. From this figure, the potential distribution was on the range between about -0.85 and -1.0V. Therefore, the appropriate effectiveness of cathodic protection can be obtained to use the method which is to keep the potential of steel bar below -0.85V at each region on the steel bar.

5 Conclusions

The conclusions derived from this study can be summarized as follows.

- (1) It was confirmed that current and potential distribution of the steel bar under cathodic protection was influenced by material properties, especially resistance of each materials, defects in concrete, and deterioration period. In particular, current flowed locally in the steel bar at concrete defects such as cold-joint and crack. Therefore, the steel bar at defects in concrete tended to be over protected for cathodic protection in spite of deterioration period.
- (2) In the case of arrangement steel bars in concrete, it was confirmed that the potential distribution of the steel bar at distance over 250mm from the anode can not be controlled both in the experiment and the numerical analysis.
- (3) A design method of cathodic protection for reinforced concrete member was proposed. During propagation period, it was important to keep the potential of the steel bar between -0.85 and -1V in order to provide better cathodic protection.

References

- [1] Concrete Library: "Guideline of Electro-Chemical Repair Methods", JSCE, 2001.11
- [2] Shigeru Aoki, Kenji Amaya, Matsuho Miyasaka, "Boundary Element Analysis on Corrosion Problems"
- [3] Toyoharu Kobayashi, Toshio Yonezawa, Keizou Shuttou, "Diagnosis of corrosion on steel bar", 1993, 5
- [4] "Guideline of corrosive protection for marine reinforced concrete structure", JCI,1983, 2

## RC 部材中の塩化物イオンと水平鉄筋周りの境界相 が鉄筋腐食に及ぼす影響

学籍番号 : 04M18222 氏名 : 宋暘 指導教官 : 大即 信明

# INFLUENCE OF CHLORIDE ION AND ITZ AROUND HORIZONTAL STEEL BARS ON THE CORROSION OF STEEL BARS IN CONCRETE

Yang SONG

本研究では、コンクリート中の内在  $\text{Cl}^-$  濃度と水平鉄筋周りの境界相が鉄筋腐食に及ぼす影響を定量的に評価した。その結果、内在  $\text{Cl}^-$  濃度と境界相厚さが鉄筋腐食に影響することを定量的に示した。またに関連して、境界相が小さい場合（平均厚さ  $8.6\ \mu\text{m}$  以下）、 $\text{Cl}^-$  濃度が  $5\text{kg}/\text{m}^3$  と高くても腐食が発生せず境界相が大きい場合（平均厚さ  $75.3\ \mu\text{m}$  以上）、 $\text{Cl}^-$  濃度  $0.3\text{kg}/\text{m}^3$  と低くても発生する場合があることが確認された。

### Introduction

Today, steel corrosion in concrete due to chloride has become a major concern around the world. Based on the Code of the Japan Society of Civil Engineers (JSCE), the steel bar in concrete should not be corroded if the  $\text{Cl}^-$  concentration is limited under the  $1.2\text{kg}/\text{m}^3$ .

On the other hand, other than the  $\text{Cl}^-$  concentration the ITZ around the horizontal steel bar may also influence the corrosion of steel bar in concrete<sup>1)2)</sup>. The threshold value of  $\text{Cl}^-$  concentration ( $1.2\text{kg}/\text{m}^3$  by JSCE) may be changed if the ITZ around the steel bar changed. But there are few studies considering the combined effect of chloride attack and ITZ thickness on the corrosion of horizontal steel bar in concrete. Given this background, the purposes of this research are as follows: (1) To evaluate the influence of chloride ion concentration on the corrosion of horizontal steel bars (2) To evaluate the influence of ITZ around the horizontal steel bars on the corrosion of reinforced concrete exposed to chloride attack. (3) To investigate the combined effect of chloride concentration and ITZ thickness on corrosion of horizontal steel bar in concrete.

### Experimental Procedure

#### 1. Experimental Cases

In order to get different ITZ thickness, three types of specimens were prepared as follows: (1) specimens with very small ITZ size (2) specimens with normal ITZ size (3) specimens with very large ITZ size.

In order to simulate different  $\text{Cl}^-$  concentration in the specimens,  $\text{Cl}^-$  content of  $0.3\text{kg}/\text{m}^3, 0.6\text{kg}/\text{m}^3, 5\text{kg}/\text{m}^3, 10\text{kg}/\text{m}^3$  of  $\text{Cl}^-$  was admixed in the concrete mix.

#### 2.1 Detail of Specimen

(1) type-1 specimen (The casting height = 5cm, steel bar covered by cement paste before casting): Fig.1 shows the outline of the concrete specimen. Fig.2 shows the outline of the divided steel bar embedded in the concrete specimen. The divided steel bars were attached together using an epoxy resin. Lead wires were also soldered in each of steel elements in order to measure the current density flowing in the bar. Prior to the casting of concrete the horizontal steel bars were coated with cement paste (W/C = 30%) in order to simulate a very small size of ITZ.  $\text{Cl}^-$  was also admixed in the cement paste.

(2) type-2 specimen (The casting height = 5cm, the steel bar was not coated with cement paste) Fig.1 also shows the outline of the concrete specimen.

(3) type-3 specimen (The casting height = 145cm),

Fig.3 shows the outline of the reinforced concrete specimen. The higher the casting position is, the more bleeding water will be concentrated under the horizontal steel bar. In this way we can get specimens with very large ITZ.

#### 2. Mix proportion

In this research, In order to form larger ITZ around horizontal steel bar, high water mix proportions ( $w=225\text{kg}/\text{m}^3$ ) was used to simulate high bleeding in concrete.

Table 3 shows the mix proportions

3. External environment

In this research, wetting (for 24 hours) and drying (for 72 hours) cycle conditions were simulated considering the condition in the tidal zone in the sea.

4. Measurement items

The measurement items considered in this study are as follows: (1) Measurement of macrocell corrosion current density by using a zero resistance ammeter device, (2) Measurement of microcell corrosion current density by using a corrosion monitor, (3) Measurement of oxygen permeability in concrete by using a potentiostat, (4) Measurement of the size of thickness of ITZ formed around the horizontal steel bar by using a Digital Microscope, (5) Measurement of bleeding ratio of fresh concrete in each experimental case, (6) Calculation of the total corrosion rate by using (1) and (2). Lastly, (7) Calculation of the corrosion propagation by using the total corrosion rate. (Corrosion rate measurement was done at the end of the 9th cycle of the wetting and drying).

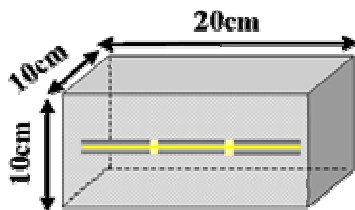


Fig.1: Outline of TYPE-1 and TYPE-2 Specimen

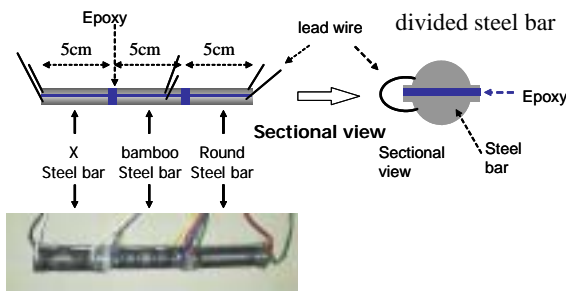


Fig.2: Outline of the divided steel bar

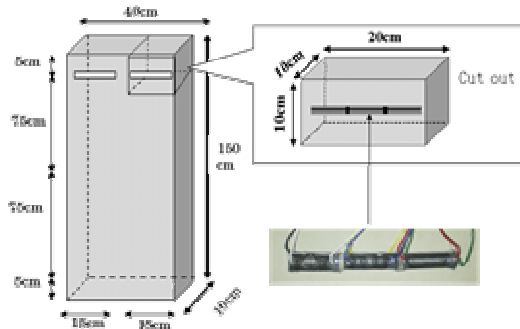


Fig.3: Outline of TYPE-3 Specimen

Table 1: Experimental Case of TYPE-1 and TYPE-2 specimen

Cl <sup>-</sup> concentration (kg/m <sup>3</sup> )	TYPE-1 specimen		TYPE-2 specimen*	
	Time of vibrating (second)			
	0	30	120	30
0.3				
0.6				
5				
10				
20				

\* Steel bar is covered by cement paste (W/C=0.3)

Table 2: Experimental Case of TYPE-3 specimen

Cl <sup>-</sup> concentration (kg/m <sup>3</sup> )	TYPE-3 specimen
0.3	
0.6	
10	
20	

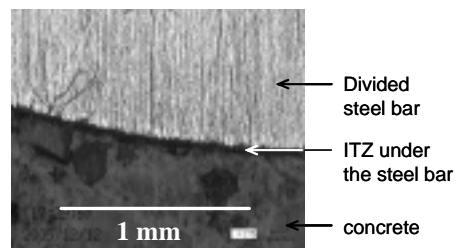


Fig.4: ITZ under the divided steel bar

Table-3 Mix Proportions

W/C (%)	W (kg/m <sup>3</sup> )	C (kg/m <sup>3</sup> )	S(kg/m <sup>3</sup> )	A(kg/ m <sup>3</sup> )	Cl <sup>-</sup> (kg/m <sup>3</sup> )	AE(g/m <sup>3</sup> )	AEWRA (g/m <sup>3</sup> )
55	225	409	760	924	10	2863	4090

AE: Air-entraining Agent

AEWEA: Air-entraining Water-reducing Agent

**Result and Discussion**

**1. Influence of Chloride Ion Concentration on the Corrosion of Horizontal Steel Bars**

Fig. 5 shows the relationship between Cl<sup>-</sup> concentration and the total corrosion rate. From the figure, we can observe that the tendency of corrosion rate in the horizontal steel bar tends to increase as the Cl<sup>-</sup> concentration increases. However, from Table 4 even in the same Cl<sup>-</sup> concentration the total corrosion rate of specimen with different ITZ thickness varies widely. This simply indicates that the Cl<sup>-</sup> concentration is not the only factor that influences the corrosion of the steel bar.

**2. Influence of ITZ around the Horizontal Steel Bars on the Corrosion of Steel in Concrete**

The criteria of corrosion is defined as follows: if the corrosion rate in the steel bar is larger than 0.00036mm/year, this means that the time until crack occurs may be under 35 years and the steel bar is said to be corroded (dangerous).

Fig.6 ~ Fig.8 shows the relationship between ITZ thickness and the total corrosion rate. As shown, in each Cl<sup>-</sup> concentration (0.3kg/m<sup>3</sup> 5 kg/m<sup>3</sup> 10 kg/m<sup>3</sup>) we can observe that the total corrosion rate in the horizontal steel bar increases as the ITZ thickness becomes larger. Presumably due to the high oxygen permeability in concrete, as shown in Fig. 9. As shown, the oxygen permeability tends to increase as the ITZ thickness becomes larger. This means that more water and oxygen diffuses into the horizontal steel bar, thereby, promoting faster and higher corrosion reaction

We can also observe that the ITZ thickness is another factor that influences corrosion in the steel bar. As shown in Fig.7, if the ITZ thickness is large enough(60.8 μm and 106 μm) the steel bar may be corroded even if the Cl<sup>-</sup> concentration is as low as 0.3kg/m<sup>3</sup>. On the other hand, in Fig.7 and Fig.9, if the ITZ thickness is small enough (less than 8.6 μm) the steel bar will not be corroded even if the Cl<sup>-</sup> concentration is higher than 5kg/m<sup>3</sup>.

**3. The Combined Effect of Chloride Concentration and ITZ Thickness on Corrosion of Horizontal Steel Bar in Concrete.**

In Fig.10, a line was drawn with the same corrosion rate (the time until the crack occur is 35years). The figure shows that both Cl<sup>-</sup> concentration and ITZ thickness significantly influences the corrosion of the steel bar. The figure also delineates the location of the safe zone and the

dangerous zone .Comparing with the safe zone as defined by the JSCE code, it was found out in this study that in some zones identified to be safe were actually not safe, on the other hand there also zones that were identified to be dangerous in the JSCE code was actually safe in this research. Defining therefore the safe zone should not only be based on the Cl<sup>-</sup> concentration but also on some other related factor such as ITZ.

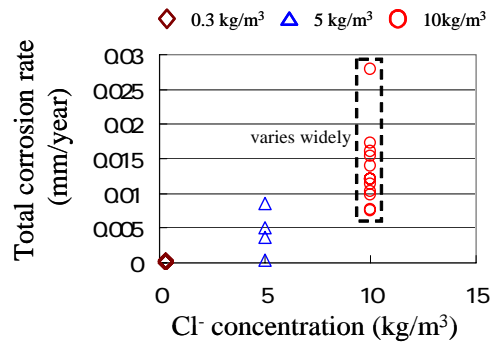


**Fig.5 Relationship between the Cl<sup>-</sup> concentration and total corrosion rate.**

**Table 4: Difference corrosion rate in same Cl<sup>-</sup> concentration**

Total Corrosion rate (mm/year)	Cl <sup>-</sup> concentration (kg/m <sup>3</sup> )		
	0.3	5	10
Maximum value	3.5 × 10 <sup>-4</sup>	8.4 × 10 <sup>-3</sup>	2.8 × 10 <sup>-2</sup>
Minimum value	9.4 × 10 <sup>-6</sup>	1.5 × 10 <sup>-3</sup>	7.7 × 10 <sup>-3</sup>
Max / Min (times)	37.45	5.48	3.64

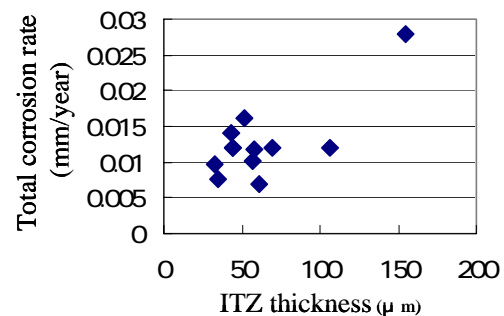


**Fig.6 Relationship between ITZ thickness and total corrosion rate. (Cl<sup>-</sup>=10kg/m<sup>3</sup>)**

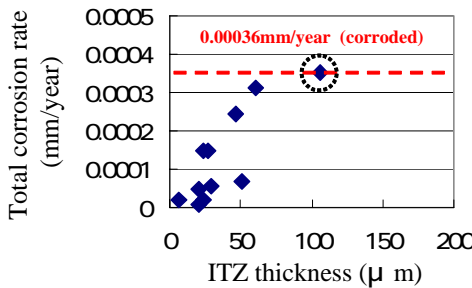


**Fig.7 Relationship between ITZ Thickness and total corrosion rate. (Cl<sup>-</sup>=0.3kg/m<sup>3</sup>)**

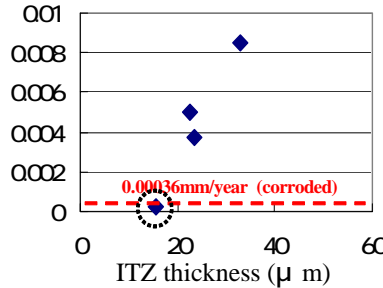


**Fig.8 Relationship between ITZ thickness and total corrosion rate. (Cl<sup>-</sup>=5kg/m<sup>3</sup>)**

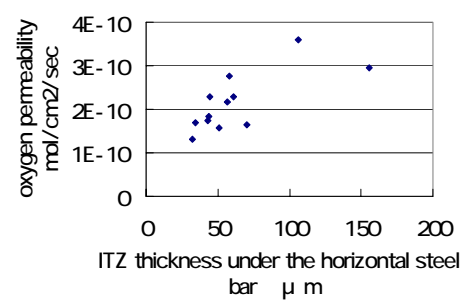


**Fig.9 Relationship between ITZ thickness and oxygen permeability. (Cl<sup>-</sup>=10kg/m<sup>3</sup>)**

- ◆ Corrosion rate = 0.00036 (mm/year)  
time until crack occur=35(years)
- Safe specimen (time until crack occur > 35 (years))
- ✕ dangerous specimen (time until crack occur < 35(years))

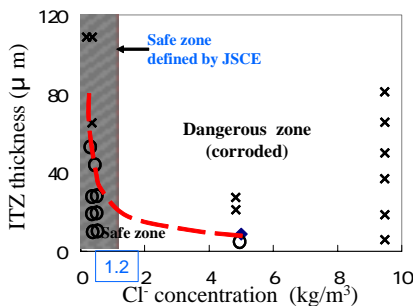


**Fig.10 Relationship between Cl<sup>-</sup> concentration and ITZ thickness**

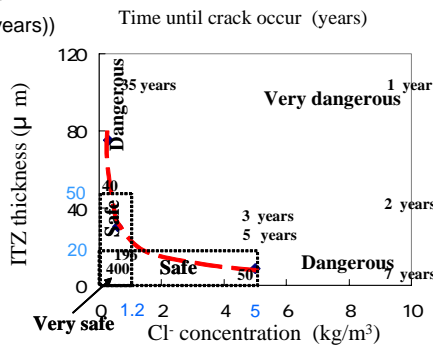


**Fig.11 Relationship between Cl<sup>-</sup> concentration and ITZ thickness**

- Time until the crack occur is over 60 years
- ✕ Time until the crack occur is less than 35 years

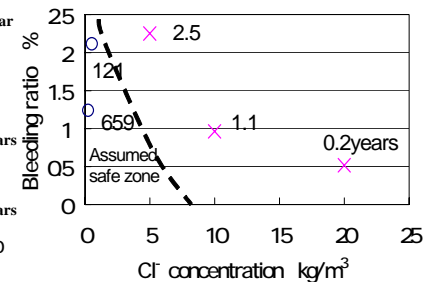


**Fig.12 Concept for finding relationship between the Cl<sup>-</sup> concentration and the bleeding ratio (casting height = 5cm)**

Fig.11 shows the time (years) until crack occurs in specimens. If the ITZ thickness is small and the Cl<sup>-</sup> concentration is low the specimens are very safe.

Fig.12 shows the concept for finding relationship between the Cl<sup>-</sup> concentration and the bleeding ratio. Since it is impractical to measure the ITZ in real structures, measurement of the bleeding ratio in the concrete mix is the best alternative. Higher bleeding ratio means more bleeding water is trapped around the horizontal steel bars causing the formation of larger ITZ. From the engineering point of view, it is important to know the relationship between the Cl<sup>-</sup> concentration and the bleeding ratio by conducting further research.

**Conclusions**

The following conclusions were derived from this study.

1. It was confirmed in this study that Cl<sup>-</sup> concentration has a great influence on the corrosion of the horizontal steel bar. However the corrosion rate of the steel bar cannot be explained only based on the Cl<sup>-</sup> concentration.
2. ITZ thickness has a great influence on the corrosion of

the horizontal steel bar. In the case of the specimens with large ITZ (over 75μm thickness), the steel bar is corroded even if the Cl<sup>-</sup> concentration is as low as 0.3kg/m<sup>3</sup>. On the other hand, in the case of the specimens with small ITZ size (less than 8.6μm thickness), the steel bar is not corroded even if the Cl<sup>-</sup> concentration is as high as 5kg/m<sup>3</sup>.

3. The corrosion rate of horizontal steel bars can be evaluated by the relationship between Cl<sup>-</sup> concentration and ITZ thickness.

**REFERENCES**

- 1) Nobuaki Otsuki et.al : Experimental Study on the effects of Rebar and Matrix Properties on the Gap at the Interfacial Transition Zones in Reinforced Concrete pp.1271-1276 , 1998 .
- 2) T.U.Mohammed et.al : Chloride-Induced Corrosion of Steel Bars in Concrete with Presence of Gap at Steel-Concrete interface , ACI Materials Journal , 99/No.2 , pp149-156 , 2002 .

# SEASONAL AND DIURNAL FLUXES OF MOMENTUM, ENERGY, WATER VAPOR AND CO<sub>2</sub> OVER TOKYO BAY

Student Number: 04M18050 Name: Ryoko ODA Supervisor: Manabu KANDA

東京湾における運動量・熱・水蒸気・CO<sub>2</sub>フラックスの季節・日変化

小田 僚子

首都圏で顕在化している都市大気環境問題に対し、隣接する東京湾における各種フラックスのシンク・ソース機構は重要な役割を果たしていると考えられる。そこで本研究では、東京湾上で長期連続的なフラックス現地観測を実施し、その結果、東京湾上の大気は都市からの移流または海陸風循環により陸域の影響を強く受けCO<sub>2</sub>のシンクになること、一般的な外洋海面と比して顕著な海表面温度日変化が現れることなど、現行の数値シミュレーションでは考慮されていない興味深い特徴が認められた。

## 1 Introduction

Most of the mega-cities in Asia are located in coastal regions. Therefore, the interaction between sea surface and the atmosphere is very important factors for understanding the Asian urban climates.

In recent years, FLUXNET have started building up since 2001 [1]. As for ocean field, sea surface flux data set for the global ocean, which were estimated from ship, in situ and satellite observations, has accomplished for the period from 1981 to 2002 [2]. Therefore various fluxes between land/ocean surface and atmosphere increase our knowledge of surface energy balance. On the other hand, few studies has reported air-water interaction in closed or semi-closed water area, such as lake and bay, especially which adjacent to the mega-cities. This is probably because that the sea surface is believed to be insensitive to diurnal variation of radiative forcing due to its large heat capacity. Actually, in most of the mesoscale numerical predictions, it is assumed that surface temperature is constant and that CO<sub>2</sub> flux is zero. These assumptions are derived from the data measured in ocean surface far from the land. However, these assumptions would not be the case for the closed/semi-closed water surface, especially which adjacent to the mega-cities. They often have limited fetch and are expected to be influenced by the advection from the land. Hence, it is necessary to measure sea surface temperature or the fluxes based on direct measurement with the aim of accurate estimating about air-water interaction.

In this study, I focused on the flux based on direct measurement in Tokyo Bay. Tokyo Bay is adjacent to Tokyo Metropolitan area, which is expected to mitigate the severe atmospheric environment in Tokyo. I constructed a flux measurement system in Tokyo Bay, and investigated the fluxes between the sea surface and the atmosphere.

The purposes of this study are (1) to evaluate the fluxes by the eddy correlation method, and (2) to understand the seasonal and diurnal pattern of the measured fluxes. Also the observational results were compared with that at a suburban area (Kugahara) in Tokyo [3].

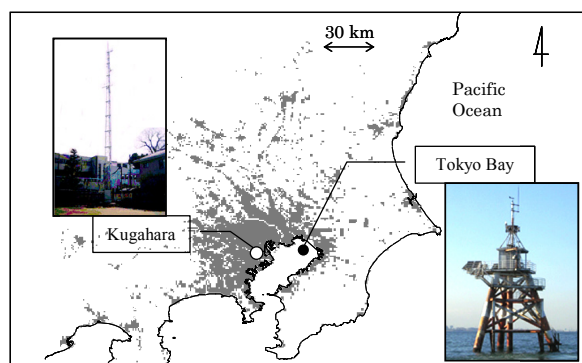


Fig.1 Environment of the study sites. Location of Tokyo Bay and Kugahara tower in Japan. Gray area indicates built-up area where artificial structures occupy significant surfaces. The data source is “Global Map” (ISCGM), available from <http://www.iscgm.org/>.

## 2 Methods

### 2.1 Site Description

The study sites belong to the monsoon region that the wind directions have the seasonal reversal. Wind blows the south during summer and from the north during winter.

**Tokyo Bay** – The measurements have been conducted at the height of 12 m above mean sea level by using an existing tower (N35.6°, E140.0°) since December, 2004. The shortest distance from the land is about 3 km in the direction of northeast. The seacoast region is almost an industrial area which includes a food complex, steel and a petrochemical complex.

**Kugahara** – The measurements have been made since May 2001 in a low-residential area, which mainly consists of densely built-up houses, paved roads and small playgrounds, in Kugahara, Tokyo (N35.6°, E139.7°). The height of a tower is 29 m. There is a homogeneous residential area that the mean building height is 7.3 m over 1 km. The distance to Tokyo Bay tower is about 30 km.

### 2.2 Experimental Setup

I measured wind speeds, air temperatures, water vapor densities, CO<sub>2</sub> densities and radiant intensities at each site. Fluctuations of wind speeds and air

Table 1 The list of the observation equipments

Items	Tokyo Bay		Kugahara	
	Instruments	sampling	Instruments	sampling
wind speed	3-D Sonic Anemometer	10Hz non ave.	Ultrasonic Anemometer	8Hz non ave. Height : 29m
air temperature	(Campbell Scientific Inc., USA ; CSAT3)	Height : 12m above mean sea level	(Metek GmbH, Germany ; USA-1)	
CO <sub>2</sub> gas	Open Path CO <sub>2</sub> /H <sub>2</sub> O Analyser	1Hz 10min. ave. Height : 12m above mean sea level	Open Path CO <sub>2</sub> /H <sub>2</sub> O Analyser	1Hz 20min ave. Height : 25m
H <sub>2</sub> O gas	(LI-COR, Inc., USA ; LI-7500)		(LI-COR, Inc., USA ; LI-7500)	
up/downward shortwave radiation	Pyranometers	(Kipp&Zonen, Netherlands ; CM3)	Pyranometers	(Eko Instruments, Japan ; MS-62,42)
up/downward longwave radiation	Pyrgeometer		Pyrgeometer	

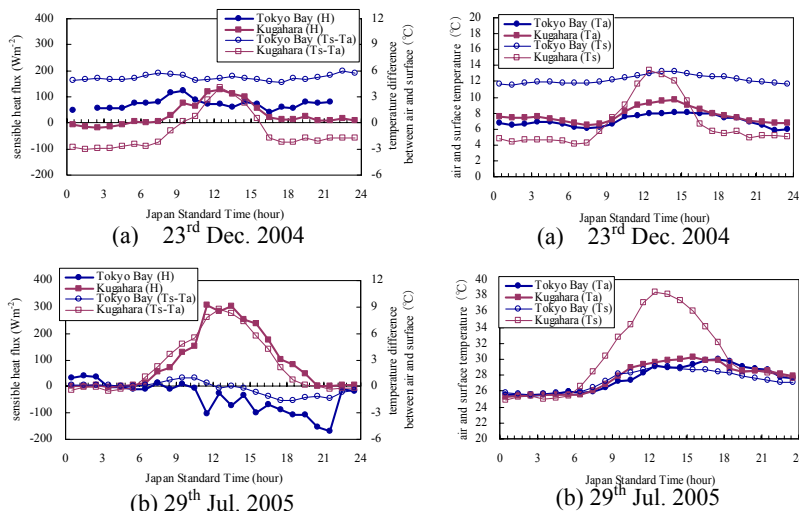


Fig. 2 Diurnal variations of sensible heat flux ( $H$ ) and a difference of temperature ( $T_s-T_a$ )

Fig. 3 Diurnal variations of air temperature ( $T_a$ ) and surface temperature ( $T_s$ )

temperatures were measured by a three-dimensional sonic anemometer. Densities of CO<sub>2</sub> and water vapor were measured by an open-path type infrared gas analyzer. Up and downward short- and long-wave radiation intensities were measured separately by using two sets of pyranometers and pyrgeometers. Table 1 shows the observation equipments which were installed at each site.

### 2.3 Data Processing

The fluxes of momentum, energy, water vapor and CO<sub>2</sub> were evaluated by the eddy correlation method every 60 minute. For example, data of 8 o'clock means an average of 8 to 9 o'clock (JST). Over Tokyo Bay, note that data of the radiant intensities were the instantaneous values every hour until the middle of July, and data of absolute air temperature was corrected using data at a nearest weather station, which was located in Tokyo Bay water front. The water vapor and CO<sub>2</sub> fluxes were corrected for the effect of fluctuations in air density. Coordinate axes were rotated so that mean vertical velocity was zero.

For the evaluation of diurnal courses, I discuss the fluxes of data from December and July because each data was representative for winter and summer, respectively.

As for the evaluation of seasonal courses, I used data of 12 o'clock, which show clearly difference between Tokyo Bay and Kugahra due to strong radiant intensity. But it was removed that the data due to precipitation or sensor malfunction. I analyzed the data from December 2004 to November 2005. Mean wind direction was

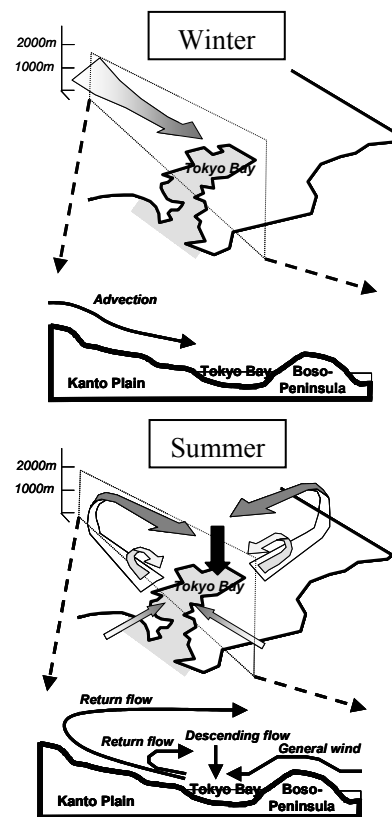


Fig. 4 Schematic depiction of advection and sea breeze circulation

calculated using mean wind vector. I defined that upward flux was positive.

### 3 Diurnal Variation of Fluxes in Summer and Winter

In this discussion, the results for two specified days, 23<sup>rd</sup> December 2004 and 29<sup>th</sup> July 2005, which are typical one in winter and summer, are used.

#### 3.1 Momentum Flux

Momentum flux  $M$  ( $\text{kgm}^{-1}\text{s}^{-2}$ ) over Tokyo Bay was smaller than that in Kugahara in spite of strong wind (not shown here). This is because that sea surface is smoother than urban surfaces.  $M$  showed a little dependency on wind speed  $WS$ , especially in the range of  $WS$  over  $10 \text{ ms}^{-1}$ . Windswell develops as  $WS$  increase over sea, i.e. the roughness of the surface becomes larger with strong  $WS$ .

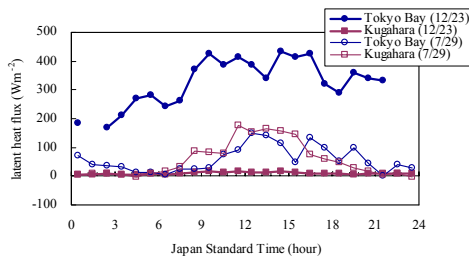


Fig. 5 Diurnal variations of latent heat flux ( $LE$ )

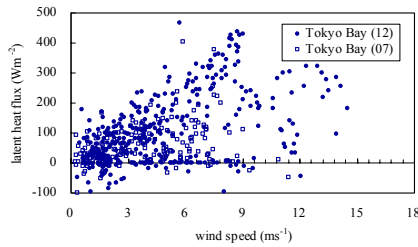


Fig. 6 The relation between latent heat flux ( $LE$ ) and wind speed

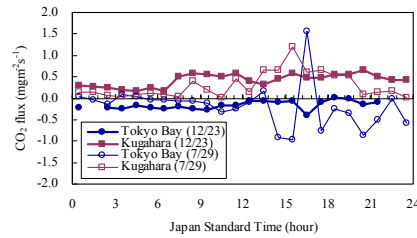


Fig. 7 Diurnal variations of  $CO_2$  flux

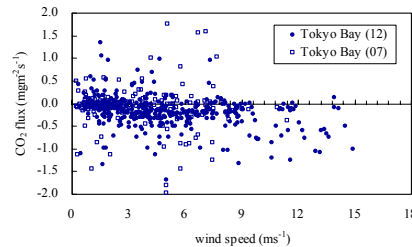


Fig. 8 The relation between  $CO_2$  flux and wind speed

### 3.2 Sensible Heat Flux

Figure 2 shows the diurnal variation of sensible heat flux  $H$  ( $Wm^{-2}$ ) and the difference of temperature  $[T_s - T_a]$  (surface temperature minus air temperature),  $T_s$  and  $T_a$  are shown in Fig. 3.  $T_a$  in Kugahara can be regarded as a representative of urban air temperature because the diurnal course of  $T_a$  in Kugahara was similar to that of Ootemachi, central business district in Tokyo (not shown here).  $T_s$  was derived from Stefan-Boltzmann law assumed that emissivity is 0.98 in Tokyo Bay and 1.0 in Kugahara.

The variation of  $H$  is corresponding to  $[T_s - T_a]$ .  $H$  over Tokyo Bay tended to begin to decrease in the midmorning (Fig. 2).  $T_s$  had a peak in the early afternoon, whereas  $T_a$  over Tokyo Bay was still high even in the late afternoon (Fig. 2). Moreover,  $T_a$  over Tokyo Bay had a wide daily range compared with  $T_s$ . This is because that the advection and sea breeze circulation occur in winter and summer, respectively. In winter, there mainly occurs the advection from land to sea due to the Asia monsoon. In summer, Ishii et al. [4] suggested that the atmosphere over Tokyo Bay was influenced by urban air due to the sea breeze circulation, and thus the air above Tokyo Bay was adiabatically heated due to the subsidence flow. These would cause air temperature over Tokyo Bay is high even in the late afternoon, and it to be warmer than the sea surface temperature. Schematic of advection and sea breeze circulation are shown in Fig. 4.

In addition, the diurnal range of  $T_s$  in Tokyo Bay was larger than that in the open sea [5]. As I described in introduction, the diurnal change of sea surface temperature is ignored in the current numerical models. But this assumption is not adequate for the closed/semi-closed water area adjacent to the mega-city.

### 3.3 Latent Heat Flux

Figure 5 shows the diurnal variation of latent heat flux  $LE$  ( $Wm^{-2}$ ).  $LE$  over Tokyo Bay was positive in all

days, and especially in winter the magnitude was much larger. This is probably because in winter drier air was advected to Tokyo Bay, and thus the evaporation was enhanced. Figure 6 shows the relationship between  $LE$  and wind speed  $WS$ .  $LE$  over Tokyo Bay varied corresponding to  $WS$  especially in winter. This result suggests that  $WS$  was a more important factor for the magnitude of  $LE$  in winter rather than radiative forcing.

### 3.4 $CO_2$ Flux

Figure 7 shows diurnal variation of  $CO_2$  flux. The flux of  $CO_2$  in Tokyo Bay was negative ( $CO_2$  sink), whereas that in Kugahara was positive ( $CO_2$  source) throughout the day. These results were attributed to that the air of high  $CO_2$  density in the urban area was transported over Tokyo Bay due to advection in winter or sea breeze circulation in summer. In recent years, several researchers have made a study on gas exchange at the air/water interface and pointed out that wind speed  $WS$  over about  $10 ms^{-1}$  increased gas transfer velocity [6]. Negative  $CO_2$  flux was corresponding to  $WS$ , especially over  $10 ms^{-1}$ , in our observation (Fig. 8).

## 4 Seasonal Variation of Fluxes

Figures 9 (a) to (e) show in the variation of the fluxes of momentum  $M$ , sensible heat  $H$ , latent heat  $LE$ ,  $CO_2$ , and net radiation  $R_n$  and storage heat  $G$ , respectively.

$M$  over Tokyo Bay was smaller than that in Kugahara throughout the year (annual mean value was  $0.03 kgm^{-1}s^{-2}$ ,  $0.39 kgm^{-1}s^{-2}$ , respectively) (Fig. 9 (a)). As mentioned in 3.1, sea surface is smooth, i.e. the surface drag is very small. Therefore the atmosphere over Tokyo Bay is not conductive to vertical exchange.

$H$  was smaller than that in Kugahara (Fig. 9 (b)).  $H$  in Tokyo Bay was positive in winter whereas it was negative in summer. As mentioned in 3.2, the variation of  $H$  over Tokyo Bay depended on the advection or sea breeze circulation.

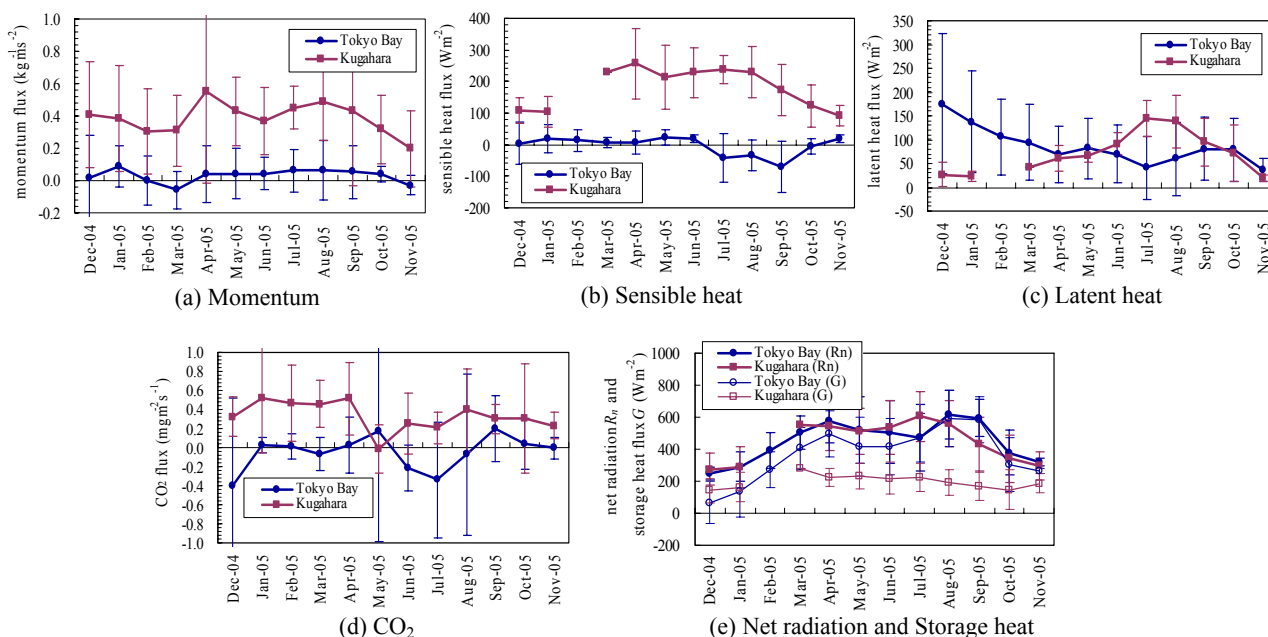


Fig. 9 Seasonal variation of the fluxes

*LE* over Tokyo Bay was positive in all seasons (Fig. 9 (c)). Dry air moved from the land to Tokyo Bay due to advection or sea breeze circulation. Therefore, the evaporation would be activated in Tokyo Bay even in summer. On the other hand, vapor-pressure deficit had not significant seasonal variation, whereas that in Kugahara was shown seasonal course correspond to *LE* (not shown here). These results suggest that *LE* over Tokyo Bay depends on wind speed *WS* rather than solar radiant intensity.

The flux of CO<sub>2</sub> in Tokyo Bay had large scatter but negative flux was sometimes obtained, whereas that in Kugahara was positive during almost all seasons (Fig. 9 (d)). These results indicate that the urban air of high CO<sub>2</sub> density was transported to Tokyo Bay. This caused a difference of the CO<sub>2</sub> density between the atmosphere and the vicinity of water surface, and thus the CO<sub>2</sub> flux was downward over Tokyo Bay. The negative flux was shown especially in December and July, because advection and sea breeze circulation is significant in winter and summer, respectively.

*G* is determined as the energy balance residual from direct observation of *R<sub>n</sub>*, *H* and *LE*.

$$G = R_n - H - LE \tag{1}$$

*G* in Tokyo Bay was larger in summer whereas that in Kugahara did not have significant seasonal change (Fig. 9 (e)). The large *G* in Tokyo Bay was because *H* and *LE* decreased (see Fig. 9 (b)(c)) and *R<sub>n</sub>* increased in summer. The large amount of energy almost equal to *R<sub>n</sub>* was stored in Tokyo Bay in summer.

## 5 Conclusions

The evaluation of closed/semi-closed water area based on direct flux measurement is very important but not well-known. I measured the fluxes in order to precisely and quantitatively evaluate the atmospheric

impact of Tokyo Bay.

Through my observation study, it was found that Tokyo Bay acts as source of heat in winter, sink of heat in summer, and source of water vapor and sink of CO<sub>2</sub> almost throughout a year. This is because the fluxes were influenced by the urban air due to advection and/or sea breeze circulation. The advection and/or sea breeze circulation also influence on larger diurnal range of sea surface temperature.

In these result, it should be noted that significant diurnal change of sea surface temperature occurred and that CO<sub>2</sub> flux was not zero. Therefore, current numerical models should include the diurnal change of sea surface temperature and the variation of CO<sub>2</sub> flux.

## References

- [1] FLUXNET: <http://www.fluxnet.ornl.gov/fluxnet/index.cfm>
- [2] Objectively Analyzed Air-Sea Fluxes (OAFlux) for the Global Oceans: <http://oafux.whoi.edu/data.html>
- [3] Moriwaki, R., Kanda, M., "Seasonal and Diurnal Fluxes of Radiation, Heat, Water Vapor, and Carbon Dioxide over a Suburban Area", *J. Appl. Meteorol.* **43**, pp.1700-1710, 2004.
- [4] Ishii, H., Kanda, M., Moriwaki, R., Okuzono, K., "Observational Study on The Atmospheric Environment over Tokyo Bay", *Annual J. Hydraulics Eng.*, **43**, pp.233-238, 1999. (in Japanese)
- [5] Kawai, Y., Kawamura, H.: "Evaluation of the Diurnal Warming of Sea Surface Temperature Using Satellite-Derived Marine Meteorological Data", *J. Oceanogr.*, **58**, pp.805-814, 2002.
- [6] Asher, W. E., Wanninkhof, R., "The effect of bubble-mediated gas transfer on purposeful dual-gaseous tracer experiments", *J. Geophys. Res.*, **103**, pp.10,555-10,560, 1998.

# Turbulent flow similarity in open air scaled models for urban micro meteorology

Student Number: 04M18073 Name: Masahiko KANEGA Supervisor: Manabu KANDA

## 屋外スケールモデル実験における乱流相似則の検討

金賀 将彦

屋外スケールモデルは都市接地層の微気象を研究するための有効な手段である。本研究ではこのスケールモデルで得られた結果の都市への応用性を調べるために、乱流相似則の成立を確認した。この検証に基づき、相似則理論の下で用いられている運動量粗度、熱粗度を算出した。運動量粗度は地表面形状の変化にかなり敏感であること、一方熱粗度は地表面形状に対して鈍感であるが、地表面代表温度のとり方でその挙動が大きく変わってしまうことがわかった。

### 1. Introduction

Atmospheric surface layer is the main sink or source of momentum, heat, and scalars in the whole atmosphere. Therefore, it is important to investigate how these quantities are transported into the air above from the surface layer. These issues have been well investigated in relatively flat terrain, or vegetation surface, but not enough in city because of its complexity and economical and social restriction. If one overcomes and observation is conducted in cities, the representativeness of these results is often doubted due to inherent inhomogeneity in city: variability of the local land use, and the configuration.

To clarify these uncertainties, scaled models were constructed in outdoor. Simple cubic elements reduced its dimension were arranged in flat concrete plate. And then, various measurement equipments were installed there. The advantages of using outdoor scaled models for the research of urban micro meteorology are following: first, natural forcing of momentum and heat, which is difficult to recreate in wind tunnel, is realized. Second, homogeneous roughness array makes the problem referred above simple. Third, various physical quantities are measurable. From these characteristics of the outdoor scaled models, it is expected that it becomes effective tool or infrastructure for the study of urban micro meteorology.

Until now, the outdoor scaled models have contributed much to the modeling of urban heat budget [1]. However, detailed analysis about air flow such as the similarity of the turbulent flow between the scaled models and real surface layer, has not been focused on. The similarity of the flow is basic, but critical assumption for the scaled models. Therefore, in this paper, the nature of the turbulent flow over the outdoor-scaled models, and the applicability of the existing similarity theory

were investigated using the same scale models with different size. And then, based on its results, roughness length for momentum and heat, which is treated within the framework of the similarity theory, and which determines the efficiency of transport of momentum and heat in many atmospheric models, was calculated and its behaviour was investigated.

### 2. Overview of Experiments

Two different scale models (named '1/5 model' and '1/50 model' after the average height of the residential area of Kugahara, Tokyo) were constructed at the private ground of Nippon Institute of Technology (39.04N, 139.7E).

The description of 1/5 model is following. 1.5m-concrete cubes are regularly arranged spacing the same distance of its length, on the flat concrete plate of 100×50 m. Land use around the site is almost rice fields. Three slender towers for measurement instruments are at the center, and both ends of the model. Instruments used, measured component, and data acquisition period is Fig.1 and table 1.

1/50 model is almost the same but its size and the way to install the instruments. The length of the cube is 0.15m, and its base is 12m-square plate placed near the 1/5 model (separated from about 15m). The configuration of cubes is completely the same as that of 1/5 model. Instead of towers, steel pipes (φ=4.8cm) were built up for the setting of instruments.

For the following analysis, temporal averaging was over 60 minutes and fluctuation was calculated with linear detrending for every component. The data acquired was almost unstable condition even in nighttime, due to the large heat capacity of concrete, so only the unstable case was analyzed.

### 3. Theoretical background

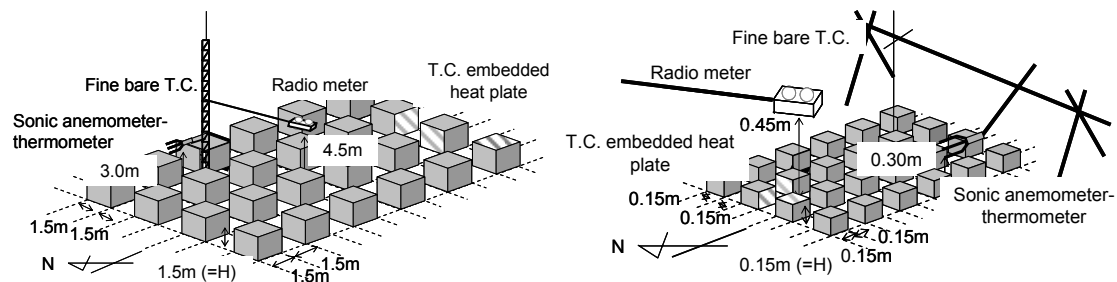


Figure 1 Schematic diagram of scale models and measurement instruments (left: 1/5model, right: 1/50model)

table 1 Instrument used, measured components, and period the data acquired

Instrument	Sonic anemometer	Fine bare thermocouple	Shortwave longwave radio meter	T.C. embedded heat plate
Measured component	wind component $u, v, w$ ( $\text{ms}^{-1}$ ) sonic temperature $T$ (K)	air temperatures $T_a(z)$ (K)	downward shortwave $S \downarrow$ ( $\text{Wm}^{-2}$ ) upward shortwave $S \uparrow$ ( $\text{Wm}^{-2}$ ) downward longwave $L \downarrow$ ( $\text{Wm}^{-2}$ ) upward longwave $L \uparrow$ ( $\text{Wm}^{-2}$ )	conductive heat flux of each face $i$ $G(i)$ ( $\text{Wm}^{-2}$ ) surface temperature of each face $i$ $T_s(i)$ ( $\text{Wm}^{-2}$ )
Period data acquired	04 12/16- 05 8/2, 05 10/21- 05 12/19 (1/5)	04 12/16- 05 8/2, 05 10/21- 05 12/19	04 12/16- 05 8/2, 05 10/21- 05 12/19	05 10/21- 05 12/19
(1/50)	the same above	the same above	the same above	04 12/27- 05 12/19

Monin-Obukhov Similarity theory (MOS) is surface layer similarity theory, discussed here. Its essence is that, in horizontally homogeneous terrain with stationary condition, any properties concerned in air flow can be scaled by  $u_*$ ,  $T_*$ ,  $z$ , and  $L$ , and the resultant nondimensional properties become only the function of  $z/L$ , a measure of atmospheric stability. Definitions of  $u_*$  ( $\text{ms}^{-1}$ ),  $T_*$  (K),  $L$  (m) are following:

$$u_* = (-\overline{u'w'})^{0.5} \quad (1)$$

$$T_* = -\overline{w'T'}/u_* \quad (2)$$

$$L = u_*^2 / k(g/T)T_* \quad (3)$$

where,  $\overline{u'w'}$  is momentum flux ( $\text{m}^2\text{s}^{-2}$ ),  $\overline{w'T'}$  is sensible heat flux ( $\text{Kms}^{-1}$ ),  $k$  is Karman constant (0.4),  $g/T$  is gravity parameter ( $\text{ms}^{-2}\text{K}^{-1}$ ),  $z$  is height from the ground (m), and  $u$ ,  $w$ ,  $T$ , is along wind, vertical wind ( $\text{ms}^{-1}$ ) and temperature (K) component, respectively. Dash denotes fluctuation from mean value and overbar denotes temporal mean.

For mean wind and temperature profile, assuming constant flux layer and integrating the flux-gradient relationships over  $z$ , following formula is derived:

$$U(z')/u_* = [\ln(z'/z_m) + \Psi_M(z'/L, z_m/L)]/k \quad (4)$$

$$-(T_{aero} - T_s(z'))/T_* = [\ln(z'/z_T) + \Psi_H(z'/L, z_T/L)]/k \quad (5)$$

where,  $U(z')$  is mean, along wind ( $\text{ms}^{-1}$ ) at height  $z'$ ,  $T_{aero}$  is representative temperature (K) at  $z_T + d$  called aerodynamic temperature (referred after),  $T_a(z')$  is air temperature (K) at height  $z'$ ,  $\Psi_M$  and  $\Psi_H$  are stability correction terms, and  $z'$  equals to  $z - d$ ,  $d$  (m) is set up value for high roughness, called displacement height. The concept of roughness length for momentum  $z_m$  and heat  $z_T$  (m) appears here. These parameters mean the conductance of fluxes against mean properties, and are determined by the characteristics of surface, not depending on the state of flow, in MOS framework.

For spectra  $S(f)$  of  $u, w, T$ , and cospectra  $Co(f)$  of  $u'w'$ ,  $w'T'$  (where,  $f$  is frequency ( $\text{s}^{-1}$ )), MOS is also valid. Kaimal and Finnigan [2] showed the nondimensional form of spectra and cospectra.

These formulae were derived from horizontally homogeneous, flat terrains, and the validity of these has been confirmed in many places. The results obtained in flat terrain are compared with the results obtained in scale models, and the similarity is discussed in following chapter. The results obtained in flat surface are indicated as 'ref', or 'MOS', hereafter.

## 4. Results and Discussion

### 4.1 Flow similarity

Figure 3 shows cospectra of  $u'w'$  and  $w'T'$  with all stability range. In unstable ( $-0.1 > z'/L$ ) ones, the plots disappear at low frequency part, and the other

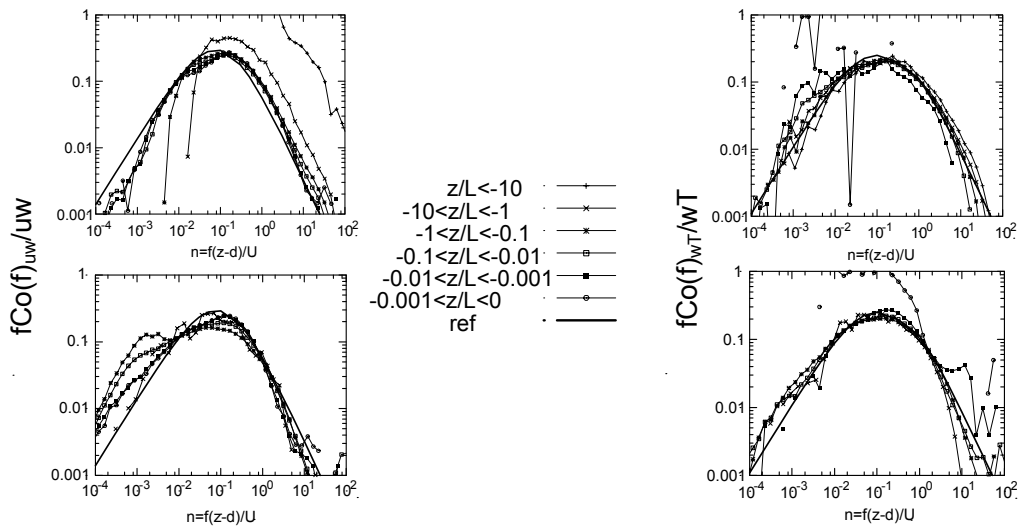


Figure2 Cospectra of  $u'w'$  and  $w'T'$  (upper: 1/5 lower: 1/50). 'ref' is from [2].

plots increase in 1/5 model of momentum transport. This means inverse correlation ( $u'w' > 0$ ) at low frequency part. On the other hand, also in unstable ( $-0.01 > z'/L$ ) case, low frequency contribution clearly appears in 1/50 model of momentum. In common, the low frequency contributions not observed in MOS appear. Assuming Taylor's frozen turbulence hypothesis, the low frequency phenomena mean large scale eddy motions beyond the measurement height or whole site scales. It is out of MOS framework. Generally, it is said that MOS works ranging to  $z'/L = -10$ , and stability indicated above is within this range. However, MOS is violated. Probably, the outer layer eddy, originated from convective mixed layer or outer surface layer affects on and thus, the local  $z'/L$  is inappropriate to a measure whether MOS works or not. Outer layer information would be needed to quantify these phenomena, but we don't have. However, qualitatively, these are suggestive results for the problem of the source area of momentum in unstable, convective conditions. In neutral case, in other words, greater  $z'/L$  than indicated above, momentum cospectra fairly agree with the MOS, even though the contribution of lower frequencies is still observed, especially in 1/50 model. From these results, we judged MOS framework for momentum transport is valid in neutral case.

Cospectra of sensible heat surprisingly agree well with MOS in unstable condition, and the low frequency contribution is not observed. This fact is also interesting. Physical interpretation about the inconsistency of turbulent transfer between

momentum and heat in convective condition observed in this site is difficult and cannot be answered here, but the result may give hints when the turbulent transfer in complex terrain is studied. In neutral case, cospectra of sensible heat cannot be define because of low correlation between  $w$  and  $T$ . Additionally,  $T$  includes the noise of sensor (from spectral results, not shown). From the results above, similarity of turbulent transfer about sensible heat holds though there remains uncertainty in neutral case.

#### 4.2 Roughness length for momentum and heat

Roughness length was estimated by least square fit to the equation (4) and (5), using observed values within the stability range specified above discussion. Displacement height was determined by the model proposed by Macdonald et al. [3]. The estimate for scale model configuration is  $d/H = 0.455$ .

Fig.3 shows the relation between roughness length for momentum and wind direction. 0 (deg) indicates the wind direction from the long axis of the site. In the site, geometric configuration for wind changes with wind direction: Frontal area index, defined as the area of roughness element projected by the wind direction over unit plan area, increases with wind direction (0.25 for 0 to 0.35 for 45 (deg)), and arrangement also changes from square array (0deg) to staggered array (otherwise). Roughness length for momentum is sensitive to the change of the configuration in this building-area ratio (0.25). The estimates from the model equation of roughness length for momentum proposed by Macdonald et al.

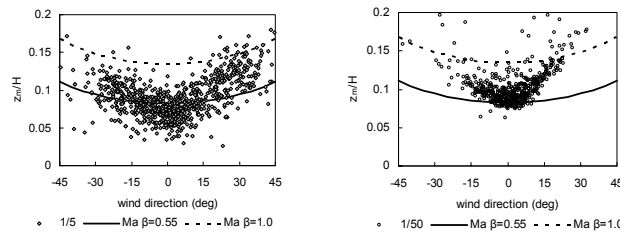


Figure3 Roughness length for momentum .vs. wind direction: Ma indicates the model estimates by Macdonald et al. [3].  $\beta$  means parameter for arranging: 0.55 is for square, 1.0 is for staggered.

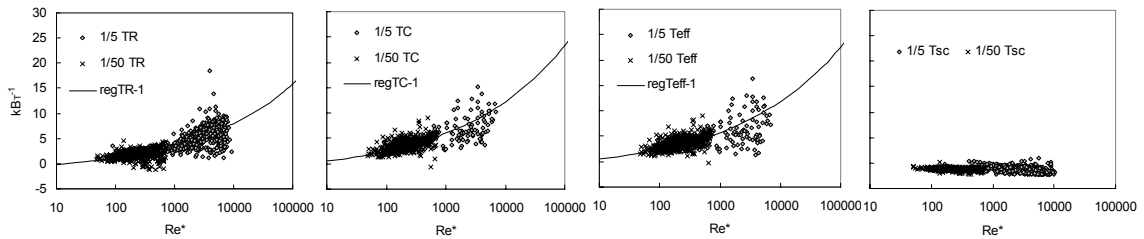


Figure4  $kB_T^{-1} = \ln(z_m/z_T)$  .vs.  $Re^*$  for various  $T_{aero}$  . Each character is defined in the text.

[3] are also plotted in Fig 3. Model parameters of this are  $d/H$  , frontal area index, and the arrangement (staggered or square). It reproduces reasonable results. As the first approximation, the existing model is sufficiently valid.

Estimation of roughness length for heat is more difficult than that for momentum, because  $T_{aero}$  is another unknown for the estimation. In this paper, three types of the representative surface temperature ( $T_R$  , radiation temperature: derived from emitted long wave radiation from the surface,  $T_C$  , complete surface temperature: area weighted surface temperature, and  $T_{eff}$  , effective surface temperature: area and local heat transfer coefficient weighted temperature [1]), and the air temperature inside the canyon space ( $T_{sc}$  screen temperature: air temperature measured at 0.5H) were examined for  $T_{aero}$  .

Fig.4 shows the ratio of roughness length for momentum to heat against roughness Reynolds number defined as  $Re^* = z_m u_* / \nu$  , where  $\nu$  is molecular viscosity. The estimates of  $z_T$  by substituting the surface temperatures for  $T_{aero}$  have dependency on roughness Reynolds number, while the estimates by  $T_{sc}$  doesn't. This result means  $z_T$  derived from the surface temperatures has dependency on scale, strength of wind shear, and molecular viscosity. MOS framework is not valid for them because they depend on the state of the flow. On the other hand,  $z_T$  from the screen temperature has no dependency on  $Re^*$  and thus, MOS framework is valid.

**5. Conclusion**

Turbulent flow similarity between real surface layer and the scaled models in open air was investigated. Momentum transfer in unstable condition does not follow the existing similarity theory due to the effect of outer layer phenomena. In near neutral case, similarity theory generally holds. For sensible heat transfer, it holds in unstable case, and is obscure in neutral case.

Based on the discussion above, roughness length for momentum and heat were calculated and its behaviour was investigated. Roughness length for momentum is sensitive to the surface configuration in this building density. Roughness length for heat derived from the surface temperature depends on roughness Reynolds number and thus beyond the framework of similarity theory. Whereas roughness length for heat derived from the screen temperature is independent of roughness Reynolds number and scalable by roughness length, and thus, it is within similarity framework.

**Reference**

[1] Kanda,M., Kawai,T., Kanega,M., Narita,K., and Hagishima,A., 2005: A Simple Energy Balance Model for Regular Building Arrays. *Boundary Layer Meteorology*, **116**, 423-443.  
 [2] Kaimal,J.C., and Finnigan,J.J., 1994: *Atmospheric Boundary Layer Flow (Their Structure and Measurement)*, Oxford University Press.  
 [3] Macdonald,R.W., Griffiths,R.F., and Hall,D.J., 1998: An Improved Method for the Estimation of Surface Roughness of Obstacle Arrays. *Atmospheric Environment*, **32**, 1857-1864.

## OBSERVATION STUDY ON WATER AND HEAT TRANSFER PROCESSES IN URBAN SEWAGE SYSTEM

Student Number: 04M18156 Name: Yu NAKAYAMA Supervisor: Manabu KANDA

### 都市下水道による水・熱輸送過程に関する観測研究

中山 有

近年、都市の過密化・拡大に伴いヒートアイランド現象をはじめとした熱環境の悪化が明らかになっている。本研究では都市において利用された水・熱が都市下水道を通じてどのように水圏へと流出していくのかを明らかにするために2つのスケールで観測を行った。1つは水・熱利用の起点となる住宅地における観測であり、もう1つは都市全体で利用された水を集める下水処理場での観測である。観測の結果、住宅地および都市全体における年間水・熱フローが明らかになり、都市の水・熱環境における下水道の役割が判明した。

## 1 Introduction

The expansion and concentration of urban areas cause the urban environment degradation, e.g. revealed as heat island phenomena. Many researchers have reported on the anthropogenic heat impact to the atmosphere, while few researchers have reported on the impact to the hydrosphere. However, the temperature of water discharged from wastewater treatment plant (WWTP) has been increasing for the past 35 years [1] and the discharged water may harm the environment of the hydrosphere such as rivers and the sea adjacent to an urban area.

The water transfer and heat transfer in urban areas consist of not only meteorological fluxes like net radiation and sensible heat flux, but also underground fluxes like tap water and sewage. Such an artificial drainage system represented by tap water and sewage is one of the major features of urban areas.

Moriwaki and Kanda have pointed out that surface water and heat flux impact on the atmosphere in an urban residential area [2], but how the fluxes contribute to an artificial drainage system was unknown. Thus, two scale observations were executed to study water and heat flow processes in the drainage network. First, the water and heat balance was observed in a residential area that generates the origin of wastewater flow [3, 4]. Second, water and heat transfers were observed at WWTP targeting whole urban area. Based on these observations, this thesis describes the estimation of anthropogenic heat due to water use, and the water and heat transfer processes in an urban drainage system.

## 2 Water Balance and Heat Balance in a Residential Area

Residential water use dominates the most of urban water use. Therefore a residential area was chosen as an origin for the measurement of the water and heat balance in an urban area.

### 2.1 Outline of the Observations

Observations were conducted in the residential area of Kugahara, Ota-ku, Tokyo metropolitan. At first, the flow rate and temperature of sewer were measured downstream of a catchment to evaluate water and heat flux discharged from the residential area (Fig. 1). The catchment area is 12-ha and 1830 residents live in 407 dwellings in this area. Analysis of aerial photographs and GIS data show that 34 % of the land cover in this area is pervious, while 66 % of it is impervious. Combined sewer system have been developed in the catchment. Moriwaki and Kanda have already observed meteorological flux by tower-based measurements a tower (Meteorological measurement site on Fig. 1).

Rain is one of the major inputs of water and heat to the catchment. Therefore, the hydrological measurement site has been set in a vegetated field near the catchment, where precipitation and air temperature are observed. To evaluate the water storage of pervious area and measure the soil temperature, soil moisture sensors and temperature sensors have been set at 6 depths from the ground to the depth of 2 m.

Tap water is another major input, and the corresponding data is provided by the bureau of waterworks, Tokyo metropolitan government.

### 2.2 Water Balance in a Residential Area

Water flow in a residential area can be divided into two drainage systems; an artificial drainage system (ADS) and a natural drainage system (NDS). The artificial drainage system consists of water supply pipes, residence and sewage pipes that receive tap water as input and discharge sewage as output. The natural drainage system comprises underground soil that receives rain as input and discharges evapotranspiration, leaching water and surface runoff into sewage pipes as output (Fig. 2). The different drainage systems and its constituents can be described by equation (1) and (2) respectively.

$$\text{ADS: } Q_I + Q_{GW} + Q_S = Q_O \quad (1)$$

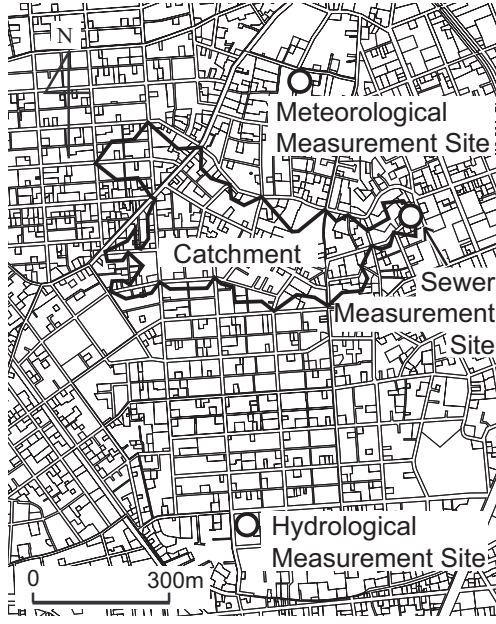


Figure 1: The arrangement of measuring instrument

$$\text{NDS: } Q_R = Q_E + Q_{GW} + Q_S + \frac{dS}{dt} + Q_A \quad (2)$$

where  $Q_I$  is tap water,  $Q_{GW}$  is leaching water from soil to sewage pipe,  $Q_S$  is surface runoff,  $Q_O$  is total runoff,  $Q_R$  is rain,  $Q_E$  is evapotranspiration,  $dS/dt$  is the change in water storage and  $Q_A$  is advection flow. Combining the two equations, we can express the whole drainage system (WDS) as equation (3).

$$\text{WDS: } Q_R + Q_I = Q_E + Q_O + \frac{dS}{dt} + Q_A \quad (3)$$

All parameters are calculated for every month. The following parameters are known:  $Q_I$  from the bureau of waterworks,  $Q_O$ ,  $Q_R$ ,  $Q_E$  and  $dS/dt$  from the observations. The unknown parameters,  $Q_{GW}$ ,  $Q_S$  and  $Q_A$  are estimated as below. To calculate  $Q_{GW}$ ,  $Q_O$  is averaged over one month excluding rain times. Thus  $Q_S$  in equation (1) becomes equal to zero, and  $Q_{GW}$  can be calculated. The threshold of no rain time is defined as is less than 1mm precipitation during the previous 12 hours. Assuming  $Q_{GW}$  is constant when it rains or not,  $Q_S$  can be calculated from equation (1).  $Q_A$  is calculated as the residual of equation (2).

As a result, the annual water balance in residential area is revealed (Fig. 2). The input water, tap water and rain have approximately the same magnitude. Sewerage transfers not only wastewater from residences but also 46% natural water  $Q_{GW}$  and  $Q_S$ . When it doesn't rain sewerage still contains 27%  $Q_{GW}$ , so that the sewerage has a function (1) of an underground river. The same situation happens in Sapporo city, the sewerage contains about 30% of ground water [5].

### 2.3 Heat Balance in a Residential Area

The heat flow in connection with water flow in a residential area is similar to that of the water flow. The focus is

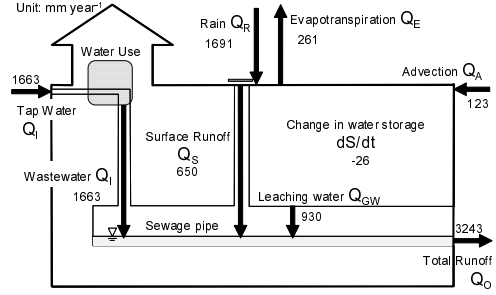


Figure 2: Annual water balance in residential area, 2004

now only set on the heat flow within an artificial drainage system. The heat balance equation of the artificial drainage system is analogous to the water equation (1):

$$H_I + \Delta H_U + H_{GW} + H_S - \Delta H_G = H_O \quad (4)$$

where  $H_I$  is the heat of tap water into the system,  $\Delta H_U$  is heat added by the water use,  $H_{GW}$  is the heat that leaching water takes from the soil into the sewage pipe,  $H_S$  is the heat that the surface runoff takes into the sewage pipe,  $\Delta H_G$  is the heat conducted from sewage out of the pipe,  $H_O$  is the heat that the sewage takes away from the system (Fig. 3).

To define each heat flux, it is necessary to set a reference temperature. Tap water temperature  $T_I$  is taken as the reference temperature because the objective is to estimate the heat added by using water and tap water is the input of artificial drainage system. Thus, each heat flux is defined as below.

$$\Delta H_U = \rho c_p Q_I (T_U - T_I) \quad (5)$$

$$H_{GW} = \rho c_p Q_{GW} (T_{GW} - T_I) \quad (6)$$

$$H_S = \rho c_p Q_S (T_S - T_I) \quad (7)$$

$$H_O = \rho c_p Q_O (T_O - T_I) \quad (8)$$

where  $\rho c_p$  is the heat capacity of water ( $= 4.19 \times 10^6 \text{ J m}^{-3} \text{ K}^{-1}$ ),  $T_U$  is temperature of used water,  $T_{GW}$  is leaching water temperature,  $T_S$  is the temperature of surface runoff,  $T_O$  is temperature of total runoff. Of course,  $H_I = 0$ .  $\Delta H_G$  is driven by the difference between the sewage temperature and the soil temperature. Thus, the sewage temperature before heat conduction  $T'_O$  is expressed as equation (9).

$$(T'_O - T_G) \cdot \exp(-kt) = T_O - T_G \quad (9)$$

where  $k$  is a coefficient,  $t$  is the time at that wastewater reaches the observation point.  $\Delta H_G$  is defined as below.

$$\Delta H_G = \rho c_p Q_O (T'_O - T_O) \quad (10)$$

$H_O$  consists of known data. If the observed soil temperature is used as  $T_{GW}$  and  $T_G$ ,  $H_{GW}$  and  $\Delta H_G$  can be calculated. If it doesn't rain,  $\Delta H_U$  is calculated from equation (4), if it rains,  $\Delta H_U$  is assumed as the same as in the no rain case, while  $H_S$  is calculated then.

As a result, the heat added by water use is up to  $0.7 \text{ W m}^{-2}$  in summer and  $3.4 \text{ W m}^{-2}$  in winter and each value

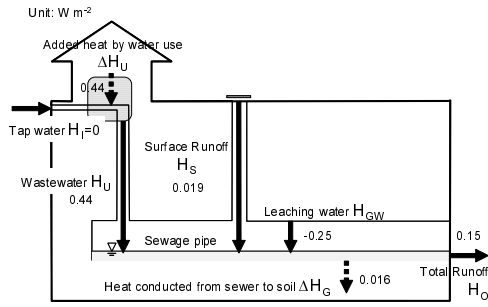


Figure 3: Heat balance in residential area in July

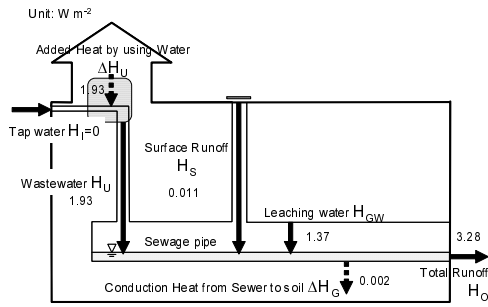


Figure 4: Heat balance in residential area in January

is equivalent to 3.2% of the whole anthropogenic heat in summer and 10% in winter (Fig. 3, 4). In summer, cold leaching water from the soil into the sewer pipe dilutes the sewage heat, whereas in winter, warm leaching water gives heat to the sewage.

### 3 Water Balance and Heat Balance in the Whole Urban Area

The used water reaches the WWTPs and is discharged to the hydrosphere after it has been treated. The WWTPs play a role of an interface between urban area and hydrosphere. Therefore, additional observations have been conducted at WWTPs in an urban area.

#### 3.1 Outline of the Observations

To estimate heat flux discharged from urban area, temperature sensors were set at all 13 WWTPs in the 23 wards of Tokyo metropolitan area. 8,396,000 residents live in catchment area of 621.49 km<sup>2</sup>. The set sensors are the same as that used in the residential area observation. The flow rate of influents into WWTPs and effluents from WWTPs are provided by the bureau of sewerage, Tokyo metropolitan government.

#### 3.2 Water Balance in the Whole Urban Area

The water flow in the whole urban area is basically the same as that in the residential area. WWTPs and pumping stations exist downstream of the urban area. When it doesn't rain, all runoff flows into WWTPs and is discharged to river or sea after the treatment. A part of water has been burned as sludge during the treatment processes and another part of water has been re-used as reclaimed

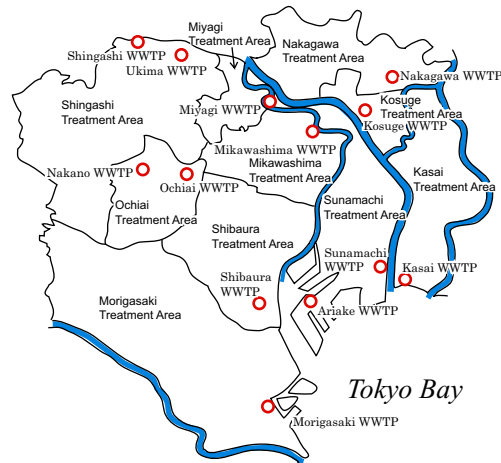


Figure 5: Wastewater treatment plant (WWTP) map

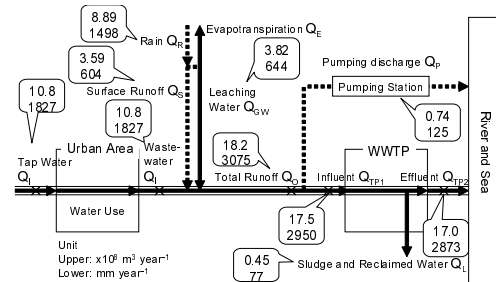


Figure 6: Annual water balance in whole urban area

water. However, when it rains, a part of the total runoff is discharged to directly rivers or the sea via pumping stations without having been treated to drain a large amount of rain. Thus, the water flow downstream of an urban area can be expressed by equations (11) and (12).

$$Q_O = Q_{TP1} + Q_P \tag{11}$$

$$Q_{TP1} = Q_{TP2} + Q_L \tag{12}$$

where  $Q_O$  is the total runoff (the same as in the residential area),  $Q_{TP1}$  is the influent into WWTP,  $Q_P$  is the pumping discharge,  $Q_{TP2}$  is the effluent from WWTP,  $Q_L$  is the sludge and reclaimed water. As  $Q_{TP1}$ ,  $Q_{TP2}$  and  $Q_P$  are known,  $Q_O$  and  $Q_L$  can be calculated (Fig. 6).

As a result, the amount of tap water supplied in urban area is larger than the amount of rain, i.e. the urban area receives some amount of water from outside of the urban area and the urban area isn't sustainable by rain falling down only the area (Fig. 6). Natural water  $Q_{GW}$  and  $Q_S$  is 35% of the total runoff  $Q_O$  which is similar to the observations in the residential area.

#### 3.3 Heat Balance in the Whole Urban Area

When estimating the heat balance in the whole urban area, the heat added in WWTP is different from the water balance (equation (14)).

$$H_O = H_{TP1} + H_P \tag{13}$$

$$H_{TP1} + \Delta H_{TP} = H'_{TP2} \tag{14}$$

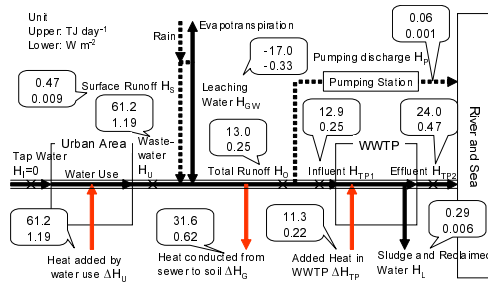


Figure 7: Heat balance in whole urban area in August

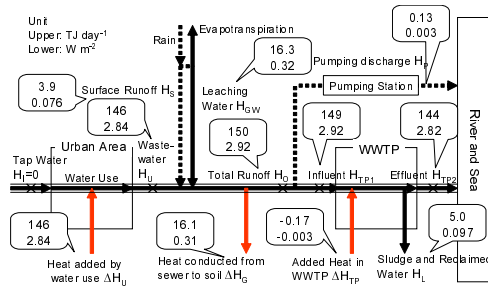


Figure 8: Heat balance in whole urban area in February

$$H'_{TP2} = H_{TP2} + H_L \quad (15)$$

where  $H_O$  is the heat, the sewage takes away from the urban area,  $H_{TP1}$  is the heat influent to WWTP,  $H_P$  is the heat drained at the pumping stations,  $\Delta H_{TP}$  is the heat added during the treatment in WWTP,  $H'_{TP2}$  is the sewage heat after treating,  $H_{TP2}$  is the heat effluent from WWTP to the hydrosphere.  $H_L$  is going out of WWTP as evaporation by burning sludge and as reclaimed water. They are defined by equations (16)-(21).

$$H_{TP1} = \rho c_p Q_{TP1} (T_{TP1} - T_I) \quad (16)$$

$$H_P = \rho c_p Q_P (T_P - T_I) \quad (17)$$

$$\Delta H_{TP} = \rho c_p Q_{TP1} (T_{TP2} - T_{TP1}) \quad (18)$$

$$H'_{TP2} = \rho c_p Q_{TP1} (T_{TP2} - T_I) \quad (19)$$

$$H_{TP2} = \rho c_p Q_{TP2} (T_{TP2} - T_I) \quad (20)$$

$$H_L = \rho c_p Q_L (T_L - T_I) \quad (21)$$

where  $T_{TP1}$  is the influent temperature into WWTP,  $T_P$  is the drained water temperature at the pumping stations,  $T_{TP2}$  is the effluent temperature from WWTP,  $T_L$  is the sludge and reclaimed water temperature. The observed temperature at influent point in WWTP is used as  $T_{TP1}$  and  $T_P$ , the other observed temperature at effluent point in WWTP is used as  $T_{TP2}$  and  $T_L$ .

As a result of the calculation, the heat added by water use in urban area for one year amounts to 9.1% of the whole energy use. The process of heat flow in sewage is revealed. In summer, the sewage loses its heat by conduction from the sewage out of the pipe and gains heat at WWTP. Totally, the sewage system reduces the heat and is discharged (Fig. 7). In winter, both the conducted heat and the heat added in WWTP are small. Thus the sewage system doesn't change the heat (Fig. 8).

## 4 Conclusions

The water balance and heat balance in a residential area are estimated, and the following results were obtained by observations.

1. Leaching water from soil into sewer pipe dominates 27% of the whole wastewater.
2. The heat added by the use of water amounts to  $0.7 \text{ W m}^{-2}$  in summer and  $3.4 \text{ W m}^{-2}$  in winter and each value is equivalent to 3.2% of whole anthropogenic heat in summer and 10% in winter, respectively.
3. In summer, cold leaching water from the soil into the sewer pipe dilutes the heat added by the use of water, whereas in winter, warm leaching water gives heat to the sewage.

The water transfer and heat transfer in the whole urban area are estimated by observation as follows.

4. The heat added by water use in urban area during one year amounts to 9.1% of whole energy use.
5. The process of heat flow in sewage is revealed. In summer, the sewage loses its heat by conduction from the sewage out of the pipe and gains heat at WWTP. Totally, the sewage system reduces the heat and is discharged. In winter, both the conducted heat and the heat added in WWTP are small. Thus the sewage system doesn't change the heat.

## References

- [1] Tsuyoshi Kinouchi. Long-term trend in thermal impact of urban water use on the receiving water - Case study of the sewerage system in the central Tokyo area and the Tokyo bay -. *J. Hydrosience and Hydraulics Eng.*, Vol. 47, pp. 25-30, 2003.
- [2] Ryo Moriwaki and Manabu Kanda. Radiation, Heat, Water Vapor and CO<sub>2</sub> Fluxes in an Urban Surface Layer. *J. Japan Society of Hydrology and Water Resources*, Vol. 16, No. 5, pp. 477-490, 2003.
- [3] Tsuyoshi Kinouchi, Yu Nakayama, Ryo Moriwaki, and Manabu Kanda. Investigation and modeling of water and heat transport in an urbanized catchment - Based on hydro-meteorological monitoring data collected in the Kugahara Experimental Site -. *J. Hydrosience and Hydraulics Eng.*, Vol. 48, pp. 175-180, 2004.
- [4] Yu Nakayama, Manabu Kanda, Tsuyoshi Kinouchi, and Ryo Moriwaki. Observation Study on Water and Heat Transfer in Urban Sewage System. *J. Hydro-science and Hydraulics Eng.*, 2006. accepted.
- [5] Yukio Hosoya. Sapporo-shi no chिकासुい shinsui boushi taisaku jigyou ni tsuite. *J. Japan Sewage Works Association*, Vol. 22, No. 249, pp. 112-123, 1985.

# Airport Capacity Analysis considering Terminal Air Traffic Flow Control and Airlines' Aircraft Sizing Behavior

Student Number: 04M18191    Name: Naoki YAMADA    Supervisor: Tetsuo YAI  
 空港管制とエアラインの行動からみた空港容量拡大に関する研究  
 山田直樹

わが国では航空需要の増加に対し、滑走路の新設等ハード面からの空港容量拡大によって対応してきており、管制方法やエアラインの行動の変化による容量増加等、ソフト面からの対策はあまり考慮されてきていない。本論文では、国内最大の混雑空港である羽田空港を対象として、容量拡大のための新たな管制方法とそれに対応した統計的容量算定方式の提案をし、さらに空港容量算定シミュレーションを活用し複数滑走路のインタラクションを考慮した容量拡大についても分析を行った。最後に、空港容量に大きな影響を与える機材構成について羽田空港再拡張後のエアラインの機材導入行動をモデル化し予測した。

## 1 Introduction

The demand of air transportation in Japan has increased steadily in recent years. The airport capacity has been improved mainly by developing infrastructure such as runway expansions. From the viewpoint of airlines, they have coped with the growth of air passenger demand by enlarging aircraft size.

In several foreign countries, airport capacity has been enhanced also by implementing flexible terminal air traffic control considering the aircraft size mix in addition to infrastructure improvements. Aircraft characteristics such as runway occupancy time, separation minima are different for each aircraft size. It is therefore important to consider these characteristics when considering airport capacity. Many academic researches also focuses on how to improve the capacity by flexible air traffic control<sup>(1)(2)(3)</sup>, but there are few researches of air traffic control for improving capacity in Japan.

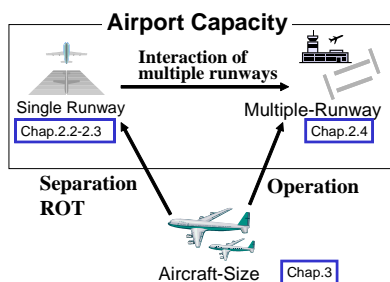


**Fig.1** Relation of runway capacity and aircraft size

With these backgrounds, first, this paper proposed a new method for calculating capacity corresponding to the flexible terminal flow control where the separation between two successive landing aircrafts is changed depending on the runway occupancy time (ROT) of the

leading aircraft. Secondly, the total capacity of HANEDA Airport after the new 4th runway construction (called re-expansion) was estimated by using the micro simulation<sup>(4)</sup> which can reproduce terminal air traffic flow in an airport with multiple runways when the several capacity enhancement scenarios were implemented. Finally, airlines' aircraft sizing behavior after the expansion of HANEDA was analyzed since the aircraft mix in the future is also important for estimating capacity.

## 2 Airport capacity enhancement by flexible terminal air traffic flow control

### 2.1 The current calculation method of airport capacity in Japan<sup>5)</sup>

This section shows the current calculation method of airport capacity of HANEDA Airport by Ministry of Land, Infrastructure and Transport (MLIT). In HANEDA, a takeoff and landing aircraft are basically operated separately in two runways before re-expansion. Since the runway capacity of landing is smaller than that of take-off, the total runway capacity is determined by the landing capacity (the number of landing and take-off aircraft should be the same). Therefore, the runway capacity of landing is only shown below.

The runway capacity is basically determined by the larger separation shown below;

- (a) The separation of the arrival aircraft in final approach ( 'Terminal radar control separation' or 'Wake turbulence separation' ) ,
- (b) Runway occupancy time (ROT) which means the time duration of passing through 1NM from runway threshold to end of exit-way.

Here, (a) is currently defined as 120 seconds regardless

of aircraft size mix, and (b) is defined as the sum of the three kinds of time duration as follows (also see Fig. 2).

30.0 (sec): the passage time of the distance of 1(NM) before the runway threshold, which is the time duration required to direct Go-Around when the leading aircraft still remains in runway (t1);

79.5 (sec): time duration between the runway threshold and the runway lateral edge at exit, which is calculated by summing 60 seconds of average and 19.5 seconds (2.6 times of 7.5 seconds of standard deviation) (t2);

15.0 (sec): time duration between the runway lateral edge (start point of exit-way) and stop line (end point of exit-way) (t3)

$$+ + = 124.5 \text{ (sec)}$$

Because of Time (a) < Time (b), the runway capacity of landing is  $3600/124.5=28.9$  28 (movements / hour). However, the latest declared capacity by MLIT is 30 (movements / hour) since t2 becomes 77 (sec) and t1 becomes 27 (sec) in the recent field survey of ROT in HANEDA Airport.

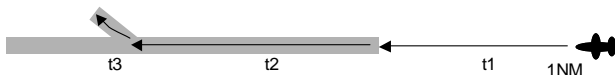


**Fig. 2** Runway occupancy time classification on runway of arrival aircraft

## 2.2 Proposal of a new terminal air traffic control and corresponding calculation method of capacity

In this section, we proposed a new flexible terminal flow control where the separation between two successive landing aircrafts is changed depending on the ROT of the leading aircraft. And we showed also the method for calculating capacity corresponding to the new air traffic control.

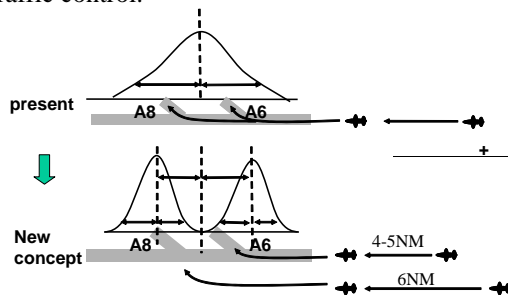


**Fig.3** Concept of new terminal air traffic flow control

**Table.1** Estimated runway capacity

The exit position of an arrival aircraft that are A6 and A8 exit (see Fig.3) can be grasped in advance in general

	ROT +Safety margin	Capacity /hour
New concept	118.84	30.29
Present	122.66	29.35

according to the aircraft size. Based on this premise, the separation of two successive landing aircrafts can be set 4-5NM when the leading aircraft is expected to use A6 exit (prior exit), and 6NM when the leading aircraft is

expected to use A8 exit (secondary exit).

This flexible air traffic control enables shortening of variation of ROT which is considered for calculating Time 2 (t2, see 2.1) because the variation of inter-group (here, group means exit A6 and A8) can be ignored by taking the risk of its variation with different separation mentioned above.

The result of calculating the landing capacity based on this new method is shown in Table.1. The actual observed data of ROT of each exit were used for this calculation. The result shows that this new air traffic control can increase the capacity of 1 (movement/hour) comparing the current method.

## 2.3 Examination of flying separation in terminal area

If ROT is less than 120 (sec), the flying separation at terminal area will become a bottleneck because it is defined as 120 (sec) uniformly. However, the ROT with the proposed new air traffic control may not be over 120 (sec). Therefore, we must consider also the capacity based on the flying separation at terminal area. According to the Air Traffic Control Standard, the separation is different depending on the combination of the size of successive aircrafts as shown in Table 2. However, in the present condition, management of the separation by the wake turbulence according to aircraft size is not performed. The flexible separation control might give the air traffic controller more workload. However, the flexible separation control is actually performed in several foreign countries such as Los Angeles international airport (LAX). Figure 4 shows the time separation of each aircraft size combination in LAX and HANEDA and Table 3&4 show the statistical test of the separation difference. From these results, we can see that LAX actually performs the flexible separation control. Therefore, HANEDA also has a potential to perform the flexible control although the current separation in HANEDA is uniform.

Average separation when considering the flexible separation control can be less than 120 (sec) because the separation after the medium size aircraft is around 90 (sec). Therefore it might not be the bottleneck to determine the capacity. However, the speed difference and the runway exit position depending on aircraft size are also necessary to consider all together. These factors are considered in the next section.

**Table.2** Separation distance of wake turbulence

leading aircraft	following aircraft	separation(NM)
Heavy	Heavy	4
	Medium	5
Medium	Heavy	3
	Medium	3

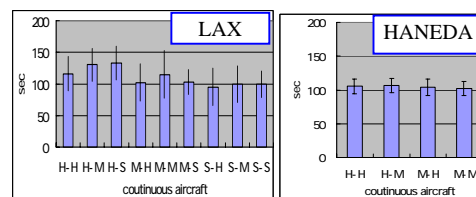


**Fig.4** Separation time at runway threshold ( Los Angeles International Airport and HANEDA )

**Table 3** Result of t-test about time separation difference in HANEDA Airport

	H-H	H-M	M-H	M-M
H-H			P=0.56	P=0.48
H-M			P=0.29	P=0.18
M-H			P=0.59	

**Table 4** Result of t-test about time separation difference in LAX

P value	H-H	H-M	H-S	M-H	M-M	M-S	S-H	S-M	S-S
H-H	x	0.011**	0.031**	0.016**	0.841	0.015**	0.007*	0.005**	0.027**
H-M	x	x	0.700	0.00*	0.002*	0.00*	0.00*	0.00*	0.00*
H-S	x	x	x	0.00*	0.014**	0.00*	0.00*	0.00*	0.00*
M-H	x	x	x	x	0.013**	0.862	0.323	0.553	0.665
M-M	x	x	x	x	x	0.010*	0.007*	0.003*	0.03**
M-S	x	x	x	x	x	x	0.252	0.418	0.571
S-H	x	x	x	x	x	x	x	0.589	0.647
S-M	x	x	x	x	x	x	x	x	0.996
S-S	x	x	x	x	x	x	x	x	x

### 2.4 Estimation of capacity enhancement after HANEDA re-expansion by using air traffic simulation system and by changing aircraft size composition

In this section, the estimation of the airport capacity of HANEDA with 4 runways (see Fig.5) is conducted by using air traffic micro simulation system developed by Hiramatsu (4). This simulation system can reproduce the microscopic behavior of landing and take-off aircraft at terminal air flow control area and it is already validated comparing with actual current capacity data. This system is very useful to estimate airport capacity because it can consider the interaction of multiple runways and can change aircraft behaviors easily. Fig.5 shows also the planned capacity after re-expansion by MLIT.

We first estimated the capacity when implementing the new air traffic control introduced in section 2.2 and 2.3. Secondly, we also designed the other two kinds of new air traffic flow control and estimated the capacity with those controls.

We hypothesized analysis scenarios as follow.

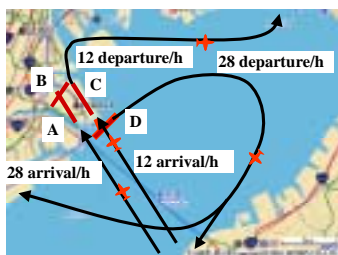


**Fig.5** Arrival and Departure route after re-expansion in HANEDA

(Operation 0)In A-runway landing separation control considering leading aircraft's ROT which introduced in section 2.2&2.3 (All scenario except Mlit plan);  
(Operation 1)Separation control of landing aircraft in C-runway for alternating control of landing in C-runway and take-off in each C- & D-runways; (Basically alternating control of landing and take-off might be most efficient in one runway, so the landing separation in C-runway is controlled based on the minimum separation required for take-off in C & D-runway between landing aircrafts of C-runway)(scenario 1, 2, 3);  
(Operation 2) Segregation of runway usage according to airlines (the airlines which use Terminal1 is landing in A-runway and which use Terminal 2 is landing in C-runway )(if aircraft which uses Terminal 2 is landing A-runway, this one tend to use far runway exit and take longer time than using C-runway)(scenario 2, 3)

(Operation 3) Segregation of runway usage according to aircraft size (only small aircrafts (B737) A-runway landing and others landing to C-runway(D). (in operation1, the separation of landing aircraft in C-runway is larger than normal separation minima, so aircraft mix has almost no effect on capacity in C&D-runway. However landing of only small (medium) aircraft may have significant effect on capacity in A-runway(scenario 3 ));

Table.5 shows the results on each scenario. It was shown that the capacity of the airport increased by each scenario. Especially by operation 1 airport capacity increase significantly because in MLIT plan there may be still unused capacity in C-runway. Then figure 6 shows relationship between airport capacity and aircraft size composition. It shows the share of aircraft has considerable influence to airport capacity. Therefore, according to it and scenario3 the trend of aircraft size mix in the future is also important for enabling abovementioned flexible air traffic controls and effect to airport capacity. In the next chapter, we developed the model of aircraft purchase behavior by airlines and analyzed the future trend of aircraft size mix after re-expansion on HANEDA Airport.

**Table.5** Analysis scenario and result of each scenario

Scenario	MLIT	Base	1	2	3	
(Operation0): Separation Control considering Leading Aircraft's ROT	-	(A)	(A)	(A)	(A)	
(Operation1): Alternating Control of Landing and Take-off in C-runway	-	-	-	-	-	
(Operation2): Segregation of Runway Usage according to Airlines (preventing large ROT caused by each airline's terminal building position)	-	-	-	-	-	
(Operation3): Segregation of Runway Usage according to Aircraft Size (medium aircraft in A-runway and heavy aircraft in C-runway)	-	-	-	-	-	
Estimated Capacity (movements / hour)	Landing in A-runway	28.0	30.0	30.1	30.2	32.1
	Landing in C-runway	12.0	10.8	19.0	19.0	18.2
	Take-off in C-runway	12.0	20.0	24.9	24.8	25.4
	Take-off in D-runway	28.0	20.4	24.9	25.1	25.4
	Landing - TOTAL	<b>40.0</b>	<b>40.9</b>	<b>49.1</b>	<b>49.2</b>	<b>50.3</b>
Take-off - TOTAL	40.0	40.4	49.8	49.8	50.7	

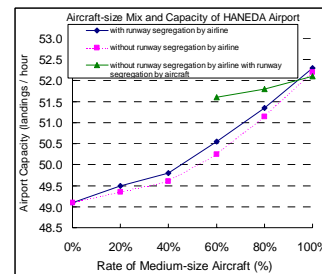


**Fig.6** Result of Aircraft size mix and airport capacity in HANEDA Airport

### 3. Model analysis of airline's aircrafts purchase behavior after HANEDA re-expansion

Officially, further expansion of the capacity of HANEDA airport is scheduled in 2009. I conducted the model analysis of airlines' aircraft sizing behavior to understand the trend which airlines purchase and hold aircrafts after the expansion.

#### 3.1 Model

We assume that there are two homogeneous airline industries in the market. Airlines seek to maximize the net present value over 20 years. The timing of decision purchasing aircrafts of airline is year 2007, by which I take into account the duration for the education of pilot and time lag between order and delivery of aircrafts. I also assume that airlines have the two options for

purchasing aircrafts. The first option is carried out in 2009 when HANEDA Airport will be re-expanded. The second option is exercised in 2014, five years' later of HANEDA's re-expansion. Except for these two timings, airlines can neither purchase aircrafts nor increase flight volume. All purchased aircrafts are used for service.

I assume that the three strategies of airlines for purchasing aircrafts for simplification.

1. Purchasing large-sized aircrafts
2. Purchasing small-sized aircrafts
3. Deferring purchase for aircrafts

When airlines purchase new aircrafts, they will decide the number of purchased aircrafts so that they can ship ten million passengers per year. I set the number of seats of large-sized aircrafts is 400 people assuming they are B747 or B777, while those of small-sized aircrafts are 100 people assuming that they are B737 or RJ.

Annual average Load Factor (LF) is fixed to be 70%. When the traffic volume which will be assigned by logit-based passenger demand model exceed the number of offered seats in the future, airlines' will choose one of the following two options: (1) changing small-sized aircrafts to large-sized aircrafts; (2) abandoning the excess demand (which will assumed to shift to other travel modes).

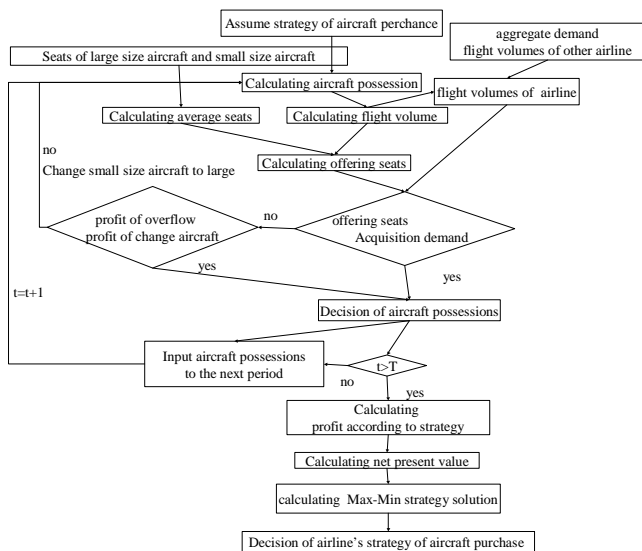


Fig.7 Algorithm for calculating airlines' profit

### 3.2 Numerical Simulation

Each airline decides the type and the number of purchased aircrafts. Finally, their owned aircrafts and profit will be calculated for each time period. This takes the form of a strategic game between competitive two airlines and they will decide the optimal strategy according to their NPV. The detailed procedure for this is shown in Fig.7. Parameters for numerical simulation are not shown due to limited space.

Fig.9 shows the equilibria (i.e. the combination of Max-Min strategies) in two-person game for several situations. For the case where the expansion of HANEDA will be conducted only in 2009 (single expansion), the solution of the game is purchasing small-sized aircrafts for each airline for each stage, while Pareto optimality in this game is pass up at first stage and purchase large-sized aircrafts at second stage. It

implies that unless two airlines try to purchase their aircrafts in cooperation with each other, airline operate highly-frequent career service with small-sized aircraft in order not to lose share of slot to competitors. On the other hand, if airlines behave cooperatively, airlines operate large-sized aircrafts with low cost per seat mile, and with low frequency in response to demand increases, keeping mint slots.

Now, we assume that the expansion of HANEDA will be conducted at two-steps and the slots for airlines are released 2 times. Fig.9 also shows the Max-Min solution for such situation: purchasing large-sized aircrafts at the first step and choosing small-sized aircrafts to buy at the second. Pareto optimality is also as same as slots released 1 times. It implies that if the government increases the airport capacity by slow degrees, airlines tends to upsize their aircrafts in earlier stage.

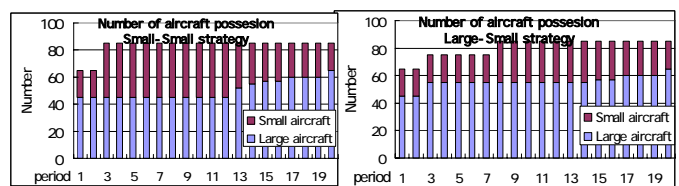


Fig.8 Number of aircraft possession

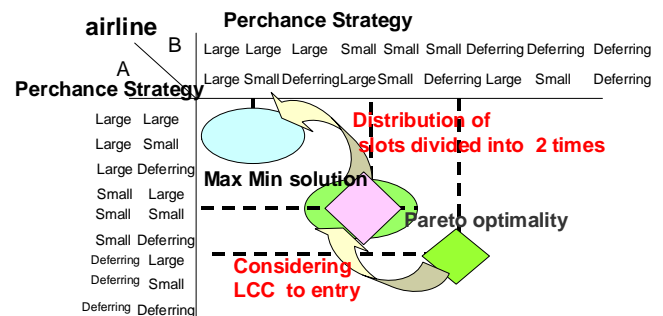


Fig.9 Optimal strategy

### 4 Conclusion

The result of this research is the following two points.

- The new terminal air traffic controls for enhancing the capacity were proposed.
- The future aircraft size mix after HANEDA re-expansion was analyzed by modeling airline's aircraft purchasing behavior.

### Reference

- 1) Eugene P. GILBO [1993], "Airport Capacity: Representation, Estimation, Optimization", IEEE Transactions on Control Systems Technology, Vol.1, No.3, pp. 144-154.
- 2) D.E.Pitfield, E.A.Jerrard [1999], " Monte Carlo comes to Rome : a note on the estimation of unconstrained runway capacity at Rome Fiumucino International Airport ", Journal of Air Transport Management, Vol.5, Issue.4, pp.185-192.
- 3) Matteo Ignaccolo [2003], "A Simulation Model for Airport Capacity and Delay Analysis", Transportation Planning and Technology, Vol.26, No.2, pp.135-170.
- 4) Takeshi HIRAMATSU [2005], "Calculation Method of Airport Capacity Considering Air Traffic Management and Aircrafts' Noise", Master's thesis of Tokyo Institute of Technology
- 5) Transport Ministry Civil Aviation Bureau et al [1999], report of survey about airport capacity